Volumetric additive manufacturing in a scattering resin

Jorge Andres MADRID WOLFF

Acknowledgements

I've been very fortunate to pursue a PhD at EPFL in the lab of Prof. Christophe Moser, my supervisor. I'd like to thank you, Chris, for giving me this opportunity and creating such a nurturing research environment. I've learned a lot from and thanks to you.

I'd like to thank the members of the jury, Profs. Martin, Serra, Glückstad, and Subramanian for their time to evaluate and correct this thesis, and to Chris for proof-reading it.

This thesis would not have been possible if it hadn't been for those who came before me; thank you Paul and Damien for your great spark of creativity! It wouldn't have been possible either without those with whom I shared the ride. To my dear collaborators, colleagues and friends Antoine, Viola, Lorenzo, and Paulina: thanks for everything you have taught me.

Most of the learning came from teaching. I thank the students who trusted in me to accompany them in their projects: Max, Roberto, Estée, Florian, Théo, Mathieu, Diego, Laura, Nicolas, Marwan, and Michael. A lot of the work in this thesis was done by you. It was a great pleasure to discover by your side. Talking discovery, I thank Alan, my favorite artist, for all the artistic science.

To Sabrina, who makes everything happen seamlessly, thank you.

The adventure would not be the same without the fun: thanks to my labmates and dear friends Chiara, Jan, Babak and Maya, Maria and Buse, and Qianyi, Ilker, Mustafa, Ulas, Carlo, Leo, Boris, Laura, Felix, and Victoria. :) Once again I'll agree with wise Chiara; LAPD *somehow* attracts fantastic people.

Thank you Margarita, Sergio, and Lukas, my loving flatmates. From my heart. Y a la familia y los amigos que están lejos pero se mantienen cerquita en el corazón.

Esta tesis está dedicada a mis padres -siempre listos a apoyarme, a Mario, mi hermano a quien tanto admiro, et à toi, Jordan, qui remplis mes journées d'autant de lumière.

Lausanne, October 10th*, 2023*   Jorge

i

Abstract

 Additive manufacturing has become a transformative fabrication method in a wide variety of applications, including prototyping, tissue engineering, aerospace, and dentistry. Recently, tomographic volumetric additive manufacturing was introduced as a new light-based fabrication method that enables the production of support-free cm-scale objects within seconds.

Tomographic volumetric additive manufacturing works by solidifying an entire 3D object simultaneously by irradiating a liquid photocurable material from multiple angles with dynamic light patterns. The method relied on homogeneous and relatively transparent resins, so that the light patterns used for photo-polymerization are not scrambled along their propagation. Many interesting materials, such as composite and nanoparticle-filled resins or cell-laden hydrogels, are scattering and were not well adapted to tomographic additive manufacturing.

In this thesis, the fabrication method is extended to scattering resins. *1)* Refractive-index matching and *2)* a computational method that considers light scattering in the resin prior to computing projection patterns are proposed. The improvement in print fidelity is quantified and the relevance of the methods are demonstrated through the bioprinting of hydrogels with up to 5 million cells mL^{-1}, pushing the application regime of light-based volumetric fabrication methods. Additionally, the scattering correction is also applied to fabricate in vitro models of the exocrine pancreatic unit containing human cells. These models are used to study the cross-talk between stromal and cancerous pancreatic cells, mimicking the early stages of pancreatic cancer.

A corollary of the computational framework for scattering is the correction of light absorbance from the resin and its photoinitiators. We exploit this to expand the library of materials for tomographic volumetric additive manufacturing to polymer-derived silicon oxycarbide ceramics and nanocomposite and phase-separating silica glasses. These ceramics, for example, are thermally resistant (up to 1400°C) and could be used in the fabrication of microsatellites.

Inspired by helical computer tomography scans, the maximum printable size for tomographic printers is expanded by incorporating a helical motion to the rotating photopolymer vial. Thanks to this, objects with 4 times larger cross-sections and up to 3 times taller can be fabricated without compromising print resolution.

Key words: 3D printing, light-based additive manufacturing, light scattering, biofabrication, polymer-derived ceramics

Résumé

L'impression 3D est devenue une méthode de production transformatrice dans une grande variété d'applications, notamment le prototypage, l'ingénierie de tissus, l'aérospatiale et la dentisterie. Récemment, la fabrication additive volumétrique tomographique a été introduite en tant que nouvelle méthode de fabrication utilisant la lumière pour produire des objets à l'échelle centimétrique sans supports en quelques secondes. Dans la fabrication additive volumétrique tomographique, un objet tridimensionnel est solidifié simultanément en entier, en irradiant un photopolymère liquide depuis plusieurs angles avec des motifs lumineux dynamiques. La méthode reposait sur des résines homogènes et relativement transparentes, de sorte que les motifs lumineux utilisés pour la photo-polymérisation ne deviennent pas flous le long de leur propagation. De nombreux matériaux intéressants, y-compris les résines composites et chargées de nanoparticules ou les hydrogels contenant des cellules, sont diffusifs et ne sont pas bien adaptés à la fabrication additive tomographique.

Dans cette thèse, la méthode de fabrication est étendue aux résines diffusantes. Deux solutions sont alors proposées : *1)* la réduction de différences dans l'indice de réfraction et *2)* une méthode computationnelle qui tient compte de la diffusion de la lumière dans la résine avant de calculer les motifs lumineux à projeter. L'amélioration de la fidélité d'impression est quantifiée et la pertinence des méthodes est démontrée par la bioimpression d'hydrogels de gélatine contenant jusqu'à 5 millions de cellules par ml. De plus, la correction est également appliquée pour fabriquer des modèles in vitro du pancréas exocrine, contenant des cellules humaines. Ces modèles sont utilisés pour étudier l'interaction entre les cellules pancréatiques stromales et cancéreuses, imitant les premiers stades du cancer du pancréas.

Un corollaire de la méthode de calcul qui tient compte de la diffusion de la lumière est la correction de son absorbance par la résine et ses photoinitiateurs. Nous exploitons ce corollaire pour inclure dans les matières imprimables de façon tomographique les céramiques d'oxycarbure de silicium dérivées de polymères et les verres de silice (nanocomposites et à séparation de phases). Ces céramiques, par exemple, sont thermiquement résistantes (jusqu'à 1400°C) et pourraient être utilisées dans la fabrication de microsatellites.

Inspirés des scans de tomographie hélicoïdale par ordinateur, la taille imprimable maximale pour les imprimantes tomographiques est étendue en incorporant un mouvement hélicoïdal au flacon rotatif de photopolymère. Grâce à cela, des objets avec des sections transversales 4 fois plus larges et jusqu'à 3 fois plus longs peuvent être fabriqués sans compromettre la résolution d'impression.

Mots clefs : Impression 3D, fabrication aditive basée sur la lumière, diffusion de la lumière, bioimpression, céramiques dérivées de polymères

Contents

List of Figures

List of Tables

1 | Light-based additive manufacturing

This chapter introduces 3D printing and describes the light-based technologies used in additive manufacturing applications. It then presents the molecular bases of photocuring and uses acrylates as an example to discuss photopolymerization. Finally, vat photopolymerization technologies are outlined and compared.

1.1 Additive manufacturing

Additive manufacturing has been a disruptive force since its wide-spread adoption. It has most directly impacted prototyping, radically reducing times between object ideation and manufacturing. Thanks to an expanded library of materials and fabrication methods, the commercial and industrial applications of additive manufacturing now reach a wide range of fields including aerospace and car racing for metallic pieces, skin grafts in tissue engineering, and dental prostheses and retainers.

Additive manufacturing methods work by solidifying a material that is otherwise in a liquid or a powder form. As an example fused deposition modelling (FDM), a popular technology among desktop 3D printers, melts a stock polymer with heat, then deposits the material sequentially, filling one voxel after the other (fig. 1.1a). Analogously, liquid gels can be extruded with pressure into a supporting bath, as is the case of FRESH, and then thermally solidified or photocured (fig. 1.1b). [1]–[3] The support bath of FRESH offers the possibility to fabricate objects with overhangs or hollow cavities. In addition to pressure, high voltage can thin an extruded material into a Taylor cone, producing micron-sized fibers of very constant diameter in a method called melt electrowriting (MEW). The fibers can be then spun onto a rapidly moving collector to build up the desired geometry, where they solidify after cooling down (fig. 1.1c). [4]

Light can also be used to give the required energy to solidify the working material. In selective laser sintering (SLS), high-intensity CO_2 lasers are typically used to locally melt and fuse metallic pellets, one voxel at a time, as the light from the laser is steered across the powder bed (fig. 1.1d). In an alternative approach, visible or UV light can be used to trigger polymerization of a liquid monomer resin. In such photopolymerization processes, liquid materials solidify typically using an intermediary molecule called a **photoinitiator**. The photoinitiator goes from a ground to an excited electronic state upon light absorption. Once in the excited state, the photoinitiator becomes reactive and triggers the polymerization of the liquid monomers. In sterolithography (SLA, fig. 1.1e), [7] voxels are polymerized in a sequential manner by projecting a laser point onto the bottom of the resin vat. SLA can be used
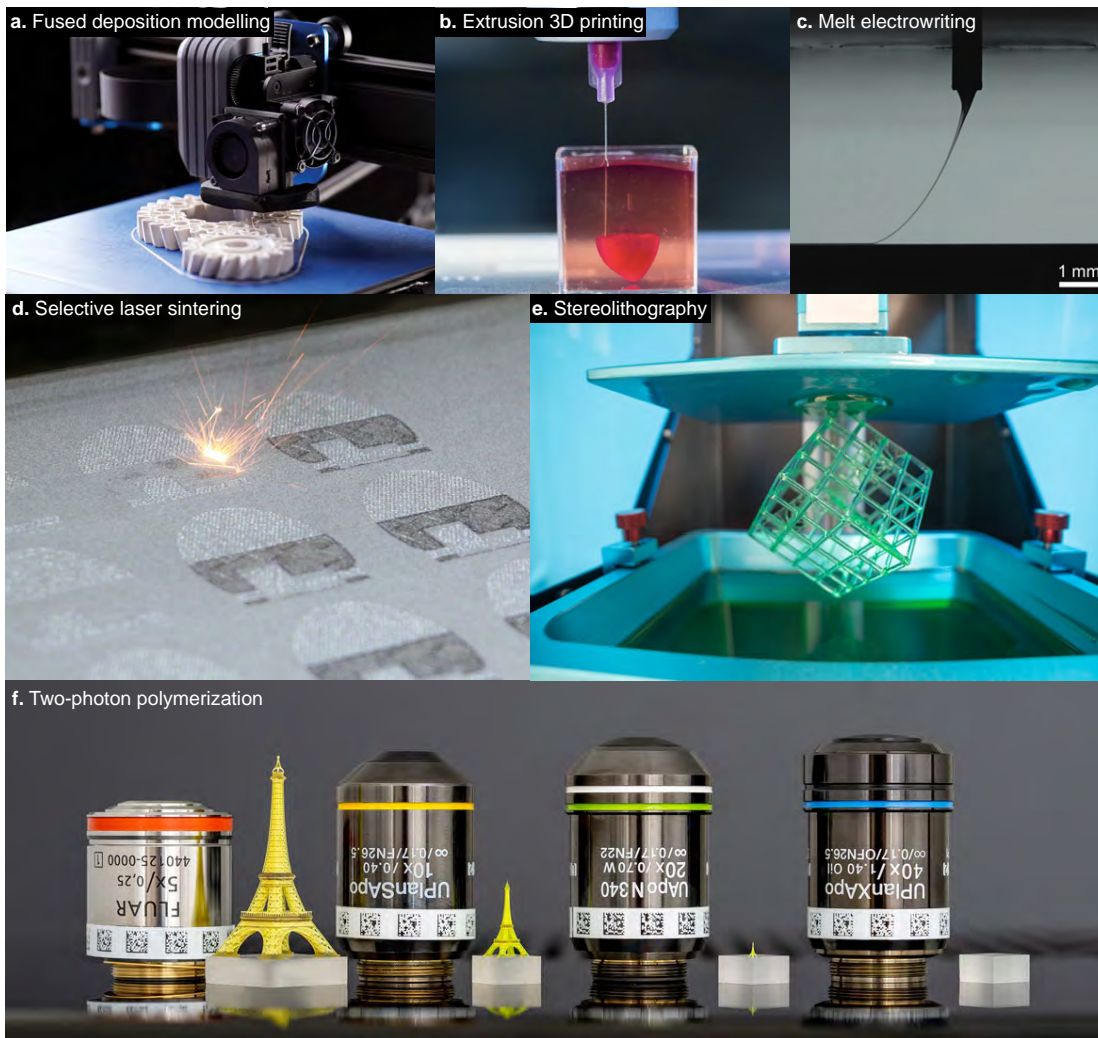
Figure 1.1: **Examples of 3D printing methods**. **a.** Fused deposition modelling (FDM). Reproduced from *hlhrapid.com/knowledge/what-is-fdm-3d-printing/*. **b.** Extrusion 3D printing, and FRESH (Freeform Reversible Embedding of Suspended Hydrogels) in this particular case. Reproduced under CC-BY 4.0 from [5]. **c.** Melt electrowriting (MEW). Reproduced under CC-BY-NC 4.0 from [6]. **d.** Selective laser sintering (SLS). Reproduced under CC BY-NC 4.0 from *all3dp.com*. **e.** Stereolithography (SLA). Reproduced from *fastradius.com/resources/vat-photopolymerization/*. **f.** Two-photon polymerization. Reproduced from *upnano.at*

to fabricate large objects with a resolution down to hundreds of microns within hours. The method has been widely adopted and is currently used by the dental retainer industry to fabricate models of patients' teeth. On the other hand, two-photon polymerization (2PP) relies on the non-linear simultaneous absorption of two photons by the photoinitiator to strongly decrease the size of each polymerized voxel. [8], [9] In two-photon polymerization, microscope objectives are used to focus pulsed lasers into micron-sized regions. Although the process is slow, it enables the fabrication of microdevices at unrivalled resolutions (fig. 1.1f).

1.2 Photoinitiators and photopolymerization

Photoinitiators are light-sensitive molecules that transition into a reactive state upon the absorption of a photon. Once in the excited reactive electronic state, photoinitiators can trigger polymerization of monomers or cross-linking of hydrogel chains by donating a free electron. Photoinitiators have particular absorbance spectra, which match the possible energy differences between the excited and the ground state. Many common photoinitiators are organic salts, splitting into two excited groups, each with a free radical, as seen in fig. 1.2a for TPO (Diphenyl(2,4,6-trimethylbenzoyl)phosphine oxide), a commonly used photoinitator. The free radical is depicted with a black circle for the unpaired electron. At a molecular level, photoinitiators typically have π-bonds connected to aromatic rings; which increase their photon absorbance cross-section. [10] Photoinitiators can be designed to absorb light at different wavelengths, [11] although most efficient initiators absorb in the UV or blue parts of the spectrum. Producing efficient photoinitiators that absorb longer wavelengths is an active field of research. [12] Fig 1.2b shows the spectral dependence of the molar extinction coefficient of TPO and camphorquinone (CQ), both photoinitiators used in tomographic VAM. The molar extinction coefficient (ϵ), a measurement of the spectral absorbance normalized by molarity, is derived from Bouguer-Beer-Lambert's law:

$$A = -\log \frac{I(l)}{I_0} = \epsilon c l$$

Where A is the absorbance, $I(l)$ is the light intensity at a given depth l, and c is the concentration of the absorber. Bouguer-Beer-Lambert law is illustrated in fig. 1.2, where a 510 nm laser beam is attenuated as it traverses three cuvettes with decreasing concentrations of an absorber, the fluorophore Rhodamine 6G. What is visible in the pictures is the fluorescence from the Rhodamine, which indicates the remaining light intensity. In the left-most cuvette, Rhodamine is so concentrated that there is no visible fluoresence from the right end of the cuvette.
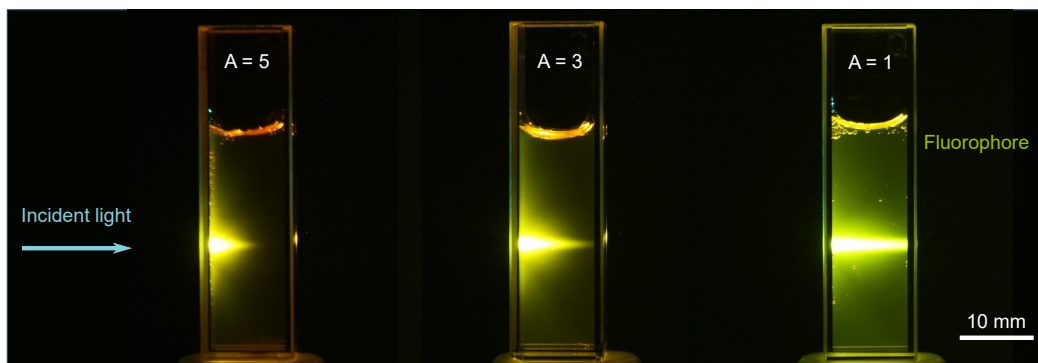
Figure 1.2: **Bouguer-Beer-Lambert's law.** The amount of light decreases exponentially as it travels through an absorbing medium. In the picture, light travels through 10-mm cuvettes filled with solutions of decreasing concentrations of Rhodamine 6G, a fluorophore. Penetration depth increases as the concencration of the absorber decreases. Adapted from Edinburgh Instruments.

Photoinitiators that are highly efficient and have low molar extinction coefficients (which means less aborbtive) are preferred for tomographic VAM. This is not necessarily the case for other 3D printing technologies such as DLP or VAM, where higher absorbance could be preferable. This is why, in

tomographic VAM, TPO was excited at 405 nm [13] and CQ at 440 nm, [14] away from their absorbance peaks (fig. 1.2b).

Acrylates are versatile materials with broad industrial applications in coatings, sealants and plastics. They can be easily cured using light; [19] so we use them as reference material in this work. After the photoinitiator is excited in a photocuring process, it can react with acrylate monomers, giving them a free radical, as seen in fig. 1.2e. Then, a chain reaction follows where new monomers are added to the polymer chain, like building blocks. The chain can continue to grow even when no more photoinitiator molecules are produced. This makes the reaction efficient and reduces the required stoichiometric concentrations of photoinitiator; but leads to unwanted effects such as dark curing, where polymerization continues even after the light source has been turned off. [19] Polymer chain growth can be terminated by the fusion of several chains, or by the reaction of the free radicals in the polymer chain with an excited photoinitiator. Acrylate polymerization is characterized by the conversion from a terminal double carbon bond (shown in blue) to a single bond (shown in red). The resonance IR spectra of these two bonds are different, thus FTIR spectroscopy can be used to quantify the proportion of double bonds that have converted to single bonds, a good indication of polymerization. Fig. 1.2f shows the progression of carbon bond conversion with light dose. Liquid acrylates solidify, or gel, only when a given proportion of monomers have been polymerized, resulting in a gelation threshold. The light dose needed to transition from liquid to solid is called the threshold dose. Conversion starts slow when initiation is inhibited by any electron-scavenging species, such as molecular oxygen diluted in the monomer resin. [20] Oxygen inhibition can be detrimental in some applications, but in tomographic VAM it simplifies thresholding between solidified and liquid parts of the resin. Once oxygen has been depleted, polymer chain growth speeds the conversion, until monomers become less abundant, and conversion decelerates. Chain-to-chain termination and the consumption of the photoinitiator make the conversion saturate at values below 100%. We use acrylate photopolymerization as an example, although tomographic VAM has been demonstrated in other photocurable materials, such as epoxies and thiols. [21], [22] Thiol-ene photopolymerization, is mostly unsensitive to oxygen inhibition and the stiffness of the resulting prints can be tuned with dose. [21], [23]
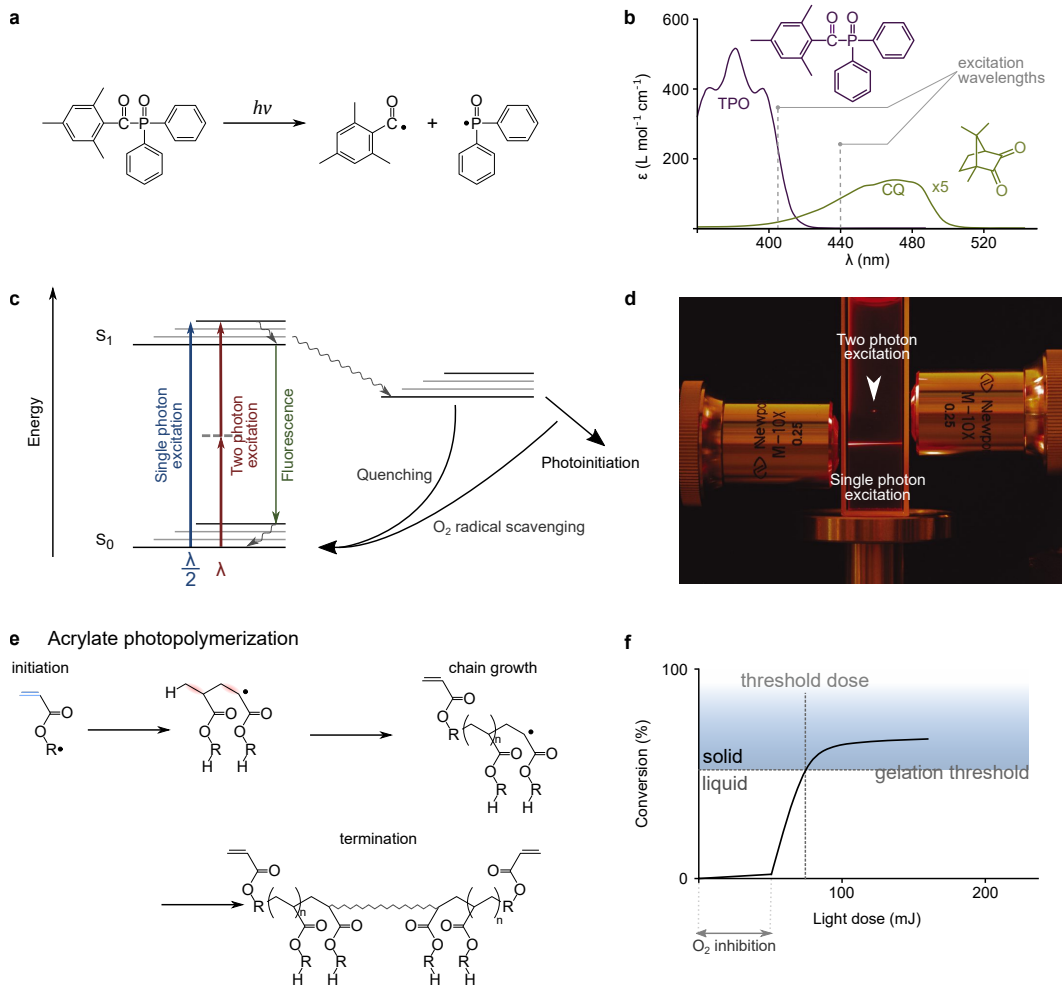
Figure 1.3: **Photoinitiation and photopolymerization**. **a.** TPO, a common potoinitiator, splits into two reactive subunits, each with a free radical, upon the absorbance of a photon. **b.** Wavelength-dependence of the molar extinction coefficients of two photoinitiators camphorquinone (CQ) and TPO (data from [15]), with the wavelengths at which they were excited in recent tomographic VAM works. **c.** Energy level diagram of photoinitiation. The photoinitiator can transition to the excited state after absorbing one high-energy photon or simultaneously absorbing two photons with double the wavelength, through a virtual state. The excited photoinitiator can relax to the base state by emitting fluorescence, or it can induce polymerization. Image adapted from [16]. **d.** Single-photon and two-photon absorption by a fluorescent medium. The cross-section of the fluorescent spot in two-photon absorbance depends on the square of the intensity, an is much more confined. Image credit: Newport corporation. **e.** Acrylate photopolymerization. Acrylate monomers (R stands for any alkyl chain), get a free radical after reacting with an excited photoinitiator. Multiple active monomers can react to form polymer chains; a process that terminates by the fusion of two chains, for example. [17] **f.** Typical conversion curve of acrylates, [18] a common photoresist in this thesis. Liquid acrylates gelate when the degree of conversion (the proportion of double carbon bonds that have been converted to single bonds) surpasses a threshold. The light dose at which gelation occurs is called the "threshold dose".

1.3   Vat photopolymerization

Until only a few years ago, the conventional approach in light-based additive manufacturing, or 3D printing, relied on constructing objects by piling 1D voxels or 2D layers on top of each other. Each layer being formed by the solidification of a photoresist under light irradiation, for example, by either scanning a laser beam point-by-point, as in stereolithography [7] or two-photon fabrication, [9], [24] or by projecting 2D light patterns, as in digital light processing (DLP) technology. [25], [26]

Recently, several new techniques for the additive manufacturing of photo-sensitive materials have been proposed, including the holographic display of light patterns, [27] tomography, [13], [28], [29] and xolography.[30] They derive from the layer-by-layer process by fabricating centimeter-scale objects in a true 3D fashion. This is achieved by illuminating the entire resin's container with one or a set of light patterns used for photo-polymerization. The cumulative light exposure results in a volumetric energy dose that is sufficient to solidify the material in the desired geometry. The main advantages of these methods is that: 1) they are **volumetric**, meaning that the object is printed within the resin, with the resin supporting the built object (which removes the need for support struts); and 2) they are **non-sequential**, meaning that voxels are not polymerized one after the other.

Here we describe these vat photopolymerization methods, present their working principle, their main strengths and shortcomings, and name some commercial applications of the technologies. The comparison between these methods are summarized in fig. 1.4 and table 1.1.

Stereolithography

In stereolithography light from a laser is rastered onto a vat of photopolymerizable resin using a steerable galvo mirror, as seen in fig. 1.4a. The laser spot is small by design, so polymerization is localized and occurs fast. Thanks to this, there is no need to integrate the laser beam for long times at each voxel. The object is built onto a platform, which moves upwards after each layer is completed. To prevent the photocuring of voxels deeper into the vat, photoresins incorporate light absorbers in addition to photoinitiators. [31] The concentration of these light absorbers, which include dyes such as Sudan I, is tuned following Bouguer-Beer-Lambert's law to the desired layer thickness. Stereolithography 3D printers have benchmark resolution among desktop 3D printers and can produce smooth, almost layer-less finish to printed parts. Stereolithography is commercially widespread, with Formlabs, a former MIT spinoff, producing desktop printers optimized for ease-of-use, and 3D systems, a company based in South Carolina, selling industrial printers for serial production.

Digital light processing

Digital light processing (DLP) uses a similar approach to stereolithography, except that instead of rastering a laser spot, full layers are polymerized at once by projecting 2D light patterns, as seen in fig. 1.4b. These light patterns, which correspond to the cross-sections of the target object, are produced by a digital micromirror device (DMD). The DMD contains millions of micrometric mirrors that can be steered at kHz frequency between an ON and an OFF state. Due to the larger area of the displayed patterns, LEDs instead of lasers are typically used as light sources. The invention of transparent windows which are permeable to oxygen increased the possible printing speeds, in a process named continuous liquid interface production (CLIP). [25] CLIP exploits oxygen inhibition of polymerization to produce a "dead zone" about 10 microns in thickness above the window, preventing the new layer to
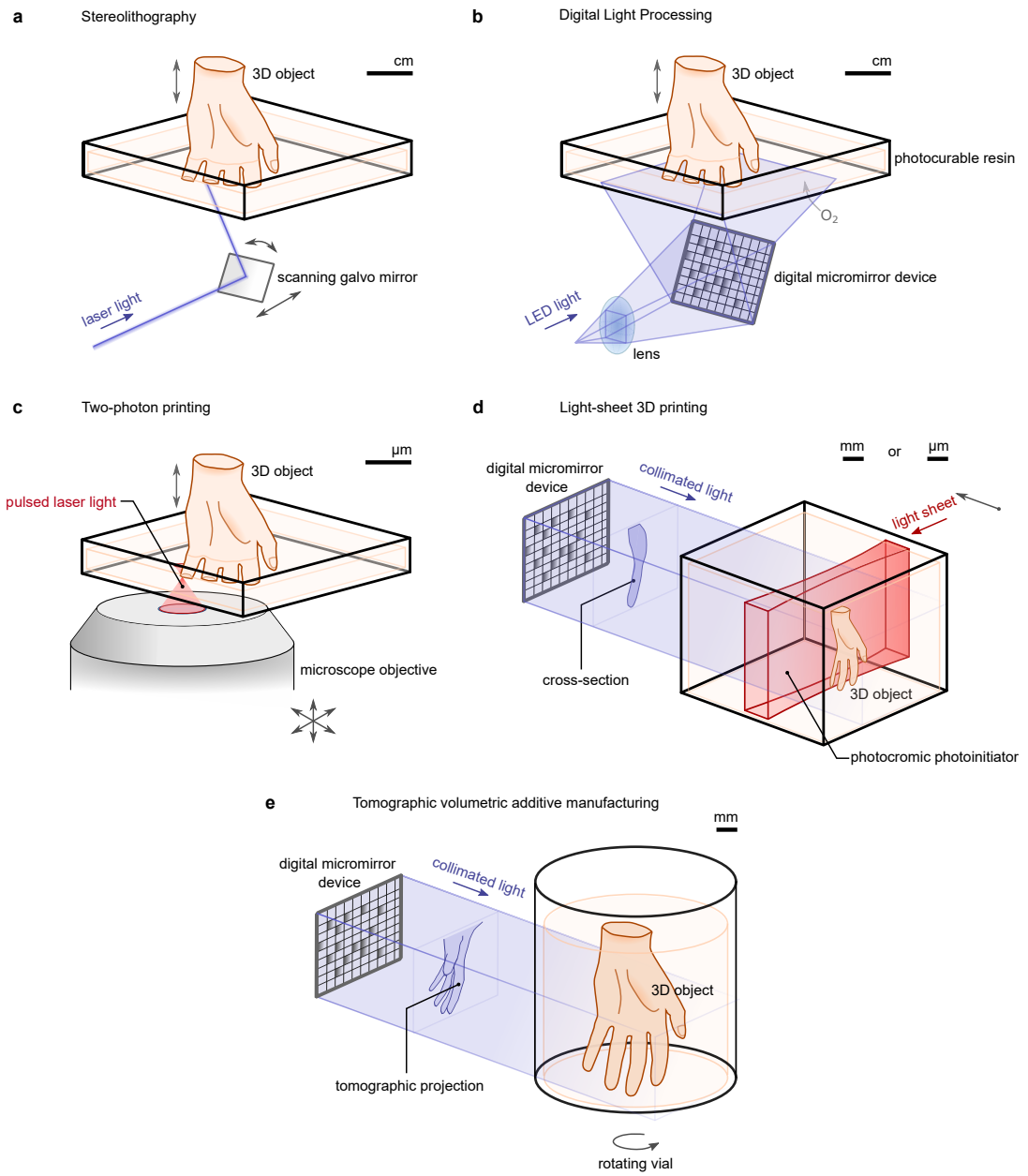
Figure 1.4: **Vat polymerization methods**. **a.** Stereolithography. **b.** Digital light processing. **c.** Two-photon polymerization. **d.** Light-sheet 3D printing. **e.** Tomographic volumetric additive manufacturing.

attach to the window instead of the 3D object. Slicing and light dose can also be adjusted to fabricate objects without layering effects. [32] Carbon 3D fabricates printers using CLIP technology, and has found a market in the dental industry, where multiple denture models must be fabricated per patient, requiring short printing times.

Two-photon printing

Maria Göppert-Mayer first described the process of multi-photon absorption theoretically in 1931. [8] Multi-photon absorption and fluorescence was only experimentally demonstrated in 1961, after the invention of the laser. [33] As the energy transition is only possible with the combined energy of both photons, they must be absorbed simultaneously by the photoinitiator. This is why the intermediate energy state, as in in fig. 1.2c, is called a virtual energy state: it has no lifetime and the molecule is never truly in this energy state. To increase the probability that both photons are absorbed simultaneously, pulsed lasers are used instead of continuous wave sources. By reducing the pulse duration, the photon flux is increased. Thanks to the dependence on simultaneous absorption, the probability of activation depends on the square of light intensity; which further confines the photopolymerization voxel. To increase efficiency, photoinitiators can be engineered to enhance their two-photon absorption cross-section. [34], [35] Additionally, high numerical aperture microscope objectives are used to focus the beam into very small volumes.

Two-photon polymerization exhibits unmatched print resolution, enabling the production of microdevices with sub-micron features. [36] Fabrication times are long, ranging into tens of hours for 100 μm devices. Recent strategies, such as spatio-temporal focusing of the pulsed beam, have drastically reduced printing times. [37], [38] Gray-scale two-photon lithography, an adaptation to two-photon polymerization, reduces fabrication times by dynamically adapting voxel size to balance print resolution and printing speed. [39] Two-photon printers are commercially available from Nanoscribe and Femtika, for example, and have been used to produce spectrometers for visible light with a footprint of only $100 \times 100 \ \mu m^2$. [40]

Light-sheet 3D printing

Xolography is a volumetric additive manufacturing method in which layers of a 3D object are fabricated sequentially within a viscous resin. [30] The method exploits dual-color photoinitiators to confine polymerization to thin layers, which are created by projecting unstructured UV light-sheets orthogonally to the main optical axis of the instrument. Structured 2D red light patterns, modulated by a DMD as in digital light processing, are projected along the optical axis. The key element behind this technology is the photochromic photoinitiators, which must absorb UV light to go into a photo-activatable state, at which they will absorb red light and induce polymerization. [41] The life-time of the photo-activatable state of the initiator imposes the maximal limit for scanning speed of the light-sheets, which means the number of layers per time unit that can be polymerized. The technology has been used to fabricate complex hollow geometries in acrylates. Its applicability to biofabrication is yet to be demonstrated, specially due to the possible cytotoxicity of the fluorinated dual-color cyanide-based photoinitiator. Volumetric additive manufacturing has sparked interest for photochromic initiators, and alternatives free of cyanide groups have been developed recently. [42] Hahn *et al.* have used biacetyl, a small organic compound, as a dual-color photoinitiator ($\lambda_1 = 440$ nm, $\lambda_2 = 660$ nm), to fabricate micrometric devices in a light-sheet configuration. [43] They used continuous-wave laser diodes (red for the photo-activating light sheet) and a high numerical-aperture objective to build objects with a peak voxel

printing rates of $7 \times 10^6 voxels \cdot s^{-1}$.

Tomographic volumetric additive manufacturing

Analogous to computer tomography (CT), Tomographic volumetric additive manufacturing works by projecting dynamic light patterns into a rotating vat of photosensitive resin. These light patterns build up a three-dimensional energy dose within the resin, solidifying the volume of the desired cm-scale object within seconds. [28], [29] Departing from established sequential fabrication methods like stereolithography or digital light printing, volumetric additive manufacturing offers new opportunities for the materials that can be used for printing. These include viscous acrylates and elastomers, epoxies (and orthogonal epoxy-acrylate formulations with spatially controlled stiffness) formulations, tunable stiffness thiol-enes and shape memory foams, polymer derived ceramics, silica-nanocomposite based glass, and gelatin-based hydrogels for cell-laden biofabrication. The method is particularly well adapted for biofabrication, and Readily3D, a startup from EPFL, designs and sells tomographic bioprinters. Tomographic volumetric additive manufacturing is the main subject of this thesis and its working principle will be treated in detail in the next chapter.

Prior to the invention of tomographic volumetric additive manufacturing, Shusteff *et al.* proposed a holographic approach instead. [27] They fabricated objects by producing a holographic light dose via the interference of three coherent light beams. Although ingenious, the method has had limited reception because it is challenging to make the beams interfere into any desired 3D geometry. Holographic patterning could be combined with other technologies to increase resolution, for example.

Technology	Sequential photopolymerization?	Volumetric?	Typical resolution	Typical print time	Printable size	Typical light source	Cost
Stereolithography	Sequential (1 voxel at a time)	No	300 μm	hours	10s of cm	Laser, continuous wave, 405 nm or UV	$$
Digital light processing [25]	Sequential (1 layer at a time)	No	500 μm	10s of mins	10s of cm	LED UV or 410 nm	$
Two photon polymerization [44]	Sequential (1 voxel at a time)	Yes	1 μm	hours	100s of μm	Laser, pulsed, IR or visible	$$$$
Light-sheet micro-printing [43]	Sequential (1 layer at a time)	Yes	10 μm	10s of mins	100s of μm	Laser continuous wave, 440 nm & 660 nm	$$$
Xolography [30]	Sequential (1 layer at a time)	Yes	10 μm	minutes	cm	Laser continuous wave, 375 & 585 nm	$$$
Tomographic volumetric additive manufacturing [28], [29]	Non-sequential (voxels polymerize almost simultaneously)	Yes	100 μm	seconds	cm	Laser continuous wave, visible	$$$
Holographic volumetric additive manufacturing [27]	Non-sequential (voxels polymerize almost simultaneously)	Yes	500 μm	minutes	cm	Laser continuous wave, visible	$$

Table 1.1: Comparison of vat photopolymerization technologies.

Tomographic volumetric additive manufacturing

2 Tomographic volumetric additive manufacturing

This chapter introduces the basic theoretical and experimental tools used throughout this thesis for tomographic volumetric additive manufacturing. It discusses tomographic back-projection, the experimental setup used for additive manufacturing, and reviews the materials used in tomographic volumetric additive manufacturing. Some of the contents of this chapter can be found in the following review papers:

- Dinc, Niyazi Ulas, Amirhossein Saba, Jorge Madrid-Wolff, Carlo Gigli, Antoine Boniface, Christophe Moser, and Demetri Psaltis. "From 3D to 2D and back again." *Nanophotonics* 12, no. 5 (2023): 777-793. https://doi.org/10.1515/nanoph-2022-0512

- Madrid-Wolff, Jorge, Joseph Toombs, Riccardo Rizzo, Paulina Nuñez Bernal, Dominique Porcincula, Rebecca Walton, Bin Wang *et al*. "A review of materials used in tomographic volumetric additive manufacturing." *MRS communications* (2023): 1-22.

2.1 Tomographic recontructions

This thesis deals with tomographic additive manufacturing, a method introduced by Loterie, Delrot and Moser at EPFL, and by Kelly, Bhattacharya, Shusteff, Taylor and Spadaccini at the University of California-Berkeley and the Lawrence Livermore National Laboratory. [45], [46]

Tomographic additive manufacturing was inspired by computed tomography (CT) scans in biomedical imaging; where a series of X-ray radiographs of a patient are acquired from multiple angles. These radiographic projections (2D) are then processed to reconstruct the body of the patient (3D), as seen in fig. 2.1a-b. The reconstruction represents the distribution of absorbed X-ray dose inside the object. [46]

2.1.1 Radon transform

The mathematical theory behind this method is the Radon transform, which relates the 3D body of the patient to the 2D radiographs at different angles. The Radon transform is a method for representing a n-dimensional function (like a body) in terms of its *(n-1)*-dimensional projections along a set of straight lines, as represented in fig. 2.1c. The X-rays shining through the patient's body are these straight lines, which, because of the different abosrbances of the various tissues in the body, will get attenuated. The photodetector *integrates* the x-rays that were not absorbed by the body. Knowing the initial intensity,

Figure 2.1: **Computed tomography a.** A patient is scanned by acquiring radiographs from multiple angles. Figure reproduced from https://thoracickey.com/basic-principles-in-computed-tomography-ct/ **b.** These radiographs (2D) can be computationally processed to reconstruct the body of the patient (3D). Figure reproduced from [47]. **c.** The Radon transform calculates the integral projection of an object for each angle.

the radiographs can be converted to measurements of attenuation.

Mathematically, for a given function $f(x, y)$ representing a cross-section of a 3D object, the Radon transform $R(r, \theta)$ is defined as the integral of $f(x, y)$ along a line with angle θ and perpendicular distance r from the origin:

$$R(r, \theta) = \int_{-\infty}^{\infty} \int_{-\infty}^{\infty} f(x, y) \delta(x \cos\theta + y \sin\theta - r) \, dx \, dy$$
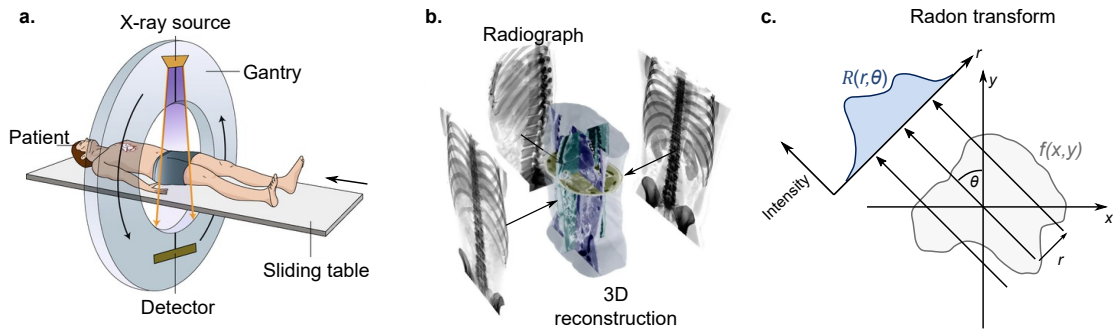
Here $\delta()$ is the Dirac delta function, which essentially extracts the value of the function along the specified line. [48] The set of projections obtained from applying the Radon transform is called a **sinogram**, $R(r, y, \theta)$ (fig. 2.2a). A sinogram has angular units along one of its axes and spatial units along the other(s). The name sinogram derives from the fact that the Radon transform of an off-center point source is a sinusoid. Consequently, the Radon transform of a number of small objects appears graphically as a number of blurred sine waves with different amplitudes and phases. In practice, projections are only obtained for every finite angle, so sinograms are discretized along the angular axis. The pixel size of the detector discretizes the sinogram along the spatial axes.

The corresponding inverse Radon transform allows to reconstruct an *n*-dimensional function (like a 3D model) from a collection of *(n-1)*-dimensional projections. The inverse Radon function reconstructs the function by back-projecting parallel beams of modulable intensities. As shown in fig. 2.1b., the body of the patient can be reconstructed by taking the radiographs and back-projecting them, each at the angle at which it was acquired. One undesired aspect of the inverse Radon transform, is that energy is unavoidably back-projected to ideally empty regions of space, like the white space around $f(x, y)$ in fig. 2.1c. Additionally, producing perfectly parallel or collimated light beams is impossible in practice due to the diffractive nature of light. [49] Discretization, non-zero background intensities, diffraction, and noise make the reconstructions obtained from the inverse Radon transform only approximate. [50]

In fig. 2.2 we see the effect of angular discretization over the quality of filtered back-projections. We compute the sinogram of the reference signal, an image of a hand, with different angular discretization: 5, 10, 50, and 100 angular projections (over 180°). We then reconstuct the signal from these sinograms, using the inverse Radon transform[I]. As the number of angular projections increases, so does the quality of the reconstruction, as seen in fig. 2.2d. A noticeable artifact when few angular projections are available are the visible rays in the reconstructions. Over the years, a variety of more advanced tomography algorithms have been developed to address these issues, artefacts, and computation time. [51]
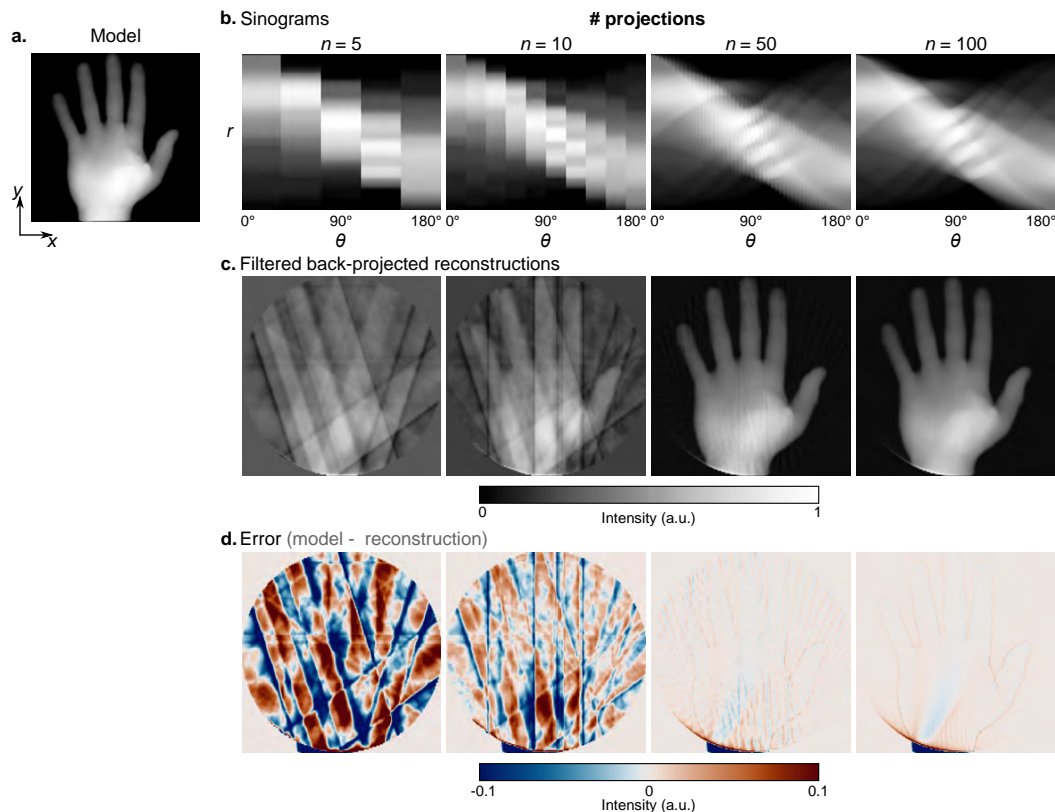
Figure 2.2: **Angular discretization of the Radon transform a.** 2D model, the image of a hand. **b.** Sinograms with increasing angular resolution (5, 10, 50, and 100 angular projections). **c.** Filtered back-projection reconstructions. **d.** Error of the reconstruction. Note that because we are computing projections around a rotation axis, we can't perfectly reconstruct the corners of the square model, so they are set to zero in the reconstruction. Calculations performed using Scikit-Image's Radon package for Python. [52]

2.1.2 Filtered back-projection

In tomographic 3D printing, the principle of CT scans is used in reverse. First, a digital model of the desired object is loaded (fig. 1.2a). Based on this model, cross-sectional images of the model are generated. (fig. 1.2b). Then, the sinogram of the obect is calculated using the Radon transform (fig. 1.2c). When all these projections are displayed into a homogeneous volume of photocurable

---

[I]We additionally apply a frequency-correcting filter, which we'll describe in the next paragraphs.

material, the cumulative absorbed dose distribution due to the projections reproduces the shape of the three-dimensional object inside the material. If a liquid photopolymer is used as a target material and visible light is used for the projections, locations inside the photopolymer where a high dose of light was applied will solidify. Regions that receive smaller light doses will remain liquid. (figs. 2.3g and 1.2f)

Because digital Cartesian 2D images are projected onto a rotating vial (which is better described by polar or cylindrical coordinates), some frequencies get more highly sampled than others, and the resulting back-projection is blurred, as seen in fig. 2.3f. [53] One way to think about why different frequencies get more energy than others is to imagine the projections of the images onto the central plane of the rotating vial. The digital images are evenly discretized (the pixel size is constant), but as they are rotated around an axis, they are more finely sampled. A blurry dose deposition is difficult to threshold into a polymerized/unpolymerized part. This means that after printing, depending on the light dose, sections of the object are overpolymerized while others are missing (fig. 2.3g).

To correct for the unequal energy distribution among frequencies, projected patterns can be filtered in the frequency domain[II], as is the case in filtered back-projection algorithms. [54] The Ram-Lak filter is a commonly used filter for back-projection reconstructions (fig. 2.3h). It linearly evens out the energy distribution accros spatial frequencies.

Applying a frequency filter on the projections has an effect, though: projections include negative values (fig. 2.3i). When back-projected, these patterns yield a perfect reconstruction. Projecting negative light intensities is physically possible, but technically challenging. It may be done through interference [27] or by producing photoinhibition in addition to photoinitiation. [55]–[57]. An alternative is to swap all negative values for zero, applying a non-negativity constrain. These back-projections are only approximate, but can be further optimized through iterative algorithms. [58]

Light patterns are projected from a spatially discrete light source, namely the DMD. By projecting the DMD with lenses onto the vial with photoresin, it's as if this discrete light source were revolving around the optical axis of the vial. The rotation creates a sampling problem: DMD pixels close to the rotational axis are sampled more finely than those far from the axis of rotation. Because of this, different spatial frequencies are sampled with different intensities. To correct for this, an intensity-normalizing filter can be applied in the frequency domain. This is the approach of filtered back-projection, which is a common solution in tomographic reconstruction methods such as computer tomography. A frequently used filter is the Ram-Lak filter (fig. 2.3h). However; filtered back-projections include negative values (fig. 2.3i-middle). So far, however, most works have employed simpler approaches in which negative values are set to zero following a non-negativity constraint. Iterative algorithms can be applied to the resulting physically-incorrect patterns to improve print fidelity. [29], [59], [60]

2.1.3   Experimental implementation

In this work, a computer is used to calculate the light patterns that will be then projected onto the photosensitive resin. The Radon transform calculates these patterns by "projecting" shadows at different angles. We use a Pytorch-based library to compute the optimized non-negative filtered Radon transform on a GPU, reducing computation time[III]. We usually calculate projections with an angular resolution of $\Delta\theta = 0.36°$, corresponding to 1000 patterns per rotation.

[II]in Fourier space

[III]computation time is still in the order of minutes
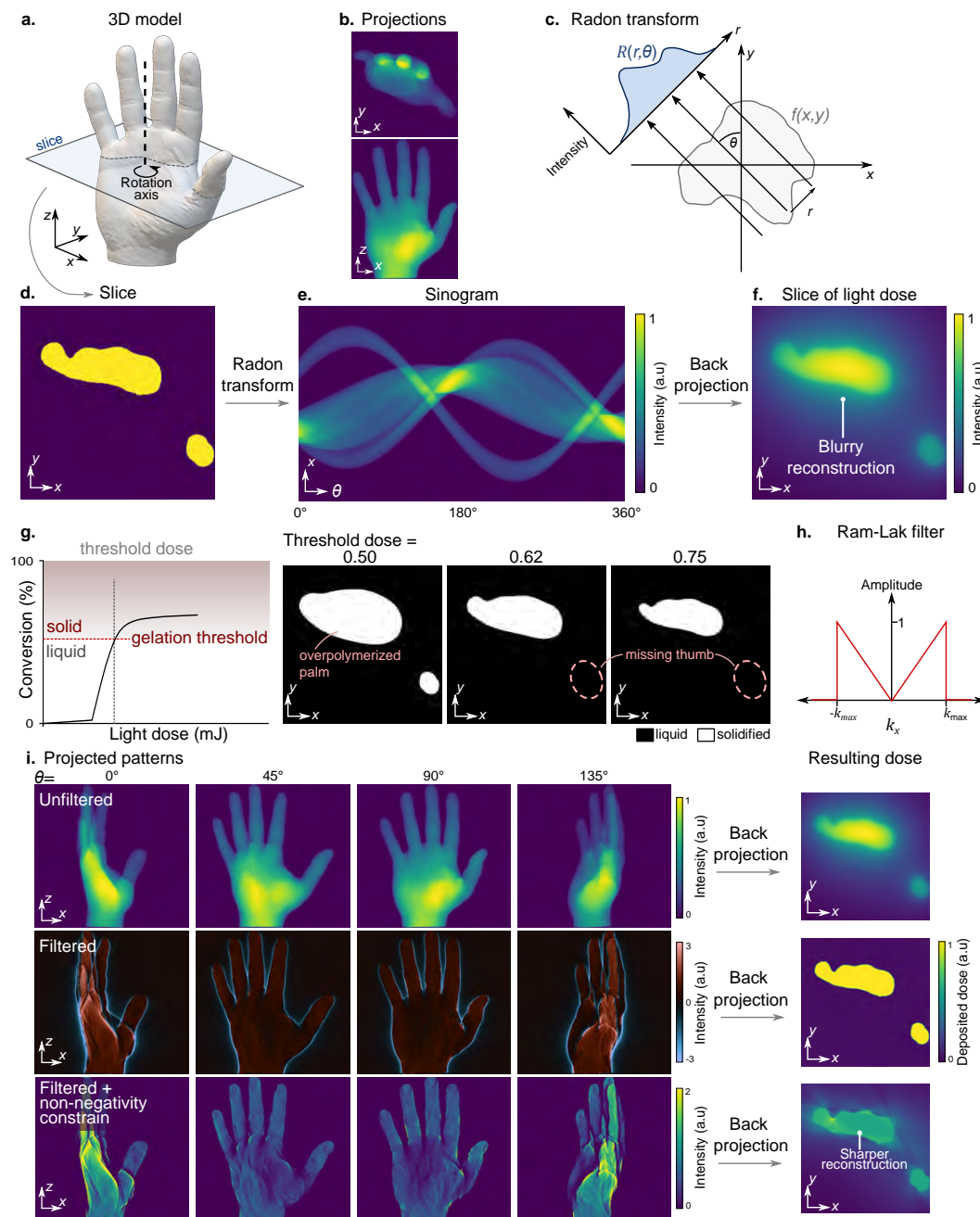
Figure 2.3: **Computation of the projected patterns a.** The 3D model of a hand and **b.** its lateral and vertical projections. **c.** The Radon transform calculates the integral projection of an object for each angle. **d.** For visualization, we take a slice of the 3D model and calculate its Radon transform around the z-axis, which yields **e.** the sinogram of the object. **f.** A light dose map results from back-projecting (inverse Radon transform) all slices from the sinogram. A "halo" surrounds objects, because, when back-projecting light, no region receives zero light. **g.** In the printer, the light dose is thresholded by the conversion response of the polymer. The blurred reconstruction leads to a threshold sensitive to over- or under-polymerization. **h.** To correct this, a frequency filter can be applied to the sinogram. **i.** The filtered back-projections (middle) produce a perfect reconstruction, but they require negative light intensities (blue.) A non-negativity constrain can produce an approximate solution that is easier to threshold.
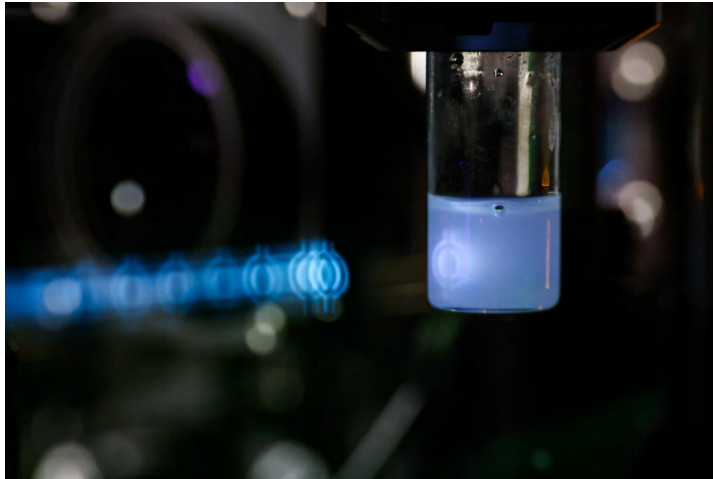
Figure 2.4: Dynamic light patterns are projected onto a rotating vial of photocurable resing. Image credit Alain Herzog/EPFL.

These patterns are saved as an array of 8-bit images. They are then transferred to a digital micromirror device (DMD); which is, in our case, a pixelated array of 1024 by 768 micrometric mirrors, steerable between an OFF- and an ON- state at up to 30 kHz. The DMD is set to sequentially display the loaded patterns while a stage rotates the vial of photocurable material at a constant speed. The DMD projects the patterned light from multiple continuous-wave high-power laser diodes onto the vial, as illustrated in fig. 2.4. The experimental setup is described in detail in section 2.2.

In summary, the computer calculates the filtered-back-projections (using Radon transform as a backbone) while the printer projects these patterns onto the photocurable vial, analogously to the inverse Radon transform.

2.1.4   Resolution, print fidelity and smoothness: advanced printing strategies

VAM exhibits unprecedented printing speed and enormous versatility across materials. However, the achievable resolution is still limited to above 50 μm. [14] Different strategies to increase print fidelity and resolution have been presented and include adaptations to the calculations of the projected patterns, [59]–[62] optical corrections to reduce aberrations; [63], [64] and feedback from sacrificial prints [13], [65] or live feedback to stop the excitation light. [66] Moreover, refractive-index changes induced by photopolymerization can produce lensing artifacts, including striations via self-writing waveguides. [67] Such striations degrade print shape accuracy and give VAM-printed parts layer-like effects despite VAM being free from layering. Rackson *et al.* presented an ingenious strategy to mitigate striations and produce smooth shapes in VAM by flooding the vat with uniform light the end of the printing process. [68]

The smallest printable feature size is at best limited by the projected image of the DMD micromirrors. Beam divergence further decreases resolution, which is why low-étendue light sources (such as laser diodes) are preferable than high-étendue sources (such as LEDs). [13] This means that resolution can't be any better than the size of the DMD micromirror on the image plane. As an example, Toombs *et al.* used lower magnification in their micro-CAL setup to demonstrate the fabrication of 3D objects with minimal feature sizes of 20 and 50 μm in polymer and fused silica glass, respectively; albeit at the cost

of smaller printable sizes. [14] The minimal fabricated features were much larger than the projected DMD mirror images in this work. Resolution is further limited due to materials, light deposition, and tomographic calculations, among others. Chemical diffusion of free radicals (be it from the activated photoinitiator or growing polymer chains) also reduces resolution. Orth *et al.* showed that larger features polymerize faster than smaller ones, and propose a deconvolution method that adapts light dose to guarantee that all features are printed simultaneously, regardless of their size. [69] Radical quenchers, such as TEMPO[IV], can be used to limit the detrimental effects of radical diffusion and dark curing. [70] In addition to this, limited light contrast also hinders resolution.

As light patterns traverse the entire vial's volume, there is light deposited in regions outside of the target volume. Algorithms that optimize light patterns so less light goes outside of the build volume can improved print fidelity. [62] Fabricating objects with sub-wavelength features with a purely back-projection approach will be challenging. However, integrating two-photon or two-step absorption into the fabrication process may bridge this resolution gap.

2.2 Optical setup

The optical setup for tomographic additive manufacturing is depicted in fig. 2.5. Blue light from 4 continuous laser diodes at 405 nm (HL40033G, Ushio, Japan) was condensed into a multimode optical fiber with a square core (WF 70×70/115/200/400N, CeramOptec, Germany) by means of aspheric lenses (C671-TME405, Thorlabs, USA). At the output of the fiber, light was then collimated by means of two orthogonal cylindrical telescopes. This yields a rectangular homogeneous beam, roughly matching the dimensions of the Digital Micromirror Device (DMD, VIS-7001, Vialux, Germany), and thus maximizing intensity efficiency. Light patterns from the DMD are then projected onto the resin by means of lens pair with focal lengths $f_1 = 100$ mm (AC254-100-A-ML, Thorlabs) and $f_2 = 250$ mm (ACT508-250-A-ML, Thorlabs). An aperture at the common focal plane of the lenses filters out high diffracting orders from the DMD and can also be used to regulate numerical aperture.

At the focal plane of lens L_2 sits the cylindrical vial containing the photoresin. These vials are held from above and set to turn with a high-precision rotary stage (X-RSW60C, Zaber, Canada). A square refractive-index matchin bath is used to reduce lensing from the resin.

Orthogonally to the optical axis of the printer, red light at 678 nm from a laser diode is used to image the printing process. A lens pair with focal lengths $f_1 = 75$ mm (AC508-075-A-ML, Thorlabs) and $f_2 = 250$ mm (ACT508-250-A-ML, Thorlabs) produces an image onto a CMOS camera (ACE ACA2000-50G, Basler, Germany).

The setup is controlled from the computer using a custom python code, written jointly by Dr. Antoine Boniface and I. A data acquisition card (DAQ, National Instruments) acts as the controller, digitally triggering the steady rotational movement of the sate, the switch on of the lasers, and the timely sequential exposure of the image patterns loaded onto the DMD.

All the 3D printing experiments in this thesis except for those on helical volumetric additive manufacturing, were performed with this setup. This setup was mostly conceived and built by Dr. Paul Delrot and Dr. Damien Loterie, two former members of the lab. Throughout my thesis, I modified and adapted the setup constantly.

[IV](2,2,6,6-Tetramethylpiperidin-1-yl)oxyl or (2,2,6,6-tetramethylpiperidin-1-yl)oxidanyl
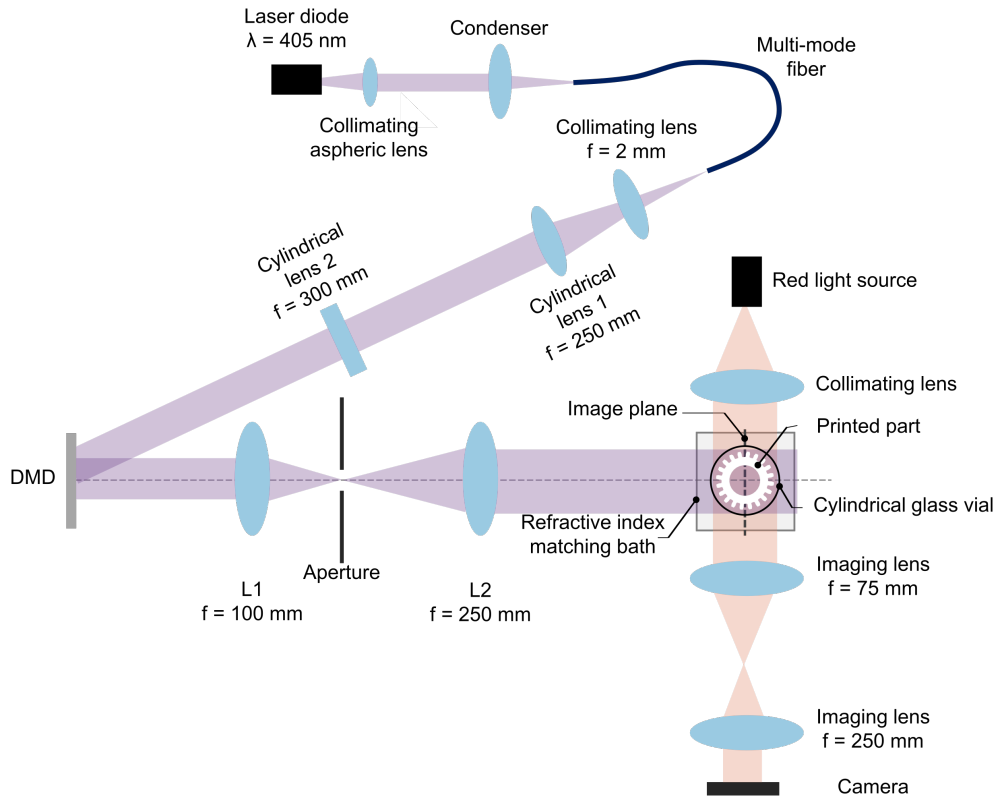
Figure 2.5: Optical setup of the tomographic volumetric 3D printer.

2.3 Materials used in tomographic volumetric additive manufacturing

When I began my PhD work, tomographic volumetric additive manufacturing had only been demonstrated in acrylates, [29], [45], [46] elastomers (such as silicones), [46] and methacrylated hydrogels, [29] like GelMA, even laden with cells. [28] The last years have seen an explosion in the materials used in tomographic VAM, as researchers have adapted previously well-established polymerization and cross-linking chemistries to the new method. Table 2.1 lists the published formulations demonstrated in tomographic VAM. They have expanded from acrylate chain polymerization reactions to also include step polymerization of thiol-enes [21] and norbornene hydrogels. [71] Organogels (e.g. ethylcellulose) have been developed to reduce the adverse effects of sedimentation. [72] Epoxies have also been mixed with acrylates to produce orthogonal polymerization systems (each initated at a different wavelength) that allow the spatial modulation of stiffness. [22]

In this thesis I have explored and introduced —alongside our collaborators and fellow lab members- the tomographic fabrication of optically-tuned organoid laden hydrogels (chapter 4),[73] fibroblast-laden hydrogels to model cellular cross-talk in pancreatic cancer (chapter 5), [74] polymer-derived ceramics (chapter 6),[75], and silica glass from phase-separating resins (chapter 7).
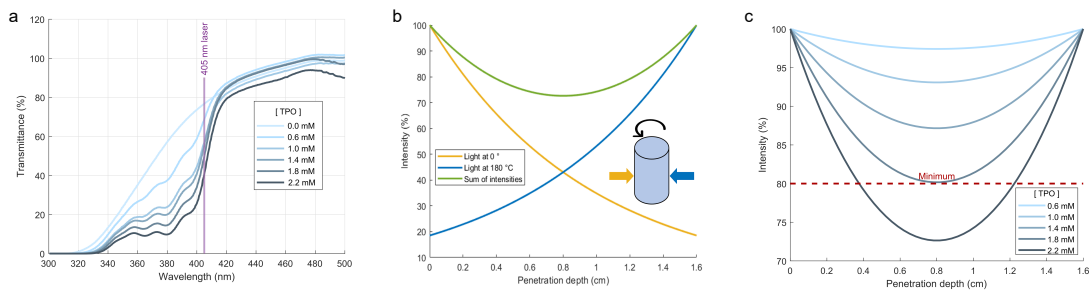
Figure 2.6: **Photoinitiators are used at low concentrations in tomographic VAM a.** Transmittance decreases rapidly as photoinitiator concentration increases **b.** Light intensity in the rotating vial. Light decays exponentially following Beer-Bouguer-Lambert law. As the vial rotates, light intensity is lowest at the center. **c.** The difference in light intensity between the edges and the center (0.8 cm) of the vial is very marked at higher photoinitiator concentrations.

2.3.1   Optical transparency

As tomographic VAM relies on light exciting the full volume at once and not layer by layer, high optical transparency is a requirement for the usable materials. Because of this, photoinitiators must be used at low concentrations, otherwise light would be rapidly attenuated following the exponential decay described by Beer–Lambert–Bouguer law. Ideal photoinitiators for VAM have low extinction molar coefficients but high polymerization yield. As seen in table 2.1, BAPO, TPO, and camphorquinone are commonly used initiators in VAM, having molar extinction coefficients in the order of 100-200 L mol^{-1} cm^{-1} at the excitation wavelength (fig. 1.2);[15] which is orders of magnitude lower than the peak molar extinction coefficients of other photoinitiators. To reduce absorbance, initiators must be used at low concentrations ($\approx 0.1 wt$%), typically an order of magnitude lower than in SLA or DLP; as seen in fig. 2.6. Their low concentration is extremely beneficial in some applications such as in bioprinting, given the cytotoxicity of most photoinitiators. [76] Light absorbers and dyes, which are common in DLP and SLA, are actually detrimental to VAM because they limit the penetration depth of light.

Many resin formulations of interest are scattering, such as cell-laden hydrogels or composite resins. Scattering deviates light from the straight path that it is assumed to follow in the computations for the tomographic patterns. The detrimental effect of scattering has been mitigated by reducing the refractive index mismatch within the components of the resin or by including the scattering profile of the material in the computational pipeline, as we will discuss in chapter 4. Possibly, scattering could be reduced by using longer-wavelength photoinitiators, [12] upconversion nanoparticles, [77], [78] or multi-photon instead of single-photon excitation. [16], [44], [79] Polymerization may also be induced with radiation outside of the visible spectrum, such as with microwaves. Although inherently subject to lower resolution due to the wave nature of light, tomographic microwave curing could be used to fabricate objects volumetrically in completely opaque materials. [80] Acoustic waves could also be used holographically or tomographically to fabricate 3D objects in opaque media, including cellularized hydrogels. [81]–[83]

2.3.2   Viscosity

Because objects are not fabricated in a layer-by-layer fashion, the resin does not need to flow at each printing step, as is the case in SLA or DLP; more viscous resins can be used in VAM. This has enabled the use of solvent-free formulations, which have higher monomer concentrations and thus polymerize

faster and yield stronger objects, and has also enabled the use as solid or gelled materials, like hydrogels or organogels. Part sedimentation during the printing process depends on print shape and resin viscosity and could compromise print fidelity if not taken into account properly. [84] Previous works have shown that sedimentation does not hinder fidelity in viscous resins, as it occurs mostly once printing has finished. [13], [75]. When the polymerization reaction is slower, increasing the viscosity improves print fidelity, as demonstrated by Toombs *et al.* in ethylcellulose organogels. [72] On the contrary, when the polymerization is highly exothermic, solidified objects can float instead of sinking. Fabricating objects under microgravity opens the possibility to use less viscous or more exothermic materials. [85] Viscosity, however, is not a intrinsic requirement for VAM, and printing in low-viscosity materials could be done by reducing the amount of time between the beginning of solidification and the end of the print, or by adjusting the displayed patterns to the expected sedimentation.

Viscosity also impacts radical diffusion and dark curing [19]. Recently, Orth *et al.* designed experiments to measure oxygen diffusion rates in viscous acrylates resins. [69] Oxygen diffusion prevents dark curing, but it also increases the required light dose to polymerize a region if light excitation is done over longer periods. Orth and collaborators computed a point spread function that accounted both for light beam divergence and for loss of resolution due to chemical diffusion. This 3D point spread function could be then used to deconvolve the 3D model before computing its tomographic back-projections. The resulting correction, similar to that of Loterie *et al.* but without the sacrificial print, [13] tackles the issue of why certain regions of the 3D objects are polymerized before others, even if they are irradiated with the same light dose. To further reduce the detrimental effects of radical diffusion on resolution, oxygen could be fully replaced by a less motile radical scavenger, such as TEMPO. This could be done in practice by bubbling nitrogen through into the resin and keeping it in hermetic containers. Alternatively, diffusion could also be reduced by printing in more viscous resins, or by cooling them down; although this reduces resins' reactivity and increases printing times. [86]

Type	Formulation	Photoinitiator (concentration)	λ (nm)	Viscosity	Other components	Notes
Acrylate – epoxy [22]	PEGDA / BPAGDA / EEC	CQ (0.02 wt%) EDAB (0.02 wt%) CAT2 (2.9 wt%)	455 / 365			CAT2 first dissolved in propylene carbonate
Acrylate [13], [61]	Di-pentaerythritol pentaacrylate	TPO (0.6mM)	405	>10 Pa·s	TiO_2 added to make resin scattering [61]	
Acrylate [22], [57]	PEGDA / BPAGDA	CQ (0.1 wt%) EDAB (0.25 wt%)	455	0.32 - 1.40 Pa·s	Viscosity adjusted adding BPAGDA	
Acrylate [55], [57]	TEGDMA / BisGMA	CQ (0.2 wt%) EDAB (0.5 wt%)	460 / 365		o-Cl-HABI (1 or 3 wt%)	HABI pre-dissolved in THF
Acrylate [55], [57]	TEGDMA / BisGMA	CQ (0.1 wt%) EDAB (0.25 wt%)	460 / 365		o-Cl-HABI (0.4 wt%)	HABI pre-dissolved in THF
Acrylate [57]	PEGDA / BPAGDA	CQ (0.1 wt%) EDAB (0.25 wt%)	455	0.32 Pa·s	TEMPO (0.004 or 0.01 wt%)	
Acrylate [85]	Urethane Dimethacrylate	DBMP (6mM)	405	11 Pa·s		Printed in microgravity
Acrylate [85]	aliphatic urethane acrylate diluted in isobornyl acrylate	DBMP (6mM)	405	25 Pa·s		Printed in microgravity
Acrylate [29]	BPAGDA 75 wt% + PEGDA 25 wt%	CQ (5.2mM) + EDAB 1:1 (weight ratio)		5.2 Pa·s		
Ethyl-cellulose organogel [72]	TMPTA + Ethyl-cellulose (7 wt%)	CQ (5mM) + EDAB 1:1 (weight ratio)	455	Thermally gelated	TEMPO (1.5 mM)	
Hydrogel [87]	GelNB/PEG4SH	LAP (0.05% w/v)	405	Thermally gelated		Printing time $\approx$ 10 s, viability >95%
Hydrogel [87]	GelNB/GelSH	LAP (0.05% w/v)	405	Thermally gelated		
Hydrogel (cell-laden) [28]	GelMA 10% w/v	LAP (0.037% wt)	405	Thermally gelated		Printing time 12.5 s, viability >85%
Hydrogel (cell-laden) [71]	GelNB/PEG4SH 2.5% w/v	LAP (0.05% w/v)	405	Thermally gelated		Laden with murine C2C12 myoblasts at 1 million cells mL^{-1}
Hydrogel (cell-laden) [88]	GelMA 5, 8 and 15% w/v	LAP (0.1% w/v)	405	Thermally gelated		Print around melt-electrowritten poly(ϵ-caprolactone) meshes
Hydrogel (cell-laden) [61]	GelMA 8 % w/v in PBS	LAP (0.16 mg mL^{-1})	405	Thermally gelated		Laden with human embryonic kidney cells at 4 million cells mL^{-1}
Hydrogel (cell-laden) [74]	GelMA 10 % w/v in PBS	LAP (0.16 mg mL1)	405	Thermally gelated		+ 0.5 million cells mL^{-1} (human fibroblasts)

Table 2.1: **Materials used in tomographic volumetric additive manufacturing**. Materials highlighted in blue are contributions of this thesis.

Type	Formulation	Photoinitiator (concentration)	λ (nm)	Viscosity	Other components	Notes
Hydrogel (organoid-laden) [73]	GelMA 5% w/v	LAP (0.1% w/v)	405	Thermally gelated	Iodixanol	+ up to 5 million cells mL^{-1} (human hepatocytes)
Hydrogel [89]	Silk sericin 2.5-5% w/v	Ru/SPS (1/10) (0.25-1 mM Ru)	525	Not measured	water	+ 5 million cells mL^{-1} (C2C12 myoblasts); printing time ~55-80 s
Hydrogel [89]	Silk fibroin 1.25-15% w/v	Ru/SPS (1/10) at (0.125-1 mM Ru)	525	Not measured	water	Printing time ~30-170 s
Hydrogel [87]	PVA-NB/PEG2SH	LAP (1.7-2 mM)	405	Thermally gelated	Sacrificial Gelatin	
Nanocomposite for glass [14]	296 g/mol trimethylolpropane triacrylate (TMPTA) + hydroxyethylmethacrylate (HEMA)	CQ (0.117 wt%) + EDAB (0.117 wt%)	442	10 Pa·s	TEMPO (0.2 M) in TMPTA (0.5 vol%)	
Phase separating glass		TPO (3mM) + 1-Hydroxy-cyclohexyl-phenyl-ketone (24mM)	405		TEMPO (0.3mM)	
Poly(ε-caprolactone) [90]	PCL-ene/ PETA-4SH	TPO-L (0.12-0.25% w/v)	442		TEMPO (0.1 mg mL^{-1})	
Polymer-derived ceramic [75]	Polysiloxane (SPR 684) 85 wt% + 1,4-butanediol diacrylate 15 wt%	TPO (2mM, 0.063 wt %)	405	0.87 Pa·s		
Shape memory foam [91]	TEGDAE: TA-ICN: TME-ICN (0.1 : 0.9 : 1 molar equivalent of functional groups)	MMMP (10 mM)	405		23.5 mM ANPHA + 0.1 mM TEMPO	
Silicone [13]	93 wt% vinyl-terminated PDMS + 4.7 wt% fumed silica reinforced vinyl-terminated PDMS + 2.3 wt% (mercapto-propyl) methylsiloxane–dimethylsiloxane	TPO-L (2.25 mM)	405			Demonstration of 3D printing of full silicones
Thiol-ene [21]	TEGDA + TEGDAE + TAE-ICN + TA-ICN + TME-ICN (in different mixing molar ratios)	MMMP (10mM)	405		TEMPO 0.1mM	

Table 2.2: (Continuation) **Materials used in tomographic volumetric additive manufacturing**. Materials highlighted in blue are contributions of this thesis.

3 Volumetric helical additive manufacturing

This chapter introduces helical additive manufacturing, an addition to the fabrication method to increase the size of the printable objects without compromising their resolution. Some of the material presented in this chapter can be found in the following paper:

- Antoine Boniface, Florian Maître, Jorge Madrid-Wolff and Christophe Moser. Volumetric Helical Additive Manufacturing. *Light: Advanced Manufacturing*; 4(12); 2023. doi: 10.37188/lam.2023.012

3.1 Motivation

As covered in the previous chapter, tomographic VAM fabricates objects by shining dynamic light patterns from all angles onto a rotating vial filled with a photo-curable material. The method has comparable resolutions to SLA or DLP[I], but is much faster, fabricating cm-scale objects in less than a minute.

Tomographic VAM is limited to small objects, though; with commonly fabricated objects being 1 cm x 1 cm x 3 cm at largest. In many applications, including dental retainers and prototyping, printing larger structures is desirable. Inspired by spiral computer tomography, [92] we propose to move the sample around the light beam with a helical trajectory. If light dose is tuned correctly, this change allows to fabricate longer objects still in a layer-less manner. [93]

Additionally, we realize that the symmetries present in sinograms allow us to project images onto only one half the vial at any time. This means that the DMD doesn't need to be centered at the rotation axis of the vial, but that it can be displaced by one radius, so that it only covers half of it, as seen in fig. 3.2a. The magnification of the two lenses in the $4f$-system can be *(1)* kept the same, so the print's diameter doubles, or *(2)* decreased by half so that resolution is improved while the footprint is the same.

3.2 Working principle

The principle of tomographic volumetric helical additive manufacturing (VHAM) is given in fig. 3.2. We combine a rotating and a linear translation stage to set the glass vial (diameter = 32 mm) containing the photoresist in a helical motion. We must emphasize here that all the resin is not illuminated at once

---

[I]Recent SLA systems have improved resolution to tens of microns

as in conventional tomographic VAM. Here, the whole resin is entirely excited only after one complete cycle comprising a bottom-up and a top-down helical pass. Half a cycle (only up or down) includes α rotations of the vial. As the vial follows a helical trajectory, α also represents the number of sets of light patterns stacked along the vertical axis. There are some overlapping regions between the patterns so that after a turn its lower and upper parts coincide. The size of the overlap is fine-tuned by adjusting the vial's rotation speed to the vertical movement of the translation stage, which is essential to ensure continuity of the printed objects.

In this work, the rotation speed is between 8 and $10° \cdot s^{-1}$ which respectively gives a vertical linear speed of 366 and $458\,\mu m \cdot s^{-1}$. After a few up and down cycles, the light dose accumulated inside the resin at different heights and over multiple angles is sufficient to solidify it as shown on the schematic fig. 3.2b. This usually happens after 2 or 3 vertical cycles and is in general completed in less than ten minutes (fig. 3.2c). Note that because of light absorption, patterns projected at θ and $\theta + 180°$ do not irradiate the volume of resin in the same way. We take this into account by performing a blank half turn (simply put, no projection and no vertical translation over 180°) between two vertical cycles.
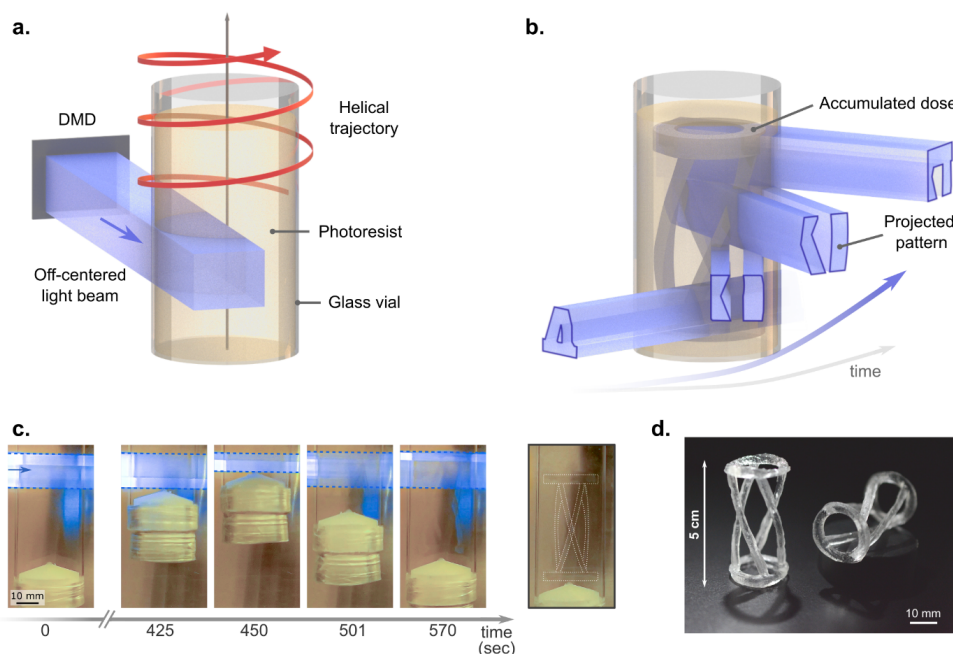
Figure 3.1: **Principle of tomographic volumetric helical additive manufacturing (VHAM). a.** Simplified schematic of the helical printer. A laser beam (λ = 405 nm) is modulated in intensity with a DMD before propagating through the photoresist. The vial containing the latter is off-centered, such that one lateral edge of the rectangular beam intersects the center of the cylindrical container. The vial is placed in rotation and move continuously up and down defining a helical trajectory. **b.** Schematic representation of the helical printing procedure. A series of patterns of light projected over multiple angles trigger at different time the polymerization. At a given time only a subpart of the resin is exposed to light. In fact, it is the helical movement that ensures the solidification of the whole object. **c.** Time lapse. Two cycles up/down and 12 turns were necessary to solidify the resin in the desired geometry (see 3D model in b.). This is achieved in less than 10 min. The rotation stage holds the vial by the bottom. A white cap prevents resin's leakage to the outside. **d.** Final part obtained after washing out the unpolymerized resin. Scale bar: 10 mm.

Without this blank half turn, the deposited light dose would not be diametrically symmetrical because of absorbance (fig. 2.6), although this could be compensated numerically (section 4.4).

It results that for 3D structures with no central symmetry, the number of projected patterns doubles. As an illustration, one may need to project around 10,000 patterns for printing with $\alpha = 3$ and an angular resolution of 0.18°.[II] The final 3D printed structure is obtained after some post-processing including a washing and post-curing steps. For the helical tower structure in fig. 3.2d, $\alpha = 3$. This extended the number of printable voxels to $4\alpha = 12$, compared to traditional tomographic VAM.

Fig. 3.2 shows the prints of five different 3D models, relatively large (2 cm wide at least), with different heights. For all of them, the DMD was off-centered with respect to the vial's rotation axis, while the parameter α was adjusted to fit the height of each object. As in conventional tomographic VAM, these complex and hollow geometries are printed in a short time (3-10 minutes, indicated on the figure) without the need for support structures.

The absence of layering offers excellent surface quality as one can see in the micrographs in fig. 3.2c, especially for the prints of the hand and the teeth. Striations, similar in appearance to a few tens of

---

[II]RAM has to be handled specially to be able to transfer continuous batches of images onto the DMD while it displays them following an external electronic trigger.
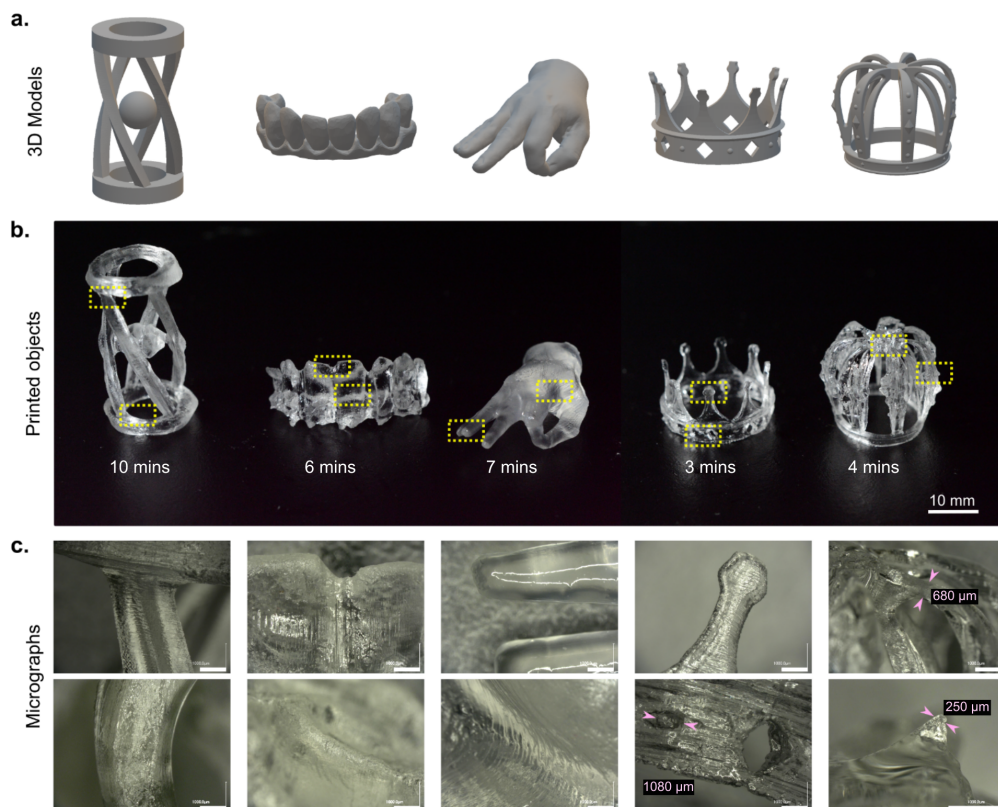
Figure 3.2: **Examples of 3D printed objects using volumetric helical additive manufacturing**. **a.** 3D models. **b.** Photographs of the obtained prints, with their printing time indicated **c.** Microscopic images of some details of the prints. Scale bars: **b**. = 10 mm, **c**.= 1 mm.

microns thick layers, can be observed. They are caused by a self-induced waveguide effect, driven by the non-linearity of the material's gelation and can potentially be removed. [68] Suspended complex structures as thin as the 680 μm double arches of the crown and its 250 μm spikes in relief can be printed with high fidelity. The printer is not only capable of printing sharp edges like the square pillars of the helical tower but also round and curved surfaces like the circular base of the structure. The speed of the process and the achieved level of details might make VHAM interesting for dental industry. However, resolution must be improved before the technique can be widely adopted in industry.

3.3   Effects of optical features of the beam on print fidelity

In VHAM, the printing cross-section was extended to several cm. By doing this, the new printer incidentally became a useful platform to explore the effects of beam divergence and beam focusing on print fidelity. Loterie *et al.* had already explored the effect of beam divergence, and realized that low étendue light sources (lasers instead of LED) were critical to preserve resolution across the print volume. [13]

Beam divergence   We investigated the effect of the beam divergence on the resulting dose deposited inside the build volume using computer simulations. Two different configurations were considered: on the one hand the DMD is on-axis and illuminates the whole volume of photoresin (as in conventional tomographic VAM) and on the other hand the DMD is off-centered as in VHAM (fig. 3.3). As a result, the way the DMD is positioned with respect to the cylindrical vial does not change much the obtained dose. In both cases the divergence results in a global blur of the light dose. The effect is stronger on the edge as the voxel size due to divergence is larger. The beam divergence is modified by adjusting the Rayleigh range of the optical beam $z_{Rayleigh}$. Shorter $z_{Rayleigh}$ corresponds to high beam divergence.

Beam focus   The light beams that we use in the tomographic printer are Gaussian, and as such, they can not be infinitely collimated. The beams, then, have a focal plane and then defocus away from it. A limited Rayleigh length marks a difference between the calculated reconstruction using the Radon transform, which assumes that light is perfectly collimated, and the experiment. Other research groups have developed iterative algorithms to correct for this mismatch. [62] As a result, light beams with shorter Rayleigh lengths blur out more rapidly and produce objects of lower resolution, as is shown in figure 3.4.

When the DMD is placed on axis, these defocusing artifacts translate into a blurred dose deposition, and a reduction of print resolution. Interestingly, due to the rotational asymmetry of the off-centered DMD in VHAM, artifacts appear when the focal plane does no fall on the center of the rotating vial. In the case of the 3D-printed gear in our example, these artifacts consisted of an asymmetric elongation of its cogs. At first, we believed this error came from errors in the synchronization of the rotational speed. Having run controls for his, we realized that the source of error was actually the defocusing.

These experiments suggest that diffraction tomography, [94]–[96] which takes into account the lack of collimation of the light beam, would be a better model to calculate light patterns. Future work is needed to develop or adapt software libraries for diffractive tomographic printing.
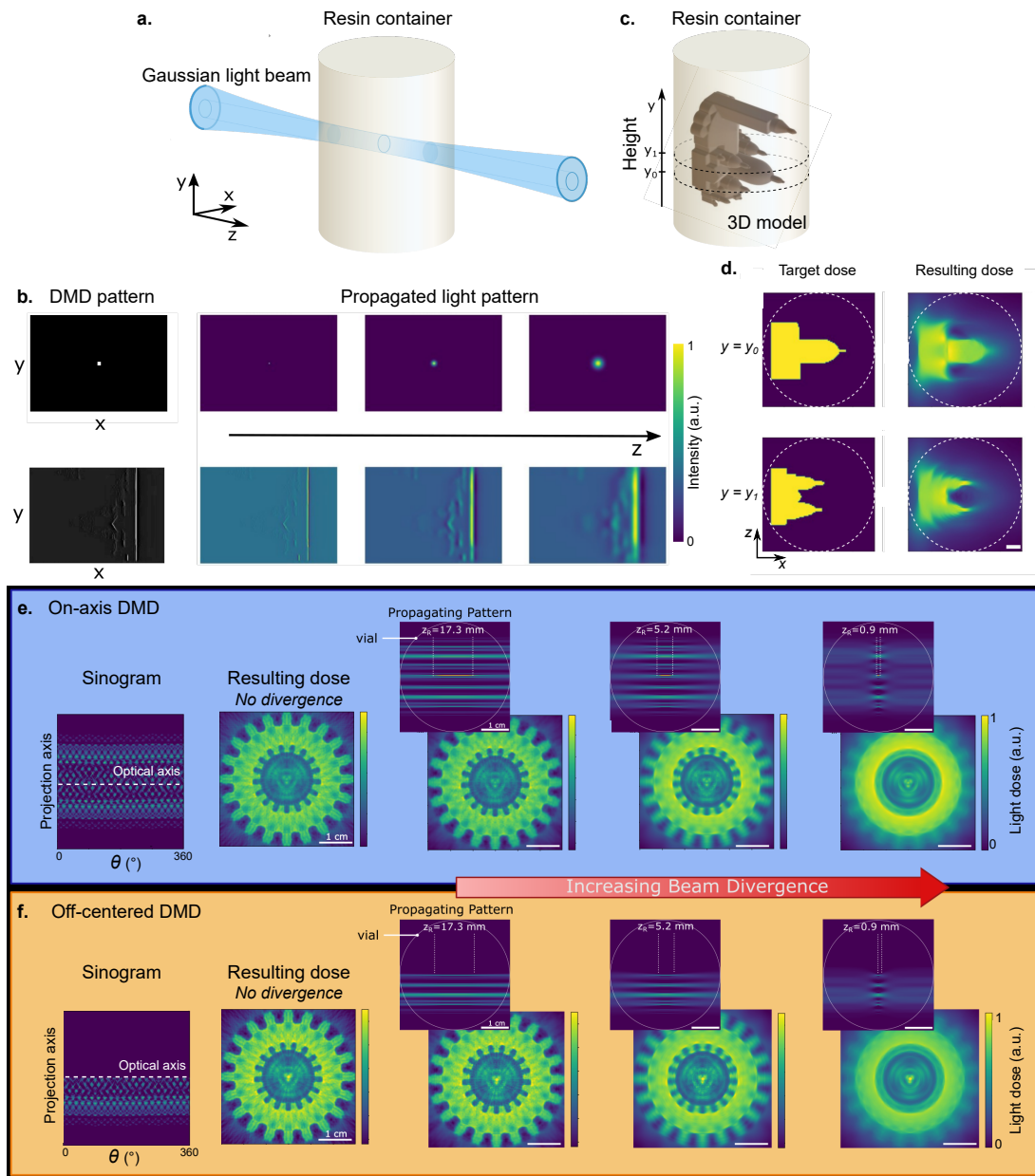
Figure 3.3: **Effect of beam divergence on the resulting dose and resolution. a.**. A diverging Gaussian beam has cross-sections of varying size as it traverses the resin container. **b.** As a result, projected light patterns are blurred out. **c.** Example of a 3D model to print and **d.** the compared target and simulated resulting light doses at different heights. **e.** When the DMD illuminates the entire printing vial. the sinogram for a 3D model of a gear has components on both sides of the optical axis. When there is no divergence, the resulting light dose is sharp. However, as divergence increases, light patterns have shorter Rayleigh lengths and they divert from the paraxial approximation assumed in the Radon transform. This results in blurred cumulative light doses. **f.** When the DMD is off-centered with respect to the optical axis, the sinogram only has components on one side of the optical axis. Although off-centered projected patterns are subject to loss of print fidelity as beam divergence increases, this change does not induce asymmetric artifacts. Scale bars: **d.** = 2 mm, **e.** and **f.** = 1 cm
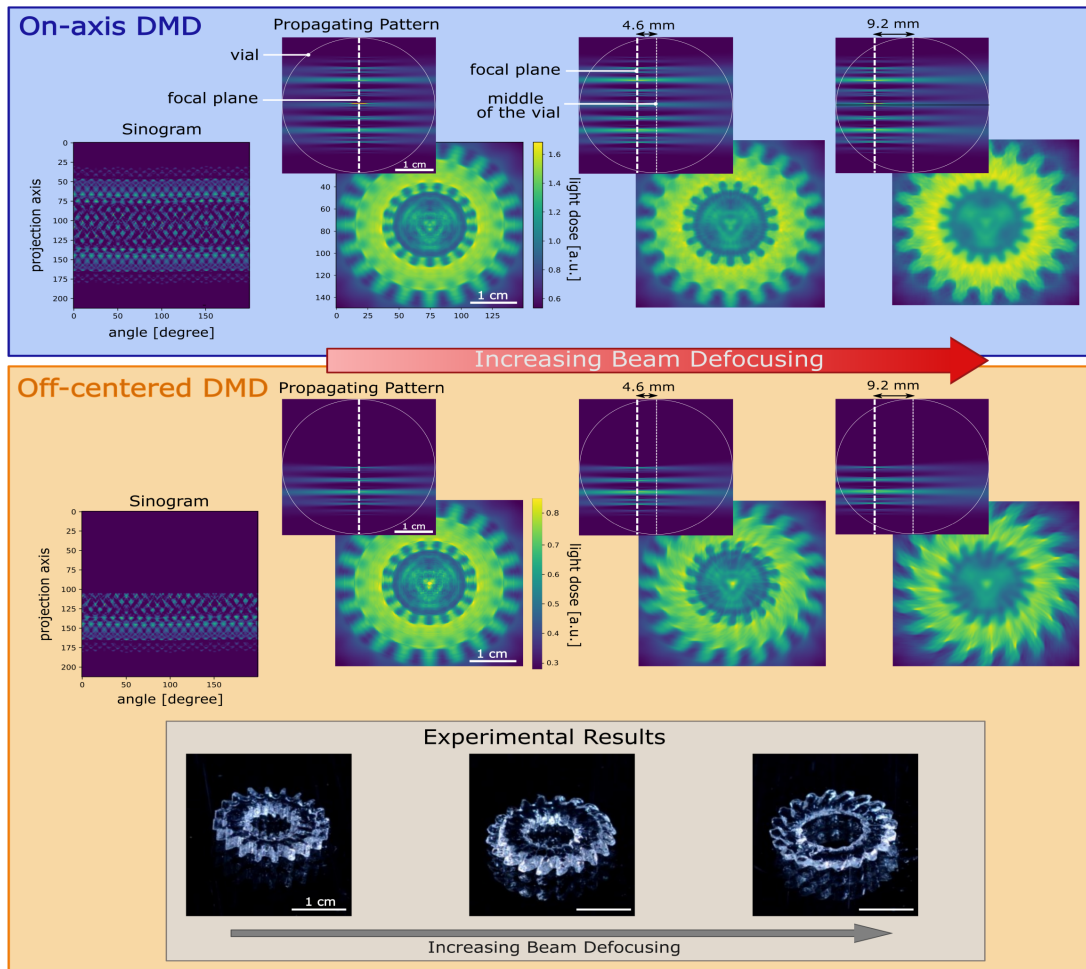
Figure 3.4: **Effect of beam divergence on the resulting dose and resolution.**

3.4   Conclusion

Having a look at conventional tomographic VAM, one rapidly foresees the advantages related to the helical motion. Usually in tomographic VAM, the available $N_x \times N_y$ pixels of the DMD illuminate the whole rotating volume of resin at once, as represented in fig. 3.5a. In theory this configuration provides $\frac{\pi}{4} N_x^2 \times N_y$ independent printable voxels. Off-centering the DMD doubles the lateral resolution or increases the number of printed voxels by a factor of 4. Additionally, the continuous translation of the vial gives the possibility of printing taller objects (fig. 3.5). The increase in the vertical direction is described by the parameter α.

In this work, we printed objects with α up to 3, meaning objects 3 times taller. Overall, this new optical configuration increases the number of printed voxels inside the vial by a factor up to $4\alpha = 12$ compared to conventional tomographic VAM, as seen in fig. 3.5. This size increase is at the cost of the printing speed since the resin must be exposed to light for a longer time to reach the threshold dose. It is possible to lower the threshold dose by increasing the concentration of photoinitiator, but one must be careful not to make the resin too absorptive, or by increasing the laser power.

As in any light-based VAM methods, printing larger structures comes at least with two challenges. On the one hand, light has to penetrate deeper inside the resin to cure the whole volume; light absorption is therefore more critical. On the other hand, light has to propagate straight over longer distances. Whatever the printing technology, light is never perfectly collimated and divergence can be at the origin of strong deviation between the model used for computing the patterns and the real experiment. [13], [62] In our case, we deliberately chose to reduce the numerical aperture of our optical projection system to reduce the beam divergence in order to preserve the printing fidelity although it is at the cost of the resolution and printing speed since we cut part (the high spatial frequencies) of the incoming light. We characterize the effect of the numerical aperture and divergence on print quality (figs. 3.3 and 3.4) through a numerical model. Although divergence inevitably affects print resolution, we successfully printed features size of 680 μm for objects as big as 2.5 cm × 2.5 cm × 3 cm (fig. 3.2).

In summary, we have presented a proof-of-concept of a new light-based technique for volumetric printing of multi-centimeter scale objects. It builds up on tomographic VAM to significantly increase (up to a factor 12) the number of printable voxels while keeping the same light modulating device for projection and without compromising too much the printing resolution. This was achieved by off-centering the light modulator and translating continuously the resin vertically along the patterned light beam. These simple modifications can be easily made on existing tomographic printers and opens up new possibilities for high-resolution and high-speed fabrication of objects whose size up to 3 cm × 3 cm × 6 cm. Helical tomographic VAM might be therefore appealing for applications in fields where cm-scale objects must be manufactured individually, such as in the dental industry (fig. 3.2), although resolution must be improved to meet the current requirements of the industry.
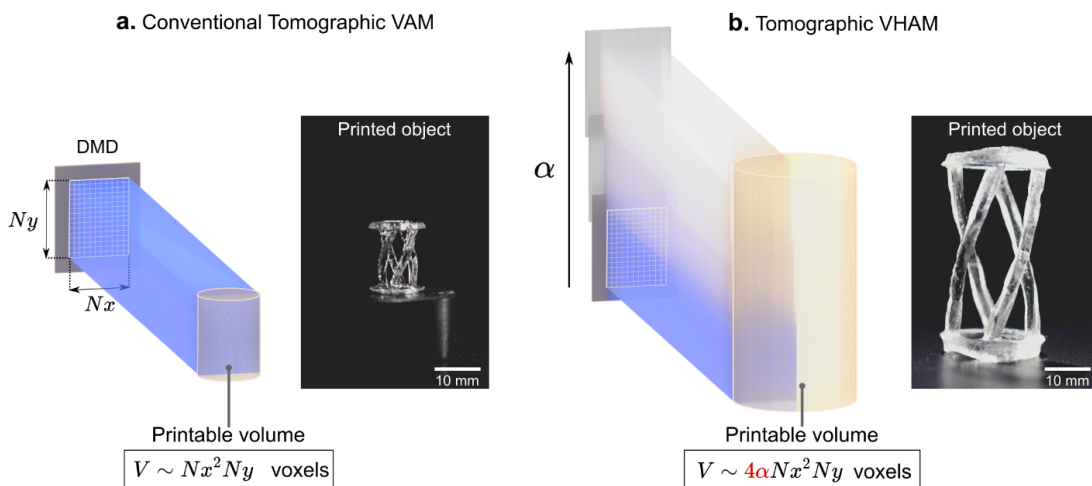
Figure 3.5: **Increasing the number of printed voxel generated from the same DMD. a.** Conventional tomographic volumetric additive manufacturing. **b.** Tomographic volumetric helical additive manufacturing. Scale bars: 10 mm.

3.5 Experimental materials and methods

3.5.1 Opto-mechanical setup

A second tomographic setup was built for this project. The optical setup for tomographic VHAM is presented in fig. 3.6. Two 405 nm laser diodes, with a combined nominal power of 1.8 W, are collimated and combined into a single beam with a D-shaped mirror (Thorlabs, BBD05-E02). The combined beam is then coupled into a square-core optical fiber (CeramOptec WF 70 × 70/115/200/400 N, core size 70 μm by 70 μm, numerical aperture 0.22), in order to spatially homogenize the beam from the two laser diodes. The outgoing square beam is then magnified to match the rectangular aperture of the DMD (Vialux, V-7000 VIS) via an aspheric lens L_3 and a set of two orthogonal cylindrical lenses L_4 and L_5 for maximizing the light efficiency. Note that the cylindrical lenses have different focal lengths ($f_4 = 250$ mm and $f_5 = 300$ mm), in order to adjust the square beam from the fiber square output facet to the rectangular area of the DMD. The DMD suffers from diffracting effects due to the blazed grating formed by the micromirrors (pitch = 13.6 μm). [97] This effect can cause a large fraction of the reflected light to be lost in diffracted orders depending on the incidence angle of the illumination beam. The surface of the DMD is imaged via a $4f$ system into a cylindrical glass vial containing the photopolymerizable resin. In the Fourier plane (between L_6 and L_7), an iris blocks the unwanted diffraction orders from the DMD. This iris also effectively controls the numerical aperture of the beam, and its aperture can be adjusted to balance beam width and Rayleigh length. A refractive-index matching bath of vegetable oil is used to remove the lensing distortion caused by the cylindrical interface of the vial. [63], [64] Compared to conventional tomographic VAM, the DMD is off-centered with respect to the vial's rotation axis and the resin can be moved vertically thanks to a linear stage with a travel range of 10 cm (Zaber, LSQ075A). A side view camera placed perpendicular to the optical axis monitors the printing process. A red LED that does not influence the photopolymerization is used for this purpose (Thorlabs, M660L4-C5).
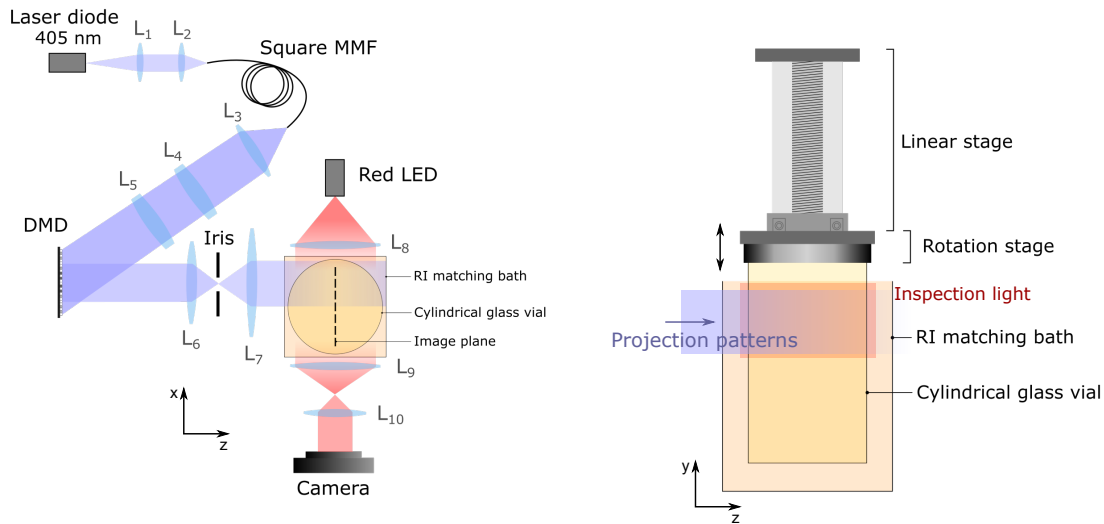
Figure 3.6: **Optomechanical setup for helical volumetric additive manufacturing.**

3.5.2 Computation of the light patterns

The computation of the light patterns from the 3D model target dose relies essentially on the Radon transform as developed for tomographic imaging. However in the case of printing, the problem to solve

is reversed: one has to compute the 2D patterns from the 3D dose whereas in imaging the algorithm aims at reconstructing the 3D object from a set of 2D measurements. As in tomographic VAM (section 2.1.2), [29], [98] the starting point is the 3D model of the object to print. This 3D model, typically stored as an `.stl` file, is first voxelized into a three-dimensional binary matrix, where the entries "1" indicate the presence of matter and "0" its absence at each particular location in space. The voxel size depends on the optical setup and is in our case around 23 μm. The dimension of the matrix is therefore given by the target object size divided by the voxel size. This matrix also represents the normalized target dose that one would need to deposit in a transparent resin to polymerize it in the desired geometry. A series of dose projections over multiple angles are calculated from the Radon transform. More precisely, the patterns are obtained using a filtered back-projection algorithm followed by an optimization subject to positivity constraint (fig. 3.7). Please note that this forward model assumes the use of optically-clear materials, in which light propagates straight and without attenuation. The obtained patterns are too large to be entirely projected with the DMD. For these reasons they are cropped twice. First, along the horizontal axis, because the DMD is off-centered and second vertically to account for the up and down moving of the vial. These two crops allow for reducing the image size to a pattern that can be projected onto the DMD. To avoid any printing discontinuity along the vertical direction the patterns are softened on the corresponding edges with a smoothing mask that contains an overlapping region of adjustable height. The last step consists of padding with zeros the patterns to fit the DMD size.
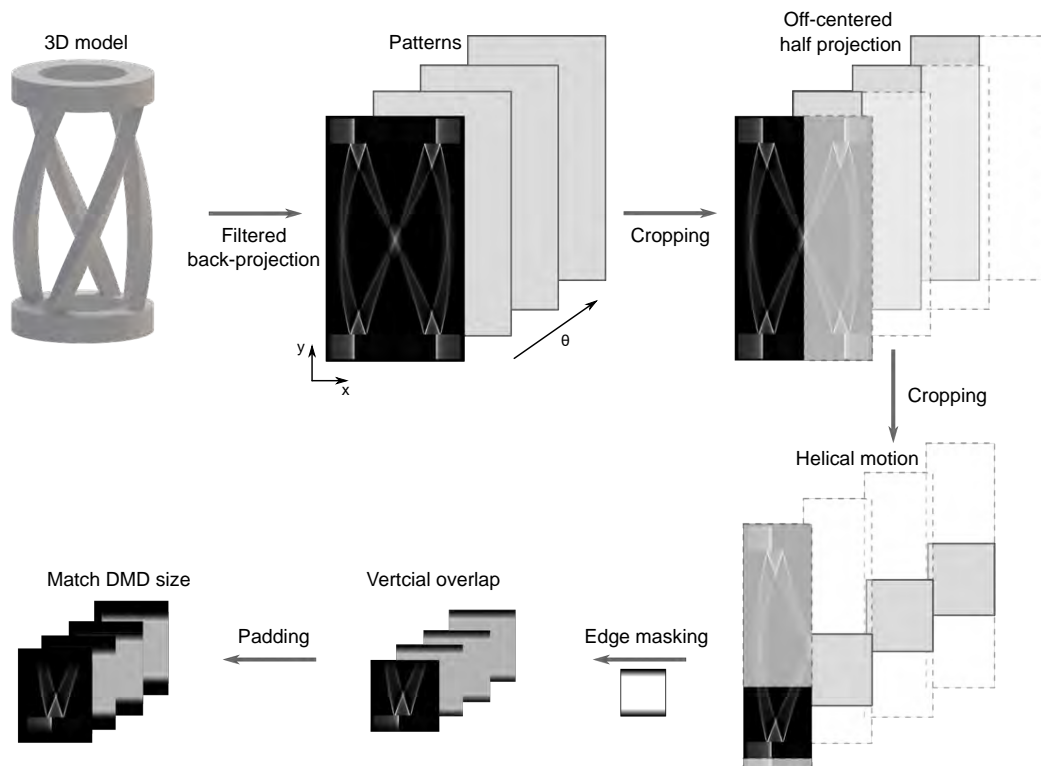
Figure 3.7: **Workflow for computing the light patterns**

3.5.3   Photocurable resin

A liquid pentaacrylate commercial resin (PRO21905, Sartomer) was mixed with 0.6 mM phenylbis (2, 4, 6-trimethylbenzoyl) phosphine oxide as a photoinitiator (TPO, Sigma Aldrich) in a planetary mixer. The mix was poured into 32 mm cylindrical glass vials, and bubbles were removed by intermittent sonication for about an hour. Printing was performed at room temperature. Under these conditions, the resin has a viscosity of 20 Pa·s. Given the printing times in the order of minutes, high viscosity is necessary to prevent the sinking of the object to be detrimental to print fidelity. [13], [72], [84]

3.5.4   Postprocessing

In order to rinse the printed objects after printing, they were gently taken from the vials with a spatula, immersed in 50 mL falcon tubes containing isopropyl alcohol, and sonicated for several minutes at room temperature. Objects were post cured immersed in glycerol in a curing chamber (Formlabs, Form Cure) under UV light to remove the stickiness of their surface.

Contributions

The work presented in this chapter was conducted jointly with Dr. Antoine Boniface, a post-doc in the lab, and Florian Maitre, a master's student. The setup was conceived and built by Dr. Boniface and I, while most of the printing experiments where conducted by Mr. Maitre.

4 Controlling light scattering in volumetric additive manufacturing

This chapter presents the concept of light scattering. It then describes a strategy to quantify scattering in a photocurable resin and to adapt tomographic light patterns to compensate for it in volumetric additive manufacturing. Some of the material presented in this chapter can be found in the following papers and patent:

- Bernal, Paulina Nuñez, Manon Bouwmeester, Jorge Madrid-Wolff, Marc Falandt, Sammy Florczak, Nuria Ginés Rodriguez, Yang Li et al. "Volumetric bioprinting of organoids and optically tuned hydrogels to build liver-like metabolic biofactories." *Advanced Materials* 34, no. 15 (2022): 2110054.

- Madrid-Wolff, Jorge, Antoine Boniface, Damien Loterie, Paul Delrot, and Christophe Moser. "Controlling light in scattering materials for volumetric additive manufacturing." *Advanced Science* 9, no. 22 (2022): 2105144.

- Moser, Christophe, Antoine Boniface, and Jorge Madrid-Wolff. High resolution and three-dimensional printing in complex photosensitive materials. *WO 2022243273A1*. 2022.

4.1   Light scattering

In homogeneous media, light travels in a straight line. When it passes through regions of different refractive indices, it will deviate, or scatter. Scattering is the redirection of radiation out of its original trajectory. It is usually due to the interaction of radiation with molecules or particles. Reflection, refraction, and diffraction are all forms of scattering.

Scattering can be elastic, as when the scattered photon has the same energy as the incident photon; or inelastic, when the scattered photon has less energy than the incident photon. There is no change in the wavelength of light when it is scattered elastically, whereas there is a redshift for inelastically scattered light. In this chapter we will focus on elastic scattering.

As shown in fig. 4.1, once a plane light wave encounters a scattering particle with a different refractive index than its surrounding medium, light will be re-emitted from its boundaries as if they were point sources, as described by Huygens-Fresnel principle. These new wavefronts will interfere to produce a scattering profile that is angle dependent. When radiation is scattered at an angle <90°, it is referred to as *forward* scattering; otherwise it's called *backward* scattering. Forward scattering is usally more likely

a

b Scattering profile of TiO$_2$ nanoparticles in an acrylic resin
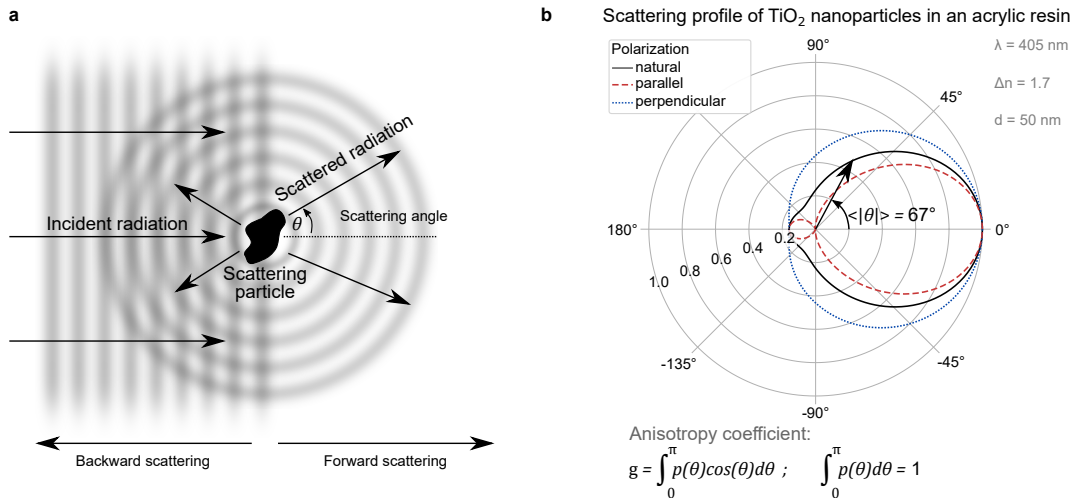
Figure 4.1: **Scattering is the redirection of radiation out of its original trajectory**. **a.** Radiation is scattered after encountering a small particle. **b.** Calculated scattering profile of TiO$_2$ nanoparticles in an acrylic resin. It depends on polarization and is symetricl along the propagation axis. When normalized so that $\int_0^\pi p(\theta)d\theta = 1$, it gives the *phase function*, a probability function of light being scattered at a given angle. The anisotropy factor g is the expected value of $\cos(\theta)$. Calculated using https://omlc.org/calc/mie_calc.html

than backward scattering, as seen in the scattering profile of TiO$_2$ nanoparticles shown in fig. 4.1b. This polar plot shows the angle-dependence of the intensity of the scattered radiation. For parallel-polarized light, for example, we see that the scattering profile has two lobes, and there is no radiation scattered at 90°. Scattering profiles are always symmetrical with respect to the optical axis, so the scattering intensity at $\phi°$ is the same as the scattered intensity at $-\phi°$. The expected value of the cosine of the scattering angle is an important parameter known as the anisotropy, as it gives an indication of how *forward* light is scattered. The anisotropy is a dimensionless quantity bound between -1 and 1, and is mathematically defined as

$$g = <\cos\theta>$$

$$g = \int_0^\pi p(\theta)\cos\theta \, d\theta$$

where $\int_0^\pi p(\theta) \, d\theta = 1$, the phase function

An anisotropy of $g = 0$ corresponds to isotropic (Rayleigh) scattering, $g = 1$ to total forward scattering (Mie scattering at large particles), and $g = 1$ to total backward scattering, as on a reflective white surface. [99] We will use the anisotropy factor to quantify how scattering different cell suspensions are.

We come back to the image of the scattering particle on fig. 4.1a. The scattered radiation is described by electromagnetic theory, so this angle dependence of the scattering probability can be calculated by solving Maxwell's equations and imposing boundary conditions on the surface of the scattering particle. The continuity of the electric field on the surface makes us separate it into its parallel and perpendicular components. From this component separation is that the polarization dependence derives. [100]

The Scattering matrix describes the relationship between incident and scattered electric field components perpendicular and parallel to the scattering plane as observed in the *far field*. [101], [102]

$$\begin{bmatrix} E_{s\parallel} \\ E_{s\perp} \end{bmatrix} = \frac{e^{-ik(\vec{r}-\vec{z})}}{ik\vec{r}} \begin{bmatrix} S_2 & S_3 \\ S_4 & S_1 \end{bmatrix} \begin{bmatrix} E_{0\parallel} \\ E_{0\perp} \end{bmatrix}$$

The exponential term, $e^{-ik(\vec{r}-\vec{z})}$ is a transport factor that depends on the distance between scatterer and observer ($\vec{r}-\vec{z}$). When we measure scattered light at a constant distance r from the scatterer (as a function of angle, for example), the transport factor becomes a constant.

The total field E_{total} depends on the incident field E_i, the scattered field E_s, and the interaction of these fields. When we observe the scattering from a position which avoids E_i, then only E_s is observed. In the far field observation (where $r \gg d$; d the radius of the sphere), the scattering elements S_3 and S_4 equal zero. [100, ch. "Absorption and Scattering by a Sphere"] In practice, we are more interested about intensities than about the amplitude of the electric field, thus $I = |EE^*| = \frac{1}{2}a^2$; where $E = ae^{(-i\delta)}$, for some amplitude a and some phase δ. Hence for practical scattering measurements, the above equation simplifies to the following:

$$\begin{bmatrix} I_{s\parallel} \\ I_{s\perp} \end{bmatrix} = constant \times \begin{bmatrix} |S_2|^2 & 0 \\ 0 & |S_1|^2 \end{bmatrix} \begin{bmatrix} I_{0\parallel} \\ I_{0\perp} \end{bmatrix}$$

To calculate the components of the scattering matrix S_1 and S_2, we can part from Maxwell's equations and impose boundary conditions for the parallel and perpendicular components of the electric field to the interface of the scatterer. Gustav Mie and Ludvig Lorenz independently found analytical solutions for the scattering of an electromagnetic plane wave by a homogeneous sphere. The Lorenz-Mie-Debye solutions to Maxwell's equations can be simplified depending on the relative size of the scatterers with respect to the incident wavelength, namely the size parameter (fig. 4.1b): [103]

$$x = \frac{2\pi d}{\lambda}$$

In the regime where $x \ll 1$, this is when particles are much smaller than the wavelength of incident light, the intensity of the scattered radiation is proportional to the inverse of the forth power of the wavelength. Rayleigh deduced this relationship by dimensional analysis. [100]

$$I_{scattered} = \frac{I_0}{\lambda^4}$$

In Rayleigh scattering, light is scattered in any direction with almost equal probability. This and the wavelength dependence of intensity explain the homogeneous blue color of the sky at noon [I] and the color transitions of sunset; as shown in fig. 4.1c. Red light, which has longer wavelengths, is not as strongly scattered as shorter blue wavelengths; as is the case of the reddish light close to the horizon at sunset. Analogously, red light will travel deeper into a turbid photoresin; which is why there is strong interest to develop photoinitiators that absorb in the red. [12]

[I]Why doesn't the sky look purple though? The lower sensitivity of our eyes to shorter violet wavelengths makes the sky *appear* blue. It is actually purple.

a

$$I(z) = I_0 e^{-\mu_s z}$$

$$l = \frac{1}{\mu_s}$$

Incident light

scattering particles

Light intensity

low   high

b

$$x = \frac{2\pi d}{\lambda}$$

Mie scattering

$x \approx 1$

scattering particle

light rays

Rayleigh scattering

$x \ll 1$

c

Mont Salève

Mont Salève
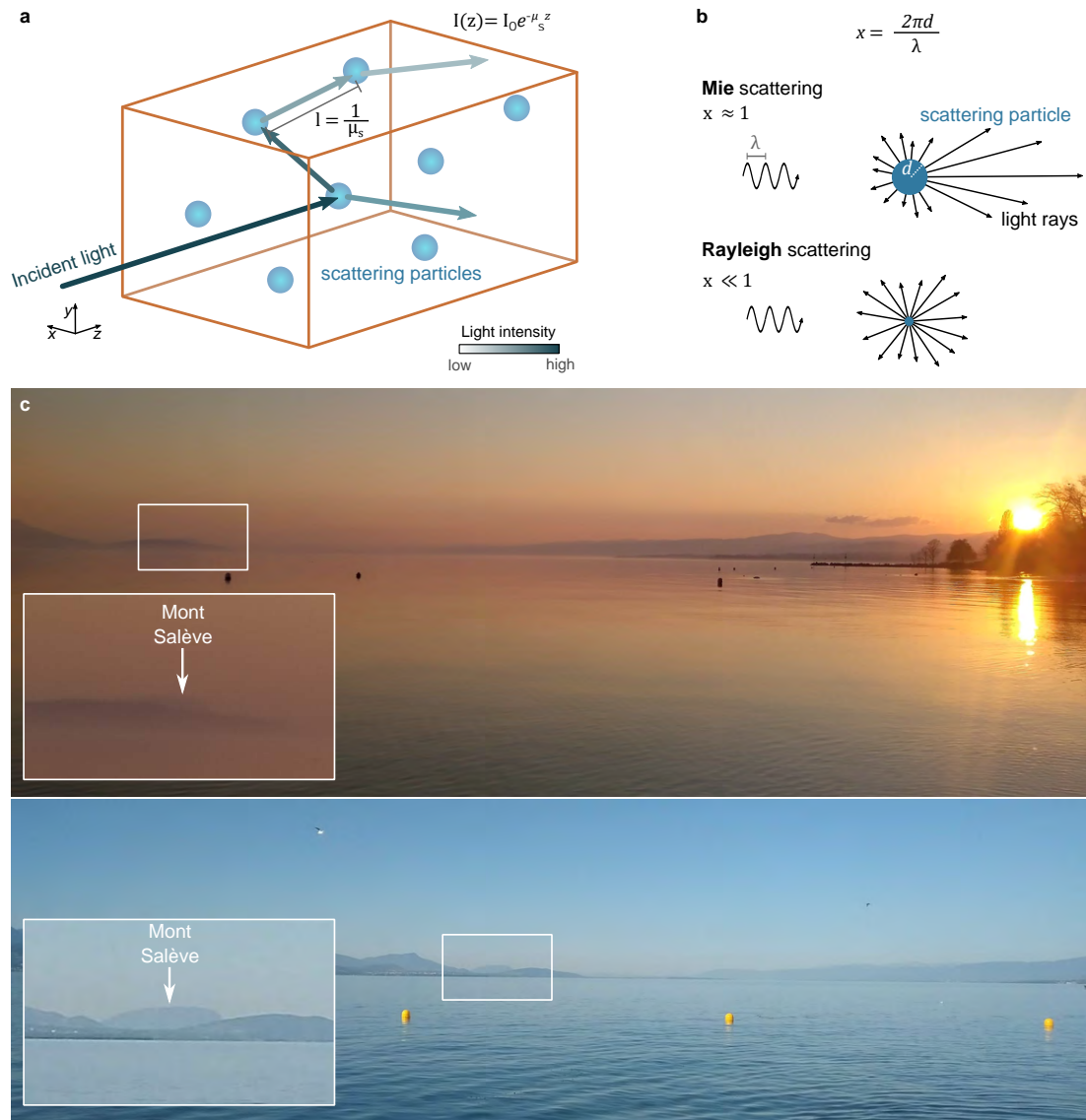
Figure 4.2: **The physical phenomenon of light scattering**. **a.** Light rays are scattered when they impinge on particles with a different refractive index from the surrounding medium. Light is then deflected with an angle-dependent probability. The average length that light travels between two scattering events is called the *mean free path*, $l = \frac{1}{\mu_s}$; where μ_s is the scattering coefficient of the medium. Light intensity decreases exponentially with length travelled through the scattering medium. **b.** The direction in which light is scattered by a particle depends on the ratio between the its radius and light's wavelength; $x = \frac{2\pi d}{\lambda}$. In Mie scattering, particles are larger than the wavelength, and most rays are scattered forward. In Rayleigh scattering, particles are comparable or smaller than the wavelength, and rays can be deflected in any direction with almost equal probability. **c.** *(Top)* Photo of the Leman at sunset, a beautiful demonstration of scattering. The colors of the sky range from blue at the zenith to red at the horizon. The gas particles in the high atmosphere scatter shorter wavelengths more strongly, according to Rayleigh scattering. At low angles from the horizon, light has travelled longer distances and only the longer wavelengths remain unscattered; as they have longer mean free paths. Mont Salève and the horizon above the water surface look blurry due to Mie scattering from water droplets floating in the humid air above the lake. *(Bottom)* A similar picture earlier on a dry afternoon shows that Mont Salève is visible when the air is clear.

When particles are comparable to or larger than the incident wavelength ($x \approx 1$), the scattering profile can be calculated using Mie's approximation. In Mie scattering, forward scattering is more likely than larger scattering angles. Thanks to this, information carried by light can travel for longer distances through Mie scattering media than through Rayleigh scattering media. An example of a Mie scattering media is the humid air above lake Leman on a warm afternoon. The water droplets floating in the air are larger than visible wavelengths and they deviate light that goes through them. This is the reason for Mont Salève to look blurry from the lakeside in Lausanne in the picture in fig. 4.1c. Due to scattering information is lost, and we can't compose a sharp image of the mountain —even if we can guess its shape.

Light can not only be scattered but also *absorbed* by the medium. When a particle absorbs light, it heats up or jumps to an excited electronic state. The particle can later on re-emit light, respectively as in black-body radiation or fluorescence, for example. Fluorescence would be an example of inelastic light scattering. The mean free path between two absorption events is called $l_a = \frac{1}{\mu_a}$. As light travels in an absorptive medium, its intensity decreases exponentially, following Bouguer-Beer-Lambert's law (fig. 1.2 and section 1.2).

In the context of light-based tomographic additive manufacturing, light scattering is detrimental because it information gets scrambled and lost as light travels through the photoresin. As a result, printing resolution and fidelity drop.

4.2   3D printing in a scattering resin

4.2.1   Motivation

Composite resins, colloids, nanoparticle-filled materials, cell-laden hydrogels, and hydrogels enriched with extra-cellular matrix proteins are all examples of turbid materials with enormous interests and applications for the additive manufacturing and biofabrication communities. Cell-laden hydrogels, in particular, are extremely interesting thanks to the perspective they offer for tissue engineering. The short printing time of tomographic VAM, its low concentrations of photoinitiators, and the sealed sterile vials it uses offer enormous advantages when compared to other biofabrication methods. **levatoLightbasedVatpolymerizationBioprinting2023**

4.2.2   Refractive index matching of cell-laden hydrogels

Scattering in volumetric bioprinting comes mainly from the refractive index mismatch between cells, their different organelles, and the supporting media —or hydrogel. Refractive indices within different cells structures vary from $n = 1.36$ for the cytoplasm to $n = 1.6$ for lysosomes. [104] Human cells can be modelled mostly as Mie scatterers, [101] as they are roughly spheres of about 10 μm in diameter. Their inner organelles are smaller, and can have Rayleigh scattering contributions, specially at short wavelengths. Cells can be made aggregate into spheroids or organoids, simple tissue-engineered cell-based in vitro models that recapitulate many aspects of the complex structure and function of the corresponding in vivo tissue. [105], [106]

To reduce the detrimental effects of light scattering in volumetric bioprinting, we reduced the mismatch between the medium and the suspended cells (fig. 4.3a). The clarification of cell suspensions was proposed at least 70 years ago, when Barer used bovine plasma albumin -a protein- to match the

a Scattering reduction

5×10^6 HepG2 cells mL^{-1}

+ Refractive-index matching with iodixanol

Single cells

Light

Single cells

d ≈ 10 μm

Organoids

d ≈ 250 μm

Refractive index ( )

Less scattering

b Refractive index of GelMA + iodixanol

Refractive index ( )

[Iodixanol] (v/v %)

c Scattering measurement set-up

Lens Photodiode
Aperture
Lens
Aperture
Cuvette optical path length 2 mm
Fiber
Lens
Laser
θ
Scattered radiation
Precision rotary stage

d

Organoids

Single cells

g ( )

* p < 0.05

[Iodixanol] (v/v %)

e Text behind scattering layer

2-mm cuvette with 4 million HEK 293T cells mL^{-1}

[Iodixanol] (v/v)

30 %

0 %

EPFL

EPFL

5 mm

f Resulting prints

Pristine GelMA

Single cells

Organoids

Single cells

Organoids

2 mm

2 mm

2 mm

2 mm

Fine feature: 500 μm

+ iodixanol 10 % (v/v)

Figure 4.3: **Refractive-index matching of cell-laden hydrogels**. **a.** Refractive index contrast, and thus light scattering, can be reduced by incorporation a contrast agent, namely iodixanol into the hydrogel. [108] **b.** Tuning the refractive index of GelMA with iodixanol ($n = 3$). **c.** Experimental setup to quantify scattering from cell and organoid suspensions in hydrogels. **d.** Anisotropy factor (g) can be increased by tuning the amount of iodixanol in cell or organoid suspensions (5×10^6 celsls mL^{-1}) **e.** EPFL text, with the letter F behind 2-mm cuvettes with 4 million HEK 293 T cells mL^{-1}. The text is sharper behind the cuvette with 30% iodixanol. **f.** Stereomicroscopy images of resulting prints in a pristine GelMA hydrogel, cell-laden hydrogels, and refractive-index matched cell-laden hydrogels.

refractive index of a bacterial suspension and perform spectrometry on it. [107] Recently, Boothe *et al.* demonstrated the use of iodixanol, a non-cytotoxic contrast agent used in angiography, as a means to tune the refractive index of a medium and improve image quality in live fluorescence microscopy. [108] We mixed iodixanol into gelatin methacryloyl (GelMA) hydrogels and showed that their refractive indices could be varied between $n = 1.36$ and $n = 1.375$, matching those of most organelles (fig. 4.3b).

We designed and built a scattering measurement apparatus, such as the one depicted in fig. 4.3c, following the model proposed by Hunt and Huffman. [109] The device was not sensitive to polarization, though. From the data recorded with this instrument on the scattering profiles of cell- and organoid-laden GelMA hydrogels (10 % w/v) tuned with different concentrations of iodixanol, we calculated

the respective anisotropy factors, as seen in fig. 4.3d. We conclude that organoid suspensions have higher anisotropy factors than single-cell suspensions. Refractive-index matching with iodixanol also increases forward scattering (higher g means more forward scattering). These measurements match the qualitative observations of fig. 4.3e, where text becomes is sharper behind a cuvette containing cells and 30 iodixanol than only cells. Reducing scattering improves fidelity of the bioprinted gels shown in fig. 4.3f, in which the organoid-laden hydrogels tuned with 10 % iodixanol resulted in the closer resemblance to printing in pristine GelMA. Organoid-laden gels have more forward scattering probably because, once aggregated in spheroids of hundreds of microns (fig 4.3a-*right*), scatterers have a larger size parameter. We did not print these models in hydrogels tuned with 30% iodixanol because at these higher concentrations, iodixanol takes the volume of cell media, hindering cell viability.

4.3   Correcting light scattering

In tomographic VAM the light patterns are, in principle, only determined from the object's 3D shape. As described in chapter 2, the conventional approach consists of, first converting the target 3D model into a 3D binary matrix of voxels, where the entries "1" indicate the presence of matter and "0" its absence at each particular location in space. This matrix also represents the normalized target dose that one would need to deposit in a transparent resin to polymerize it in the desired geometry. But, this forward model assumes that light is neither attenuated nor distorted along its propagation, which is no longer valid in turbid materials.

a To characterize light scattering, a thin structured beam of light is projected across the resin while a side-view camera records pictures.

b Picture of the setup, with a light sheet imaged through a TiO_2 nanoparticle suspension.
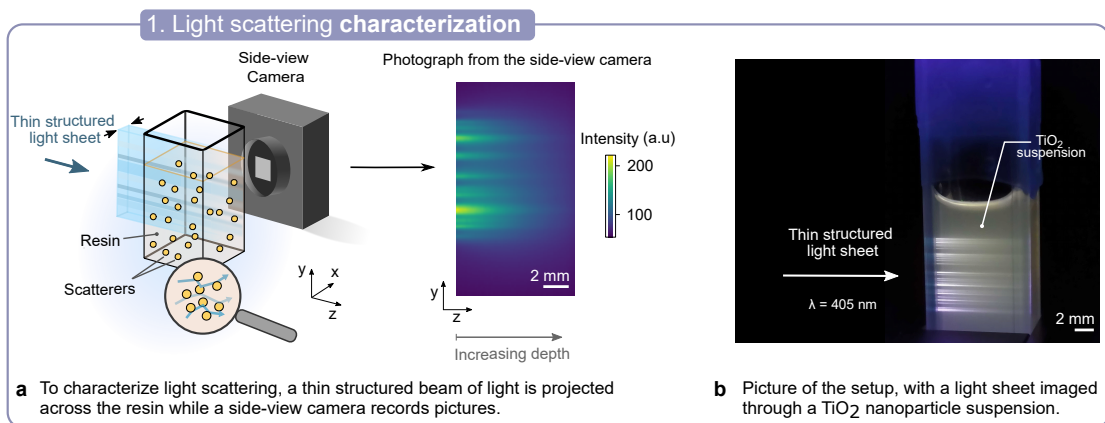
Figure 4.4: **Characterization of light scattering**.

To improve resolution in scattering materials, I propose to optimize the set of projected patterns. The patterns shouldn't be modified individually, but rather as a whole set to make sure that the results of their back-projections over one rotation fits the scattering-corrected dose. The proposed correction is based on the measured bulk scattering properties of the material (and not on simulations), and is to be applied to each new material used in the tomographic printer. The necessary data acquisition and calculations are straight forward and can be integrated into the printing process relatively easily.

4.3.1   Scattering correction method: spatial frequency boosting

I measure the bulk scattering properties of the photoresin in the same setup used for printing. The DMD is used to project a series of (typically) 100 computer-generated light patterns. The patterns are

thin along the *x*-axis to ensure that the camera only receives photons that were scattered once, as seen in fig. 4.4a. This exemplary photograph shows that scattering results in *(i)* an exponential decrease of ballistic light with depth and *(ii)* an increased blur of the light pattern along its propagation. The light patterns should be representative of the spatial frequencies necessary to fabricate the object; so one-dimensional cuts of the uncorrected tomographic patterns are a good set. The resin to be characterized is imaged within a spectroscopy cuvette with 4 optical-grade walls, as in fig. 4.4b; however no photoinitiator is added to the resin to prevent polymerization during the characterization process. A computer code synchronizes the acquisition of one image per displayed pattern. All recorded photographs are then analyzed by an algorithm which follows the steps of fig. 4.5. For the sake of clarity, in figs. 4.4 and 4.5, blue-green intensity color maps are used for real-space measurements, like photographs or light dose maps, while black-purple amplitude color maps are used for *k*-space calculations.

2. Light scattering correction

a To correct for light scattering in the photocurable resins, images for different incoming light structures are captured by the side-view camera.

b The Fourier transform of this dataset shows that high spatial frequencies are, in average, attenuated more rapidly with depth

c By inverting this attenuation map in frequency space, we obtain a correction mask, which indicates how to boost spatial frequencies at different depths to counterbalance the effect of scattering

d To print an object in a scattering resin, the 3D model is binarized and the correction mask is applied (in *k*-space) to the cross sections. Note that, because of rotation, the *z*- axis transforms to *r*- in cylindrical coordinates. The tomographic patterns for the gray-scale 3D object are then calculated.

Figure 4.5: **Correction of light scattering**.

First, the one-dimensional Fourier transform each image is calculated along the *y*-axis. Note that, according to the geometry of the setup, the camera acquires pictures along the *yz*-plane, where *z*- is the optical and *y*- is the vertical axis. The result of averaging all 100 one-dimensional Fourier transforms is a map of spatial frequency attenuation along depth, as seen in fig. 4.5. The map has a marked bright section at the center, which corresponds to a spatial frequency of 0, that is the DC component. Moving away from the center of the vertical axis, higher spatial frequencies, those that correspond to fine

details, are attenuated after shorter depths. Thinking of the example of Mont Salève in fig. 4.1c, this means that the information about the broad shape of the mountain (its DC component with low spatial frequencies) travels longer than the information about the fine detail (with higher spatial frequencies).

The map of spatial frequency attenuation along depth can the be inverted (map^{-1}) to calculate a correction mask, which is shown in 4.5c. The mask indicates by how much to boost spatial frequencies at different depths to counterbalance the effect of scattering. In practice, this correction mask is obtained by dividing the incident averaged spectrum at $z = 0$ mm by each spectrum taken at different depths. This mask is applied in k-space to the cross-sections of any target 3D object to print, as in fig. 4.5d. In our tomographic system, the penetration depth within the rotating vials increases radially and is maximal at the center of the vial (i.e., 8 mm in our case). This is where the light scattering causes the highest distortion for printing. Therefore, it is also where the correction is the strongest, as one can see in fig. 4.5d.

The result is a gray-scale 3D model on which to calculate the tomographic back-projections using the computational pipeline described in section 2.1.2. In this gray-scale 3D model, intensity indicates the dose that should be sent into the volume so that, after scattering, the deposited light dose matches the target model. Gray-scale tomographic reconstruction algorithms have also been used to improve print resolution [21], [62] or locally tune stiffness. [22]

4.3.2 Quantification of print fidelity improvement
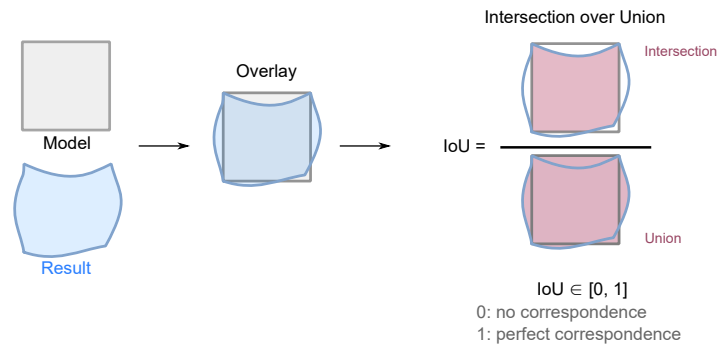
Figure 4.6: **Intersection over Union** is a good metric for print quality. It is bound between 0 and 1; higher means more print fidelity.

We experimentally studied the performances of the method through the printing of different objects in a scattering material made of an organic pentaacrylate doped with TiO_2 nanoparticles (diameter <100 nm). We then compared the obtained 3D printed objects with and without scattering correction. We compute the intersection over union (IoU) between the model and the resulting print as a metric to quantify print fidelity (fig. 4.6). [110] Intersection over union was introduced by Jaccard over 100 years ago, and is a commonly used metric in computer vision to evaluate accuracy of automatic image segmentation. [111] We evaluate the intersection over union in 2D, as it is computationally less expensive.

We used an organic resin with a pentaacrylate as a backbone in which a controlled amount of TiO_2 nanoparticles as a scattering agent was homogeneously dispersed using a sonicator. The concentration of TiO_2 was set to 0.30 mg mL^{-1}. Although this concentration is low, the scattering induced by TiO_2 nanoparticles is very high because the refractive index of TiO_2 is 2.9 at 400 nm compared to 1.5 for the
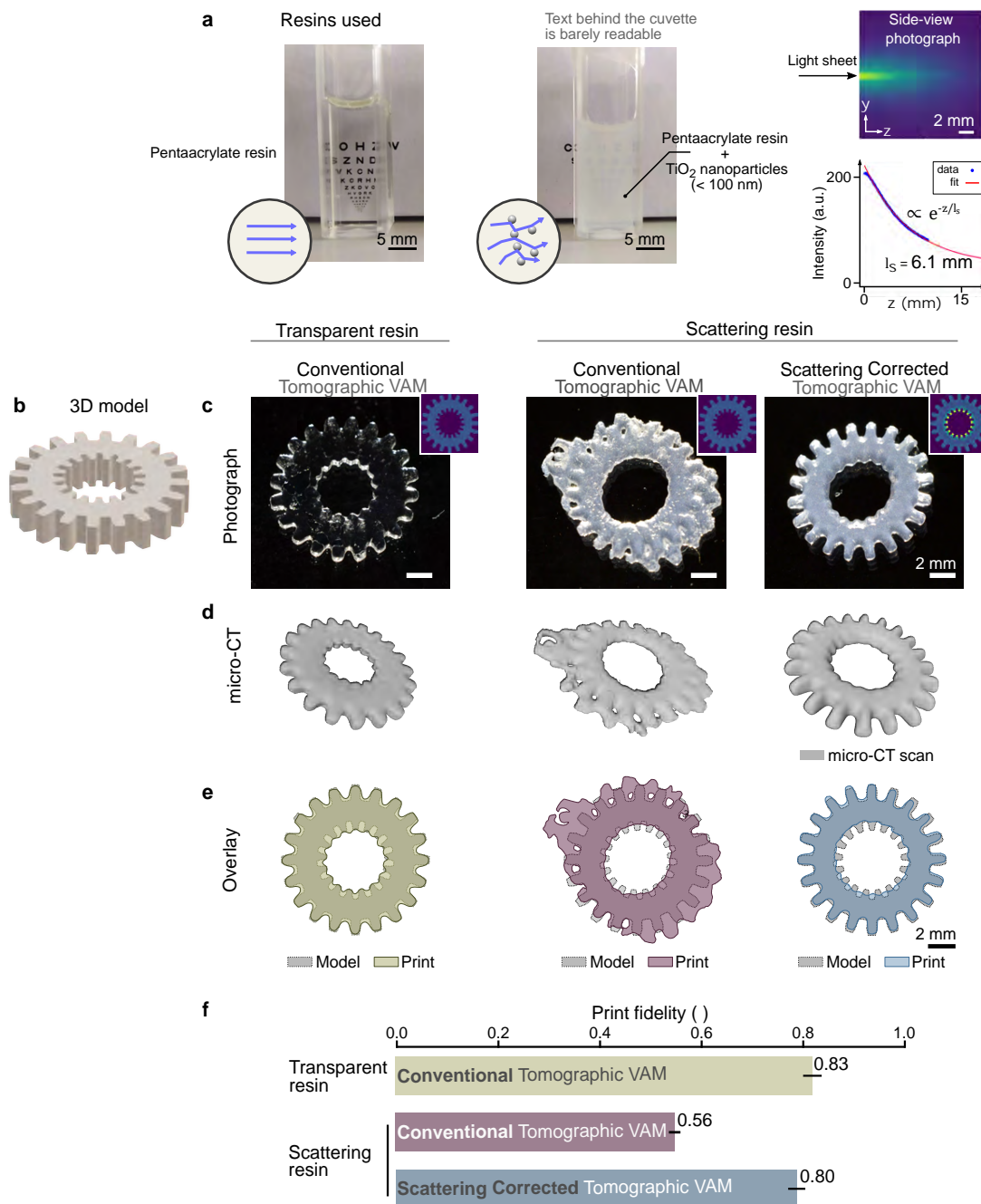
Figure 4.7: **Quantification of print fidelity improvement after light scattering correction**. **a.** Photographs of 10 mm cuvettes with a transparent and a scattering resin with some text behind. Side-view photograph (as in fig. 4.4a) of the scattering resin; and intensity vs. depth profile from this picture. The scattering mean free path is calculated to be $l_s = 6.1$ mm. **b.** 3D model of a gear with inner and outer cogs, a good resolution target. **c.** Photographs of the gear printed in the transparent or the scattering resin (with and without the scattering correction). **d.** X-ray micro-CT scans of the printed gears. **e.** Overlay of the top view of the micro-CT scans with the model. **f.** Print fidelity for the comparison, calculated as the intersection over union (fig. 4.6).

monomer. Knowing the size of the particles and the refractive index mismatch we can derive from Mie scattering formulas the theoretical phase function [II]. [101] This reveals a low anisotropy factor $g = 0.39$ (average cosine of phase function, ref. [112], fig. 4.1b). Experimentally, from the ballistic light exponential decay we can retrieve the scattering mean free path ($l_s = 6.1$ mm) by fitting an exponential function to the decaying light intensity with depth, as seen in fig. 4.7a. This protocol allows us to increase the amount of scattering to ensure that it is deleterious for volumetric printing.

We then used this resin to assess the gain in print fidelity. For this purpose we used the 3D model of a gear with inner and outer cogs as a target for print fidelity (fig. 4.7b). These features are challenging to print because of their small size (inner cogs: width of 460 μm, outer cogs: width of 750 μm) and their position in the vial far from the center, where light is mostly scattered. If no correction is applied, the only way to deposit more light at the rotation axis of the vial and thus print the inner cogs is to increase light dose. This can be done either by rising the laser power or by printing during a longer time. While these two strategies would bring more light at depth, they would also overexpose sections close to the wall of the vial. It results that when the inner cogs start to form, the outer ones are already over-polymerized. It is in this precise situation that the correction intervenes to limit the damaging effects of scattering on the print. Instead of computing the light patterns from the binary dose, we use the target dose reconstructed from the experimental characterization of light scattering. Corresponding printed gears reported in fig. 4.7c, show the inner cogs are better defined and no over-polymerization of the outer structure is observed after applying scattering correction in the TiO_2-loaded resin. The printed gears were scanned with a X-ray transmission tomograph (voxel size of 8.4 μm × 8.4 μm × 8.4 μm). From these scans, we could compute the intersection over union (IoU, 4.6) for their top views, as in figs. 4.7e-f. We report improvements in print fidelity from IoU = 0.56 ± 0.02 to IoU = 0.80 ± 0.03 by printing with a set of corrected tomographic patterns. The baseline print fidelity for this shape in a transparent resin was IoU=0.83 ± 0.03. More importantly, applying corrections for scattering allows to fabricate a functional part with protrusions and indentations.

4.4   Corollary: Attenuation correction

Note that here the correction compensates for the exponential decrease of ballistic light due to scattering; but the effect of absorption can be treated similarly. A useful application would be to correct light absorption from dyes or photoinitiators.In terms of spatial frequencies, one can think of an absorber as a scatterer that attenuates all spatial frequencies by the same amount, as in fig. 4.5b. The corresponding compensation mask would be constant along the k_y-axis. Absorption from photoinitiators is essential to polymerize the resin, but it limits the performance of the printer, such as for resolution or print size. Usually, the concentration of one or more photoinitiators is chosen so that absorption is very small across the vial, but this means that more light (i.e, more time) is needed to print. Also, correcting for the absorption one or more photoinitiators offers the possibility to print faster, to print in weakly polymerizing or crosslinking materials, or to produce larger objects.

4.5   Application example: vasculature model

To emphasize the importance of the scattering correction on the final print we report on the tomographic VAM of hydrogels containing 4.0×10^6 human embryonic kidney 293 cells mL^{-1}. Here, the HEK 293 cells in suspension play the role of optical scatterers as their refractive index does not match

---

[II]open source calculator: https://omlc.org/
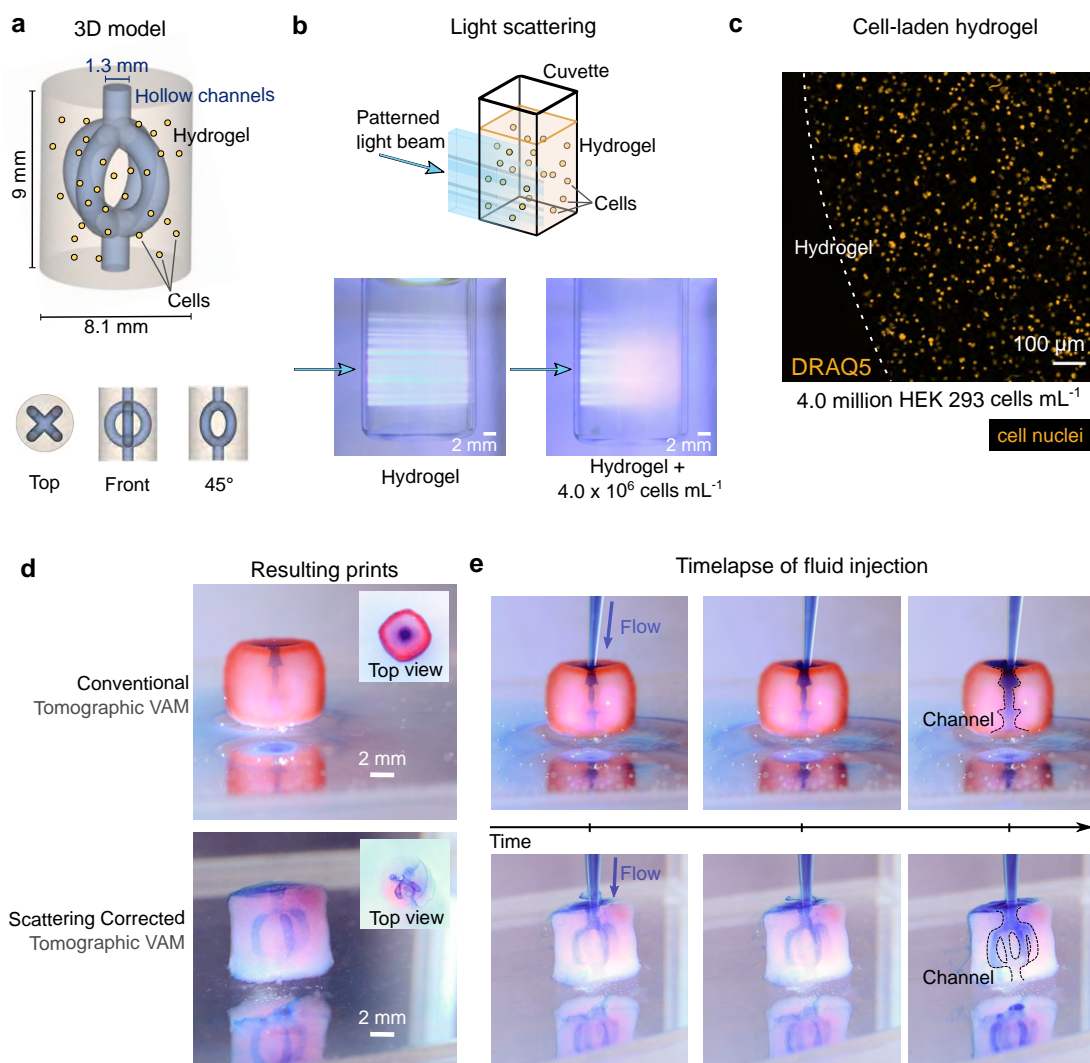
Figure 4.8: **Biofabrication of a perfusable vascular model in cell-laden hydrogels**. **a.** 3D model of a construct with a core surrounded by four channels, emulating vasculature. **b.** Side view of how light is blurred as it penetrates into the hydrogel with cells. **c.** Fluorescence microscopy image of stained nuclei of cells in the fabricated hydrogels (4.0 million cells mL^{-1}). **d.** Photographs of the resulting printed constructs after dying them with red. **e.** Timelapses of a blue dye flowing through the constructs. The scattering corrected tomographic VAM produces an object that matches the geometry and function of the model; while conventional tomographic VAM results in an unintended malfunctioning tube at the center of the construct.

exactly the one of the gel. [113] The target object is a vasculature model of which is, as any hollow structure, challenging to print. Optical scattering makes it difficult for light to reach the middle of the vial without over-polymerizing the outer cylinder.

We use scattering corrected tomographic VAM to fabricate cell-laden constructs that would be difficult to print otherwise. [114]–[116] Bioprinting cm-scale constructs is challenging because hollow channels must be left open to allow for the inflow of nutrients and oxygen to the cells deep inside the hydrogel.

[117]–[121] For this, we used a complex geometry of a 4-mm solid core surrounded by four millimetric channels, as shown in fig. 4.8a. Cell-laden hydrogels may be highly scattering (fig. 4.8b), specially at high cell concentrations (fig. 4.8c). [73] For volumetric light-based biofabrication methods, this constrains cell concentration. The proposed scattering correction spatially redistributes light as it is sent in the tomographic patterns. The overall light dose (19.1 ± 5.2 mJ cm^{-2}, equivalent to 6.4 mJ cm^{-3}) and printing time (36 s) were the same to produce the uncorrected and corrected objects in fig. 4.8d.
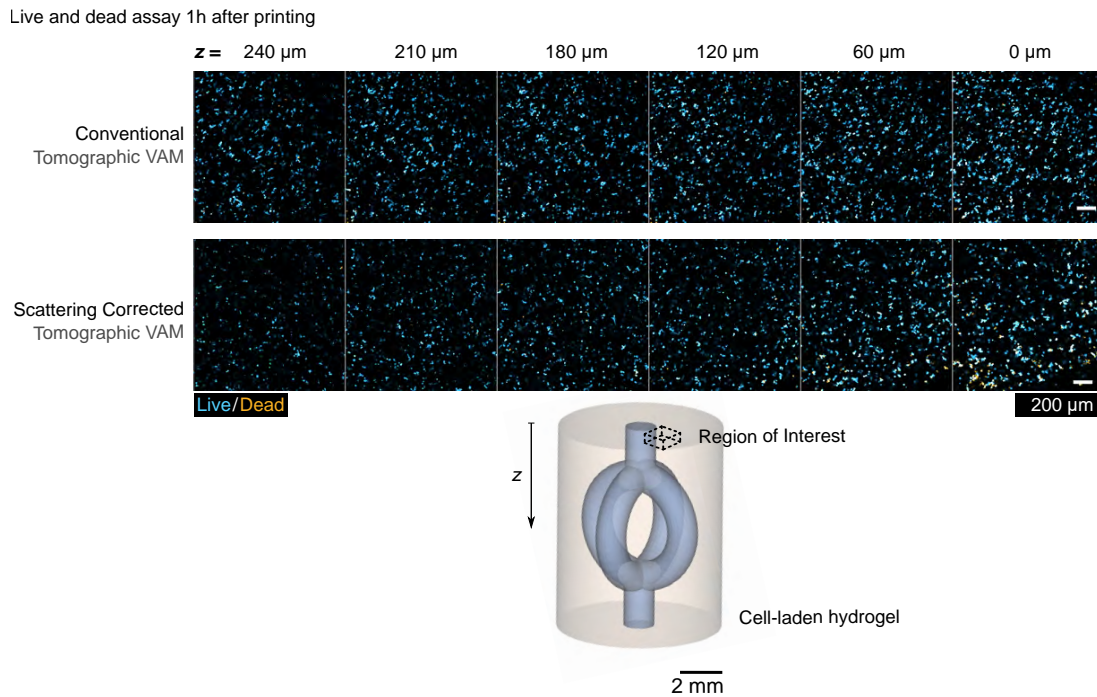
Figure 4.9: **Cell viability after printing with scattering correction**.

Photoinitiators are known to be cytotoxic even at low concentrations (< 50 μM), and are more toxic after light irradiation, probably due to the creation of free radicals. [76] Light irradiation on its own is detrimental to cells, with shorter wavelengths and higher intensities being more phototoxic. [122] In volumetric bioprinting, however, cell viability remains high (>90 %) and is sustained over several days after printing. [28], [71], [73], [123] Cell viability is volumetric bioprinting than in other biofabrication methods such as casting, [28], [73] probably thanks to the lack of shear stress. [124] A qualitative analysis of the images from the Live/Dead assay shown in fig. 4.9 shows that there is no major difference between the hydrogels printed with conventional and with scattering-corrected tomographic VAM, with most cells were alive 1 hour after printing. As our proposed scattering correction does not change the required light dose to produce a print, and results in small changes in the local light intensities of the projected patterns, it is not expected that cell viability should be compromised.

Instead of evaluating the fidelity of the prints (these hydrogels are soft and deform on their weight), we evaluate if all design features are present. The timelapses in fig. 4.8e show a blue liquid dye as it is perfused through the constructs. Conventional tomographic VAM yielded clogged channels and a void core. This comes from the fact that the correct light distribution does not reach the center of the vial during fabrication. Note that a functional object could not be achieved by using neither a lower light dose (this would produce unclogged channels, but the core would still be void) nor a higher

light dose (this would produce a solid core, but channels would still be clogged). Scattering-corrected Tomographic VAM produced a cm-scale construct with all four channels unclogged and a solid core in a soft hydrogel loaded with 4.0×10^6 HEK 293 cells mL^{-1}.

4.6   Printability regime

The amount of light scattering is generally characterized by the scattering mean free path, denoted l_s. It physically represents the average mean free path length between two successive scattering events and is reached when the amount of ballistic component of light, denoted $I_{z=l_s}$, is a fraction of $e^{-1} \approx 37\%$ of the incoming light. In the case of tomographic VAM printing, this parameter is not sufficient to well characterize the printability of the system; the vial's diameter L (along with the light patterns propagate) is also a parameter to consider. For a given l_s, the larger L is the more difficult it is to transmit light, thus printing with high fidelity. Hence, we report on the ratio L/l_s that best takes into account the effect of light scattering in tomographic printing.

It was previously reported that a conventional tomographic printer works well only if the vial's diameter L does not exceed the penetration depth. [28] Originally, this was first investigated to determine the maximal concentration of photoinitiator (resulting in a maximal absorption of light within the build resin) using the Beer-Lambert law, as discussed in sections 1.2 and 2.3.1. In this case, it was found that the absorption length, l_a often referred to as the penetration depth, should be at least $l_a >$ L. If we translate this absorption analysis to scattering that also follows an exponential decay (more precisely the ballistic component of the incoming light is exponentially attenuated with depth), we can state that a first requirement for a scattering resin to be tomographically printed is $L/l_s >$ 1. It is important to emphasize here that this is an idealistic case where absorption from the photoinitiator is neglected as well as the spatial distortion of the light patterns that naturally occurs in scattering materials, preventing from high resolution printing. So in practice, we expect this upper bound to be even lower.
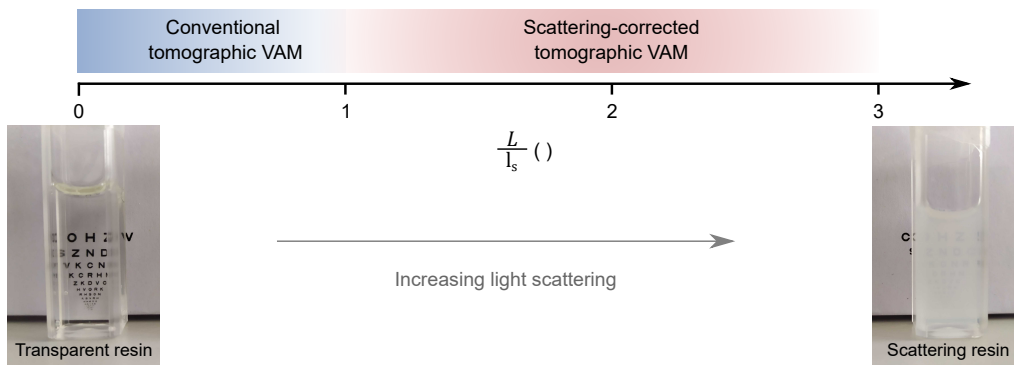
Figure 4.10: **Performance of conventional and scattering-corrected tomographic VAM in different scattering regimes**.

If $L/l_s >$ 1 a conventional tomographic printer does not perform well. Additional scattering corrections like the one presented here are necessary to extend the printability of tomographic printing in this regime. As reported in our work, the implementation of the scattering correction allows printing in cell-laden hydrogels in vials whose inner diameter is L = 13 mm with a scattering length of l_s = 3.6 mm which represents a ratio of $L/l_s \approx$ 3.6. We also printed in scattering acrylates with high fidelity in vials

whose inner diameter is $L = 15$ mm with a scattering length down to $l_s = 4.8$ mm which represents a ratio of $L/l_s \approx 3.1$. With these two experiments in two different scattering materials, we can claim that our scattering correction enables to extend the capabilities of conventional tomographic printing from $L/l_s \approx 1$ to $L/l_s > 3$. This is further illustrated in the fig. 4.10.

4.7 Conclusion

In this chapter, we reported on the necessity of characterizing and correcting for light scattering to improve the quality of volumetric 3D printing in complex non-transparent materials. We proposed to make a correction based on a spatial frequency analysis of a stack of images captured with a side-view camera, perpendicular to the optical axis. Corresponding experimental data reveal the poor transmission of high spatial frequencies due to light scattering by the photocurable resin. Following this image analysis, a numerical correction can be performed to compensate for this frequency-dependent attenuation by accentuating the features of highest spatial frequencies. The resulting corrected light dose presents an increased contrast compared to the standard binary map conventionally used to calculate the tomographic back-projections. Through the printing of several object geometries in two different scattering materials (acrylics and hydrogel-based resins), we demonstrate that the correction improves printing fidelity and resolution.

The proposed apparatus to characterize light propagation through the resin with the side-view camera may also be used for other type of correction. As an example, correcting for the exponential decrease of ballistic light is also feasible and it can be done in real space with a single image. Correction for absorption can be applied to a broad class of materials, like non-scattering but absorptive resins.

The method still relies on the projection system and hence the use of a ballistic light like in the conventional VAM, regardless of the correction applied. This means that printing in opaque material where light undergoes multiple scattering may not be feasible even if a strong scattering-correction is applied, simply because the projected patterns become rapidly random. However, the scattering regime studied here, where the correction shows significant improvements on the printing fidelity, is still very relevant for many interesting materials such as bioresins. Cells suspended in such resins are considered as weak scatterers because of their large size (around 10 μm, i.e. mostly forward scattering) but at high concentration this effect becomes detrimental for tomographic printing. Reaching high cell concentration is however necessary to preserve the viability of the print over time. Here, we show that the scattering correction offers the possibility to increase the cell density in the hydrogel without affecting the printed cellular constructs. Here we show significant improvements using a concentration of 4×10^6 HEK 293 cells mL^{-1} when printing centimeter-scale structures in vials whose inner diameter is 13 mm, which is relevant for maintaining cell viability over time. [28] Correcting for scattering did not seem to affect cell-viability 1 hour after printing; however, future studies to assess and reduce the possible cytotoxicity and mutagenicity of light-based bioprinting methods are necessary. The results presented in this work pushes the applicability of Tomographic VAM to highly cell-loaded hydrogels while keeping its higher printing speed (tens of seconds compared to typically tens of minutes for DLP [125]) and the small amount of photoinitiator needed (0.16 mg mL^{-1} in this work, compared to typical values of 0.5-10mg mL^{-1} for DLP bioprinting. [126]

Similar corrections could also be applied to other printing technologies, such as light-sheet 3D printing, [30], [43] two photon fabrication, longitudinal or multi-axial setups. These corrections could also be used in combination with optical tuning and refractive-index matching of resins to further improve fidelity. [73], [108]

4.8   Experimental materials and methods

Acrylate resins

The photo-curable resins used in this work were prepared by combining di-pentaerythritol pentaacrylate (SR399; Sartomer, France) or PRO21905 (Sartomer, France) with 0.6 mM phenylbis (2,4,6-trimethylbenzoyl) phosphine oxide (97 %; Sigma Aldrich, USA) in a planetary mixer (KK-250SE, Kurabo, Japan). These resins are highly transparent. To make them scattering, TiO_2 nanoparticles (<100 nm particle size, 99.5 %, Sigma Aldrich, Switzerland) were first diluted in ethanol (99.8 %, Fischer Chemical, South Africa) and then added to the resins before planetary mixing. The resins were poured into cylindrical glass vials (diam 16 mm) and sonicated for 15 minutes to remove bubbles.

Post-processing of printed parts

Parts were post-processed by rinsing them in isopropyl alcohol (99 %, Thommen-Furler, Switzerland) for 3 minutes under sonication.

Hydrogels

Synthesis of Gelatin methacryloyl

Gelatin (G2500, Sigma-Aldrich) was used to synthetize gelatin methacryloyl (GelMA) following the protocol in Refs. [127], [128] Then, it was filtered and diluted to a concentration of 8% (w/v) in Phosphate Buffered Saline (PBS, 79382, Sigma-Aldrich). Lithium phenyl-2,4,6-trimethylbenzoylphosphinate (LAP, 900889, Sigma-Aldrich) was added as photoinitiator to the liquid hydrogel at a concentration of 0.16 mg/mL. The material was then bottled in glass containers (inner diameter = 13 mm) and refrigerated to 4°C for at least 2 hours to let them gelify.

Cell culture

Human Embrionic Kidney 293 (HEK 293) cells were cultured in DMEM -high glucose (D6429, Sigma-Aldrich) supplemented with 10 % Fetal Bovine Serum (F9665, Sigma-Aldrich). Cells were incubated in flasks under a humidified atmosphere with 5 % CO2 at 37°C. [129] To prepare cell-laden hydrogels, cells were detached with 0.25 % Trypsin + EDTA (Sigma-Aldrich) for 3 minutes followed by DMEM + FBS 10 %. Cells were then centrifuged at 2000 rpm for 2 minutes and resuspended in PBS. The concentration of cells was calculated by counting cells in a Neubauer chamber. The corresponding volume of cell suspension was pippetted into the liquid GelMA hydrogel prior to adding the photoinitiator, and gently agitated for 2 minutes.

HEK 293 cells are immortalized cells, and as such, are not the most representative cell line to demonstrate functional biofabrication. They are, on the other hand, very representative of light scattering induced from loading a bioink with cells.

Post-processing of printed hydrogels

Printed hydrogels were rinsed with pre-warmed PBS for 15 minutes at 28 °C. The washing medium was changed every 5 minutes.

Imaging of flow through hydrogels

Hydrogels were colored by immersing them in Allura Red AC (CAS 25956-17-6, Sigma-Aldrich) in PBS (1 mg/mL) for 5 minutes. Then, they were rinsed with PBS and immersed in de-ionized water for photographs. To show the functionality of the hydrogels with hollow unobstructed channels, a dark-blue suspension was pippetted through the constructs. The suspension consisted of Alcian Blue 8GX (A5268, Sigma-Aldrich) at 1mg/mL in 90 % glycerol - 10 % PBS.

Fluorescence microscopy of hydrogels

Printed hydrogels were rinsed in PBS 1x, stained with DRAQ5 (1:500, ThermoFischer) for 30 minutes, and rinsed in PBS again. They were then imaged under a confocal fluorescence microscope at 638 nm excitation (SP8, Leica). TrackMate on FIJI was used to count cells in the hydrogel after applying a median filter to the 3D stack. [130]

Live/Dead assay

We evaluated cell viability 1h after printing by means of a Live/Dead fluorescence assay. GelMA hydrogels containing 4 million HEK 293 cells mL^{-1} were printed with and without scattering corrections. The constructs were gently washed in pre-warmed PBS at 28 °C. They were then post-cured for 2 minutes under a blue LED (λ = 410 nm) in in RU/SPS (0.2 μM/2 μM) in PBS. The stiffer hydrogels were rinsed twice in PBS and re-immersed in DMEM without phenol red. Then, the constructs were stained for 1 hour with Calcein, AM (3 μM) and Propidium Iodide (5 μM) in PBS at room temperature in the dark under gentle agitation. They were rinsed three times with PBS before imaging them under an inverted Leica SP8 confocal microscope. The constructs were imaged immersed in PBS in a 24-well Corning plate. Calcein, AM was excited using a laser at λ = 488 nm, and its emission was collected between λ = 500 and 545 nm. Propidium iodide was excited using a laser at λ = 552 nm, and its emission was collected between λ = 600 and 650 nm. Imaging was done using a 10x/NA=0.30 HC PL Fluotar air objective. Stacks of images at different depths were collected with a slicing of 20 μm. The dual-channel images were produced using ImageJ and the LUTs of Christophe Leterrier (https://github.com/cleterrier/ChrisLUTs).

Characterization of the scattering profile of resins

A small amount of the resins (acrylates or hydrogels) was put aside before adding the photoinitiator and poured into 10mm cuvettes with 4 polished windows. The cuvettes were placed at the image plane of the printer. Series of patterns were displayed on the DMD while photographs were recorded simultaneously with the orthogonal camera.

Measurement of Scattering Phase Function of Cell Suspension

In the apparatus, light from a laser diode at 405 nm (HL40033G, Ushio, Japan) is condensed by an aspherical lens (C671-TME405, Thorlabs, USA) into a multimode optical fiber (WF 70×70/115/200/400N, CeramOptec, Germany). Then, a lens (AC254-030-A-ML, Thorlabs) collimates the light at the output of the fiber. An aperture placed right after the lens limits the extension of the outgoing beam to 1 mm. The light is sent straight onto a 2 mm thick square quartz cuvette (CV10Q7FA, Thorlabs). The thickness of the cuvette was chosen so that only single scattering events were present in the hydrogel. Light scattered from the sample is collected by a photodiode (SM05PD3A, Thorlabs). The photodiodes rotate along a circumference of r = 250 mm by means of a precision rotational stage (X-RSW60A-E03, Zaber, Canada). The cuvette is held static on top of the center of the circumference. The signal from the photodiode is amplified (PDA200C, Thorlabs) and digitized by a data acquisition device (USB-6003, National Instruments, USA) and recorded in a computer. A custom MATLAB code controls and synchronizes the laser, the rotational stage, and the data acquisition device to acquire intensities 5 times at every angle with an angular resolution of $0.05°$ between $0°$ and $20°$ (scattered light beyond this angle was 3 orders of magnitude less intense than at $= 10°$, and thus approached to zero). A custom python code is used to process and convert the raw measured currents on the photodiode into light intensities, and to calculate scattering properties from them. For each hydrogel, we report the anisotropy coefficient g, which is the expected value of the scattering angle. [131] The number of samples for all measurements was $n = 3$.

Hepatocytes and hepatocyte organoids

Single-cell experiments were performed on HepG2 hepatocytes grown in DMEM + GlutaMAX (Gibco, 31966, The Netherlands) supplemented with fetal bovine serum (FBS, 10% v/v, Gibco) and penicillin/streptomycin (1%, Gibco, The Netherlands). HepG2 were detached with Trypsine/EDTA 2% for 5 minutes, then reconcentrated by centriguging at 1000 rpm.

Liver organoids were prepared by Paulina Bernal at the University Medical Center Utrecht, Utrecht University following the protocol in ref. [73] Organoids were shipped at $4°$ and used within 24h.

MicroCT imaging and assessment of print fidelity

Printed objects were imaged under a 160 kV X-ray transmission tomograph (Hamamatsu, Japan) with voxel sizes of 8.4 µm x 8.4 µm x 8.4 µm. 3D visualizations of the pieces were obtained with Avizo software (ThermoFischer, USA).

Quantitative analysis of 3D scans were performed on ImageJ. [132] To quantify print fidelity, the object in the microCT scan data was segmented and binarized using Otsu's thresholding [133]. The images of the object were centered around its center of mass and rotated to align them with the orientation of the reference shape. The processed stack of images was then saved and imported into a python code, which automatically computed the Intersection over Union (IoU) for several affine transformations (excluding shear) of the image. From this, we obtained the distribution of IoU indices for each part. We reported the mean IoU and its standard deviation.

To measure the thickness of the parts, the data from the microCT scan was imported into Python as an array. After thresholding it to remove background noise, the array was binarized. Thickness was measured by counting the number of positive voxels

3D models

We used FreeCAD (https://www.freecadweb.org/) to design the 3D models for the gears and the vasculature model.

Contributions

Refractive-index matching   Paulina Núñez Bernal, a doctoral candidate at the Universal Medical Center at Utrecht University, provided the liver organoids and bioptrinted the cell- and organoid-laden constructs shown in fig. 4.3f. I measured the refractive index and anisotropy of cell- and organoid-laden hydrogels.

correction software   This work was done jointly with Dr. Antoine Boniface, a post-doc in the lab. Conceptualization, experiments, data visualization and analysis, and code were done with equal contributions from both of us.

Acknowledgements

Volumetric bioprinting Part II

5 Tomographic volumetric bioprinting of the exocrine pancreatic unit

This chapter presents the application of tomographic volumetric bioprinting to the 3D in vitro modelling of the exocrine pancreatic unit. Pancreatic cancer is a devastating disease, with low survival rates. *In vitro* models of the disease could shed light on the interaction between pancreatic ductal cells and the stromal fibroblasts that surround them.

This chapter describes the cell cross-talk that defines pancreatic cancer inflammation. It then presents a pipeline to use tomographic volumetric bioprinting to fabricate models of the exocrine pancreatic unit. The viability of these heterocellular constructs is assessed. Finally, the chapter presents a strategy to quantify stromal cell *activation*, the aforementioned inflammatory process, from microscopy images. Some of the material presented in this chapter can be found in the following preprint:

- Sgarminato, Viola, Jorge Madrid-Wolff, Antoine Boniface, Gianluca Ciardelli, Chiara Tonda-Turo, and Christophe Moser. "Tomographic volumetric bioprinting of 3D pancreatic cancer models." *bioRxiv* (2023): 2023-01.

5.1 Motivation

Pancreatic cancer represents one of the leading causes of cancer-related death worldwide, with a five-year survival rate below 9%. [134], [135] Among all types of known pancreatic cancer subtypes, pancreatic ductal adenocarcinoma (PDAC) is the most frequent, accounting for 93% of cancers arising from the pancreas. [136] The absence of clear symptoms in the first stages of PDAC evolution reduces the chances of an early diagnosis, resulting in a poor clinical prognosis. Indeed, only approximately 10% of the patients are eligible for surgical resection in combination with adjuvant or pre-operative therapy, since the majority of cases present metastases and extended lesions at diagnosis. [137], [138] Moreover, the unique architecture of the pancreatic tumor microenvironment (TME) weakens the effectiveness of the current treatments that, despite advances in new therapeutic strategies, result insufficient to treat this particularly aggressive pathology. [137], [139], [140]

The PDAC microenvironment is composed of approximately 90% desmoplastic stroma consisting of collagen, fibronectin, fibrillar collagen and hyaluronic acid. [142] This dense stromal tissue creates a hypoxic environment that impedes therapeutics access, leading to disease progression and drug resistance. The stroma arises from the excessive extracellular matrix deposition by pancreatic stellate cells (PSCs). [143], [144] More precisely, in healthy tissue PSCs are located in the periacinar space around
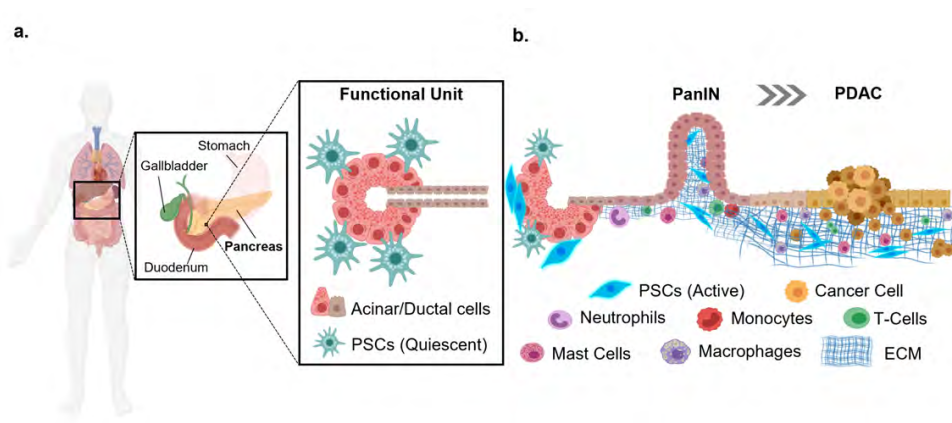
Figure 5.1: **Biological bases of pancreatic cancer**. **a.** Pancreatic cancer typically occurs within the functional unit of exocrine pancreas, composed by epithelial cells (acinar and ductal cells) surrounded by pancreatic stellate cells (PSCs). **b.** Schematic representation of pancreatic intraepithelial neoplasia (PanIN) progression inspired from Liot *et al.* [141]

the acinar and ductal epithelial cells that constitute the pancreatic functional unit (fig. 5.1a), responsible for the secretion of the digestive enzymes. It is in this region where pancreatic intraepithelial neoplasia (PanIN) develops. [137], [145], [146] PanIN is the early lesion which progresses to the development of PDAC through the mutation of specific genes in epithelial cells (fig. 5.1b).

Although the alterations that give rise to PanIN precursor lesions are still to be clarified, hallmarks associated with pathology onset have been identified. Indeed, the oncogene KRAS in the epithelial cells has been reported as the more frequent mutation leading to the progression of PanIN. [141] Besides mutation in the epithelial tissue genome, PDAC formation is also characterized by the desmoplastic reaction induced by cancer cells. Therefore, during pancreatic carcinogenesis, the PSCs, which are in a quiescent state and exhibit a star-shaped morphology, activate in response to inflammatory cues and cancer-cell derived factors, acquiring a myofibroblasts-like phenotype which is characterized by spindle-shaped morphology (fig. 5.1b). [147] Typically, activated PSCs assemble in a core-shell structure surrounding the cancer cells and start to interact with them by generating a complex autocrine and paracrine signaling interplay. [148], [149] In this intricate framework, the stromal components interact with pancreatic cancer cells in different ways that affect gene expression, metabolic activities, invasion or metastasis and resistance mechanisms. [150] In particular, the activated PSCs release cytokines such as interleukin 6 (IL-6) and growth factors (e.g., TGF-β) —inflammatory cues fostering the mutation of the oncogene KRAS in the epithelial cells and the progression from PanIN to PDAC (fig. 5.1b). [148], [151] The understanding of such dynamic phenomena involved in PDAC-stroma crosstalk might expand the knowledge of the pathology and consequently discover innovative biological targets. Indeed, even though important risk factors can contribute to the development of pancreatic cancer (like smoking, obesity, type 2 diabetes, chronic pancreatitis, and alcoholism [152]) and although the mechanisms of evolution from the neoplasia are well documented, [153], [154] the alterations causing the early lesions still remain unclear. [155] Therefore, the understanding of pancreatic cancer raises interest among the scientific community, currently developing efficient PDAC in vitro models in order to detect the disease earlier and design effective therapies thus improving patients' prognosis. [156]–[161] Although recent works have shown the possibility of modeling the PDAC microenvironment in vitro, [156], [158], [160], [162]–[167] the tumor-stroma interplay remains arduous to replicate and monitor in functionally effective models. [168]–[170]
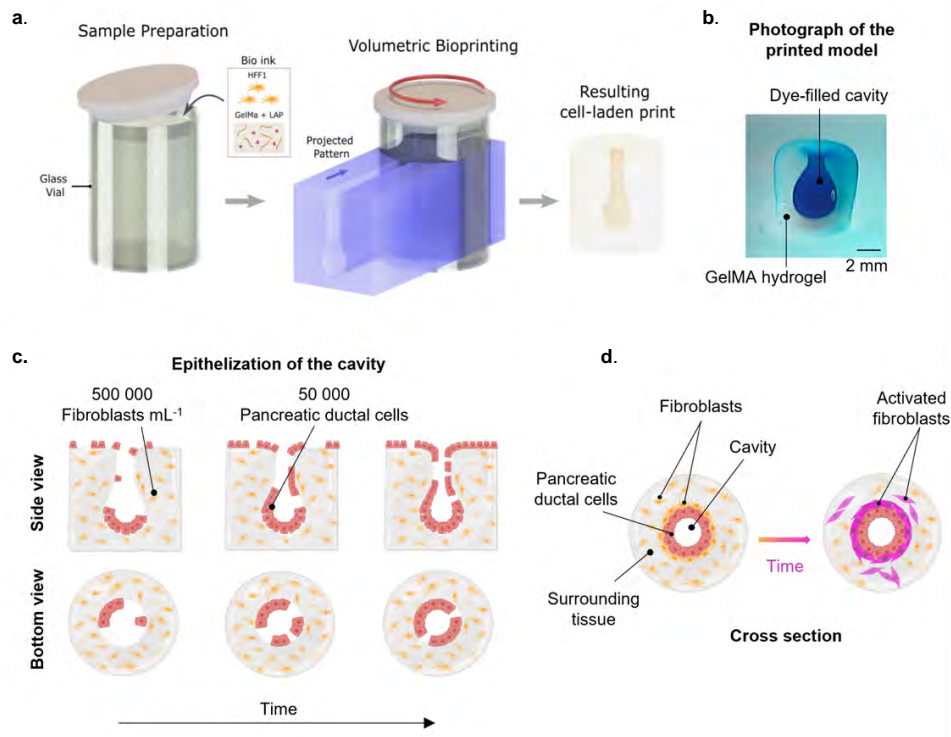
Figure 5.2: **Experimental pipeline for tomographic volumetric bioprinting of pancreatic cancer models**. **a.** In tomographic volumetric bioprinting, a gelatin metacryloyl 5% solution in cell medium containing a photoinitiator and 0.5 million fibroblasts (HFF1) mL^{-1} is poured into glass vials and printed. **b.** Photograph of a bioprinted construct (immersed in water) with the cavity filled with a blue dye (for visualization purpose only). **c.** Schematic of Human Pancreatic Ductal Epithelial (HPDE) cells, healthy or cancerous, can injected into fibroblast-laden bioprinted constructs. They attach and coat the inner surface of the duct. **d.** To recapitulate fibroblast-associated inflammation, the interaction between HPDE cells stably expressing the KRAS oncogene (HPDE-KRAS) and the surrounding fibroblasts is monitored by measuring the expression of αSMA versus actin in the cytoskeletons of the latter. (Figure drawn using Biorender.com).

Heterotypic 3D spheroids, patient-derived organoids, cancer-on-a-chip platforms, and 3D biofabricated constructs are the currently available bioengineered 3D models mimicking the pancreatic tumor-stroma interplay. [149] However, only a few novel studies in literature focus on the development of biomimetic platforms reproducing the microanatomy (in terms of 3D architecture and cellular composition) of the exocrine pancreas and lack to resemble the native compartmentalized architecture of tumor microenvironment that is widely recognized to affect cell functionality and cancer-cell response to therapeutics. [171]–[173] In particular, the gland complex geometry has been reproduced in simplified ways by employing different techniques like viscous fingering and extrusion-based methods, [174]–[177] that have disadvantages such as the low reproducibility, throughput and shape fidelity. These limitations can be overcome by the use of volumetric bioprinting (VBP) which represents an emerging light-based technology capable of fabricating 3D constructs with high-resolution and complex geometries rapidly. [61], [71], [73], [123] Indeed, this technique permits to print hollow structures without the need for support and in a very short building time (down to a few tens of seconds compared to tens of minutes for layer-by-layer approaches). [28] Furthermore, one of the main advantages of VBP

is the cell-friendly procedure lying in the one-step manufacturing process which reduces the stress experienced by cells as compared to other multi-step techniques such as the common solvent-casting method. [178] More specifically, VBP consists of illuminating a photosensitive cell-laden hydrogel with visible light from multiple angles, using a sequence of tomographic back projections of the desired object, [13], [28], [29] leading to the photopolymerization of the material.

We adopt VBP to develop a fully human 3D in vitro model resembling the physiological acinar- and ductal-like structure of the pancreatic gland (fig. 5.2a-b). In particular, a gelatin methacrylate hydrogel (GelMA) has been ad hoc prepared, tailoring the polymer and the photoinitiator concentrations, and loaded with human fibroblasts (stromal cells) to mimic the stromal compartment. We fabricated numerous fibroblast-laden structures by VBP (fig. 5.2a-b). Then, we introduced healthy human pancreatic ductal epithelial cells (HPDE-WT) or stably expressing the KRAS oncogene (HPDE-KRAS) inside the construct's cavity and monitored the co-culture overtime (fig. 5.2c). We analyzed the tumor-stroma crosstalk effect measuring the appearance of a myo-fibroblast phenotype by quantifying expression of alpha smooth muscle actin (αSMA) proteins in fibroblasts (fig. 5.2d). This proposed geometry, although simple, is difficult to realize with other biofabrication methods such as casting or extrusion. Tomographic volumetric bioprinting allows to fabricate fibroblast-laden duct models within seconds. The high throughput of the manufacturing method was fundamental to producing enough models to investigate stromal cell activation.

5.2 Fabrication of exocrine pancreatic units through volumetric bioprinting
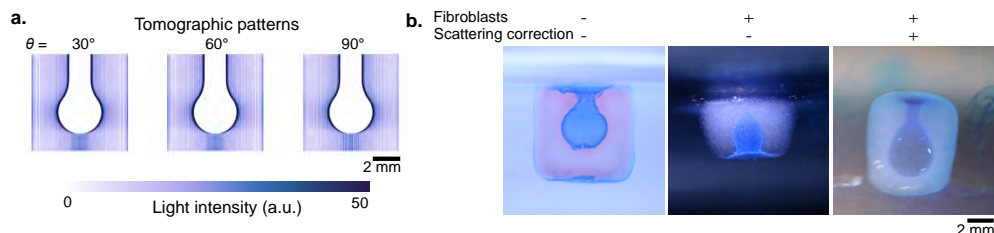
Figure 5.3: **Fabrication of viable 3D pancreatic ductal models**. **a.** Some tomographic patterns used to fabricate the scattering-corrected constructs. In total, 1000 different tomographic patterns are displayed along each turn of the cylindrical vial during printing. **b.** Photographs of 3D printed GelMA constructs, immersed in water and with the duct filled with a glycerol-based blue dye for illustrative purposes. Including cells in the gel affects print fidelity, but it can be compensated by correcting for scattering effects.

The fabricated constructs followed a ductal geometry, with an acinus of larger diameter at the end (sup. video 1). This geometry is challenging to fabricate without employing support structures or without joining two compartments. In VBP, we projected a set of tomographic light patterns into cell-laden GelMA (5% w/v in DMEM w/o phenol red + 0.5 million fibroblasts mL^{-1}) in which we added the photoinitiator at a low concentration (0.16 mg mL^{-1}) (fig. 5.3a). The selected concentration of the photoinitiator allows the crosslinking of GelMA upon visible light irradiation at 405 nm wavelength and is low enough to reduce cytotoxicity and light absorption. The storage modulus (G') of the crosslinked GelMA increased with light dose until reaching a stable plateau at 0.4 kPa, indicating the elastic response of the material, whose viscoelastic properties are comparable to that of pancreatic tissue. [179] The light-scattering effect caused by the presence of cells within the gel caused resolution loss in

the constructed object, such as a an obstructed duct or an incomplete acinus. We used the scattering correction described in section 4.3 to improve print fidelity and resolution. Features of the final geometry, such as the wall thickness and the duct diameter, were optimized to guarantee printability and maximize anatomical relevance. This is because there is a trade-off between structural integrity and cell viability, as metabolic activity in cells within hydrogels is known to decrease with distance from the outer borders of the hydrogel. [119]

5.3 Viability of exocrine pancreatic units
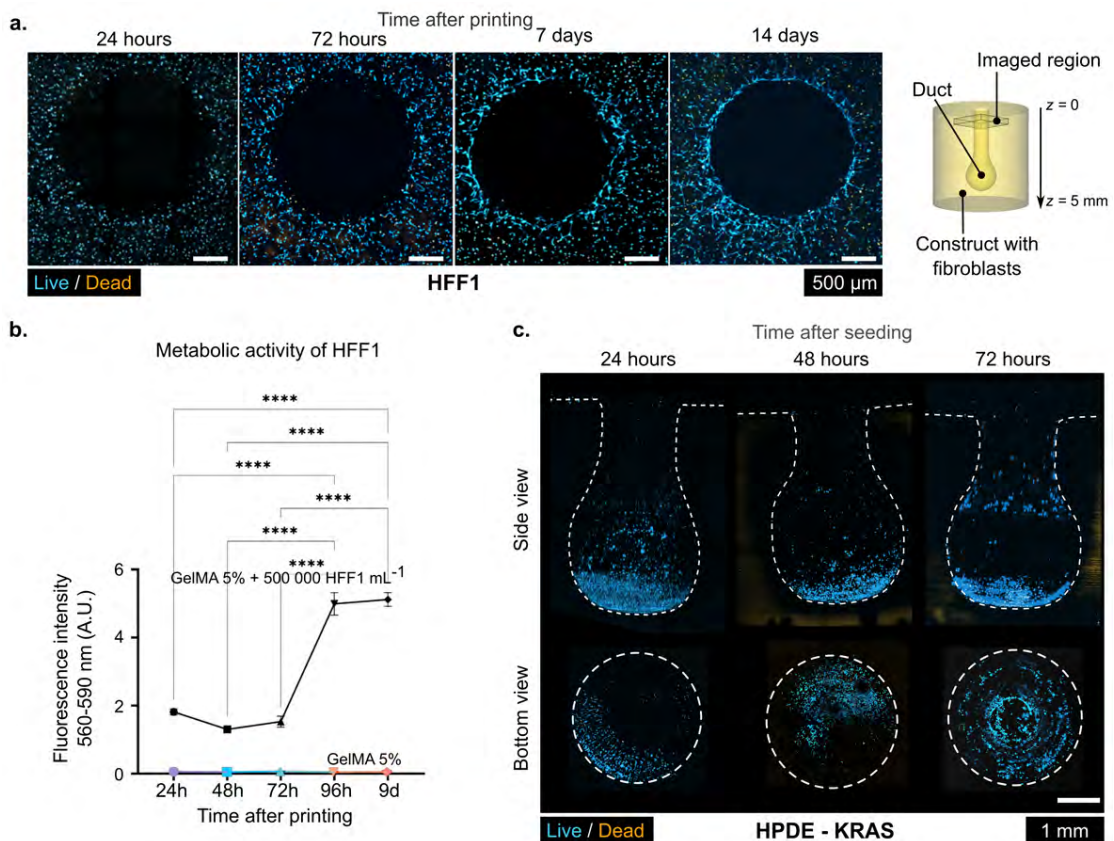
Figure 5.4: **Viability of pancreatic ductal models**. **a.** Live/Dead assay of fibroblasts performed on different samples 1, 3, 7 and 14 days after volumetric bioprinting. A schematic shows the region where these microscopy images were acquired. **b.** Metabolic activity of fibroblasts (black) as a function of time, measured from the reduction of resazurin. Cell-free printed hydrogels (color) are used as a control ($n_{GelMA+cells} = 7$, $n_{GelMA} = 7$). Tukey's multiple comparisons test: $^*p < 0.05$, $^{**}p < 0.01$, $^{***}p < 0.001$, $^{****}p < 0.0001$. Error bars represent one standard deviation. **c.** Injected HPDE cells progress over time to line the inner face of the 3D bioprinted pancreatic model duct.

We assessed the viability of cells within the bioprinted pancreatic ductal models first by monitoring the state of the fibroblasts. Fig. 5.4a shows fluorescence microscopy images of constructs 24 hours, 72 hours, 7 days, and 14 days after printing. Live cells, shown in blue, were stained with calcein-AM, a membrane-permeant dye that is converted into a fluorescent calcein by intracellular esterases. Dead cells, shown in orange, were stained with ethidium homodimer-1, a membrane-impermeant high-

affinity nucleic acid stain that is weakly fluorescent until bound to DNA. The micrographs show the region around the duct, 300 μm deep inside the constructs, with fibroblasts assuming an elongated shape and fully colonizing the inner walls of the duct over time. Micrographs also demonstrate that most cells were alive after the printing process and that they were homogenously distributed within the hydrogels at 24h. Then, cell proliferation and maturation occurred over two weeks as confirmed by the metabolic activity of fibroblasts, which increased with time. Indeed, fig. 5.4b shows fluorometric measurements of the CellTiter-Blue cell-viability assay ($n_{GelMA+cells} = 7$, $n_{GelMA} = 7$), in which resazurin is reduced by metabolic reactions in the cells to resorufin, a fluorescent molecule. Higher fluorescence intensity indicates higher cell viability. We see a significant ($p < 0.0001$), marked increase in metabolic activity 72 to 96 hours after printing, which is sustained at least until 9 days after printing. This significant increment in cell viability at 96h is probably associated to the cell recovery from stress that the biofabrication process may cause. GelMA hydrogels have residual free radicals left after gelation, which can themselves account for the reduction of rezasurin. [180] We control for this effect by measuring the fluorescence intensity also in cell-free bioprinted GelMA hydrogels, and observe that their fluorescence is 2 orders of magnitude lower than in cell-laden hydrogels (fig. 5.4b).
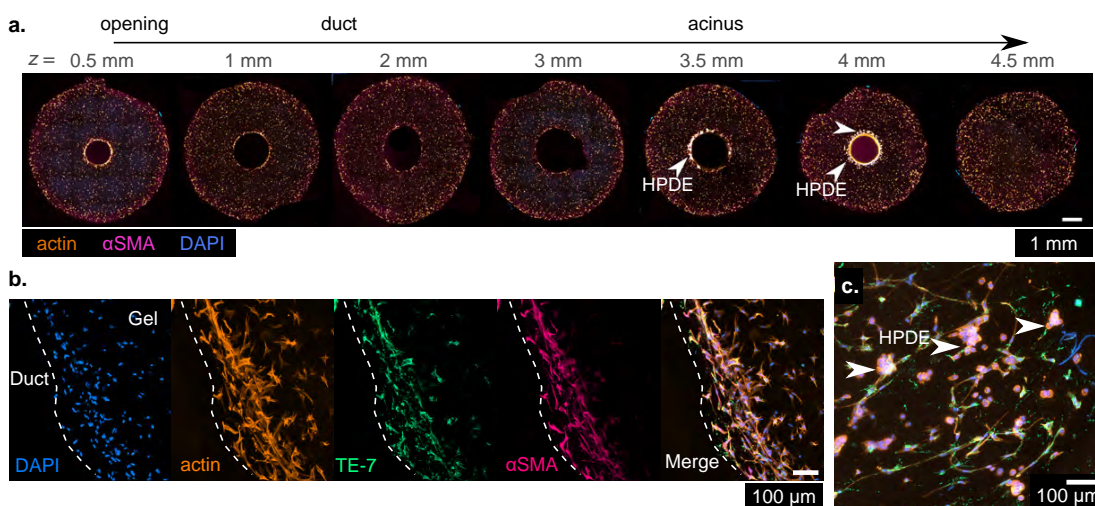
Figure 5.5: **Seeding of HPDE cells in pancreatic duct models**. **a.** Immunofluorescence micrographs of seven 300-μm thick slices of a 3D bioprinted pancreatic model taken 72 hours after HPDE-KRAS cells seeding and 5 days after bioprinting process. White arrows highlight migration of HPDE-KRAS cells inside the fibroblast-laden hydrogel. **b.** High-magnification multi-channel fluorescence microscopy images of the duct wall of a fibroblast-laden construct co-cultured with HPDE-KRAS cells. Fibroblasts take long shapes. **c.** HPDE cells, shown with arrows, form grape-like clusters of smaller round cells (color scheme is the same as *b*).

We also evaluated the capacity of HPDE cells to epithelize the walls of the cavity (duct and acinus) of the bioprinted constructs. For this, we manually injected HPDE cells into the GelMA bioprinted structures without fibroblasts. Fig. 5.4c shows microscopy images from a Live/Dead assay (calcein-AM and ethidium homodimer-1) of HPDE cells 24, 48, and 72 hours after seeding into the cavity of the constructs. Dashed lines indicate the contour of the cavity. The images, which correspond to the intensity sum over planes along 500 m of the microscope's optical axis, show that HPDE cells cover larger extents of the duct walls with time and produce a lining of > 1 mm^2 72 hours after seeding. When co-cultured with fibroblasts, form large linings and invade the bulk, as shown with arrows in fig. 5.5. We followed the progression of epithelization non-destructively by labelling HPDE (WT and KRAS)

with a cell-tracker, a fluorescent dye which does not compromise the viability of cells. We then injected these HPDE cells into printed constructs containing fibroblasts (whitout any fluorescent labels) and followed them for up to 78 hours under a confocal microscope. We acquired full image stacks of the two constructs every 18 hours. These preliminary experiments show that HPDE cells may progress more slowly, probably due to the competition for resources in cell medium (fig. 5.6).
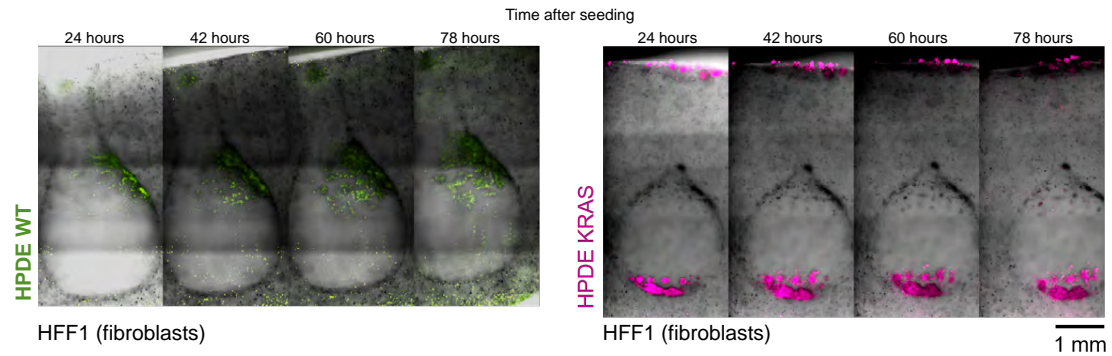
Figure 5.6: **Timelapse of progression of HPDE cells injected into fibroblast-laden cavities**.

5.4 Evaluation of cell-cell crosstalk within the pancreatic in vitro model

We studied the effect of crosstalk between HPDE cells and HFF1 evaluating changes in the cytoskeleton composition of the latter. In particular, healthy HPDE (HPDE-WT) and HPDE overexpressing the KRAS mutation (HPDE-KRAS) were seeded in the fibroblast-laden hydrogels 4 days after the bioprinting process. We exploited the HFF1 recovery occurring during the first 96 hours, when the viability significantly increased, to implement the co-culture conditions. Immunofluorescence microscopy was performed on 300 μm thick transversal slices of HFF1-laden constructs containing HPDE-WT cells, HPDE-KRAS, and without HPDE cells as a control ($n = 4$ replicas for HPDE-WT 72 hours; $n = 3$ for all other treatments) at 5 and 7 days after printing (24 and 72 hours after HPDE seeding), as seen in fig. 5.7a. We used thin slices of the gel obtained with a vibratome to guarantee that antibodies would penetrate evenly throughout the constructs and that all cells in them could be imaged. Anti-αSMA antibody, phalloidin-FITC (an actin marker), and DAPI (a DNA marker) were used to identify cells morphology and to evaluate the appearance of a myofibroblast phenotype associated with an increased expression of αSMA. Qualitatively, we see that fibroblasts in constructs seeded with HPDE-KRAS cells exhibit stronger expression of αSMA, and that this expression increases with time.

We developed an algorithm to automatically and blindly quantify the expression of αSMA with respect to actin over hundreds of cells in several complete slices of the constructs, which were imaged under a confocal microscope following a standardized protocol. The automated analysis used the DAPI signal to detect cells, from which it would then compute the ratio of the intensities of αSMA vs. actin, a proxy of fibroblast activation, as shown in fig. 5.7b. This analysis shows that the mean fibroblast activation increases after exposure to HPDE-KRAS, but not so after exposure to the non-cancerous HPDE-WT. The level of fibroblast activation is also significantly higher after being in co-culture with HPDE-KRAS for 72 hours compared to 24 hours ($p = 0.018$). We also studied the dependence of fibroblast activation with the distance to the duct at the single cell level. Fig. 5.7c shows these measurements, suggesting an increased activation for fibroblasts closer to the duct, where HPDE-KRAS cells lay. In contrast,
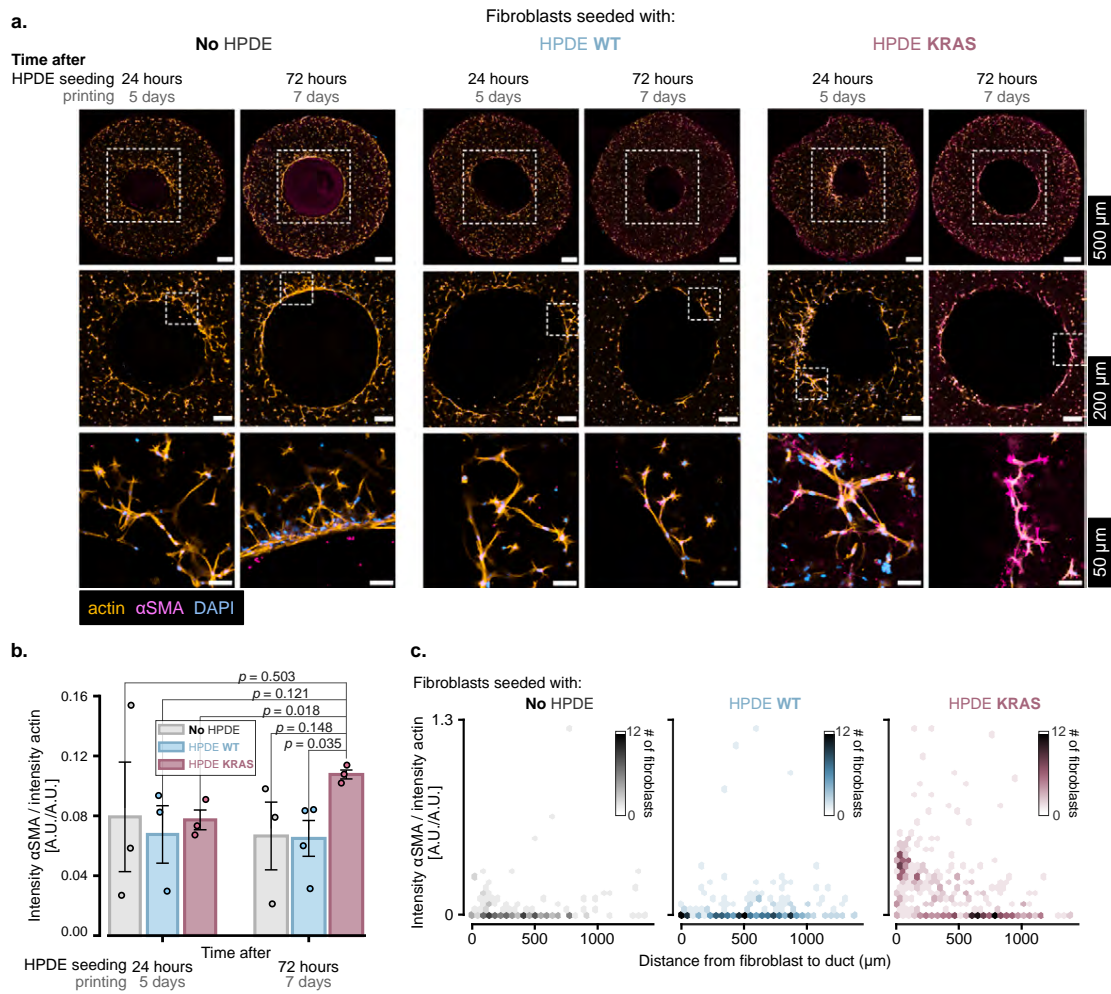
Figure 5.7: **Tomographic biofabricated 3D pancreatic models recapitulate inflammation of cancer-associated fibroblasts**. **a.** Fluorescence microscopy images of full slices of constructs without HPDE cells and seeded with HPDE-WT or HPDE-KRAS cells 24 hours (5 days) and 72 hours (7 days) after bioprinting. Lower rows correspond to close-ups of the dashed regions. **b.** Ratio of fluorescence intensity of αSMA vs. actin. ($n = 4$ for HPDE-WT 72 hours after seeding, $n = 3$ for all other treatments). Error bars indicate standard error of the mean. p-values come from one-way ANOVA tests. **c.** Density maps of the ratio of αSMA intensity over actin intensity in individual fibroblasts vs. distance from the cell to the edge of the duct. Data come from samples 7 days after printing (72 hours after seeding). Number of fibroblasts: $n_{\mathrm{NoHPDE}} = 143$, $n_{\mathrm{HPDE-WT}} = 231$, $n_{\mathrm{HPDE-KRAS}} = 350$.

fibroblasts co-cultured with HPDE-WT cells or with no HPDE cells did not exhibit a decaying degree of activation with distance to the duct. These results indicate that the activation of fibroblasts occurs predominantly when they are co-cultured with HPDE-KRAS cells and that the dependence of αSMA expression on the distance from the duct is evident only in this condition.

5.5   Discusion

Despite several efforts focused on the investigation of pancreatic cancer progression over the past decades, pancreatic ductal adenocarcinoma (PDAC) remains one of the most lethal tumors, with the highest 1-year, 5-year, and 10-year mortalities of any cancer type3. Modeling the dynamic phenomena involved in tumor-stroma interplay is essential to not only increase the knowledge of the disease but also experiment with new and more effective treatments to cure it. Indeed, the stromal tissue surrounding the PDAC site represents a histopathological hallmark of pancreatic cancer [181]–[186] and plays a fundamental role in tumor progression. [187], [188] In this study we developed a 3D in vitro model of the exocrine pancreas which mimics the compartmentalized architecture of the native tissue and allows to recapitulate the stromal and pancreatic cancer cells crosstalk on the same miniaturized construct. We co-cultured human fibroblasts to model the stromal component and human pancreatic epithelial cells, healthy or expressing the KRAS oncogene, to reproduce the exocrine pancreatic tissue, respectively normal or pathological (fig. 5.2). To microfabricate the acinar- and ductal-like geometry, typical of the functional unit of the exocrine pancreas, tomographic volumetric bioprinting was adopted. This one-step, cell-friendly and scalable approach guaranteed high shape fidelity allowing to obtain in a few minutes a 3D cell-laden hydrogel incorporating a cavity, which is constituted of a duct converging to an enlarged lumen (acinus) (figs. 5.2 and 5.3). We demonstrated the printing of relevant object shape for biological studies while maintaining a suitable environment for the growth of stromal cells (HFF1) that remain viable and active for at least 2 weeks after the manufacturing process (fig. 5.4a-b). This is in line with other works, which have cultured viable tomographically printed constructs for several weeks. [28], [71], [189] Therefore, the results proved the beneficial effects given by GelMA as bioink, matching with previous reports on the extensive use of this material in biomedical applications. [190]–[193] Moreover, by exploiting VBP features, the complex hollow structure of the exocrine pancreas can be fabricated without the use of a mould and without the need for sacrificial or support materials as opposed to more conventional (bio)printing and additive manufacturing methods that typically build 3D objects in a layer-by-layer fashion. [194] This innovative biofabrication approach also avoids the technical difficulties and time-consuming procedures associated with the assembling of different cellularized compartments into a unique 3D structure. [175] The cavity within the printed construct constitutes a biomimetic niche which can be easily epithelized by seeding the human pancreatic ductal epithelial cells, suspended in a proper volume of cell medium. We monitored the proliferation of HPDE cells over time and we assessed their ability to cover the inner walls of the lumen by growing as an epithelial monolayer, as already reported by other studies in literature. [177], [195] However, the total coverage of the cavity has not been achieved (figs. 5.4 and 5.6) during the experiment period (3 days) and we observed a slower proliferation rate of HPDE seeded in fibroblast-laden hydrogels with respect to cell-free GelMA constructs (fig. 5.6). This behavior could be ascribed to the competition for nutrients in cell medium by both the cell lines reducing cell proliferation without affecting cell viability. [196] Under co-culture conditions we monitored the activation of stromal cells by quantifying, through a custom-made Python code, the signal intensity coming from the expression of αSMA proteins (fig. 5.7). The results, showing a higher αSMA expression in fibroblasts co-cultured with HPDE-KRAS rather than in contact with HPDE-WT, allow to validate this in vitro model as it can efficiently replicate the physiological inflammation cascade occurring in activated stromal cells. [163]–[165], [197] Moreover, the developed model is the first to recapitulate the tumor-stroma interplay occurring in pancreatic cancer while also accurately reproducing the anatomical structure of the exocrine gland. The geometrical and morphological features of tissue can affect cell function and therefore represent another crucial aspect to consider in the design of a biomimetic model. [171], [198] Although different engineering strategies have been adopted to obtain tubular lumen structures, [171], [175], [177], [195], [199] they lack in fully creating the 3D acinar- and ductal-like geometry [175], [195] or in incorporating the stromal

component. [177], [199] However, our model currently replicates the glandular structure with 5:1 rescaled dimensions as compared to the physiological human gland (diameter of acinar portion 200 μm, of duct portion 50 μm). This ratio is comparable to or smaller than that of other models replicating the morphology of the pancreactic gland, including a hollow duct. [177] Additional work should be performed to enhance the resolution of the printed cavity, to make it more anatomically relevant. [199] In this context, the methodology applied to produce the in vitro model allows for a highly versatile approach, therefore, this model could be further improved by incorporating other cells involved in pathology development. For instance, tissue-resident immune cells could be included inside the construct to assess the role of the immune system in the early stages of pancreatic cancer progression. Finally, this model recapitulating the tumor-associated fibroblasts activation could open new avenues to understand the role of tumor microenvironment in pancreatic cancer progression and offers a new and relevant platform to establish effective therapeutical strategies. Our approach permits to overcome the limitations of the existing in vitro models that do not properly mimic the morphology, the cell composition and the cell-stroma interplay of the exocrine pancreas environment. In addition, it represents a valid alternative to the costly and low-throughput animal models which are ethically questionable and limited in emulating the stromal components of PDAC. [200], [201] Indeed, the rapid fabrication process allows obtaining several scalable human models that can be tested and validated according to a high throughput screening approach.

5.6   Conclusion and future work

In this study, we have developed a 3D in vitro model which mimics the complex three-dimensional microanatomy of the exocrine pancreas to study the mechanisms that take place during the early stages of pancreatic cancer. We used VBP, a recently-developed and powerful printing technique, to fabricate acinar- and ductal-like structures. We showed that this biofabrication approach allows the series production of several human models with shape-fidelity, high resolution and geometrical accuracy. The GelMA-based environment resulted optimal in promoting the proliferation of stromal cells which remain viable and active for several weeks within the gel structure thus permitting a long follow-up. The co-culture of human pancreatic ductal epithelial cells, healthy or overexpressing the KRAS oncogene, and stromal cells in this biofabricated in vitro model can recapitulate the pancreatic TME as confirmed by the stromal cells' activation through the tumor-stroma crosstalk. In particular, we demonstrated the ability of this model in reproducing the stromal cells activation, involved in pancreatic cancer evolution, in a very short period (3 days under co-culture and 7 days after biofabrication). Moreover, the construct can be monitored over time in an accessible and non-destructive way by microscopy to quantitively interrogate the model and easily get the information. These results validate our approach that is scalable and therefore potentially applicable in a personalized medicine workflow, in which the patients' own cells are used to build many models of the exocrine pancreas' microanatomy in a short period of time to rapidly adjust the therapy to the patient. This could enhance treatment outcomes and reduce healthcare costs. Thus, the demonstration of this fully human 3D model represents a powerful tool for the understanding of mechanisms implicated in pancreatic cancer insurgence and for developing new diagnostic and therapeutical approaches. [202]

5.7   Experimental materials and methods

Materials are summarized in table 5.1

Fluorescence microscopy				
Material	**Type**	**Provider**	**Catalogue Number**	**Dilution used**
mouse monoclonal fibroblasts antibody TE-7	primary antibody	Novus Biologicals	NBP2-50082	1 : 80
Rabbit polyclonal to alpha smooth muscle Actin	primary antibody	Abcam	ab5694-100ug	1 : 50
Donkey anti-Rabbit IgG + Alexa 647	secondary antibody	Thermofisher	A-31573	1 : 200
Donkey anti-Mouse IgG+ Alexa 568	secondary antibody	Thermofisher	A10037	1 : 200
DAPI	dye	Sigma	CAS: 28718-90-3	300 nM
((R)-4-Hydroxy-4-methyl-Orn(FITC))-Phalloidin	dye	Bachem AG	# 4095647.0001	0.16 nmol mL[1]
Ethidium homodimer Solution	dye	AdipoGen	CDX-E0512-M001	4 μM
Calcein-acetoxymethyl Ester, Diacetate	dye	Merck	206700-1MG	2 μM

Cell lines				
Cell line	**Type**	**Provider**	**Catalogue Number**	**Sex**
Human foreskin fibroblasts (HFF1)	Human	ATCC	SCRC-1041	Male
Human pancreatic duct epithelial (HPDE) cells	Immortalized	Prof. F. Bussolino (Università di Torino)	NA	Female
Human pancreatic cancer epithelial + KRAS oncogene (HPDE-KRAS) cells	Immortalized	Prof. F. Bussolino (Università di Torino)	NA	Female

Cell culture				
Material	**Type**	**Provider**	**Catalogue Number**	**Concentration**
DMEM (without phenol red)	cell medium	ThermoFisher	31053028	1x
DMEM/F-12, no phenol red	cell medium	ThermoFisher	21041025	1x
Bovine Fetal Serum	complement	Merck	F9665-50ML	15%
Penicillin-Streptomycin	antibiotic	ThermoFisher	15140122	1%
L-glutamine	complement	Sigma	G5792	2%
Trypsin-EDTA PBS 1:250 (0.25%/0,02%) without Ca++/Mg++ w/o Phenolred 100 ml		BioConcept AG	5-52F00-H	
PBS	buffer	Sigma	806552	1x

Hydrogels				
type A porcine gelatin powder		Sigma	G2500	
Methacrylic anhydride		Sigma	760-93-0	
Phosphate buffered saline		Sigma-Aldrich	P4417-100TAB	1x
Lithium phenyl-2,4,6-trimethylbenzoylphosphinate		Sigma-Aldrich	900889-1G	0.16 mg mL[1]

Table 5.1: List of materials used in bioprinting of pancreatic unit models

GelMA Hydrogels

GelMA was produced from porcine gelatin (Sigma) following the protocol by Van De Bulcke et al.81. Briefly, type A porcine gelatin powder (Sigma, G2500) was fully dissolved at 10% w/v into Phosphate Buffered Saline (PBS) 1x at 50°C. Methacrylic anhydride (Sigma, 760-93-0) was added dropwise for gelatin modification at 50°C for 3 h. The solution was then lyophilized and stored away from light at 20°C until use. The 5% w/v GelMA solution was created by reconstituting lyophilized GelMA powder into sterile DMEM without phenol red (ThermoFisher, 31053028) with Lithium phenyl-2,4,6-trimethylbenzoylphosphinate (LAP, Sigma-Aldrich, 900889) at a concentration of 0.16 mg mL−1 and filter-sterilized at 40°C. GelMA solutions were stored away from ambient light at 4 °C for no longer than 2 weeks. Before use, the rheological properties of GelMA hydrogels were evaluated employing a stress-controlled rheometer (AntonPaar GmbH, MCR302) equipped with 25 mm parallel plate geometry. In order to evaluate the photocrosslinking kinetics, filtered GelMA solution + LAP were poured on the rheometer plate and time sweep test was performed using a visible light source at 405 nm wavelength (Prizmatix, FC-LED-405A) at constant temperature (approximately 25°C), a applying a rotational oscillation of 1 Hz and a strain amplitude of 1% in the linear viscoelastic region (measured through strain sweep test).

Cell culture of HFF1

Human foreskin fibroblasts (HFF1) cells were purchased from ATCC and cultured in Dulbecco's Modified Eagle's Medium (DMEM) without phenol red, supplemented with 1% Penicillin-Streptomycin (Gibco), 2% L-glutamine (Gibco) and 15% Foetal Bovine Serum (Gibco). Cells were maintained in a humidified CO_2 incubator at 37°C and 5% CO_2.

Tomographic bioprinting

For printing, fibroblasts were detached, counted, and centrifuged. A small volume of cells, corresponding to a final density of 0.5 million cells mL^{-1}, was resuspended into GelMA with LAP and gently agitated using a 1000 μL pipette tip with a cut tip. 1.5 mL of the GelMA + LAP + HFF1 mix was poured into ethanol sterilized cylindrical glass vials (diameter 12 mm) with a hermetically sealing cap. All these manipulations were carried out under sterile conditions in a biosafety cabinet. The glass flasks were dipped into water at 2°C to gel the GelMA. They were then printed using the tomographic volumetric printer (section 2.2), this time only using three laser diodes. We used a cubic glass container filled with cold water as a refractive-index matching bath. It also kept the temperature of hydrogels constant and prevented them from degelling. The calculations to produce the required tomographic patterns were performed using the pipeline described in chapter 2 with scattering corrections applied to compensate for the diffusive effects of the cell-laden hydrogels, as described in section 4.3.

These calculations were performed on a GPU using PyTorch. [203] This software takes 3D models in the shape of .stl files, which we designed using AutoCAD, and calculates tomographic projections using non-negative tomographic filtered back-projections. We used sets of 1000 8-bit tomographic patterns, each displayed for an angular interval of $\Delta\theta = 0.36°$. The cylindrical vials were set to rotate at a constant angular speed of $12°s^{-1}$ during printing. Prints were completed in around 2.5 minutes. After printing, hermetically closed glass vials were slowly heated to 27°C for 5 minutes by dipping them into luke-warm water. Under sterile conditions in a biosafety cabinet, pre-warmed PBS at 37°C was gently pipetted into the glass vials, then they were gently manually agitated to rinse away the uncross-linked GelMA. The rinsed bioprinted fibroblast-laden constructs were carefully transferred to 24-well plates filled with cell medium and kept in the humidified CO2 incubator at 37°C.

Cell viability in bioprinted constructs

CellTiter-Blue Viability Assay   The viability of human fibroblasts embedded in the bioprinted gel constructs was analyzed by monitoring the metabolic activity through the fluorometric resazurin reduction method (CellTiter-Blue, Promega, G8080) at 1, 2, 3, 4 and 9 days after the tomographic bioprinting process. The test was performed according to the manufacturers' protocols. Briefly, culture medium was carefully removed and constructs were washed with PBS (500 μL). A solution of 16% CellTiter-Blue in complete cell culture medium was prepared and added to the constructs, followed by 5-6 h incubation at 37°C. At the end of the incubation period, 200 μL of the medium was pipetted into different wells of a 96-well plate, and fluorescence was measured from the bottom of the plate using a plate reader (BioTek) at 530 nm excitation and 590 nm emission. Fluorescence of CellTiter-Blue solutions in contact with GelMA hydrogels without cells were subtracted to avoid overestimations. Plates were covered with an adhesive film to prevent evaporation during the measurements.

Live/Dead Assay   Live/Dead Assay was carried out to furtherly evaluate the HFF1 viability over the culture period, at pre-determined time points (1, 3, 7 and 14 days). Specifically, the Live/Dead solution was prepared by adding ethidium homodimer-1 (Adipogen, CDX-E0512-M001, 2mM in DMSO) and calcein-AM (Merck, 206700-1MG, resuspended to 4mM in DMSO) to PBS in concentrations of 4 μM and 2 μM respectively. The solution, prepared afresh every time it was used, was vortex-agitated for some seconds and kept at room temperature (RT) protected from light. The cellularized constructs were rinsed once with pre-warmed PBS at 37°C and transferred to a 24-well plate with wells filled with 800 μL of Live/Dead solution. Constructs were incubated in the dark for 1h, with gentle manual

agitation every 15 minutes. Samples were rinsed twice with PBS and placed in optical-grade multiwell microscope slides for imaging. Imaging was conducted immediately after staining and performed in a fluorescence confocal inverted microscope (Leica, SP8) with 5x NA 0.15 (Leica, HC PL Fluotar, WD 13.7 mm), 10x NA 0.30 (Leica, HC PL Fluotar, WD 11.0 mm), and 20x NA 0.75 (Leica, HC PL APO, WD 0.62 mm) objectives. In the microscope, calcein-AM was excited at 488 nm and its emission collected from 498 to 542 nm. Ethidium homodimer was excited at 552 nm. To avoid crosstalk with the emission spectrum of calcein-AM, the emission of Ethidium was collected from 620 nm to 650 nm.

Epithelization of the cavity

Human pancreatic ductal epithelial cells (HPDE) stably expressing activated KRAS (HPDE-KRAS) and wild-type HPDE (HPDE-WT) were cultured in RPMI-1640 medium (Gibco, Thermo Fisher Scientific) supplemented with 1% Penicillin-Streptomycin (Gibco), 1% L-glutamine (Gibco) and 10% fetal bovine serum (FBS) (Gibco). Cells were maintained in a humidified CO_2 incubator at 37°C and 5% CO_2. To epithelize the constructs, HPDE cells were detached from the culture flask, counted and resuspended to a 10 L volume. Then, they were gently manually injected with micropipette into the duct of the fibroblast-laden hydrogel. Specifically, before the epithelization, the rinsed bioprinted fibroblast-laden constructs were cultured for 96h. The cell ratio between HPDE cells and HFF1 was fixed at 1:3, In accordance with studies reporting the relevancy that ratios of 1:1 to 1:3 have in vivo. [204]–[206] After injection, the constructs were placed in 24-well plates, with enough cell medium to keep them hydrated, but not enough to cover the entry of the lumen, to prevent HPDE cells from floating into the media. Co-cultures were maintained in DMEM/F-12 supplemented with 15% FBS (Gibco), 1% Penicillin-Streptomycin (Gibco) and 2% L-glutamine (Gibco) since previous tests demonstrated the efficacy of this culture medium composition in promoting the cell viability. [207] Two hours later, more medium was added to the wells, this time covering the full constructs. The constructs were maintained in a humidified CO_2 incubator at 37 °C and 5% CO_2.

Immunofluorescence microscopy

Slicing constructs for immunostaining   Bioprinted constructs were fixed in formaldehyde 4% v/v in PBS for 5 minutes, then rinsed with PBS twice and kept at 4°C. The fixed constructs were embedded in low-melting point agarose 4% w/v in pre-warmed PBS and sliced to a thickness of 300 μm with a vibratome (Leica Biosystems, VT1000S) filled with PBS 1x. Samples were sliced orthogonally to the axis of the duct, in order to obtain circular cross-sections. After slicing, the surrounding agarose was detached gently with a brush. Slices were put onto microscope slides with adhesive imaging spacers making wells (Merck, GBL654004-100EA), covered with PBS and with a coverslip and kept at 4°C in a dark wet chamber until they were stained for imaging

Immunostaining   Samples were permeabilized with 0.1% Triton X-100 in PBS for 10 minutes at RT, then washed 3 times for 5 minutes with PBS + 0.1% Triton X-100 (PBST) at RT. Then, samples were blocked with 2% bovine serum albumin (BSA) in PBST for 60 minutes and rinsed once with PBS. Primary antibodies, rabbit polyclonal to alpha smooth muscle actin (Abcam, ab5694-100ug, 1:50), and mouse monoclonal fibroblasts antibody TE-7 (Novus Biologicals, NBP2-50082, 1:80) in PBST + 1% BSA were incubated for 36h at 4°C. Samples were then rinsed 3 times with PBST at RT for 5 minutes. The secondary antibodies, donkey anti-rabbit IgG + Alexa 647 (Thermofischer, A-31573) and donkey anti-Mouse IgG + Alexa 568 (Thermofischer, A10037), were incubated at a concentration

of 1:200 in PBST + 1% BSA for 2h at RT. Samples were rinsed with PBST for 5 minutes at RT 3 times. ((R)-4-Hydroxy-4-methyl-Orn(FITC)[7]-Phalloidin (1:60, 0.16 nmol mL^{-1}) was incubated in PBST + 1% BSA for 30 minutes at RT. Samples were rinsed with PBS for 5 minutes at RT 3 times. Samples were then stained with DAPI in PBS (1:1000) for 5 minutes at RT, washed once with PBS, and finally covered with coverslips for imaging. Samples were kept in wet chambers and protected from intense light during all the immunostaining protocol.
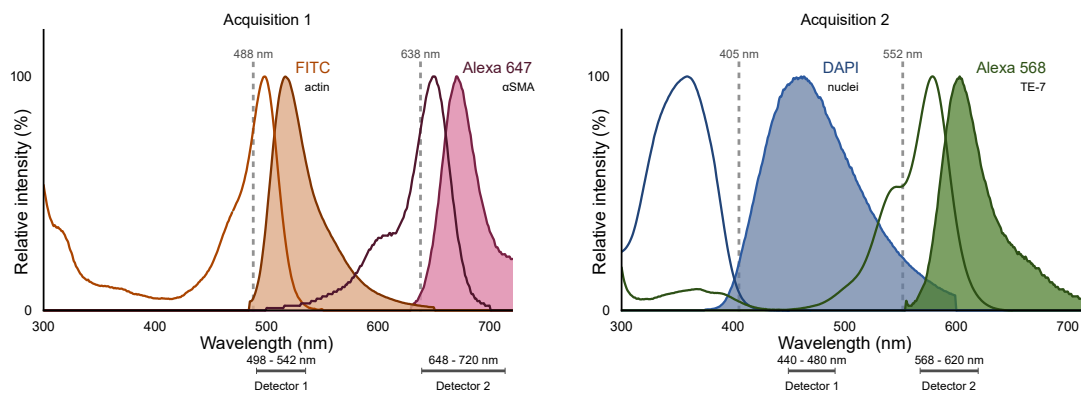
Figure 5.8: **Fluorescence spectra of markers**. Schematic of fluorescence excitation and acquisition in a two-channel confocal microscope (Leica SP8). Data from https://www.thermofisher.com/order/fluorescence-spectraviewer#!/

Confocal Microscopy   Samples were imaged with a motorized inverted confocal microscope (Leica SP8) using a 10x NA 0.30 air objective (WD = 11.0 mm, HC PL Fluorotar, Leica). Fluorescence excitation was performed with solid-state lasers at 405, 488, 552, and 638 nm, and its emission was collected with two twin Hybrid Detectors. An additional photomultiplier tube collected transmitted light from the excitation laser. To acquire images of the full cross sections of the bioprinted constructs, the automatic motorized stage was used to take sequential images along grids that were later stitched together. Two sequential two-channel acquisitions were performed for each sample; one collecting the fluorescence from DAPI (440-480 nm) and TE-7-bound secondary antibody (568-620 nm), and another collecting the fluorescence from Phalloidin-FITC (498-542 nm) and αSMA-bound secondary antibody (648-720 nm), as schematized in fig. 5.8. Both acquisitions used the same grid coordinates of the motorized stage and included a bright field image acquisition. Lasers intensities, detector gain, and optical path were kept unchanged across image acquisitions to guarantee intensities were comparable. Microscopy images were automatically acquired using LAS X software (Leica). Images were acquired for almost 100 slices of 14 independent biological samples.

Image processing   Due to the large area of the acquired microscopy images (> 250 mm^2 in some cases) and to the fact that we were imaging soft, elastic hydrogels, there was displacement between the DAPI-TE-7 and the Phalloidin-αSMA images for some samples (note however, that because Phalloidin and αSMA were always acquired in parallel and not sequentially, there was never displacement between these two channels). Displacement between the DAPI-Te-7 and Phalloidin-αSMA images was corrected with a custom-made Python code. The code compared the bright-field channels of corresponding DAPI-Te-7-BF and Phalloidin-αSMA-BF tiles, calculated the necessary homography ($n_{features}$ = 5000) that needed to be applied to the DAPI-Te-7-BF image so that it matched the Phalloidin-αSMA-BF image.

[208] The code would then apply such homography and save a transformed copy of DAPI-Te-7-BF image. Images were batch-stitched together using the Grid/Collection stitching plugin on ImageJ using the Phalloidin channel as reference. [132], [209] Multichannel microscopy images (DAPI, Phalloidin, Te-7, αSMA, BF) depicting multiple slices of the same bioprinted construct were then manually cropped to fit only one slice per image.

Inflammation quantification from fluorescence data

Inflammation was quantified from microscopy images by measuring the ratio between the intensity of αSMA vs. actin. This calculation was done with a custom-made Python code. The code first segments cell nuclei from the DAPI channel. Then, the code segments all regions of at least $13.4\ \mu m^2$ with a non-zero actin or αSMA intensity in size and which are adjacent to a cell nucleus. An average intensity is calculated for these masked regions for the actin and αSMA channels, and a ratio is reported. Actin and αSMA intensities were additionally normalized to excitation light intensities, to make the ratio comparable across multiple acquisitions.

Single-cell measurements of inflammation   The ratio of actin to αSMA intensities was also computed for segmented single cells. Hand-made digital annotations of the outline of the inner channel of the bioprinted pancreatic constructs (based on the bright field and fluorescence channels of the microscopy images) were used to measure the distance of the individual cells to the channel.

Visualization of microscopy images

Multi-channel microscopy images were visualized using ImageJ and the Look-Up Tables from Christophe Leterrier (https://github.com/cleterrier/ChrisLUTs) for the Live/Dead experiments and from the BioImaging and Optics Platform at EPFL (https://biop.epfl.ch/Fiji-Update/luts/) for the co-culture inflammation experiments. Brightness and contrast were set the same for each channel of all images that were compared (particularly actin and αSMA). Sketches of cell-laden constructs were created with BioRender.com. Plots were produced using matplotlib.org and seaborn.pydata.org. [210], [211]

Statistical analysis

Data were arranged and analyzed using Pandas. [212] The graph data are presented as the mean ± standard deviation (SD) for at least three independent experiments ($n \geqslant 3$). Significance was measured with one-way ANOVA followed by pairwise comparison with Tukey's multiple comparisons test, using GraphPad Prism 9.3.1 for metabolic activity experiment ($*p < 0.05$, $**p < 0.01$, $***p < 0.001$, $****p < 0.0001$) and using SciPy's statsmodels (https://www.statsmodels.org/stable/index.html) for inflammation quantification.

Contributions

This chapter is a joint work with Viola Sgarminato, a visiting PhD student from Politecnico di Torino, and Antoine Boniface, a post-doc in the lab. Experimental work was conducted during between the months of March and June 2022, with data analysis and additional measurements done until October

2022. Ms. Sgarminato, Mr. Boniface, and I printed the 3D constructs using code by Mr. Boniface and I. Cells were cultured mainly by Ms. Sgarminato with my assistance. All three of us participated in sample preparation and microscopic imaging. Automatic data analysis of stromal cell activation was done with codes written by Mr. Boniface and I.

Sinterable materials Part III

6 Volumetric additive manufacturing of silicon oxycarbide ceramics

This chapter presents the application of tomographic additive manufacturing to polymer-derived ceramics. It introduces the field of additive manufacturing of ceramics and how they can be molded with light into a so-called green body, to later get pyrolyzed into a ceramic part. The ceramization of the pyrolyzed parts is demonstrated using FTIR, Raman, and X-ray photoelectron spectroscopy. The thermal and chemical resistance of the 3D printed parts is tested. Finally, the possible applications of the techonlogy are discussed. Some of the material presented in this chapter can be found in the following paper:

- Kollep, Max, Georgia Konstantinou, Jorge Madrid-Wolff, Antoine Boniface, Lorenz Hagelüken, Pradeep Vallachira Warriam Sasikumar, Gurdial Blugan et al. "Tomographic volumetric additive manufacturing of silicon oxycarbide ceramics." *Advanced Engineering Materials* 24, no. 7 (2022): 2101345.

Most of the data reported in this chapter are freely available from the Zenodo repository: https://doi.org/10.1002/adem.202101345

6.1 Polymer-derived ceramics

Ceramics are industrially interesting materials for their hardness, durability and stability in extreme environments. Ceramics are used, for example, in nuclear reactors, in lightweight space mirrors, in electrical insulators, and in knee-replacement prostheses. [213]–[218]

6.1.1 Motivation

Unfortunately, the fabrication of complex ceramic parts remains very challenging. Mainly because of their hardness and brittleness, conventional manufacturing processes such as machining or molding, are limited to simple object geometries as well as being costly and time-consuming. Additive manufacturing represents an attractive alternative. Not only does it offer more flexibility in terms of architecture and significantly reduce material waste but also it leads to cost-effective production in a shorter time. Photopolymerization of polymer-derived ceramics was introduced by Liew *et al.* in 2002, [219] while Zanchetta *et al.* demosntrated the use of stereolithography to prototype ceramics in 2016. [218] When this work was conducted, it was the first demonstration of a polymer-derived ceramic 3D printed with

tomographic volumetric additive manufacturing. Tomographic VAM is interesting in the production of ceramic devices because its design freedom allows for the fabrication of hollow structure, such as the vias in ceramic insulators in microsatelites or chemical sensors. With this work, we intend to explore the possibility to fabricate ceramic components which can include hollow channels. The additive manufacturing of ceramics from liquid pre-ceramic stocks follows this process: [220]

1. The liquid preceramic polymer (PCP) is first solidified into a 3D object: the so-called green body.

2. The green body is then rinsed and transformed into a brown body by burning all highly volatile organic solvents. This is done through a de-binding step at $T \approx 200 - 400°C$.

3. The brown body is pyrolyzed into a ceramic material, by heating it to $T \geqslant 800°C$. During this step, all organic components of the mixture are either burned or transformed into inorganic ceramics.

Initially, preceramic polymer resins were processed or shaped using conventional polymer-forming techniques such as injection molding or extrusion. Later, it was demonstrated that by adding a photo initiator to the liquid precursor, the solid green body can be formed by exposure to UV radiation. [219] Through photopolymerization, laser-based stereolithography (SLA) has enabled the fabrication of preceramic polymer components with high resolution and a good surface quality. [26] It consists of scanning a laser beam on the photosensitive resin and selectively hardening the material, building the 3D green body voxel by voxel. Using this DLP approach it is possible to print in a few tens of minutes complex scaffold structures of typical size $5 \times 5 \times 5$ mm^3 with a resolution of 50-100 μm that maintain their initial shape during pyrolysis at temperatures of $1000°C$. [221], [222] Two-photon photopolymerisation (2PP) is yet another lithography-based AM process characterized by its very high resolution and accuracy, making it ideal for the manufacture of microscopic structures. Pham *et al.* reported the fabrication of complex SiCN ceramic microstructures with a submicron resolution via nano-stereolithography of a preceramic polymer. [223] The process is based on the two-photon absorbed crosslinking of the photosensitive preceramic polymer. Later, more complex structures were also reported using the commercial two-photon photopolymerisation system by Nanoscribe with higher pyrolysis temperatures. [224], [225]

6.2   Volumetric printing of polymer-derived ceramics

Here, we report on the volumetric additive manufacturing of silicon oxycarbide ceramic cm-scale components using a polysiloxane ceramic precursor with a crosslinker. Photopolymerization was induced by tomographic back-projection. The resin used in the printer is composed of a commercial polysiloxane (SPR 684) with 1,4-butanediol-diacrylate (BDDA) as crosslinker. The photoinitiator diphenyl-(2,4,6-trimethylbenzoyl)-phosphinoxide (TPO) was added to trigger the polymerization. The polysiloxane resin and crosslinker are highly transparent in the visible range. Most of the light absorbance of the resin comes from TPO, the photoinitiator (fig. 6.1). Light attenuation, although weak, can hinder the printability of cm-scale shapes; thus we correct for the optical attenuation following the method described in section 4.3. [61]

The radical polymerization mechanism illustrated in fig. 6.2b begins with single-photon absorption by the photoinitiator (TPO). This generates the primary radicals (C-centered acyl and P-centered phosphinoyl radicals) after the α-cleavage of the C-P bond (as in fig. 1.2a). [226], [227] The efficiency of the crosslinking at the propagation step is enhanced thanks to BDDA. In fact, the primary radicals of
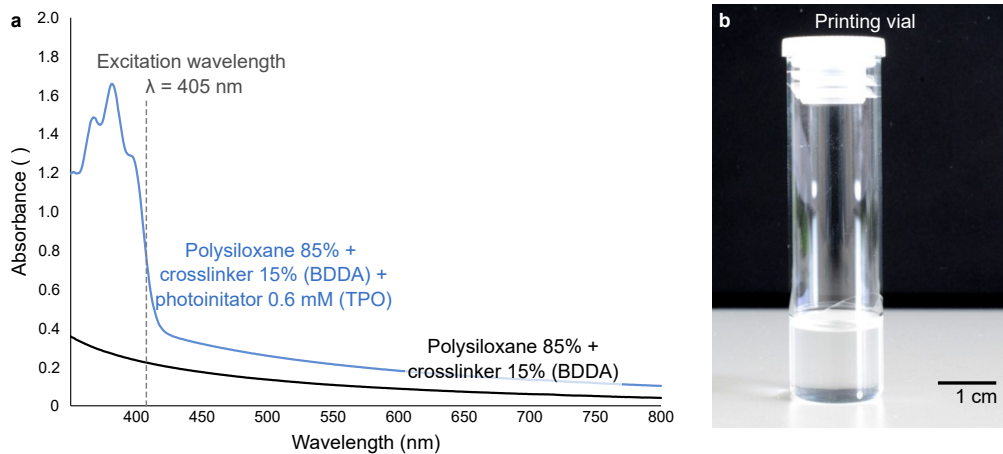
Figure 6.1: **Absorbance of the preceramic formulation**. **a.** Absorbance spectra of the preceramic formulation without photoinitiator (black, mostly transparent) and with photoinitiator (light blue). **b.** Photograph of one of the printing vials with the photoresin.

the initiation step (TPO) activate the radical polymerization of the BDDA by cleaving the methylene bond. The high reactivity of BDDA correspondingly assists the chain growth of the PCP by a similar mechanism of methylene cleavage. In this way, the crosslinking propagates to a direction perpendicular to the chain of the preceramic polymer and should terminate after irradiation stops.

In the volumetric printer, parts are printed within rotating glass vials filled with the photo-curable resin as a set of light patterns are exposed onto it (fig. 6.2a). To ensure high printing fidelity with the target object, it is crucial that the projected light patterns propagate through the resin without being distorted or attenuated.

The used preceramic resin has a viscosity of 870 mPa.s, which is high enough to prevent sinking of the polymerized part within the printing times of 30 to 60 seconds. The printed green bodies are rinsed in isopropyl alcohol and postcured under UV light to make them stiffer. Then, they were pyrloyzed up to $1000°$C. We performed FTIR, Raman and X-ray photoelectron spectroscopy to verify that the pieces were fully ceramized into amorphous SiOC after pyrolysis.

Figure 6.2: **Pipeline of tomographic volumetric additive manufacturing of ceramics**. **a.** the 3D model of the desired part is used to calculate a set of light patterns which are projected onto a rotating vial filled with a photo-curable preceramic resin. The resulting solid green body is retrieved from the liquid resin, and pyrolyzed at $T = 1000°$C. **b.** Schematic representation at the molecular level. A polysiloxane preceramic resin is mixed with a cross-linker and a photoinitiator. After excitation with blue light, a stiff network of polymerized and cross-linked polysiloxane chains forms the green body. During a 48 h pyrolysis process, different organic compounds volatilize while the part transforms into a silicon oxycarbide ceramic amorphous network. [228]

6.3   Pyrolysis and ceramization

6.3.1   Pyrolysis

Fig. 6.3a shows the results of thermogravimetric analysis. Samples of photopolymerized resin were heated at a rate of 5 K/min to maximum temperature under controlled argon atmosphere. During the measurement, the mass loss percentage and the Differential Scanning Calorimetry are obtained. In the calculated Derivative thermogravimetry profile (DTG- blue line) two major decomposition intervals are observed with the appearance of two peaks, first one starting at 375 °C and the second one above 470 °C. The second one is common for PDCs and it appears to be completed above 600 °C. The first mass loss is mainly due to the decomposition of BDDA, which starts above 370 °C. This explains the dwelling step applied at that temperature (to allow smooth release of all the volatile gases) in the pyrolysis profile. Additionally, this step contributes to reduce significantly the formation of bubbles.

Similarly, in DSC (gold line) we can observe a small peak around this temperature, which is attributed to this process. The mass loss is completed at ~ 600 °C and there are no more mass losses as seen from the TG curve (mass loss %).

Fig. 6.3b shows the temperature profile followed to transform the green bodies into polymer derived ceramics. The main dwell time is at T = 1000°C, which is the temperature at which the preceramic polymer loses all its organic components and becomes silicon oxycarbide. The cross-linker also has to be decomposed and evacuated, which is mostly done at the other dwell time at T = 380°C for one hour. Since the cross-linker is completely decomposed, this resin composition has a lot of matter to be outgassed. This makes the pyrolysis challenging and very prone to cracks and swelling. To hinder these negative effects, the heating and cooling rates are very low to provide more time for the gases to escape. This makes the pyrolysis more gentle and allows for a better success rate. The first heating ramp is done at 1 K/min because no component gets decomposed under 300 °C. The second ramp is done at 0.3K/min. At this step, we are approaching the cross-linker decomposing temperature of 380 °C and this has to be done gently. After the first dwell time of 1 hour, most of the cross-linker is evacuated and so the heating ramp can be brought up to 0.6K/min. After the second dwell time, the parts have become ceramics, so the cooling step can be faster. The cooling rate is 1.3 K/min. After around 40 hours, the cooling is not fast enough anymore to follow the desired rate. Since the furnace does not have active cooling, the temperature decreases exponentially. The decomposition temperature of the cross-linker was determined by thermogravimetric analysis.
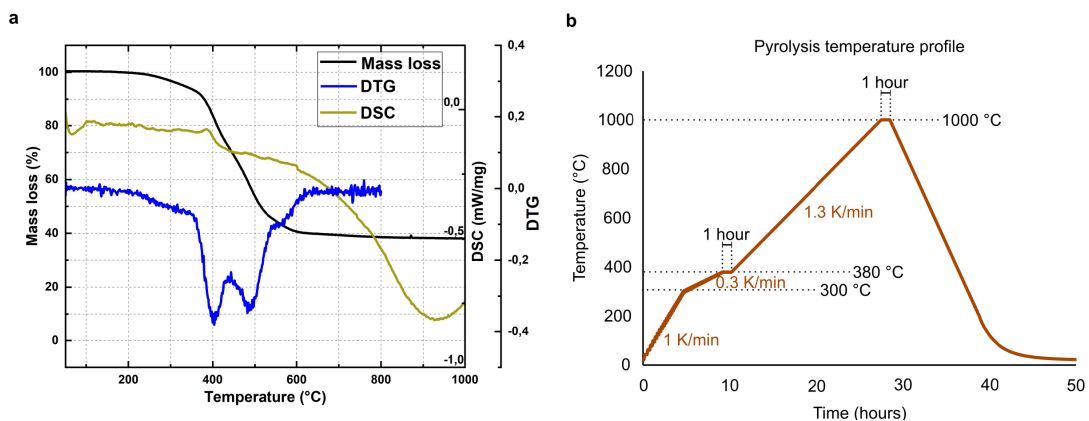
Figure 6.3: **Pyrolysis profile a.** Thermogravimetric analysis of polymerized samples. Mass loss in percentage (black line), Derivative thermogravimetry (DTG- blue line) and Differential Scanning Calorimetry (DSC- gold line) profiles. **b.** Derived temperature pyrolysis profile.

6.3.2   Ceramization

In fig. 6.4a, the FTIR spectra of the green and pyrolyzed state are presented. In the spectrum of the green body, several bands are observed which are mostly referred to the organic siloxane backbone and its functional groups. In the pyrolyzed state, the bands appear as a smoother curve presenting mainly Si-O and Si-C type bonds after ceramization. Both spectra are in good agreement with prior work of the exact same preceramic polymer in the green state, including the added cross-linker and photoinitiator, [229]–[232] and in the pyrolyzed state. [229], [230]

As seen in fig. 6.4b, Raman spectroscopy of green bodies and pyrolyzed parts suggests a conversion from
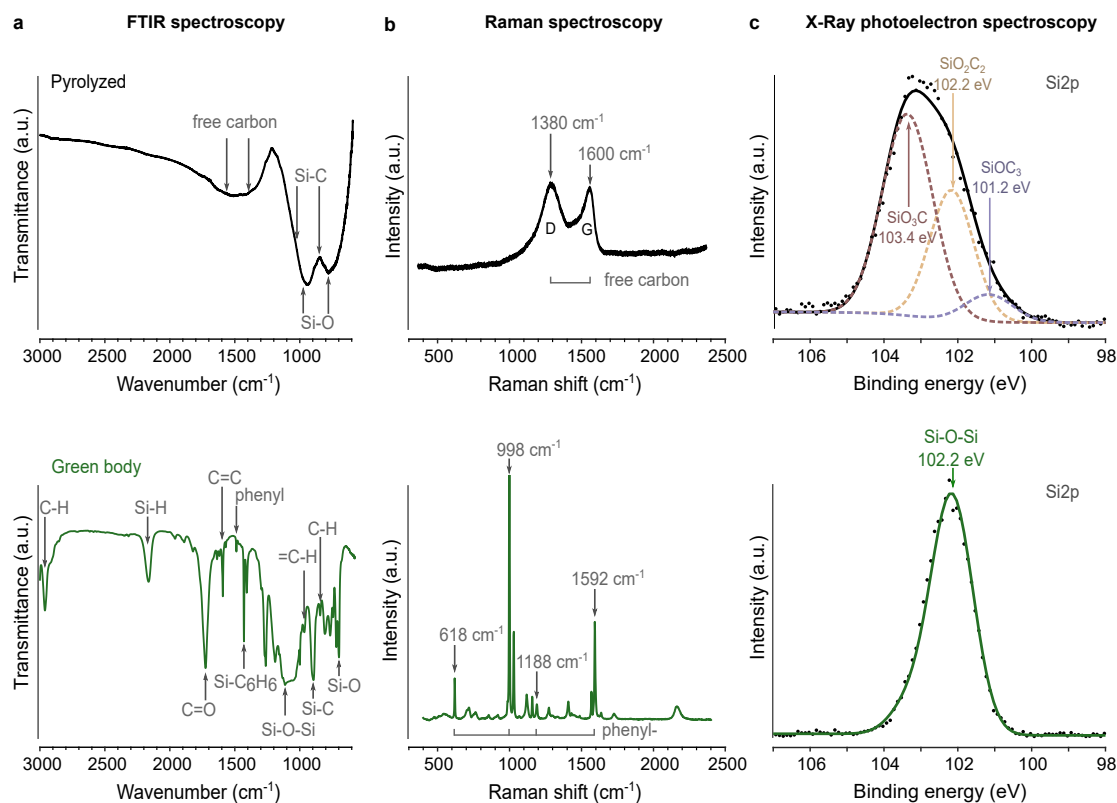
Figure 6.4: **Pyrolysis leads to material transformation from organic green bodies (bottom) to ceramic pyrolyzed parts (top) a.** FTIR spectra suggests conversion from the organic green body with numerous thin absorbance bands, many attributable to the organic bonds in the crosslinked preceramic polymer, to an inorganic silicon oxycarbide material, with Si-C and Si-O bonds. The absorbance region around $1500\,\text{cm}^{-1}$ is attributable to the free carbon phase. **b.** Raman spectra corroborates the findings from FTIR. In the green body spectrum, four strong emission peaks match the spectral fingertip of the phenyl group present in the siloxane. In contrast, the pyrolyzed parts show a smoother emission spectrum, with two marked peaks representing the *D* and *G* bands of the free carbon phase. **c.** X-ray Photoelectron Spectra around the Si2p bond. The spectrum for the pyrolyzed part spans the binding energies that are characteristic to intermediate mixed silicon oxycarbide species, namely SiO_3C, SiO_2C_2, and $SiOC_3$. For the green body, the energy spectrum may be attributed to organic siloxanes.

an organic to an inorganic material after pyrolysis. The spectrum of the green body shows numerous narrow bands, characteristic of the organic siloxane backbone and cross-linker. Most notably, peaks at 618, 998, 1188, and $1592\,\text{cm}^{-1}$ are likely those of the phenyl group in the backbone. [233] The Raman spectrum of the pyrolyzed parts mainly exhibits two broad bands at 1380 and $1600\,\text{cm}^{-1}$, namely the *D* and *G* bands of free carbon. [234] So-called free carbon intrusions have been previously documented in pyrolyzed polymer-derived ceramics. [235], [236] The organization of this free carbon phase segregated within the microstructure and the gradual degradation of the amorphous Si-O-C network have been linked to higher pyrolysis temperatures. This free carbon, as illustrated in fig. 6.2b, has been suggested to explain the high thermal resistance of these materials. [220]

XPS spectra around the Si2p show a broadening of the peak for the pyrolyzed parts, with respect to the green bodies, as seen in figure 6.4c. The spectrum for the pyrolyzed part spans the binding energies

that are characteristic to intermediate mixed silicon oxycarbide species, namely SiO_3C, SiO_2C_2, and $SiOC_3$ with binding energies at 103, 102, and 101 eV respectively. [237] Bonds of lower energies, such as SiC, [238] might be present in these sample, although at much lower concentrations; as the appearance of nanocrystalline SiC has been documented in PDCs only at higher pyrolysis temperatures (>1300 °C). [239] Recent studies have shown that the site of binding between phenyl groups and the silicone backbone may result in mixed Si-O and Si-C bonding, particularly at the interface between the silica rich nanodomains and the free carbon nanodomains. [240] In contrast, the XPS spectrum of the Si2p bond for the green body shows a narrower peak, with an energy distribution that matches that of siloxanes with organic funtional groups. [241]

6.3.3 Shrinkage
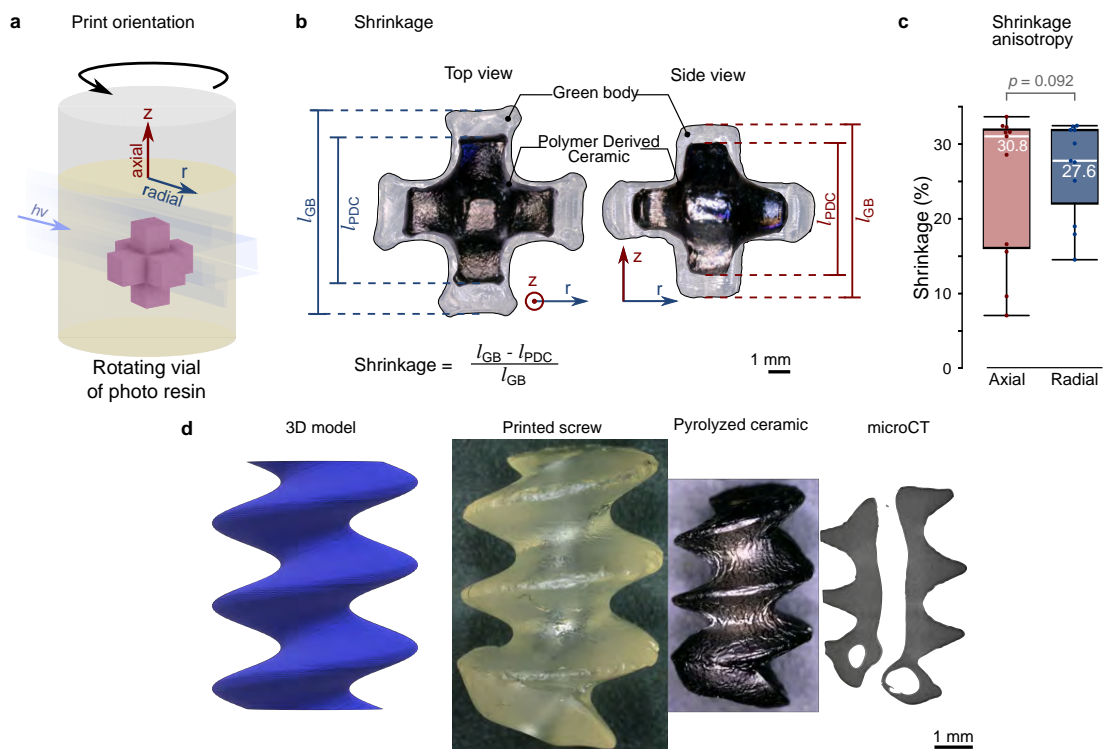
Figure 6.5: **Pyrolysis leads to shrinkage a.** In tomographic volumetric additive manufacturing, the object is printed upon the simultaneous polymerization of the resin in the rotating vial. Unlike SLA or DLP, here there is a clear anisotropy in the printing procedure between the horizontal and vertical axes, the cylindrical coordinate system supposes less anisotropy and less layering effects. **b.** Shrinkage was quantified by measuring the corresponding dimensions before and after pyrolysis, as ashown for this overlay of a green body and pyrolyzed 3D cross. **c.** Shrinkage along the axial and radial dimensions of prints. An paired one-tail t-Test shows that there is no significant difference between the shrinkage along the radial and axial dimensions (n = 7 prints, 14 measurements per print). **d.** A screw with a channel.

Shrinkage poses a difficulty to fabricate functional pieces from preceramic polymers. [242] Recent works measured the resulting shrinkage after pyrolysis and applied corrections to the 3D model to obtain accurate parts. [243] Such corrections are more straightforward if the shrinkage is isotropic.

Previous works on volumetric additive manufacturing have shown that tomographic back-projection results in isotropic, smooth polymerization, contrary to extrusion-based printing and DLP. [28] Since the green bodies are formed volumetrically, without a preferential direction, it is expected that the shrinkage is isotropic. Indeed, the pyrolyzed parts did not show significant differences in shrinkage along any direction (p = 0.092). This allows the PDCs to keep their shape along the axial and radial dimensions of printing, as shown in fig. 6.5. Additionally we report an average shrinkage of $31.0 \pm 1.7\%$ and a mass loss of $54.0 \pm 0.2\%$ from printing to pyrolysis. Although the reported shrinkage is high, it is in line with those of previous works. [218], [242]

6.4   Thermal and chemical resistance

We tested the physical and chemical properties of the fabricated PDCs. To test their thermal resistance, we exposed the parts to rapid thermal shock cycles of 15 seconds heating up under the flame of a butane torch and 10 seconds of cooling down. The temperature of the flame ($T \approx 1400\,^\circ$C) is higher than the pyrolysis temperature. Figure 6.6a shows a time-lapse sequence of a spherical woodpile under its fifth thermal stress cycle. The first and last frames of the time-lapse show that the part retained its shape and did not crack, even withstanding the stress induced by the holding clamp. A supplementary video that matches this timelapse is available from https://doi.org/10.1002/adem.202101345. To assess the chemical inertness of the parts, we submerged them for one hour in aqueous corrosive baths. Figure 6.6b shows a 3D cross PDC sitting in a HCl solution of pH = 2 on the left and a 3D cross PDC sitting in a KOH solution of pH = 14 on the right. Both parts retained their mass (within 0.1 mg on a precision scale). This demonstrates that they are very resistant to high temperatures, rapid heating and cooling for several cycles, and to corrosion.
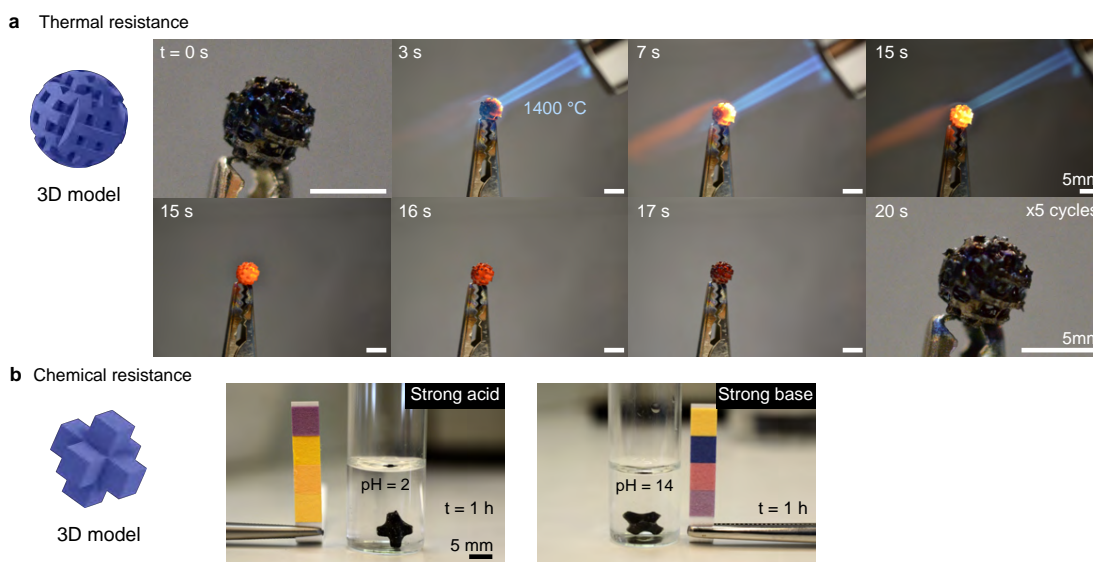

Figure 6.6: **Resistance of 3D printed ceramic parts. a.** Timelapse of a ceramic part being heated to incandescence with a butane torch ($T \approx 1400\,^\circ$C) and then let cool down. The last frame shows the part after five cycles of thermal stress. Scalebars 5 mm. **b.** Parts after being immersed for one hour in a strong acid (pH = 2) or a strong base (pH = 14) for 1 hour.

6.5   Conclusion

Figure 6.7: **Examples of printed silicon oxycarbide ceramic components**; including a screw with an open axial channel, two three-dimensional crosses, and two spherical woodpiles.

In this chapter, we demonstrated the applicability of tomographic volumetric additive manufacturing to produce polymer-derived silicon oxycarbide ceramics. The preceramic polymer resin, a mix of a commercial polysiloxane and a diacrylate cross-linker was sufficiently transparent and viscous to be adapted to tomographic volumetric fabrication. Using back-projections calculated as described in chapter 2 and including corrections for absorption from the photoinitiator following the method proposed in section 4.3, we could volumetrically fabricate objects of various geometries within seconds.

Printed parts were then pyrolyzed up to 1000°C, which transformed the green bodies from an organic cross-linked polysiloxane to an amorphous silicon oxycarbide ceramic. Although pyrolysis was performed following slow heat ramps, degassing from the evaporation of the organic backbone lead to some of the parts getting cracked or fractured, or having bubbles inside. For parts that were sufficiently thin to allow for crack-free degassing, the shrinkage was not anisotropic, with no significative difference between shrinkage along the axial and the radial direction during printing. The amedian linear shrinkage was 30.8 and 27.6 % along the axial and radial directions respectively. The average mass loss from printing to pyrolysis was $54.0 \pm 0.2\%$.

Print geometry determines the success of the pyrolysis. Very thick features (> 2 mm) hinder gases from escaping during debinding and pyrolysis. This leads to cracks and breaks in the ceramized parts. When designing usable ceramic components, attention should be paid to keep features thin and to maximize surface-to-volume ratios. Algorithmic design, which consists of letting a computer software design the desired piece given a set of constrains, [244], [245], can be used to produce parts of very complex geometries and possibly improved mechanical, degassing, or fluidic performances. Such geometries would otherwise be extremely time-consuming to design by a person. The fabricated woodpiles, for example, maximize surface-to-volume area, and served as a good example of a geometry on which shrinkage could be measured while having a high yield of succesfully pyrolyzed parts.

FTIR spectroscopy confirmed the conversion from an organic polysilxane green body to an inorganic ceramic. Raman spectra further confirmed this, while also demonstrated the existence of free-carbon phases within the bulk of the ceramized parts, as seen in the spectral fingerprints for the D and G carbon bands. X-ray photoelectron spectroscopy, which gives information on the energy of electronic bonds within a material, suggests that the resulting ceramic is a mix of ntermediate silicon oxycarbide species, namely SiO_3C, SiO_2C_2, and $SiOC_3$. We can conclude that the resulting objects are made of a silicon oxycarbide ceramic.

The ceramized parts were resistant to thermal stress cycles of rapid heating and cooling cycles between room temperature and 1400°C. Also, they proved to be chemically inert, resisting immersion in strong acids or strong bases for one hour without mass loss or evident changes on their surface.

With this, we showed for the first time that tomographic volumetric additive manufacturing can be used to fabricate polymer-derived ceramics. The printed objects included hollow screws, which could be filled with conductive pastes, as shown in figs. 6.5d and 6.7. Such devices are interesting for biomedical applications, as in pacemakers, [246] or for space, as in microsatellites. [247] This work was a proof-of-concept demonstration and an exploration into possible pathways to fabricate polymer-derived ceramics with greater flexibility. As a fabrication approach, the photocuring of polymer-derived ceramics faces major applicability issues due to the long times an low throughput of pyrolysis. Cracks, fractures, shrinkage and deformations are still common and hinder the applicability of the method. Compared to the 48 hours of pyrolysis, taking one minute to print the green body is almost insignificant. The short fabrication times can be exploited to test multiple materials or geometries rapidly, and to increase the number of prints to ensure that some are successful after pyrolysis. Future work could use the technology to test libraries of materials (or their mixing ratios) rapidly and systematically. This could lead to more robust fabrication strategies that are less prone to deformations from post-processing and pyrolysis.

6.6 Experimental materials and methods

Preceramic resin

The preceramic resin was prepared by combining a polysiloxane (SPR 684, Starfire Systems, USA) with 1,4-butanediol diacrylate (BDDA) as a crosslinker (1070-70-8, Sigma Aldrich, USA), and Diphenyl (2,4,6-trimethylbenzoyl) phosphine oxide (TPO) as a photoinitiator (75980-60-8, Sigma Aldrich). The resin preparation consisted of 85 wt% polysiloxane, 15 wt% BDDA and 2 mM TPO (0.063 wt%).

To produce the resin, a solution of diluted TPO in BDDA is prepared to a concentration of 30 mg/mL which is then vortexed. Following this, the polysiloxane precursor is combined with the TPO in the BBDA solution. The components are then simultaneously mixed and degassed using a planetary mixer (Mazerustar KK-250SE, Kurabo, Japan). Finally, the resin is poured into glass vials of 16.5 mm, which are used for printing.

Optical absorbance

The absorbance spectra of the resin were measured with a Cary 50 (Varian, Australia) UV-vis spectrometer using a scan rate of 60 nm/min. The resin was poured in 10 mm plastic cuvettes. Before each analysis, a background acquisition was performed and then subtracted from the resin's spectra.

Viscosity

The viscosity of the resin was measured using a rheometer (MCR 102, Anton-Paar, Austria) with a (25 mm) parallel plate and a gap of (350 μm) at a shear rate of 0.108 Pa.

Postprocessing of prints

After printing, the parts are recovered from the glass vials and dipped into a toluene bath, which is manually stirred for 5 minutes until all uncured resin dissolves. The parts are then placed in a bath of isopropyl alcohol (IPA) to dilute the toluene and stop the solving action on the parts. The bath is manually stirred again for about 1 minute. The parts are then left to dry in air at room temperature until all IPA fully evaporated, leaving them free of any unpolymerised resin.

The parts are then postcured in a UV curing station (FormCure, Formlabs, USA) for 1 hour at room temperature. After this, all remaining photoinitiator has been consumed, but the surface of the parts is still sticky. To remove the stickiness, the green bodies are submerged in a concentrated solution of TPO in IPA (10 mg mL^{-1}) and left for 1 hour to allow TPO to diffuse inside. The bath with the parts is then placed for 15 minutes in the UV curing station. Then, the parts are removed from the bath and postcured one last time for 45 minutes in the curing station. After that, the green bodies are placed in an oven for 24 hours at 80 °C to remove most of the solvent soaked into the part.

Pyrolysis

The rinsed, postcured, and aged green bodies are then pyrolyzed in an alumina tube furnace (STF 15/450, Carbolite Gero, Germany) in a flowing argon atmosphere following the temperature profile described and explained in the supplementary materials. The pyrolysis peak temperature was set to T = 1000 °C, for a dwell time of 1 hour, and a total cycle duration of 48 hours. The detailed pyrolysis temperature profile is shown in fig. 6.3b.

Imaging

µCT Imaging   Printed objects were imaged with voxel sizes of 10 µm × 10 µm × 10 µm under a 160 kV X-ray transmission tomograph (Hamamatsu, Japan). 3D visualizations of the pieces were obtained using Fiji-ImageJ. [132]

Photographic Imaging   Green bodies and pyrolyzed parts were imaged with a DSLR camera (D3100, Nikon, Japan) with a f=2.8 macro lens (AF-S Micro Nikkor 40 mm, Nikon) , and a digital microscope (VHX-5000, Keyence, USA) with magnifications between 20 and 100x.

FTIR spectroscopy

FTIR spectra of samples of polymerized and pyrolyzed parts were collected with a VERTEX 70v FT-IR Spectrometer (Bruker, USA). The spectrometer is coupled to a Hyperion upright microscope (Bruker). The sample of polymerized resin was prepared by depositing 50 µ of liquid preceramic resin on a gold mirror and spinning it at 6000 rpm. The sample was then polymerized under UV light for 5 minutes. The sample of pyrolyzed material was prepared by grinding pyrolyzed pieces with a mortar and a pestle until pulverized. The powder was resuspended in isopropyl alcohol. 100 µL of the suspension were deposited on a gold mirror and the alcohol was let to dry.

Raman spectroscopy

Raman spectra of the inside of green bodies and pyrolyzed parts were acquired with a LabRam HR800 spectrometer (HORIBA Scientific, USA) confocally coupled to an upright microscope (BX1, Olympus, Japan). To image the inside of the parts, green bodies were cut with a clean blade and pyrolyzed pieces were broken with a hammer. Samples were placed on microscope slides and excited at 532 nm (with a diode laser). Light was collected with a 10x 0.25 NA air objective. Spectra were acquired using a grating with 1800 lines/mm, after 3 repetitions with integration times of 30 seconds. No postprocessing was performed on the data.

X-ray photoelectron Spectroscopy

XPS measurements were performed using a Physical Electronics Versa Probe III system with a hemispherical analyser and monochromated Al Kα source. The energy scale linearity was calibrated with Au4f7/2 at 84.00 eV and Cu2p3/2 932.62 eV. All data were measured at room temperature with a pass energy of 26 eV, at a take off angle of 45° and angular acceptance angle of +/- 20°. The samples were electrically isolated during measurement and a low-energy Ar+ and electron flood gun dual beam charge compensation system was used. The X-ray beam size on the sample was 100 μm. Energy scale referenced to major C1s peak at 284.8 eV which was assumed to originate primarily from C-C. No beam damage was observed.

Shrinkage

To compare the differences between shrinkage along the axial and radial dimensions of the prints, a set of lengths were measured on green bodies and their corresponding PDCs ($n_{parts} = 7$, $n_{measurements} = 14$), most of them woodpiles. Flat geometries were chosen because they reduced ambiguity in measuring lengths. Measurements were made from microscopic images acquired with an optical microscope (VHX-5000, Keyence).

Statistical analysis

Statistical analysis of the isotropy of shrinkage was conducted by running a one-tailed unpaired t-Test assuming unequal variances on Microsoft Excel.

Thermal stress resistance

To show resistance of the ceramic parts to high temperature, a butane torch was heating the ceramic parts (T $\approx$ 1400 °C) for some seconds until they became incandescent and then let cool down. A typical thermal stress cycle was 20 seconds. The spherical woodpile shown in Figure 6.6a was subjected to 5 thermal stress cycles.

Chemical resistance

Parts were dipped into vials containing aqueous solutions of HCl and KOH solutions (pH = 2, and pH = 14 respectively) for one hour and photographed at the beginning and the end of the experiment. The pH

of the aqueous solutions was measure using 0-14 paper pH indicators (MQuant, Merck, Switzerland).

Contributions

The work presented in this chapter was done jointly with Max Kollep and Georgia Konstantinou, as part of his master's and her doctoral thesis at LAPD, respectively. We contributed equally to this work. Ms. Konstantinou and I supervised Mr. Kollep during his master's thesis. Mr Kollep performed most of the 3D printing (using code written by Dr. Antoine Boniface and I, as well as software by Dr. Damien Loterie and Dr. Paul Delrot at Readily3D). He also measured printed parts before and after pyrolysis to quantify shrinkage. Ms. Konstantinou and I formulated the polymer-derived ceramic for tomographic VAM in collaboration with Dr. Pradeep Sasikumar, formerly at EMPA. I contributed to spectroscopy, to the evaluation of thermal and chemical resistance, and to statistical analyisis. I also contributed to planning and designing experiments and to visualize data.

Acknowledgements

7 Volumetric additive manufacturing of multimaterial glasses

This chapter presents the multimaterial volumetric additive manufacturing of silicate glasses. It introduces the additive manufacturing of glass, which, as covered in the past chapter on ceramics, relies on the 3D-printing of a green body that is later transformed into glass through a thermal process called sintering. We demonstrate the fabrication of transparent glass objects from viscous silica nanoparticle-filled acrylic resins, as well as the production of porous glass from phase-separating resins. We use this approach to demonstrate the fabrication of a milifluidic filtering device. Some of the materials in this chapter can be found in the paper:

- Barbera, Lorenzo, Jorge Madrid-Wolff, Roberto Emma, Kunal Masania, Antoine Boniface, Christophe Moser, André R. Studart. "Multimaterial Volumetric Printing of Silica-based Glasses". *In preparation.*

7.1 Additive manufacturing of glass: state of the art

Thanks to their transparency, chemical inertness, and thermal resistance, silicate glasses have played a major role in human civilization since ancient Egypt. Despite their widespread use and importance in modern society, silica glasses with complex geometries have only recently been fabricated in automated processes using three-dimensional printing. [248]–[253] The unique shape complexity achieved by 3D printing may find use in several microfluidic, biomedical and optical applications. [254]–[256] Various approaches have been reported for the three-dimensional printing of silica-based glasses. Most strategies involve either the deposition of molten glass at temperatures above 1000°C [249], [254] or the room-temperature printing of suspensions and resins loaded with inorganic precursors followed by a heat treatment procedure. [252], [253] Printing at room temperature has been conducted using light- or extrusion-based techniques using silica particles [251], [253], [256]–[264] or metal alkoxides [248], [252], [255], [265]–[267] as inorganic precursors. Extrusion-based methods benefit from their multimaterial capabilities, whereas light-based approaches are most suitable for printing intricate geometries at higher spatial resolutions. Importantly, most of the technologies demonstrated so far rely on the layer-by-layer deposition of material, which is a relatively slow process that requires caution to prevent the formation of interlayer defects during fabrication.

Volumetric additive manufacturing of silica nanoparticle-filled resins   The advent of volumetric printing techniques opened a new pathway for the fabrication of complex-shaped objects at high speeds circumventing the potential fabrication issues of layer-by-layer approaches. Volumetric additive manufacturing has been recently exploited for the rapid fabrication of heat-resistant silicon oxycarbide ceramics (as described in chapter 6, [75]) and silica glass objects with surface roughness down to 6 nm. [14] Such a low surface roughness makes this technology especially attractive for the 3D
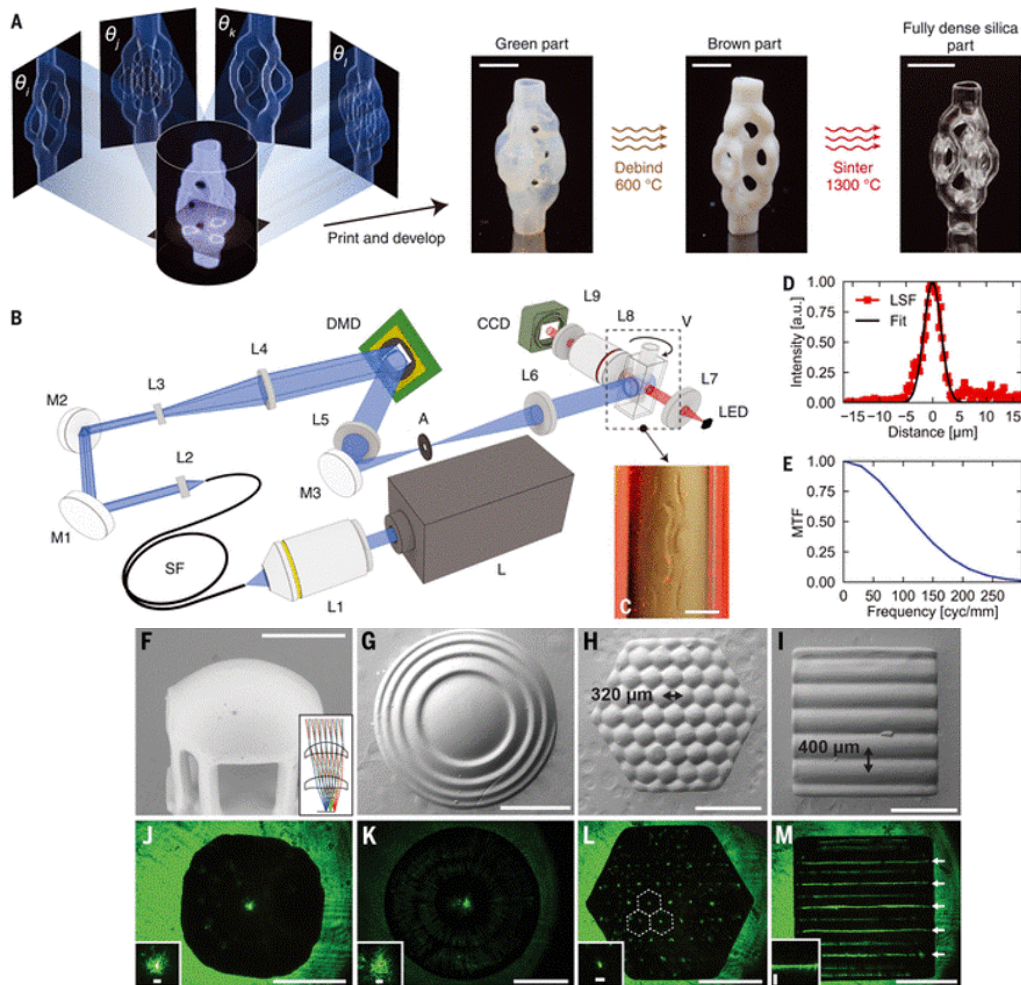
Figure 7.1: **State-of-the-art: Printing transparent fused silica glass with microscale computed axial lithography**. **A** Volumetric printing of a green body from a silica nanoparticle suspension in a photopolymerizable acrylate resin. The green body is thermally treated to sinter it into glass. Scale bars 2 mm. **B** Optomechanical setup using a 442 nm laser. **C** Immediately after light exposure, the printed object can be observed in the container. Scale bar 2.5 mm. **(D** Line spread function (LSF) and **(E)** Modulation Transfer Function at the focal plane of the setup. **(F to I)** SEM micrographs of printed optical elements. **(J to M)** Point spread functions (PSFs) of the optical elements in (F) to (I) after focusing of 532-nm laser illumination. Insets show zoomed PSFs. Scale bars are 1 mm [(F) to (M)] and 50 μm [insets of (J) to (M)]. From Toombs, Joseph T., et al. "Volumetric additive manufacturing of silica glass with microscale computed axial lithography." *Science* 376.6590 (2022): 308-312.. Reprinted with permission from AAAS.

printing of complex-shaped optical components. as seen in fig. 7.1. Toombs *et al.* used a formulation of silica nanoparticles embedded into photopolymerizable acrylic resin. The refractive index of the acrylic mix needs to be tuned to that of the nanoparticles to prevent undesirable scattering effects. The high loading of nanoparticles (35 vol %) makes the resin very viscous, which reduces sedimentation during printing but makes post-processing more challenging. Despite these promising features, volumetric additive manufacturing of glass is currently limited to the microscale and a single material composition. [14] Since most functional silica glasses require tuning of their physical and chemical properties through the introduction of other oxides into the composition, printing technologies for multicomponent glasses are crucial to broaden the possible application scenarios of these complex-shaped objects.

DLP-printing of porous glass from phase-separating resins   Recently, the group of André Studart at ETH Zurich introduced the DLP printing of multicomponent glasses using metal alkoxides as inorganic precursors in photoreactive resins. [252] In this approach, the metal alkoxides provide the cations of interest for the formation of multioxide glasses after heat treatment, whereas monomer mixtures are utilized for the photopolymerization of the resin under the illumination imposed by the printer. Recent work has demonstrated the fabrication of complex-shaped SiO_2-B_2O_3-P_2O_5 glasses using this light-based printing method (fig. 7.2I).

Notably, the photo-reactive resin was found to phase-separate into interpenetrating inorganic-rich and organic-rich domains during the photopolymerization process. Such an effect was harnessed to create multicomponent glasses with complex macroscopic shapes and interconnected porosity at the nanoscale, as seen in fig. 7.2II. The **nanoporosity** arises from the controlled thermal decomposition of the organic-rich domains of the phase-separated polymerized resin. An undesirable effect of this intensity-dependant pore size is shown in figs. 7.2III-IV. In DLP and SLA, as objects are printed layer by layer, light intensity decays rapidly within the several microns of each layer. This is normally due to high concentrations of photoinitiators and absorbent dyes. Because of this, the resulting prints may have marked layering effects in their pore-size distributions, which results in anisotropic mechanical properties and may lead to cracks and fractures. Heat-treating the printed material at higher temperatures eventually sinters the inorganic phase, leading to dense multicomponent glasses with intricate three-dimensional geometries. [252] Because they are photoreactive and can be designed to be transparent, resins with metal alkoxide precursors may offer a viable approach for the volumetric printing of multicomponent silica-based glasses including both dense and porous microstructures. Additionally, the porous structure offers huge benefits during the debinding step of the fabrication, as organic gases can escape from the bulk of the object without inducing cracks or bubbles. [220]
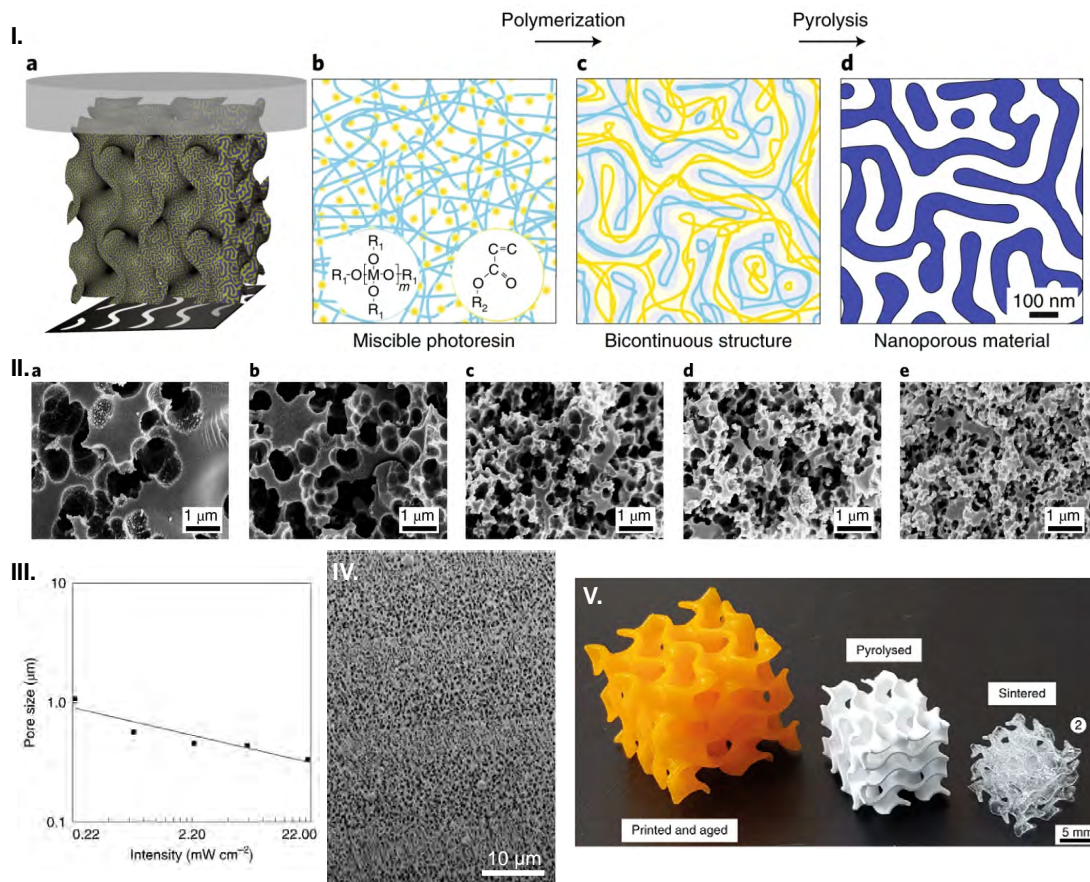
Figure 7.2: **State-of-the-art: DLP-printing of multicomponent glasses using phase-separating resins.** **I.** Schematics of the process, **(a)** illustrating the geometrical complexity generated by the illumination pattern and the nanostructure emerging from the phase separation phenomenon. **(b,c)**, In this process, acrylate monomers and pre-ceramic precursors such as poly(diethoxysiloxane) (PDEOS) are photopolymerized (b) to form a three-dimensionally defined bicontinuous structure of organic polymer and pre-ceramic polymer (c). **(d)** The as-printed object is pyrolysed to form a nanoporous structure that can be optionally further sintered into transparent multi-material glasses and glass-ceramics. **II.** Light-controlled pore size in 3D printed glass objects **(a–e)**, Scanning electron microscopy (SEM) images of porous ceramics obtained with light intensities of 0.22, 0.66, 2.20, 6.60 and 22.00 mW cm^{-2} (from left to right). **III.** The effect of the light intensity on the average pore size of the printed structures after pyrolysis. **IV.** Scanning electron micrograph of a pyrolyzed phase-separating resin (with a high concentration of a light-absorbing dye) showing in-layer pore size gradients. Light during printing came from the top of the image. **V.** Illustrative picture of a complex-shaped object along different stages of the process. Image reproduced with permission from Moore, David G., et al. "Three-dimensional printing of multicomponent glasses using phase-separating resins." *Nature Materials* 19.2 (2020): 212-217. Copyright Springer Nature.

7.2   Motivation

Here, we build on the state of the art and study a multimaterial volumetric printing platform for the fast fabrication of cm-scale complex-shaped glass objects with tunable chemical composition and porosity. We'd like to demonstrate that tomographic volumetric additive manufacturing can be used to fabricate larger objects in solid silicate glasses from nanoparticle-filled resins and also from phase-separating formulations. Moreover, the two strategies can be merged to fabricate multi-component devices, as the milifluidic filter depicted in fig. 7.3.
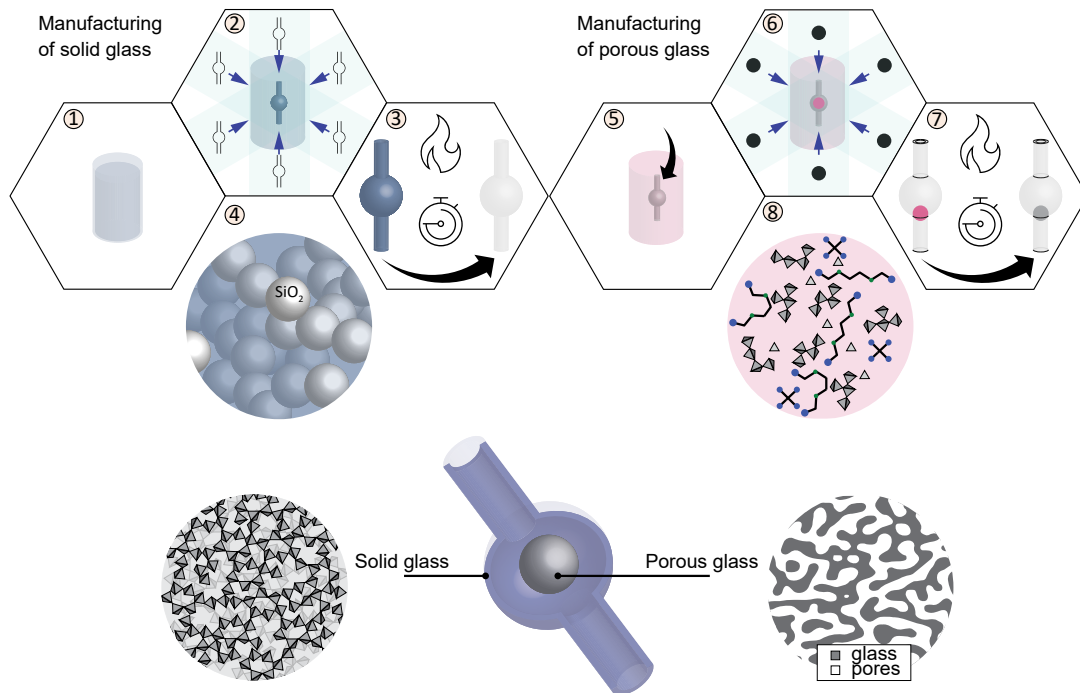
Figure 7.3: **Schematics of the multimaterial volumetric printing of glass objects.** *(top)* Sequential manufacturing steps for *(left)* the fluidic cage with dense silica walls and *(right)* the enclosed sphere made from porous multicomponent glass. In this workflow, the resin with silica nanoparticles **(1)** or phase-separating mixture **(5)** is placed in the transparent vial **(2,6)** and exposed to light projections during volumetrically printing **(3,7)** before the final step of heat treatment to convert the polymerized resin into the final dense **(4)** or porous **(8)** glasses. *(bottom)* Exemplary glass object consisting of a porous glass sphere encapsulated inside a dense-walled fluidic cage. The porous sphere displays a multicomponent silica-based glass composition, whereas the fluidic cage is made of pure amorphous silica glass.

This device uses volumetric printing to fabricate a solid silicate glass channel with a spherical chamber. After sintering the channel, it is placed back in the printer, and a spherical porous-glass filter is printed within. Both parts of the device are then calcinated together.

To fabricate this cm-scale multimaterial object, we investigated the optical, rheological, and photo-polymerization properties of both nanoparticle-filled and phase-separating resins. These two materials entail extremely different printing conditions: the first is very viscous (more than honey) while the second one is very thin (more than ethanol). The nanoparticle-filled resin suffers from low contrast probably due to diffusion during polymerization. The polymerization of the phase-separating is

highly exothermic, and convection hinders printability. TEMPO, a radical quencher, can be used to compensate for these effects, as we will cover in the next sections. Sections 7.3 and 7.4 cover the material analysis and design to produce resin formulations that are well adapted to volumetric printing.

7.3 Glass from nanocomposite resins

The nanoparticle resin comprises amorphous silica aggregates (Aerosil Ox50) suspended in a reactive organic mixture consisting of the monomers hydroxyethylmethacrylate (HEMA) and trimethylolpropane ethoxylate triacrylate (TA) combined with the photoinitiator (TPO)[I] and the polymerization-inhibitor (TEMPO)[II] (fig. 7.4a). The concentration of silica particles has a strong impact on the optical transparency and viscosity of the resin, whereas the relative weight ratio between TEMPO and TPO strongly affects the resin's polymerization behavior.

1. High loading of SiO$_2$ nanoparticles reduces shrinkage, but increases light scattering
Optical transparency is key in the volumetric printing process, because it directly affects the intensity of light within the illuminated resin during manufacturing. To achieve high fidelity, empirical observations have shown that the light intensity at the center of the printing vial should reach at least 75% of the intensity of the light source. [61] In particle-filled resin, the optical transparency is reduced by particle scattering events, which can be minimized by reducing the mismatch in the refractive index between the silica and the monomer mixture. The calculated tomographic patterns used for printing can also be computationally corrected to account for scattering from the resin or attenuation from the photoinitiator. While a lower index mismatch enhances light penetration, a reduction in optical transparency in resins with high particle concentration is inevitable. High silica particle contents promote undesired scattering events, but are essential to minimize shrinkage of the printed object and crack formation during heat treatment. Clearly, a trade-off exists between optical transparency and silica particle concentration. In addition to transparency, the silica content is also limited by the viscosity of the resin, which should be fluid enough to enable effective washing and removal of unreacted monomer from the as-printed parts.

To establish an optimized resin composition that balances the trade-offs of the system, we measured the optical transmittance and the relative viscosity of resins prepared with increasing concentrations of silica particles (fig. 7.4b). The transmittance across the resin was quantified by UV-vis spectroscopy for the wavelength range 300-500 nm, whereas the relative viscosity was determined by steady-state shear measurements in a stress-controlled rheometer. The results show the optical transmittance at 405 nm of the resin decreases from 92% to 81% as the silica particle concentration is increased from 10 to 40 vol% (fig. 7.4b). Such reduction in transmittance is accompanied by a marked increase in relative viscosity from a factor 3 to a factor 1400 measured at 1 s^{-1} with respect to the unloaded resin, whose apparent viscosity is 10.1 Pa·s^{-1}. On the basis of these experiments, we found the silica particle concentration of 35 vol% to offer a reasonable balance between a high optical transmittance while keeping the viscosity low enough for the effective washing of the printed parts. In addition to particle scattering, the presence of the photo-initiator also causes light attenuation by absorbing photons to generate free radicals. Although high initiator concentrations are desired to accelerate the polymerization process, such an attenuation effect sets an upper limit to the TPO content in the resin. Light transmittance measurements indicate that this upper limit lies at 1 mM, since higher concentrations reduce the light below the 75% threshold for an arbitrary penetration depth of 1 cm

---

[I]diphenyl(2,4,6-trimethylbenzoyl)phosphine oxide
[II](2,2,6,6-tetramethylpiperidin-1-yl)oxyl

into the resin (figs. 7.4c and 2.6).

2. Photoinitiation and inhibition can be tuned to improve print fidelity

Next to light transmittance, the polymerization behavior of the resin is the other essential parameter controlling the shape fidelity of objects manufactured via the volumetric printing process. The polymer-
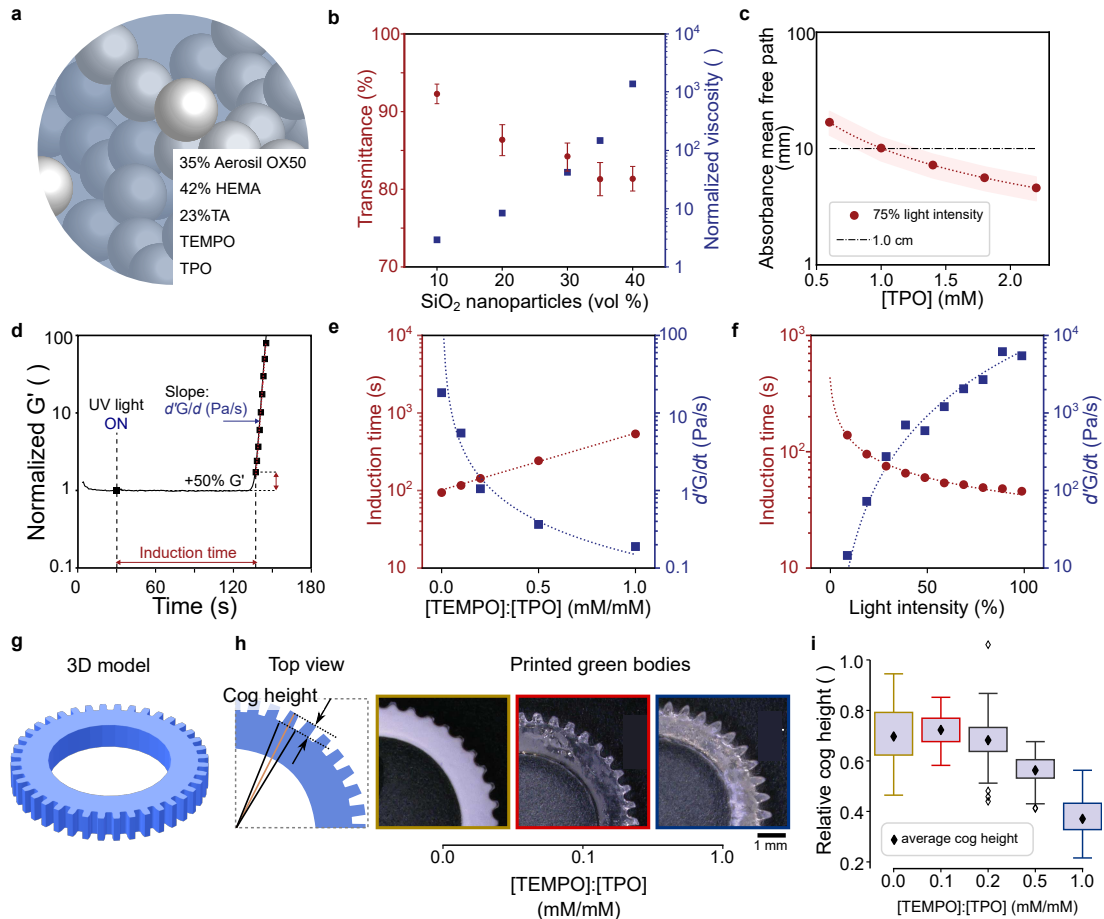
Figure 7.4: **Optical properties, polymerization behavior and printing of particle-filled resins. a.** Cartoon indicating the main constituents of the resin filled with silica nanoparticles. **b.** Optical transmittance and relative viscosity of the resin as a function of the concentration of silica nanoparticles. The relative viscosity corresponds to the apparent viscosity of resin at a shear rate of $11\ \text{s}^{-1}$ relative to that of the particle-free monomer mixture. **c.** Penetration depth of light into the resin as a function of the initiator (TPO) concentration. The penetration depth is arbitrarily defined here as the depth at which the light intensity drops to 75% of the incident value. **d.** Evolution of the storage modulus G' of the illuminated resin during photo-rheology experiments. The plot shows how the induction time (t_i) and the stiffness change rate dG'/dt are extracted from the data. **e., f.** Effect of the **(e)** TEMPO:TPO ratio and **(f)** light intensity on the induction time and stiffness change rate of a resin containing 35 vol% silica nanoparticles and TPO content of 1.8 mM. **g.** 3D model of the cog wheel used to assess the resolution and repeatability of the printing process. **h.** Photographs of cog wheels printed with particle-filled resins containing distinct TEMPO:TPO rations. **i.** Effect of the TEMPO:TPO ratio on the average relative cog height of the printed model.

ization behavior can be expressed in terms of the polymerization speed and the induction time needed for the onset of the reaction. To achieve high shape fidelity, it is important that the polymerization is restricted to the regions of the resin that are illuminated by the printer. This requirement is met under conditions that lead to high induction times and fast polymerization. The high induction time ensures that only the regions illuminated for longer than a certain threshold will initiate polymerization. Fast polymerization prevents the free radicals and reactive monomers created by the incoming photons to diffuse away from the illuminated area. However, induction time and reaction speed are mutually antagonistic properties in free-radical polymerization processes. This trade-off calls for an optimization of the ratio between the inhibitor (TEMPO) and the photo-initiator (TPO) concentrations, which controls the induction time and the polymerization speed.

The optimum ratio between inhibitor and photo-initiator was established by measuring the induction time and polymerization speed of resins prepared with varying TEMPO and TPO concentrations using photo-rheology. In this approach, the polymerization reaction is captured by the increase in storage modulus (G') of the resin as a function of time while the sample is illuminated with constant light intensity. The induction time is taken as the time needed for the G' value to increase by an arbitrary value of 50% (t_i). This represents the gelation point of the resin and it reflects the rate of the initiation relative to the termination reactions involved in the polymerization process. The polymerization speed is represented by the rate of change of the modulus ($\frac{dG'}{dt}$) after the onset of gelation (fig. 7.4d) and expresses the rate of the propagation reaction relative to the termination reaction. The results of photo-rheology experiments with resins formulated with distinct TEMPO:TPO ratios confirm the trade-off between induction time and polymerization speed (fig. 7.4e). Higher TEMPO:TPO ratios represent an excess of inhibitor relative to initiator, thus increasing the induction time at the cost of slower polymerization speeds. Notably, the light intensity applied during printing provides external control parameter to tune the polymerization behavior of the resin (fig. 7.4f). By increasing the rate of initiation and propagation reactions relative to termination events, intense light shortens the induction time and speeds up the polymerization process.

To determine the polymerization behavior required to maximize print resolution and shape fidelity, we volumetrically printed 3D cog wheels using resin formulations with distinct TEMPO:TPO ratios (fig. 7.4g). Shape fidelity in this model system was quantified by the relative height of the cog, which is given by the ratio between the outer and inner radii of the wheel (fig. 7.4h). The average cog height provides a measure of the print resolution, whereas the standard deviation indicates the repeatability of the printing process. Our experiments show that an intermediate TEMPO:TPO molar ratio of 0.1 leads to maximum resolution and repeatability, as evidenced by the highest average cog height and smallest standard deviation among all the resin compositions tested (fig. 7.4h,i). In the absence of TEMPO, the repeatability is poor probably due to the short induction time of the polymerization reaction. By contrast, higher TEMPO:TPO ratios in the range 0.1-1.0 translate into lower average cog heights and a poorer resolution that likely results from a slower polymerization process.

3. Sintered solid cm-scale silicate glass
We illustrate the capability of the MVP process by first printing a complex-shaped object in the form of a centimeter-scale swan using a particle-filled formulation (fig. 7.5a). The complex geometry of the swan is printed in less than a minute and the resulting three-dimensional object replicates very well the original model. Despite the large dimension of the object and the 11±3% shrinkage during calcination and sintering, the structure maintains its integrity throughout the entire heat treatment procedure. Calcination and sintering also come with mass loss, as the organic components are burned. The progress of density from green to sintered bodies is reported in table 7.1.
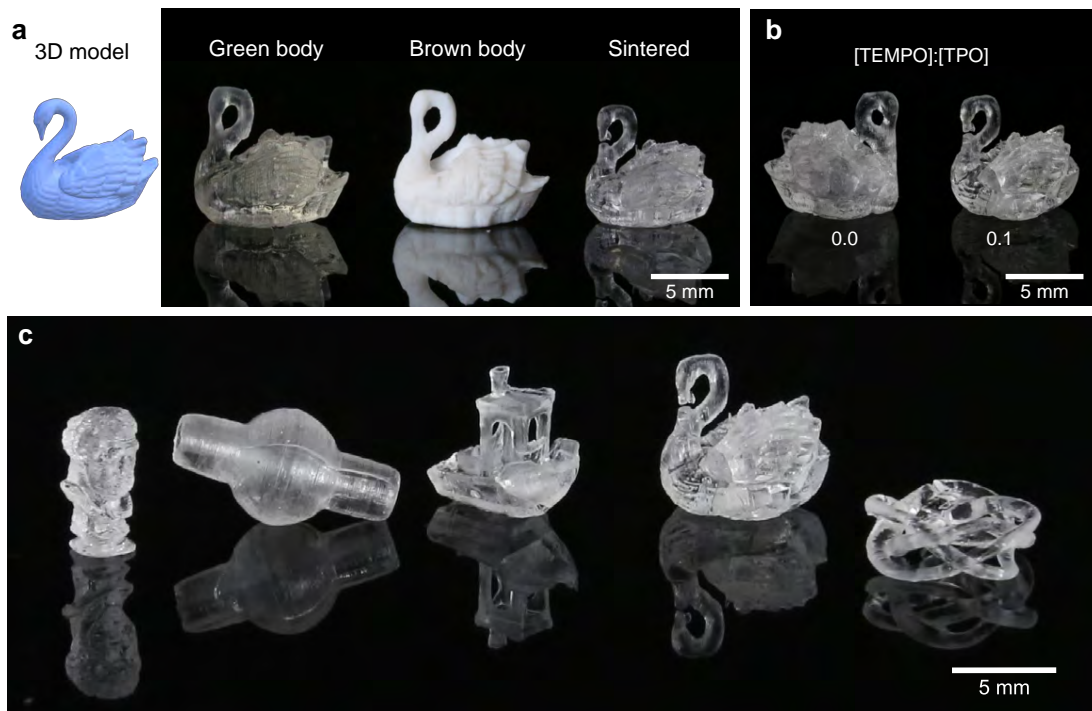
Figure 7.5: **Volumetrically 3D-printed silica nanocomposite glass a.** Photographs of a three-dimensional swan-shaped object at the different stages of the manufacturing process using a particle-filled resin. **b.** Fine-scale resolution of the swan-shaped glass objects printed with or without the polymerization inhibitor (TEMPO). **c.** Complex-shaped glass objects obtained by printing, calcination and sintering of a particle-based resin containing 52.2 wt% silica, 31 wt% HEMA, 16.8 wt% triacrylate, 0.18 mM TEMPO and 1.8 mM TPO.

Printing experiments with and without TEMPO indicate that the presence of this photo-inhibitor in the particle-filled resin is essential to replicate the fine details of the swan geometry in the final sintered structure (fig. 7.5b). Indeed, the finely resolved features on the swan's wings are only distinguishable in the structure printed from the formulation containing the photo-inhibitor. Such optimized formulation can eventually be used to volumetrically printed silica-based glass objects in a variety of intricate geometries and shapes, such as the bust, bottle, benchy boat, and self-whirling ring shown in fig. 7.5c.

	Green body	Brown body	Sintered body
Density (g/cm^3)	1.535 ± 0.015	2.083	2.187 ± 0.005

Table 7.1: Averages and standard deviations of measured densities for green, brown and sintered body.

7.4   Glass from phase-separating resins

The resin formulation design performed for the particle-filled mixture was extended to the phase-separating resins. This was done by first exploring possible highly transparent resin compositions. The phase-separating resin is composed mainly of metal alkoxides as inorganic precursors mixed with photo-reactive monomers. In the exemplary formulations, polydiethoxysiloxane (PDEOS) and triethyl borate (TEB) were utilized as silicon- and boron-containing inorganic precursors, respectively. These

constituents were mixed with diurethane dimethacrylate (DUDMA) and pentaerythritol tetraacrylate (PETA) as photo-reactive bifunctional and tetrafunctional monomers, respectively. The photoinitiator TPO[III] and the inhibitor TEMPO were also added to the mixtures to complete the phase-separating resin formulation (fig. 7.6a).

1. Phase-separating resins for VAM, need to be transparent, but not all are

Mixing experiments with various resin compositions were performed to identify the conditions needed to obtain miscible and transparent formulations. The composition was systematically varied by changing the weight ratio between bifunctional (DUDMA) and tetrafunctional (PETA) monomers for different relative fractions of inorganic precursors in the resin constant. Since high concentrations of inorganic precursors reduce the shrinkage during calcination, we focused on compositions with high contents of PDEOS and TEB. While most of the formulations were found to be immiscible at room temperature, heating the mixture to $55°$C for up to 20 minutes effectively increases the miscibility for most resins. Heating might improve the miscibility by enabling the partial hydrolysis of the alkoxide precursors with water molecules from the environment and within the resin. The resulting hydrolyzed inorganic precursors should interact favorably with the urethane polar groups of the DUDMA monomer.

Taking resins with a constant PDEOS:TEB weight ratio as an example (fig. 7.6b), we observe that most compositions containing up to 70 wt% inorganics are fully transparent. Higher concentrations of the inorganic precursors (PDEOS and TEB) lead to an immiscible resin, if the PETA content is too high. This lower miscibility might be related to the strong hydrophobic nature of PETA, which leads to unfavorable interactions with the more hydrophilic inorganic precursors. Importantly, the highly transparent resins obtained clearly benefit from the absence of scattering particles in the formulations. On the basis of these experiments, we selected a composition with relatively high inorganic content while retaining full miscibility and transparency after the heating protocol (fig. 7.6c).

2. High concentrations of photoinitiator are needed to form the object, but they are limited by optical absorbance

Besides optical transparency, the selected phase-separating resin was also evaluated in terms of polymerization behavior using the photo-rheology tool previously used for the particle-filled formulations. The polymerization behavior was found to be strongly affected by the relative ratio between photo-inhibitor and photo-initiator, as evidenced by the evolution of the storage modulus of the resin upon illumination (fig. 7.6d). To systematically assess the effect of these control parameters, we measured the induction time (t_i) and the stiffness change rate ($\frac{dG'}{dt}$) of resins with varying TEMPO:TPO ratios at three different TPO concentration levels. Combined the experimental results indicate that an increase in the inhibitor:initiator ratio from 0.2 to 5.0 increases the induction time by a factor of nearly 100 and reduces the polymerization speed ($\frac{dG'}{dt}$) by 4 orders of magnitude. These trends are in line with the results obtained for the particle-filled resin and reflect the change in the balance between the initiation (propagation) and the termination reactions of the polymerization process.

To correlate this polymerization behavior with the shape fidelity of the process, we volumetrically printed a three-dimensional helicoidal object using resin formulations with varying TEMPO and TPO concentrations (fig. 7.6g). Photographs of the resin-filled vial at the end of the printing process reveal that high fidelity is achieved with a formulation with well-defined intermediate TEMPO:TPO ratio. Too high concentrations of the initiator (TPO) led to uncontrolled over-polymerization of the resin on the

---

[III]a second UV-absrobing photoinitiator (1-Hydroxy-cyclohexyl-phenyl-ketone) was also added to the mix at a concentration of 18 mM to make the soft printed parts stiffer after printing. This initiator has virtually no absorbance at 405 nm, so it does not affect volumetric printing

walls of the printing vial. By contrast, formulations containing high inhibitor (TEMPO) contents do not fully polymerize during the illumination process, thus resulting in incomplete printed geometries.
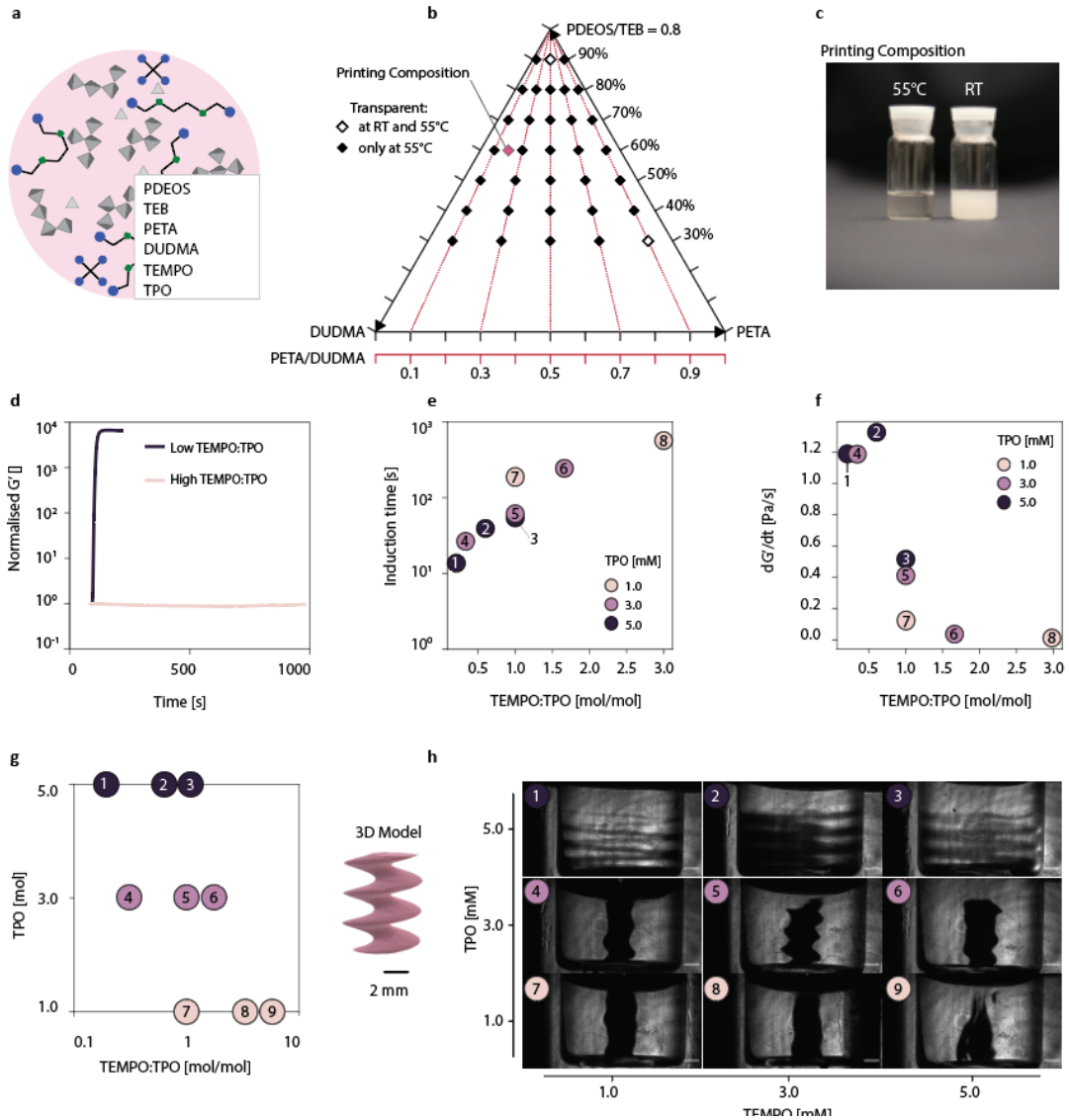
Figure 7.6: **Transparency, polymerization behavior and shape fidelity of phase-separating resins.**
a. Cartoon depicting the main constituents of the phase-separating resin. **b.** Ternary diagram indicating the resin compositions that become optical transparent after heated to 55°C. **c.** Photographs showing examples of immiscible (opaque) and miscible (transparent) resins. **d.** Evolution of the storage modulus (G') of illuminated resins during photo-rheology experiments. The plot shows two examples of formulations with low and high TEMPO:TPO ratios. **e.,f.** Effect of the TEMPO:TPO ratio on (**e.**) the induction time and (**f.**) the stiffness change rate of a selected resin containing 48 wt% PDEOS, 12 wt% TEB, 32 wt% DUDMA, and 8 wt% PETA. **g.** Diagram indicating the sets of compositions with different TEMPO and TPO concentrations used to test the shape fidelity of the selected resin. **h.** Photographs of the vials containing resins with distinct TEMPO and TPO concentrations after volumetric printing of a three-dimensional model helicoidal structure.

These experiments indicate that high shape fidelity is possible if the polymerization behavior is tuned to enable induction times of approximately 100 s combined with a sufficient stiffening rate. Such behavior reflects the existence of a light dose threshold below which no reaction occurs, thus limiting the polymerization to the volumes of the resin corresponding to the desired geometry.

7.5   Multimaterial fabrication

The multimaterial volumetric printing (MVP) process involves the two sequential steps of three-dimensional printing and heat treatment. By using two or more different resins, the MVP process enables the fabrication of glass parts featuring both dense and porous components within the same printed object. Besides porosity, the glass composition of the object can also be deliberately tuned through the choice of the building blocks present in the resin formulation. To illustrate the technology and demonstrate these features, we select an exemplary complex glass part comprising a 3D fluidic cage enclosing a spherical nanoporous object (Figure 1A). The glass walls of the fluidic cage are designed to be dense and made of pure silica, whereas the encapsulated sphere is a multicomponent B_2O_3-SiO_2 glass with nanoscale porosity.

The complex glass part is manufactured by volumetrically printing first the three-dimensional fluidic cage and then the encapsulated nanoporous sphere in a second stage. To print the fluidic cage, we selected a resin formulation consisting of amorphous silica nanoparticles suspended in a photo-curable monomer mixture (fig. 7.3). For volumetric printing, the fluid resin is first cast into a transparent vial and exposed to light projected from the printer while the vial is rotating at constant speed. Upon exposure, the illuminated resin selectively polymerizes to generate an object with the desired cage geometry in less than 1 minute. The polymerized nanocomposite is then carefully washed and heat-treated at temperatures up to $1300°C$ to yield a dense and transparent silica glass object.

The multimaterial volumetric printing proceeds with the fabrication of the nanoporous sphere enclosed within the fluidic cage (fig. 7.3b). The encapsulated sphere is printed using a phase-separating resin containing metal alkoxide inorganic precursors and a photo-curable monomer mixture. [252] To print the enclosed sphere, we place and align the fluidic cage inside the transparent vial already filled with a fluid phase-separating resin. A resin with low viscosity is crucial to ensure flow into the channel of the fluidic cage. The resin-filled object is then illuminated again with a specific light pattern to create a sphere that is large enough to remain trapped inside the previously printed part. Distortion effects from the cylindrical vial are taken into effect and corrected for. However, the correcting for the distorsion of the first printed part remains future work. Adding this correction would improve print resolution. The print is then carefully removed from the printing vial, washed, and aged to allow for the condensation reaction of the inorganic precursors. The whole assembly comprising the printed sphere within the fluidic cage is afterwards heat treated at temperatures between 500 and $700°C$ to generate the final multimaterial glass object. During heat treatment, the phase-separated resin is converted into a nanoporous structure with glass composition defined by the metal alkoxide precursors present in the initial formulation.

Following the sequential two-step procedure, it is possible to volumetrically print the envisioned complex glass object comprising a porous borosilicate sphere entrapped inside a 3D fluidic cage with silica dense walls (fig. 7.7a). The resulting object displays multimaterial, microstructural and geometrical features that cannot be obtained in the same part using conventional glass manufacturing processes. To characterize the structure of this complex object, we performed microcomputed tomography (microCT) of the sample and created three-dimensional reconstructions from the obtained images (fig.
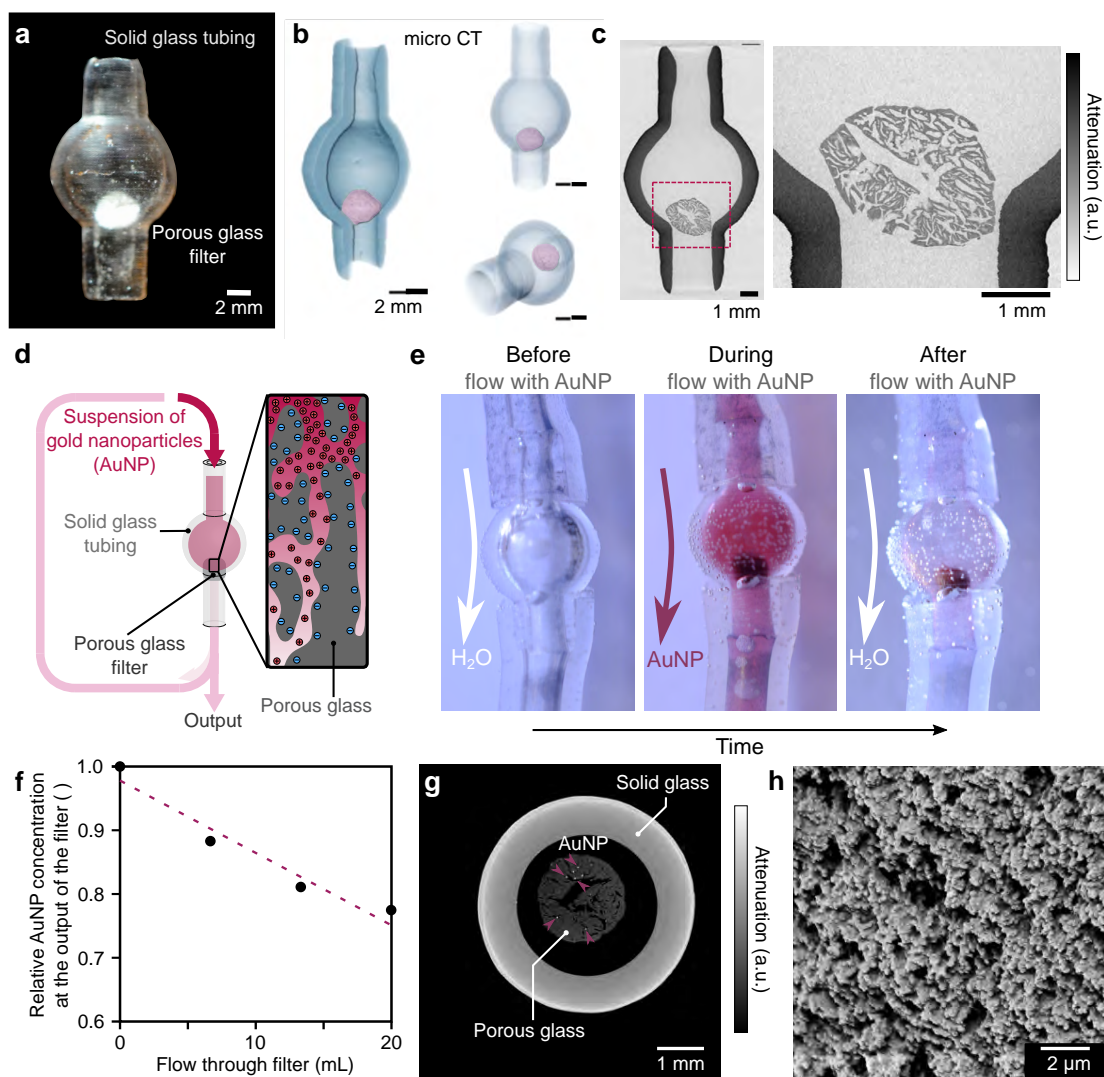
Figure 7.7: **Three-dimensional fluidic cage with entrapped porous sphere fabricated by multimaterial volumetric printing of particle-filled and phase-separating resins. a.** Photograph of the device. **b., c.** Micro computer tomography data showing (**a.**) a reconstructed 3D image and **c.** a cross-section of the glass object comprising a borosilicate porous sphere entrapped in a cage with dense silica walls. **d.** Filtration of nanoparticles by flowing a suspension of gold colloids through the fluidic glass cage. **e.** Timelapse of the filtering process. Note how the sphere, which appears almost tranparent immersed in water at first, gets a pink color from the adhered gold nanoparticles. **f.** Relative concentration of gold nanoparticles in the filtrate as a function of the volume of suspension filtrated. **g.** Micro computer tomography cross-section image of the multimaterial glass object indicating the entrapment of the gold nanoparticles within the interconnected nanoporosity of the enclosed borosilicate sphere. **h.** SEM image of the calcinated phase-separating resin, showing the characteristic nanoporosity.

7.7b-c).

The reconstructed 3D object reveals that the entrapped sphere features a slightly oblate shape, which probably results from focusing effect in the proximity of the cage's walls. Cross-sections of the structures show that the long axis of the sphere is sufficiently large to prevent it from escaping the cage. Closer inspection of the sphere indicates the presence of a microscale inner pore that likely forms during the removal of the organic phase of the polymerized resin during the calcination process. Importantly, the formation of such pore does not affect the shape and mechanical integrity of the sphere, allowing it to be used as a high-surface-area porous substrate entrapped in the fluidic cage.

To demonstrate the functionality of the sphere-in-cage glass object, we conducted a simple filtration experiment in which the porosity of the encaged sphere is exploited to separate 40 nm gold particles dispersed as a model colloid in an aqueous suspension (fig. 7.7d-e). Separation is favored by adsorbing positively charged cysteamine on the gold nanoparticles, so as to promote electrostatic interactions with the negatively charged surface of the silica sphere. Experiments are performed by flowing the gold suspension through the fluidic cage and collecting the filtrate for analysis. To quantify the effectiveness of the filtration process, we measured the concentration of gold nanoparticles in the filtrate using UV-visible spectroscopy.

The sphere-in-cage object was found to effectively separate the gold nanoparticles from the water phase by flowing the suspension through the fluidic device. The gold content left in the filtrate decreases linearly with the volume of filtrated suspension, indicating that the positive effect of the electrostatic interactions between the particles and the porous glass sphere. MicroCT images of the device after the filtration experiment show that the gold nanoparticles are entrapped within the inner nanopores of the sphere. This confirms the interconnected nature of the nanoporosity generated upon calcination of the phase-separated resin, which is essential to provide a high surface area for the filtration process. Combined with the chemical and thermal stability of silica glass, such interconnected **homogeneous nanoporosity** makes our multimaterial glass object attractive for membrane-based separation technologies.

7.6   Conclusion

Volumetric printing of resins loaded with silica particles or metal alkoxides enables the manufacturing of silica-based glasses featuring complex three-dimensional geometry combined with compositional and microstructural control. Particle-laden resins are suitable for the fabrication of glass structures with dense silica walls, whereas resins with the metal alkoxides can be used to tune the chemical composition and local porosity of the glass. The design of the resin formulation is key to volumetrically print structures with high shape fidelity. By tuning the concentration of particles or molecular inorganic precursors, it is possible to formulate resins with the optical transparency required for the volumetric printing process. To print such resins into high-fidelity structures, the induction time and polymerization speed need to be optimized through the concentrations of photo-initiator and inhibitor. Under optimal conditions, the initiation, propagation and termination reactions of the polymerization process reach a balance that allows for controlled cross-linking of the resin within the desired projected volume. The combination of resins with particles and molecular precursors enables the multimaterial volumetric printing of three-dimensional glass objects with unprecedented control over the geometry, porosity and chemical composition of the printed structure. This printing platform should open new opportunities for the fabrication of complex glass structures for potential microfluidic and biomedical applications.

Future work   Future work is needed to correct for distorsion induced by the first object during sequential multimaterial printing. Additionally, the resolution of volumetrically-printed glasses from phase-separating resins can be improved.

7.7   Experimentl materials and methods

Particle-filled resin

The particle-filled resin was designed for computed axial lithography based on the formulations originally developed by Wozniak *et al.* [256], [268] and Kotz *et al.* [262] 65 vol% of hydroxyethylmethacrylate (HEMA, Sigma-Aldrich) was first mixed with 35 vol% trimethylolpropane ethoxylate triacrylate (TA, Sigma-Aldrich). Next, amorphous silica nanopowder (Aerosil OX50, Evonik, Germany) was added in small amounts to the mixture using a laboratory stirrer (type R 1303, IKA, Germany). The dispersion was then mixed for 3 minutes at 1200 rpm and degassed for 5 minutes at 1400 rpm using a planetary mixer (ARE 250, Thinky, USA). Finally, the initiator diphenyl-(2,4,6-trimethylbenzoyl)-phosphinoxid (TPO, Sigma-Aldrich) and, if needed, the inhibitor 2,2,6,6-tetramethylpiperidine 1-oxyl (TEMPO, Sigma-Aldrich) were added using a concentrated HEMA stock solution as vehicle. Before printing, a second and last step of mixing and degassing was performed in a planetary mixer (Mazerustar KK-250SE, Kurabo, Japan).

Phase-separating resin

The phase-separating resin was designed based on the original formulation described by Moore *et al.* [252] The resin comprised a mixture of 40 wt% of a monomer phase and 60 wt% of glass-forming precursors. The monomer phase consisted of 80wt% diurethane dimethacrylate (DUDMA, Sigma Aldrich) and 20wt% pentaerythritol tetraacrylate (PETA, abcr GmbH). The 60 wt% glass-forming phase contained a blend of 80 wt% poly(diethoxysiloxane) (PDEOS, 45-47% SiO_2, abcr GmbH) and 20 wt% triethyl borate (TEB, Sigma-Aldrich) as molecular precursors for silicon and boron glass-forming oxides, respectively. The desired amount of diphenyl(2,4,6-trimethylbenzoyl)phosphine oxide (TPO, 97%, Sigma Aldrich) and 2,2,6,6-tetramethylpiperidine 1-oxyl, free radical (TEMPO, Sigma Aldrich) was added to the formulation to control the polymerization behavior of the resin. Additionally, 1-Hydroxy-cyclohexyl-phenyl-ketone was incorporated into the resins as a second photoinitiator at a higher concentration (18 mM). This initiator has a strong absorbance in the UV up to 380 nm, but has practically zero absorbance for longer wavelengths. This allowed to rapidly post-cure the parts after printing, so that they become stiffer, without increasing the resin's absorbance.

Rheological characterization

The rheological behavior of the resins was characterized on a stress-controlled rheometer (MCR 302 Anton-Paar, Graz, Austria) equipped with a cone-plate geometry (CP25, diameter: 24.98 mm, gap: 106 µm, and angle: 2°). Steady-shear measurements were performed at 25 °C by applying a ramp-up and ramp-down protocol with shear rates between 0.1 and 100 s^{-1} in logarithmic scale. Amplitude sweeps under oscillatory mode were performed with an angular frequency of 1 Hz and shear strain values of 0.1 up to 100 %.

Photorheological characterization

Photorheology experiments were carried out on a stress-controlled rheometer (MCR 301, Anton Paar, Graz, Austria). The setup was equipped with a 6 mm thick glass base and a UV curing station (Omnicure Series1000, Lumen Dynamics) in combination with a 400–500 nm filter. In the described arrangement, the setup had a maximum output power of 12.2 mW/cm^2. For the particle-filled resin, oscillatory measurements were performed at 25 °C by applying a 1% strain amplitude and frequency of 1 Hz using a cone-plate geometry (CP25). The gap size was set to 173 μm and data were acquired every second. The resins were pre-sheared and equilibrated for 30 s before the UV light was turned on. The set of measurements with distinct TEMPO:TPO ratios was performed at 2.44 mW/cm^2 (20% of output power capacity). For the phase-separating resin, oscillatory measurements were performed at 25 °C by applying a 1 % strain amplitude and 1 Hz frequency in a plate-plate geometry (PP50) with a 50 μm gap. Data points were acquired at a rate of 0.5Hz. The phase-separating samples were pre-sheared and equilibrated for 60 s before the UV light was turned on. The measurements were carried out at the full power capacity of 12.2 mW/cm^2.

Optical transmittance of resins

The light transmittance of the particle-filled resin was measured with a UV-vis spectrometer (Cary 50, Varian, Australia) using a scan rate of 60 nm/min. The resin was carefully poured in a 10 mm plastic cuvette making sure no air bubbles were incorporated in the sample. For each analysis, a background measurement was performed before acquiring the spectra between 340 and 420 nm. Transmittance at 405 nm was then reported.

Volumetric printing

The volumetric 3D printer described in section 2.2 was used in this work. Patterns were calculated following a non-negative constrained filter back-projection, as described in section 2.1.2. Additional corrections to compensate for the absorbance of the phase-separating resin were applied following the method described in section 4.4.

Sequential multi-material printing To fabricate the filter in channel described in fig. 7.7, a 3D-printed sintered channel was carefully placed at the center of a glass vial and fixed to the bottom with melted wax, as shown in fig. 7.8. The phase-phase separating resin was poured into the vial, and the object was printed within. Lensing effects from the solid silica channel were not taken into account during printing and probably affected resolution. The device was post-processed and calcinated as described as follows.

Post-processing of printed parts

Particle-filled resin The objects printed using the particle-filled formulation were recovered from the glass vial and immersed for 3 minutes in a 1:1 mixture by volume of water:methanol to remove residual unreacted resin. For samples containing cavities or channels, an air gun was used to free the voids from the viscous unpolymerised material. The green bodies were then left to dry in air at room temperature until residual solvent evaporated, leaving them free of any unreacted monomers.
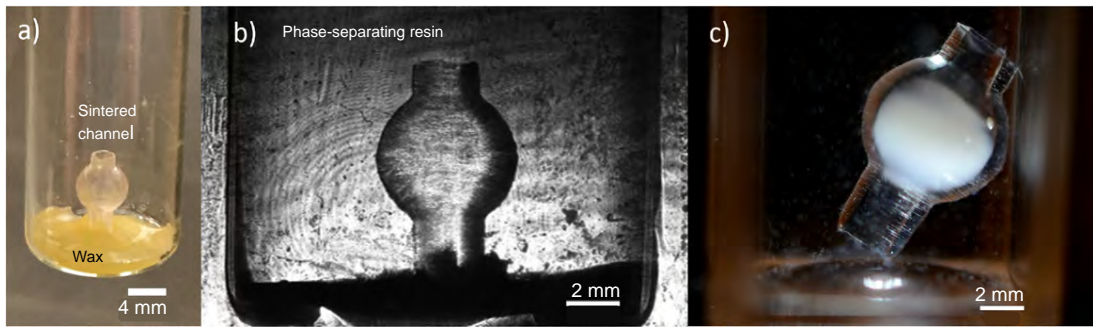
Figure 7.8: Sequential overprinting with phase-separating resins. **a.** Glass channel fixed at the bottom of the vial **b.** Photograph of glass channel filled with the phase-separating resin in the printer. **c.** Printed PS sphere

Phase-separating resin   The objects printed using the phase-separating resin were transferred to a basic bath containing 65 wt% ethanol and 35 wt% water at pH=10 for 24 hours. Subsequently, the printed samples were left drying in a closed container with a saturated atmosphere of basic bath for additional 24 hours. Finally, the objects were left drying at ambient atmosphere for another day before calcination in an electrical furnace.

Thermal calcination and sintering

Particle-filled resin   Calcination of the printed and rinsed green bodies was performed in a muffle furnace (Nabertherm LT, Germany) under atmospheric conditions by applying a heating rate of 0.5 °C/min. During this heat cycle, isotherm holds were performed at 120 °C, 320 °C and 600 °C for 2 h, 4 h , 2 h, respectively. This calcination protocol was established based on the thermal gravimetric analysis of the particle-filled resin (fig. 7.9). The parts were afterwards sintered at 1300 °C at a pressure between 10^5 and 10^6 bar in a tube furnace (HTRH 70- 600/18, Nabertherm, Germany) using a heating rate of 3 °C/min. Prior sintering of the calcined (brown) samples, the furnace was kept at room temperature for 2 hours to ensure high vacuum. The heating profiles optimized in the work of *Kotz et al.* were utilized for the sintering process. [250]
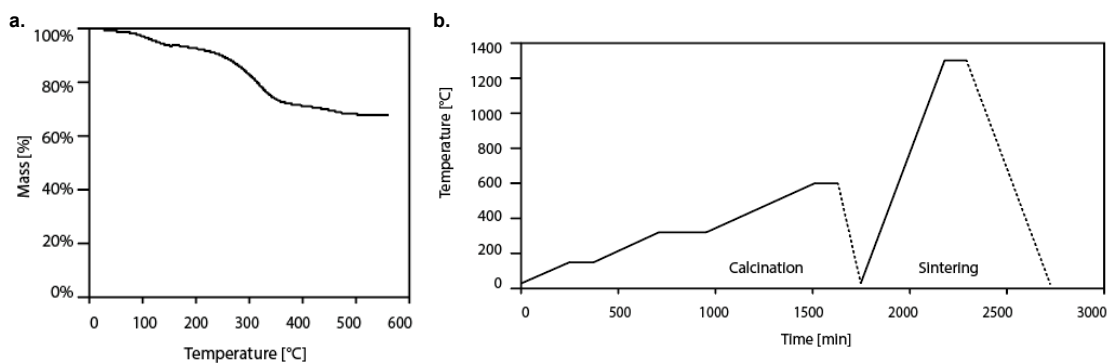
Figure 7.9: **Sintering of particle-filled resins a.** Thermogravimetric analysis of the particle-filled resin measured at a heating rate of 1°C/min **b.** Heating and cooling profiles used for the calcination and sintering of the nanocomposite samples shown in fig. 7.5c.

Phase-separating resin   Objects printed with the phase-separating resin were calcined in a muffle furnace (Nabertherm LT, Germany) under atmospheric conditions with a heating rate of 0.4 °C/min. Isotherms at 250 °C for 6 hours and at 700 °C for 4 hours were performed to enable calcination of the organic phase and the generation of nanoporosity in the final glass. This calcination protocol was established based on the thermal gravimetric analysis of the phase-separating resin (fig. 7.10).
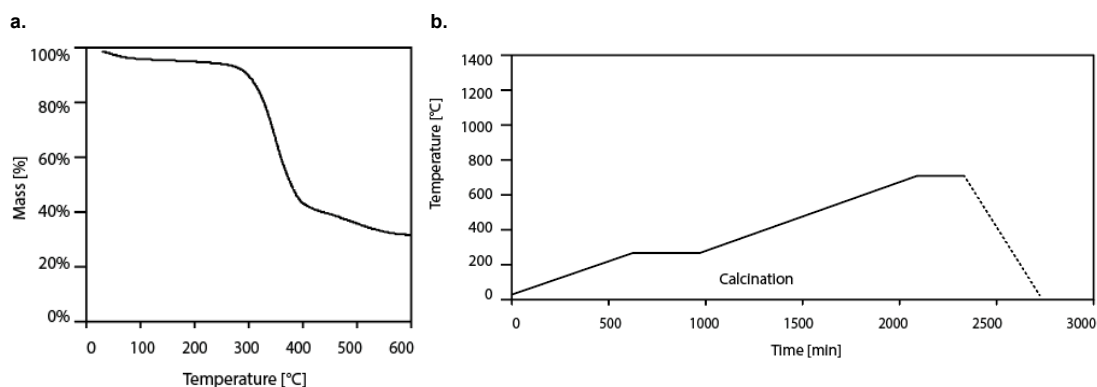
Figure 7.10: **Calcination of phase-separating resins a.** Thermogravimetric analysis of the particle-filled resin measured at a heating rate of 1°C/min **b.** Heating and cooling profiles used for the calcination of samples printed with the phase-separating resin. The same program was used to calcine the three-dimensional fluidic cage shown in fig. 7.7.

Microcomputed tomography of glass device

Printed and heat-treated glass objects were imaged using a 160 kV X-ray transmission tomograph (Hamamatsu, Japan) with voxel sizes of 8.4 μm x 8.4 μm x 8.4 μm. 3D visualization of the pieces was achieved using the softwares Fiji-ImageJ [269] and Avizo (ThermoFischer).

Synthesis of gold nanoparticles

Positively charged gold nanoparticles were synthesized following the procedure described by Niidome *et al.* [270] In this synthesis, $AuCl_3$ is reduced in presence of $NaBH_4$ and 2-aminoethanethiol. To this end, 400 μL of 213 mM 2-aminoethanethiol were added to 40 mL of 1.42 mM $AuCl_3$. After stirring for 20 minutes, 10 mL of 10 mM $NaBH_4$ were added and further stirred for 10 minutes. Finally, the clear wine-red sample was stored in a fridge at 5 °C and used within 2 months.

Filtration experiments

The filtering efficiency of the sphere-in-a-cage glass device (fig. 7.7) was assessed by quantifying the removal of positively charged gold nanoparticles (AuNP) from an aqueous solution as it passed through the fluidic device. The suspension of gold nanoparticles was flowed through the device using a peristaltic pump (AL-9000, World Precision Instruments, Germany). Using a flow rate of 5 mL per minute, the particles were continuously filtered by the porous sphere in a closed-loop circulatory setup. Samples of 200 μL were taken every 20 seconds to quantify the amount of gold particles left in the suspension. This was possible by measuring the change in absorbance of the samples using a UV-Vis spectrometer (Cary 50, Varian, Australia).

Characterization of print fidelity

To assess the fidelity of the printing process, each gear was printed with a different TEMPO concentration and imaged under an optical microscope (VHX-5000, Keyence VHX-5000, Japan). The cog heights were measured with ImageJ. [269]

Phase diagrams of phase-separating resins

The ternary phase diagrams depicting the miscibility of the resin mixture (fig. 7.6b-c) were constructed mixing known amounts of resin components and observing for turbidity at room temperature. Next, the same specimens were heated to 55°C and inspected for turbidity. For each specimen, the total sample volume was 2 mL.

Contributions

This work was conducted jointly with Dr. Lorenzo Barbera, a PhD student in material sciences at the group of Prof. André Studart at ETH Zurich, and with Roberto Emma, a student who conducted his master's project at LAPD in EPFL. Mr. Emma was co-supervised by Dr. Barbera and I.

Dr. Barbera developed the nanoparticle-filled and the phase separating resins. He performed most of the rheological analysis, with some other photorheological measurements performed by Mr. Emma under my supervision. I performed optical characterizations of the materials. Mr. Emma did most of the printing with nanoparticle-filled resins using software by Dr. Antoine Boniface and I, or the commercial software Apparite from Readily3D. I performed most the printing of phase-separating resins. The multi-material filteing experiment was done jointly by Mr. Emma and I. Dr. Barbera sintered printed parts into glass. Data analysis and visualization was done jointly by Dr. Barbera and I.

Acknowledgements

Conclusion Part IV

8 Conclusion

This thesis presents new developments to the novel field of tomographic volumetric additive manufacturing, including software corrections to improve print fidelity in scattering materials, the expansion of the materials palette, and applications in bioprinting.

8.1   Summary of the results

The maximum footprint of fabricated objects was increased by incorporating a helical motion during tomographic manufacturing. Off-centering the digital micromirror device with respect to the optical axis further increased the cross-section of the printable objects. This asymmetric projection system served as a platform to evaluate the effects of beam defocusing and divergence on print quality. It turns out that an off-centered asymmetric projection system is less robust to defocusing: a mismatch between the image plane and the center of the rotating vial.

Tomographic volumetric additive manufacturing, a fabrication method that relies on the deposition of light throughout a photocurable material, was formerly limited to transparent resins. The method was extended to scattering materials by refractive-index matching and software corrections to the way light patterns are calculated. Scattering materials include cell-laden hydrogels, the main building block of tissue engineering.

The refractive index of embedding hydrogels can be tuned with iodixanol, a cytocompatible contrast agent, to reduce the detrimental effects of light scattering from cells on the projected light patterns. Moreover, organoids (cell agglomerates) instead of single cells can be suspended into hydrogels to locally increase cell density without increasing light scattering.

The scattering correction, which can be understood as a depth-dependent frequency boosting, was applied to fabricate hollow unobstructed channels within densely cell-laden hydrogels. Hollow channels are a main feature of human tissues, including vasculature and ducts. We apply the scattering correction to fabricate in vitro models of the pancreatic exocrine unit. These models consisted of volumetrically bioprinted fibroblast-laden duct models, in which human pancreatic ductal cells were injected. These cells could include or not the oncogene KRAS, a hallmark of pancreatic cancer. After following the co-culture for several days, it was seen that the constructs were *(1)* highly viable and *(2)* the fibroblasts in constructs containing cancerous cells exhibited an increased expression of the protein αSMA. In vivo, αSMA is an indicator of tissue stiffening. These results suggest that our volumetrically

fabricated models replicate the stromal activation that is characteristic to pancreatic cancer, and which hinders treatment.

The library of available materials for volumetric printing was also expanded to include sinterable materials. These included polymer-derived ceramics and glass (from fused silica and metal alkoxides).

In the fabrication of polymer-derived ceramics, a commercial polysiloxane was crosslinked to produce cm-scale green bodies, which were then pyrolyzed into carbon-rich silicon oxycarbide ceramics. We demonstrated that volumetric fabrication did not lead to anisotropy in shrinkage after heat treatment, a common challenge in the additive manufacturing of ceramics. The ceramization was evaluated through FTIR, Raman, and x-ray photoelectron spectroscopy. The fabricated microcomponents were proven to be resistant to thermal and chemical stress.

Solid glass was volumetrically fabricated from acrylic resins highly filled with silica nanoparticles. These resin formulations were tuned to make them optically transparent. An inhibitor was added to increase contrast during printing and improve resolution. Porous glass was fabricated from phase-separating resins, also tuned to adapt their transparency and photorheology to meet the requirements of volumetric printing. The two materials were combined to fabricate a multi-component milifluidic filtering device, comprising a porous filter within a solid channel. The filter was used to remove gold nanoparticles from an aqueous solution.

8.2   Future work

Volumetric additive manufacturing is an interesting novel fabrication method, particularly thanks to its short printing times (less than a minute), the possibility to print in closed hermetic vials, the design freedom (and lack of need for support struts), and the low concentrations of photoinitiator needed.

Printing in closed vials is useful because it allows to rapidly browse through material libraries. In this sense, the method could be adopted to automatically test large numbers of material formulations, a process that would be extremely time consuming with other methods

The low concentrations of photoinitiators makes the method less cytotoxic and better-adapted to bioprinting. Tissue engineering technologies are advancing fast and the need for more more biomimetic artificial tissues is urgent (to reduce animal experimentation or to develop personalized therapies, for example).

A more widespread adaptation of volumetric additive manufacturing depends on the improvement of print resolution. So far, it has been challenging to push the method to fabricate cm-scale objects with resolutions below 50 μm. Resolution could be improved by combining the method with two-photon (or two-step) photoinitiation, by incorporating photoinhibitors (enabling the projection of negative light doses, as resulting from filtered back-projection algorithms), or by developing alternative reconstruction software to the Radon transform. This last point is particularly interesting because experiments suggest that the diffractive nature of light plays a role in limiting resolution. As such, in any experimental setup for volumetric printing, the paraxial approximation does not hold. Diffractive tomography or 3D-aware Radon reconstructions could be possible solutions to this issue.

A major challenge in bioprinting is that of cell density. The densest constructs volumetrically fabricated are still two orders of magnitude away from native tissue cell densities. But light transmission will drop rapidly at these cell concentrations. The development of photoinitiators absorbing in the red

or infrared sections of the spectrum could reduce this detrimental effect, as longer wavelengths are less sensible to scattering. Volumetric bioprinting could also be combined with acoustic assembly and patterning of cells to locally increase cell density.

Finally, if volumetric additive manufacturing is to make part of the prototyping industry, efforts should be made to reduce its environmental impact. Resins that do not require solvents in their post-processing, resins with a smaller carbon footprint than oil-derived plastics, or non-toxic plant-derived photoinitiators could all be more environmentally friendly alternatives.

Bibliography

[1] T. Bhattacharjee, S. M. Zehnder, K. G. Rowe, *et al.*, "Writing in the granular gel medium", *Science Advances*, vol. 1, no. 8, e1500655, Sep. 25, 2015. DOI: 10.1126/sciadv.1500655.

[2] C. B. Highley, C. B. Rodell, and J. A. Burdick, "Direct 3D Printing of Shear-Thinning Hydrogels into Self-Healing Hydrogels", *Advanced Materials*, vol. 27, no. 34, pp. 5075–5079, 2015, ISSN: 1521-4095. DOI: 10.1002/adma.201501234.

[3] T. J. Hinton, Q. Jallerat, R. N. Palchesko, *et al.*, "Three-dimensional printing of complex biological structures by freeform reversible embedding of suspended hydrogels", *Science Advances*, vol. 1, no. 9, e1500758, Oct. 23, 2015. DOI: 10.1126/sciadv.1500758.

[4] T. D. Brown, P. D. Dalton, and D. W. Hutmacher, "Direct Writing By Way of Melt Electrospinning", *Advanced Materials*, vol. 23, no. 47, pp. 5651–5657, 2011, ISSN: 1521-4095. DOI: 10.1002/adma.201103482.

[5] N. Noor, A. Shapira, R. Edri, I. Gal, L. Wertheim, and T. Dvir, "3D Printing of Personalized Thick and Perfusable Cardiac Patches and Hearts", *Advanced Science*, vol. 6, no. 11, p. 1 900 344, 2019, ISSN: 2198-3844. DOI: 10.1002/advs.201900344.

[6] T. M. Robinson, D. W. Hutmacher, and P. D. Dalton, "The Next Frontier in Melt Electrospinning: Taming the Jet", *Advanced Functional Materials*, vol. 29, no. 44, p. 1 904 664, 2019, ISSN: 1616-3028. DOI: 10.1002/adfm.201904664.

[7] C. W. Hull, "Apparatus for production of three-dimensional objects by stereolithography", pat., 1984.

[8] M. Göppert-Mayer, "Über Elementarakte mit zwei Quantensprüngen", *Annalen der Physik*, vol. 401, no. 3, pp. 273–294, 1931, ISSN: 1521-3889. DOI: 10.1002/andp.19314010303.

[9] K.-S. Lee, D.-Y. Yang, S. H. Park, and R. H. Kim, "Recent developments in the use of two-photon polymerization in precise 2D and 3D microfabrications", *Polymers for Advanced Technologies*, vol. 17, no. 2, pp. 72–82, 2006.

[10] H. Zhang, X. Zheng, N. Xie, *et al.*, "Why Do Simple Molecules with "Isolated" Phenyl Rings Emit Visible Light?", *Journal of the American Chemical Society*, vol. 139, no. 45, pp. 16 264–16 272, Nov. 15, 2017, ISSN: 0002-7863. DOI: 10.1021/jacs.7b08592.

[11] C. Dietlin, T. T. Trinh, S. Schweizer, *et al.*, "Rational Design of Acyldiphenylphosphine Oxides as Photoinitiators of Radical Polymerization", *Macromolecules*, vol. 52, no. 20, pp. 7886–7893, Oct. 22, 2019, ISSN: 0024-9297. DOI: 10.1021/acs.macromol.9b01724.

[12] A. Bagheri and J. Jin, "Photopolymerization in 3D Printing", *ACS Applied Polymer Materials*, vol. 1, no. 4, pp. 593–611, Apr. 12, 2019. DOI: 10.1021/acsapm.8b00165.

[13] D. Loterie, P. Delrot, and C. Moser, "High-resolution tomographic volumetric additive manufacturing", *Nature Communications*, vol. 11, no. 1, p. 852, Dec. 2020, ISSN: 2041-1723. DOI: 10.1038/s41467-020-14630-4.

[14] J. T. Toombs, M. Luitz, C. C. Cook, *et al.*, "Volumetric additive manufacturing of silica glass with microscale computed axial lithography", *Science*, vol. 376, no. 6590, pp. 308–312, 2022, ISSN: 0036-8075.

[15] M. G. Neumann, W. G. Miranda, C. C. Schmitt, F. A. Rueggeberg, and I. C. Correa, "Molar extinction coefficients and the photon absorption efficiency of dental photoinitiators and light curing units", *Journal of Dentistry*, vol. 33, no. 6, pp. 525–532, Jul. 1, 2005, ISSN: 0300-5712. DOI: 10.1016/j.jdent.2004.11.013.

[16] V. Hahn, T. Messer, N. M. Bojanowski, *et al.*, "Two-step absorption instead of two-photon absorption in 3D nanoprinting", *Nature Photonics*, vol. 15, no. 12, pp. 932–938, 2021.

[17] Y. Sanai, S. Kagami, and K. Kubota, "Initiation and termination pathways in the photopolymerization of acrylate using methyl phenylglyoxylate as an initiator", *Polymer Journal*, vol. 52, no. 4, pp. 375–385, Apr. 2020, ISSN: 0032-3896, 1349-0540. DOI: 10.1038/s41428-019-0288-y.

[18] J.-P. Fouassier and J. Lalevée, *Photoinitiators for Polymer Synthesis: Scope, Reactivity, and Efficiency*. John Wiley & Sons, Aug. 7, 2012, 505 pp., ISBN: 978-3-527-33210-6.

[19] C. Decker, T. Nguyen Thi Viet, D. Decker, and E. Weber-Koehl, "UV-radiation curing of acrylate/epoxide systems", *Polymer*, vol. 42, no. 13, pp. 5531–5541, Jun. 1, 2001, ISSN: 0032-3861. DOI: 10.1016/S0032-3861(01)00065-9.

[20] S. C. Ligon, B. Husár, H. Wutzel, R. Holman, and R. Liska, "Strategies to reduce oxygen inhibition in photoinduced polymerization", *Chemical reviews*, vol. 114, no. 1, pp. 557–589, 2014, ISSN: 0009-2665.

[21] C. C. Cook, E. J. Fong, J. J. Schwartz, *et al.*, "Highly Tunable Thiol-Ene Photoresins for Volumetric Additive Manufacturing", *Advanced Materials*, p. 2 003 376, Oct. 2020, ISSN: 0935-9648, 1521-4095. DOI: 10.1002/adma.202003376.

[22] B. Wang, E. Engay, P. R. Stubbe, *et al.*, "Stiffness control in dual color tomographic volumetric 3D printing", *Nature communications*, vol. 13, no. 1, pp. 1–10, 2022, ISSN: 2041-1723.

[23] S. Huang, S. M. Adelmund, P. S. Pichumani, *et al.*, "One-pot ternary sequential reactions for photopatterned gradient multimaterials", *Matter*, vol. 6, no. 7, pp. 2419–2438, Jul. 2023, ISSN: 25902385. DOI: 10.1016/j.matt.2023.05.040.

[24]   M. Farsari and B. N. Chichkov, "Two-photon fabrication", *Nature photonics*, vol. 3,
        no. 8, pp. 450–452, 2009.

[25]   J. R. Tumbleston, D. Shirvanyants, N. Ermoshkin, *et al.*, "Continuous liquid interface
        production of 3D objects", *Science*, vol. 347, no. 6228, pp. 1349–1352, 2015.

[26]   D. A. Walker, J. L. Hedrick, and C. A. Mirkin, "Rapid, large-volume, thermally controlled
        3D printing using a mobile liquid interface", *Science*, vol. 366, no. 6463, pp. 360–364,
        2019.

[27]   M. Shusteff, A. E. Browar, B. E. Kelly, *et al.*, "One-step volumetric additive manufactur-
        ing of complex polymer structures", *Science advances*, vol. 3, no. 12, eaao5496, 2017,
        ISSN: 2375-2548.

[28]   P. N. Bernal, P. Delrot, D. Loterie, *et al.*, "Volumetric Bioprinting of Complex Living-
        Tissue Constructs within Seconds", *Advanced Materials*, vol. 31, no. 42, p. 1 904 209,
        Oct. 2019, ISSN: 0935-9648, 1521-4095. DOI: 10.1002/adma.201904209.

[29]   B. E. Kelly, I. Bhattacharya, H. Heidari, M. Shusteff, C. M. Spadaccini, and H. K. Taylor,
        "Volumetric additive manufacturing via tomographic reconstruction", *Science*, vol. 363,
        no. 6431, pp. 1075–1079, Mar. 8, 2019, ISSN: 0036-8075, 1095-9203. DOI: 10.1126/science.
        aau7114.

[30]   M. Regehly, Y. Garmshausen, M. Reuter, *et al.*, "Xolography for linear volumetric 3D
        printing", *Nature*, vol. 588, no. 7839, pp. 620–624, 2020, ISSN: 1476-4687.

[31]   M. Gastaldi, F. Cardano, M. Zanetti, *et al.*, "Functional Dyes in Polymeric 3D Printing:
        Applications and Perspectives", *ACS Materials Letters*, vol. 3, no. 1, pp. 1–17, Jan. 4,
        2021. DOI: 10.1021/acsmaterialslett.0c00455.

[32]   R. Janusziewicz, J. R. Tumbleston, A. L. Quintanilla, S. J. Mecham, and J. M. DeSimone,
        "Layerless fabrication with continuous liquid interface production", *Proceedings of the
        National Academy of Sciences*, vol. 113, no. 42, pp. 11 703–11 708, Oct. 18, 2016. DOI:
        10.1073/pnas.1605271113.

[33]   W. Kaiser and C. G. B. Garrett, "Two-Photon Excitation in CaF2:Eu2+", *Physical Review
        Letters*, vol. 7, no. 6, pp. 229–231, Sep. 15, 1961. DOI: 10.1103/PhysRevLett.7.229.

[34]   T. Chi, P. Somers, D. A. Wilcox, *et al.*, "Tailored thioxanthone-based photoinitiators
        for two-photon-controllable polymerization and nanolithographic printing", *Journal
        of Polymer Science Part B: Polymer Physics*, vol. 57, no. 21, pp. 1462–1475, 2019, ISSN:
        1099-0488. DOI: 10.1002/polb.24891.

[35]   C. Mendonca, D. Correa, T. Baldacchini, P. Tayalia, and E. Mazur, "Two-photon absorp-
        tion spectrum of the photoinitiator Lucirin TPO-L", *Applied Physics A*, vol. 90, no. 4,
        pp. 633–636, Mar. 2008, ISSN: 0947-8396, 1432-0630. DOI: 10.1007/s00339-007-4367-0.

[36]   C. N. LaFratta, J. T. Fourkas, T. Baldacchini, and R. A. Farrer, "Multiphoton Fabrication",
        Angewandte Chemie International Edition, vol. 46, no. 33, pp. 6238–6258, Aug. 13, 2007,
        ISSN: 1521-3773. DOI: 10.1002/anie.200603995.

[37]   S. K. Saha, D. Wang, V. H. Nguyen, Y. Chang, J. S. Oakdale, and S.-C. Chen, "Scalable submicrometer additive manufacturing", *Science*, vol. 366, no. 6461, pp. 105–109, 2019, ISSN: 0036-8075.

[38]   P. Somers, Z. Liang, J. E. Johnson, B. W. Boudouris, L. Pan, and X. Xu, "Rapid, continuous projection multi-photon 3D printing enabled by spatiotemporal focusing of femtosecond pulses", *Light: Science & Applications*, vol. 10, no. 1, p. 199, 1 Sep. 24, 2021, ISSN: 2047-7538. DOI: 10.1038/s41377-021-00645-z.

[39]   T. Aderneuer, O. Fernández, and R. Ferrini, "Two-photon grayscale lithography for freeform micro-optical arrays", *Optics Express*, vol. 29, no. 24, pp. 39 511–39 520, Nov. 22, 2021, ISSN: 1094-4087. DOI: 10.1364/OE.440251.

[40]   A. Toulouse, J. Drozella, S. Thiele, H. Giessen, and A. Herkommer, "3D-printed miniature spectrometer for the visible range with a 100×100 m^2 footprint", *Light: Advanced Manufacturing*, vol. 2, no. 1, pp. 20–30, Mar. 1, 2021, ISSN: 2689-9620. DOI: 10.37188/lam.2021.002.

[41]   H. Bouas-Laurent and H. Dürr, "Organic photochromism (IUPAC Technical Report)", *Pure and Applied Chemistry*, vol. 73, no. 4, pp. 639–665, Jan. 1, 2001, ISSN: 1365-3075. DOI: 10.1351/pac200173040639.

[42]   C. M. Sousa, J. R. Fernandes, and P. J. Coelho, "Naphthopyrans as efficient dual color photoinitiators for volumetric 3D printing", *European Polymer Journal*, p. 112 312, Jul. 17, 2023, ISSN: 0014-3057. DOI: 10.1016/j.eurpolymj.2023.112312.

[43]   V. Hahn, P. Rietz, F. Hermann, *et al.*, "Light-sheet 3D microprinting via two-colour two-step absorption", *Nature Photonics*, pp. 1–8, 2022.

[44]   S. Maruo, O. Nakamura, and S. Kawata, "Three-dimensional microfabrication with two-photon-absorbed photopolymerization", *Optics Letters*, vol. 22, no. 2, pp. 132–134, Jan. 15, 1997.

[45]   B. E. Kelly, I. Bhattacharya, M. Shusteff, H. K. Taylor, and C. M. Spaddacini, "Computed axial lithography for rapid volumetric 3D additive manufacturing", in *2017 International Solid Freeform Fabrication Symposium*, University of Texas at Austin, 2017.

[46]   D. Loterie, P. Delrot, and C. Moser, "Volumetric 3D printing of elastomers by tomographic back-projection", *Preprint at https://doi. org/10.13140/RG*, vol. 2, no. 20027.46889, 2018.

[47]   L. Shen, W. Zhao, and L. Xing, "Patient-specific reconstruction of volumetric computed tomography images from a single projection view via deep learning", *Nature Biomedical Engineering*, vol. 3, no. 11, pp. 880–888, 11 Nov. 2019, ISSN: 2157-846X. DOI: 10.1038/s41551-019-0466-4.

[48]   S. Helgason and S. Helgason, *The Radon Transform*. Springer, 1980.

[49] M. Born and E. Wolf, "Elements of the theory of diffraction", in *Principles of Optics: Electromagnetic Theory of Propagation, Interference and Diffraction of Light*, 7th ed., Cambridge: Cambridge University Press, 1999, pp. 412–516, ISBN: 0-521-64222-1.

[50] P. Toft, "The Radon Transform - Theory and Implementation", Technical University of Denmark, Denmark, 1996.

[51] A. C. Kak and M. Slaney, *Principles of Computerized Tomographic Imaging*. SIAM, 2001, ISBN: 0-89871-494-X.

[52] S. Van der Walt, J. L. Schönberger, J. Nunez-Iglesias, *et al.*, "Scikit-image: Image processing in Python", *PeerJ*, vol. 2, e453, 2014.

[53] P. J. Withers, C. Bouman, S. Carmignato, *et al.*, "X-ray computed tomography", *Nature Reviews Methods Primers*, vol. 1, no. 1, p. 18, Feb. 25, 2021, ISSN: 2662-8449. DOI: 10.1038/s43586-021-00015-4.

[54] R. Schofield, L. King, U. Tayal, *et al.*, "Image reconstruction: Part 1–understanding filtered back projection, noise and image acquisition", *Journal of cardiovascular computed tomography*, vol. 14, no. 3, pp. 219–225, 2020, ISSN: 1934-5925.

[55] M. P. De Beer, H. L. Van Der Laan, M. A. Cole, R. J. Whelan, M. A. Burns, and T. F. Scott, "Rapid, continuous additive manufacturing by volumetric polymerization inhibition patterning", *Science advances*, vol. 5, no. 1, eaau8723, 2019, ISSN: 2375-2548.

[56] H. L. Van Der Laan, M. A. Burns, and T. F. Scott, "Volumetric photopolymerization confinement through dual-wavelength photoinitiation and photoinhibition", *ACS Macro Letters*, vol. 8, no. 8, pp. 899–904, 2019, ISSN: 2161-1653.

[57] B. Wang, W. Sun, J. P. C. Narag, *et al.* "Creating negative illumination for tomographic 3D printing via binary photoinhibition". (Mar. 24, 2023), preprint.

[58] A. Boniface, M. Mounaix, B. Blochet, R. Piestun, and S. Gigan, "Transmission-matrix-based point-spread-function engineering through a complex medium", *Optica*, vol. 4, no. 1, pp. 54–59, 2017.

[59] I. Bhattacharya, J. Toombs, and H. Taylor, "High fidelity volumetric additive manufacturing", *Additive Manufacturing*, vol. 47, p. 102 299, 2021.

[60] T. Chen, H. Li, and X. Liu, "Statistical iterative pattern generation in volumetric additive manufacturing based on ML-EM", *Optics Communications*, vol. 537, p. 129 448, Jun. 15, 2023, ISSN: 0030-4018. DOI: 10.1016/j.optcom.2023.129448.

[61] J. Madrid-Wolff, A. Boniface, D. Loterie, P. Delrot, and C. Moser, "Controlling Light in Scattering Materials for Volumetric Additive Manufacturing", *Advanced Science*, p. 2 105 144, 2022, ISSN: 2198-3844.

[62] C. M. Rackson, K. M. Champley, J. T. Toombs, *et al.*, "Object-space optimization of tomographic reconstructions for additive manufacturing", *Additive Manufacturing*, vol. 48, p. 102 367, 2021, ISSN: 2214-8604.

[63] D. Webber, Y. Zhang, M. Picard, J. Boisvert, C. Paquet, and A. Orth, "Versatile volumetric additive manufacturing with 3D ray tracing", *Optics Express*, vol. 31, no. 4, pp. 5531–5546, Feb. 13, 2023, ISSN: 1094-4087. DOI: 10.1364/OE.481318.

[64] A. Orth, K. L. Sampson, K. Ting, J. Boisvert, and C. Paquet, "Correcting ray distortion in tomographic additive manufacturing", *Optics Express*, vol. 29, no. 7, pp. 11 037–11 054, 2021, ISSN: 1094-4087.

[65] C. Chung Li, J. Toombs, and H. Taylor, "Tomographic color Schlieren refractive index mapping for computed axial lithography", in *Symposium on Computational Fabrication*, Virtual Event USA: ACM, Nov. 5, 2020, pp. 1–7, ISBN: 978-1-4503-8170-3. DOI: 10.1145/3424630.3425421. [Online]. Available: https://dl.acm.org/doi/10.1145/3424630.3425421 (visited on 01/05/2021).

[66] A. Orth, K. L. Sampson, Y. Zhang, *et al.*, "On-the-fly 3D metrology of volumetric additive manufacturing", *Additive Manufacturing*, vol. 56, p. 102 869, 2022.

[67] A. S. Kewitsch and A. Yariv, "Self-focusing and self-trapping of optical beams upon photopolymerization", *Optics Letters*, vol. 21, no. 1, pp. 24–26, Jan. 1, 1996, ISSN: 1539-4794. DOI: 10.1364/OL.21.000024.

[68] C. M. Rackson, J. T. Toombs, M. P. De Beer, *et al.*, "Latent image volumetric additive manufacturing", *Optics Letters*, vol. 47, no. 5, pp. 1279–1282, 2022, ISSN: 1539-4794.

[69] A. Orth, D. Webber, Y. Zhang, *et al.*, "Deconvolution volumetric additive manufacturing", *Nature Communications*, vol. 14, no. 1, p. 4412, 2023.

[70] J.-P. Fouassier, *Photoinitiation, Photopolymerization, and Photocuring: Fundamentals and Applications*. Munich: Hanser, 1995, 375 pp., ISBN: 978-1-56990-146-5.

[71] R. Rizzo, D. Ruetsche, H. Liu, and M. Zenobi-Wong, "Optimized Photoclick (Bio)Resins for Fast Volumetric Bioprinting", *Advanced Materials*, vol. 33, no. 49, p. 2 102 900, 2021, ISSN: 1521-4095. DOI: 10.1002/adma.202102900.

[72] J. T. Toombs, I. K. Shan, and H. K. Taylor, "Ethyl Cellulose-Based Thermoreversible Organogel Photoresist for Sedimentation-Free Volumetric Additive Manufacturing", *Macromolecular Rapid Communications*, vol. 44, no. 7, p. 2 200 872, 2023, ISSN: 1521-3927. DOI: 10.1002/marc.202200872.

[73] P. N. Bernal, M. Bouwmeester, J. Madrid-Wolff, *et al.*, "Volumetric Bioprinting of Organoids and Optically Tuned Hydrogels to Build Liver-Like Metabolic Biofactories", *Advanced Materials*, p. 2 110 054, Feb. 15, 2022. DOI: 10.1002/adma.202110054.

[74] V. Sgarminato, J. Madrid-Wolff, A. Boniface, G. Ciardelli, C. Tonda-Turo, and C. Moser. "Tomographic volumetric bioprinting of 3D pancreatic cancer models". (Jan. 24, 2023), [Online]. Available: https://www.biorxiv.org/content/10.1101/2023.01.23.525142v1 (visited on 04/19/2023), preprint.

[75] M. Kollep, G. Konstantinou, J. Madrid-Wolff, *et al.*, "Tomographic Volumetric Additive Manufacturing of Silicon Oxycarbide Ceramics", *Advanced Engineering Materials*, p. 2 101 345, 2022, ISSN: 1438-1656.

[76]   B. Zeng, Z. Cai, J. Lalevée, *et al.*, "Cytotoxic and cytocompatible comparison among seven photoinitiators-triggered polymers in different tissue cells", *Toxicology in Vitro*, vol. 72, p. 105 103, Apr. 1, 2021, ISSN: 0887-2333. DOI: 10.1016/j.tiv.2021.105103.

[77]   V. V. Rocheva, A. V. Koroleva, A. G. Savelyev, *et al.*, "High-resolution 3D photopolymerization assisted by upconversion nanoparticles for rapid prototyping applications", *Scientific Reports*, vol. 8, no. 1, p. 3663, Dec. 2018, ISSN: 2045-2322. DOI: 10.1038/s41598-018-21793-0.

[78]   S. N. Sanders, T. H. Schloemer, M. K. Gangishetty, *et al.*, "Triplet fusion upconversion nanocapsules for volumetric 3D printing", *Nature*, vol. 604, no. 7906, pp. 474–478, 7906 Apr. 2022, ISSN: 1476-4687. DOI: 10.1038/s41586-022-04485-8.

[79]   V. Hahn, N. M. Bojanowski, P. Rietz, *et al.*, "Challenges and Opportunities in 3D Laser Printing Based on (1 + 1)-Photon Absorption", *ACS Photonics*, vol. 10, no. 1, pp. 24–33, Jan. 18, 2023. DOI: 10.1021/acsphotonics.2c01632.

[80]   S. Mukherjee, T. Chang, and J. W. Tringe, "System and method for microwave volumetric additive manufacturing", U.S. Patent 20230135458A1, May 4, 2023.

[81]   A. G. Guex, N. Di Marzio, D. Eglin, M. Alini, and T. Serra, "The waves that make the pattern: a review on acoustic manipulation in biomedical research", *Materials Today Bio*, vol. 10, p. 100 110, 2021.

[82]   R. Hirayama, G. Christopoulos, D. Martinez Plasencia, and S. Subramanian, "High-speed acoustic holography with arbitrary scattering objects", *Science Advances*, vol. 8, no. 24, eabn7614, Jun. 17, 2022. DOI: 10.1126/sciadv.abn7614.

[83]   R. Tognato, R. Parolini, M. Alini, *et al.*, "Sound-based assembly of three-dimensional cellularized and acellularized constructs", *bioRxiv : the preprint server for biology*, pp. 2023–05, 2023.

[84]   R. Salajeghe, D. H. Meile, C. S. Kruse, D. Marla, and J. Spangenberg, "Numerical modeling of part sedimentation during volumetric additive manufacturing", *Additive Manufacturing*, vol. 66, p. 103 459, Mar. 25, 2023, ISSN: 2214-8604. DOI: 10.1016/j.addma.2023.103459.

[85]   T. Waddell, J. Toombs, A. Reilly, *et al.*, "Use of volumetric additive manufacturing as an in-space manufacturing technology", *Acta Astronautica*, Jul. 6, 2023, ISSN: 0094-5765. DOI: 10.1016/j.actaastro.2023.06.048.

[86]   J. Madrid-Wolff, J. Toombs, R. Rizzo, *et al.*, "A review of materials used in tomographic volumetric additive manufacturing", *MRS Communications*, Aug. 29, 2023, ISSN: 2159-6867. DOI: 10.1557/s43579-023-00447-x.

[87]   W. Qiu, J. Gehlen, M. Bernero, *et al.*, "A Synthetic Dynamic Polyvinyl Alcohol Photoresin for Fast Volumetric Bioprinting of Functional Ultrasoft Hydrogel Constructs", *Advanced Functional Materials*, vol. n/a, no. n/a, p. 2 214 393, ISSN: 1616-3028. DOI: 10.1002/adfm.202214393.

[88] G. Größbacher, M. Bartolf-Kopp, C. Gergely, *et al.*, "Volumetric Printing across Melt Electrowritten Scaffolds Fabricates Multi-Material Living Constructs with Tunable Architecture and Mechanics", *Advanced Materials*, p. 2 300 756, ISSN: 1521-4095. DOI: 10.1002/adma.202300756.

[89] M. Xie, L. Lian, X. Mu, *et al.*, "Volumetric additive manufacturing of pristine silk-based (bio)inks", *Nature Communications*, vol. 14, no. 1, p. 210, 1 Jan. 13, 2023, ISSN: 2041-1723. DOI: 10.1038/s41467-023-35807-7.

[90] Q. Thijssen, A. Quaak, J. Toombs, *et al.*, "Volumetric Printing of Thiol-Ene Photo-Cross-Linkable Poly(-caprolactone): A Tunable Material Platform Serving Biomedical Applications", *Advanced Materials*, vol. n/a, no. n/a, p. 2 210 136, ISSN: 1521-4095. DOI: 10.1002/adma.202210136.

[91] J. J. Schwartz, D. H. Porcincula, C. C. Cook, E. J. Fong, and M. Shusteff, "Volumetric additive manufacturing of shape memory polymers", *Polymer Chemistry*, vol. 13, no. 13, pp. 1813–1817, 2022.

[92] W. A. Kalender, W. Seissler, E. Klotz, and P. Vock, "Spiral volumetric CT with single-breath-hold technique, continuous transport, and continuous scanner rotation.", *Radiology*, vol. 176, no. 1, pp. 181–183, 1990.

[93] A. Boniface, F. Maître, J. Madrid-Wolff, and C. Moser, "Volumetric helical additive manufacturing", *Light: Advanced Manufacturing*, vol. 4, no. 2, p. 1, 2023, ISSN: 2831-4093. DOI: 10.37188/lam.2023.012.

[94] A. J. Devaney, "A filtered backpropagation algorithm for diffraction tomography", *Ultrasonic imaging*, vol. 4, no. 4, pp. 336–350, 1982.

[95] N. U. Dinc, A. Saba, J. Madrid-Wolff, *et al.*, "From 3D to 2D and back again", *Nanophotonics*, Jan. 4, 2023, ISSN: 2192-8614. DOI: 10.1515/nanoph-2022-0512.

[96] P. Müller, M. Schürmann, and J. Guck, "The theory of diffraction tomography", 2015.

[97] S. Popoff. "Setting up a DMD: Diffraction effects - Wavefrontshaping.net". (), [Online]. Available: https://www.wavefrontshaping.net/post/id/21 (visited on 08/07/2023).

[98] D. Loterie, "Microscopy and digital light shaping through optical fibers", Doctoral Thesis, EPFL, Switzerland, Jun. 23, 2017.

[99] A. Douplik, G. Saiko, I. Schelkanova, and V. V. Tuchin, "3 - The response of tissue to laser light", in *Lasers for Medical Applications*, ser. Woodhead Publishing Series in Electronic and Optical Materials, H. Jelínková, Ed., Woodhead Publishing, Jan. 1, 2013, pp. 47–109, ISBN: 978-0-85709-237-3. DOI: 10.1533/9780857097545.1.47.

[100] C. F. Bohren and D. R. Huffman, *Absorption and Scattering of Light by Small Particles*. John Wiley & Sons, Sep. 26, 2008, 547 pp., ISBN: 978-3-527-61816-3.

[101] S. L. Jacques, "Optical properties of biological tissues: a review", *Physics in Medicine and Biology*, vol. 58, no. 11, R37–R61, Jun. 7, 2013, ISSN: 0031-9155, 1361-6560. DOI: 10.1088/0031-9155/58/11/R37.

[102]   S. L. Jacques and S. A. Prahl. "The math of Mie scattering". (), [Online]. Available: https://omlc.org/classroom/ece532/class3/mie_math.html (visited on 07/23/2023).

[103]   H. C. van de Hulst, *Light Scattering by Small Paticles*. New York: John Wiley & Sons, 1964.

[104]   E. C. Costa, D. N. Silva, A. F. Moreira, and I. J. Correia, "Optical clearing methods: An overview of the techniques used for the imaging of 3D spheroids", *Biotechnology and Bioengineering*, vol. 116, no. 10, pp. 2742–2763, Oct. 2019, ISSN: 0006-3592, 1097-0290. DOI: 10.1002/bit.27105.

[105]   N. S. Bhise, V. Manoharan, S. Massa, *et al.*, "A liver-on-a-chip platform with bioprinted hepatic spheroids", *Biofabrication*, vol. 8, no. 1, p. 014 101, Jan. 2016, ISSN: 1758-5090. DOI: 10.1088/1758-5090/8/1/014101.

[106]   Z. Zhao, X. Chen, A. M. Dowbaj, *et al.*, "Organoids", *Nature Reviews Methods Primers*, vol. 2, no. 1, p. 94, Dec. 1, 2022, ISSN: 2662-8449. DOI: 10.1038/s43586-022-00174-y.

[107]   R. Barer, "Spectrophotometry of Clarified Cell Suspensions", *Science*, vol. 121, no. 3151, pp. 709–715, May 20, 1955. DOI: 10.1126/science.121.3151.709.

[108]   T. Boothe, L. Hilbert, M. Heide, *et al.*, "A tunable refractive index matching medium for live imaging cells, tissues and model organisms", *eLife*, vol. 6, e27240, Jul. 14, 2017, ISSN: 2050-084X. DOI: 10.7554/eLife.27240.

[109]   A. J. Hunt and D. R. Huffman, "A new polarization-modulated light scattering instrument", *Review of Scientific Instruments*, vol. 44, no. 12, pp. 1753–1762, Nov. 6, 2003, ISSN: 0034-6748. DOI: 10.1063/1.1686049.

[110]   P. Jaccard, "The distribution of the flora in the alpine zone. 1", *New Phytologist*, vol. 11, no. 2, pp. 37–50, 1912.

[111]   A. A. Taha and A. Hanbury, "Metrics for evaluating 3D medical image segmentation: analysis, selection, and tool", *BMC Medical Imaging*, vol. 15, no. 1, p. 29, Aug. 12, 2015, ISSN: 1471-2342. DOI: 10.1186/s12880-015-0068-x.

[112]   V. V. Tuchin, "Light scattering study of tissues", *Physics-Uspekhi*, vol. 40, no. 5, p. 495, May 31, 1997, ISSN: 1063-7869. DOI: 10.1070/PU1997v040n05ABEH000236.

[113]   A. Brunsting and P. F. Mullaney, "Differential Light Scattering from Spherical Mammalian Cells", *Biophysical Journal*, vol. 14, no. 6, pp. 439–453, Jun. 1974, ISSN: 00063495. DOI: 10.1016/S0006-3495(74)85925-4.

[114]   A. D. Benjamin, R. Abbasi, M. Owens, *et al.*, "Light-based 3D printing of hydrogels with high-resolution channels", *Biomedical Physics & Engineering Express*, vol. 5, no. 2, p. 025 035, 2019.

[115]   R. Raman, B. Bhaduri, M. Mir, *et al.*, "High-resolution projection microstereolithography for patterning of neovasculature", *Advanced Healthcare Materials*, vol. 5, no. 5, pp. 610–619, 2016.

[116] A. Schwab, R. Levato, M. D'Este, S. Piluso, D. Eglin, and J. Malda, "Printability and shape fidelity of bioinks in 3D bioprinting", *Chemical Reviews*, vol. 120, no. 19, pp. 11 028–11 055, 2020.

[117] C. Feng, W. Zhang, C. Deng, *et al.*, "3D printing of Lotus root-like biomimetic materials for cell delivery and tissue regeneration", *Advanced Science*, vol. 4, no. 12, p. 1 700 401, 2017.

[118] B. Grigoryan, S. J. Paulsen, D. C. Corbett, *et al.*, "Multivascular networks and functional intravascular topologies within biocompatible hydrogels", *Science*, vol. 364, no. 6439, pp. 458–464, 2019.

[119] I. S. Kinstlinger, S. H. Saxton, G. A. Calderon, *et al.*, "Generation of model tissues with dendritic vascular networks via sacrificial laser-sintered carbohydrate templates", *Nature Biomedical Engineering*, vol. 4, no. 9, pp. 916–932, 2020.

[120] J. S. Miller, K. R. Stevens, M. T. Yang, *et al.*, "Rapid casting of patterned vascular networks for perfusable engineered three-dimensional tissues", *Nature Materials*, vol. 11, no. 9, pp. 768–774, 9 Sep. 2012, ISSN: 1476-4660. DOI: 10.1038/nmat3357.

[121] R. Suntornnond, E. Y. S. Tan, J. An, and C. K. Chua, "A highly printable and biocompatible hydrogel composite for direct printing of soft and perfusable vasculature-like structures", *Scientific Reports*, vol. 7, no. 1, pp. 1–11, 2017.

[122] J. Icha, M. Weber, J. C. Waters, and C. Norden, "Phototoxicity in live fluorescence microscopy, and how to avoid it", *BioEssays*, vol. 39, no. 8, p. 1 700 003, 2017, ISSN: 1521-1878. DOI: 10.1002/bies.201700003.

[123] J. Gehlen, W. Qiu, G. N. Schädli, R. Müller, and X.-H. Qin, "Tomographic volumetric bioprinting of heterocellular bone-like tissues in seconds", *Acta Biomaterialia*, 2022, ISSN: 1742-7061.

[124] H.-Q. Xu, J.-C. Liu, Z.-Y. Zhang, and C.-X. Xu, "A review on cell damage, viability, and functionality during 3D bioprinting", *Military Medical Research*, vol. 9, no. 1, p. 70, Dec. 16, 2022, ISSN: 2054-9369. DOI: 10.1186/s40779-022-00429-5.

[125] W. S. Harley, C. C. Li, J. Toombs, *et al.*, "Advances in biofabrication techniques towards functional bioprinted heterogeneous engineered tissues: A comprehensive review", *Bioprinting*, vol. 23, e00147, 2021.

[126] K. S. Lim, J. H. Galarraga, X. Cui, G. C. Lindberg, J. A. Burdick, and T. B. Woodfield, "Fundamentals and applications of photo-cross-linking in bioprinting", *Chemical reviews*, vol. 120, no. 19, pp. 10 662–10 694, 2020.

[127] A. I. Van Den Bulcke, B. Bogdanov, N. De Rooze, E. H. Schacht, M. Cornelissen, and H. Berghmans, "Structural and Rheological Properties of Methacrylamide Modified Gelatin Hydrogels", *Biomacromolecules*, vol. 1, no. 1, pp. 31–38, Mar. 14, 2000, ISSN: 1525-7797. DOI: 10.1021/bm990017d.

[128] M. Zhu, Y. Wang, G. Ferracci, J. Zheng, N.-J. Cho, and B. H. Lee, "Gelatin methacryloyl and its hydrogels with an exceptional degree of controllability and batch-to-batch consistency", *Scientific Reports*, vol. 9, no. 1, p. 6863, 1 May 3, 2019, ISSN: 2045-2322. DOI: 10.1038/s41598-019-42186-x.

[129] P. Thomas and T. G. Smart, "HEK293 cell line: a vehicle for the expression of recombinant proteins", *Journal of pharmacological and toxicological methods*, vol. 51, no. 3, pp. 187–200, 2005.

[130] J.-Y. Tinevez, N. Perry, J. Schindelin, *et al.*, "TrackMate: An open and extensible platform for single-particle tracking", *Methods*, vol. 115, pp. 80–90, 2017.

[131] D. Fukutomi, K. Ishii, and K. Awazu, "Determination of the scattering coefficient of biological tissue considering the wavelength and absorption dependence of the anisotropy factor", *Optical Review*, vol. 23, no. 2, pp. 291–298, Apr. 1, 2016, ISSN: 1349-9432. DOI: 10.1007/s10043-015-0161-y.

[132] J. Schindelin, I. Arganda-Carreras, E. Frise, *et al.*, "Fiji: an open-source platform for biological-image analysis", *Nature methods*, vol. 9, no. 7, pp. 676–682, 2012.

[133] N. Otsu, "A threshold selection method from gray-level histograms", *IEEE transactions on systems, man, and cybernetics*, vol. 9, no. 1, pp. 62–66, 1979.

[134] A. Khomiak, M. Brunner, M. Kordes, *et al.*, "Recent Discoveries of Diagnostic, Prognostic and Predictive Biomarkers for Pancreatic Cancer", *Cancers*, vol. 12, no. 11, p. 3234, Nov. 2, 2020, ISSN: 2072-6694. DOI: 10.3390/cancers12113234.

[135] R. L. Siegel, K. D. Miller, and A. Jemal, "Cancer statistics, 2020", *CA: a cancer journal for clinicians*, vol. 70, no. 1, pp. 7–30, Jan. 2020, ISSN: 1542-4863. DOI: 10.3322/caac.21590.

[136] R. L. Siegel, K. D. Miller, H. E. Fuchs, and A. Jemal, "Cancer statistics, 2022", *CA: A Cancer Journal for Clinicians*, vol. 72, no. 1, pp. 7–33, 2022, ISSN: 1542-4863. DOI: 10.3322/caac.21708.

[137] M. Orth, P. Metzger, S. Gerum, *et al.*, "Pancreatic ductal adenocarcinoma: biological hallmarks, current status, and future perspectives of combined modality treatment approaches", *Radiation Oncology*, vol. 14, no. 1, p. 141, Aug. 8, 2019, ISSN: 1748-717X. DOI: 10.1186/s13014-019-1345-6.

[138] A. Porciuncula, C. Hajdu, and G. David, "The Dual Role of Senescence in Pancreatic Ductal Adenocarcinoma", *Advances in Cancer Research*, vol. 131, pp. 1–20, 2016, ISSN: 2162-5557. DOI: 10.1016/bs.acr.2016.05.006.

[139] L. R. Brunet, T. Hagemann, G. Andrew, S. Mudan, and A. Marabelle, "Have lessons from past failures brought us closer to the success of immunotherapy in metastatic pancreatic cancer?", *Oncoimmunology*, vol. 5, no. 4, e1112942, Apr. 2016, ISSN: 2162-4011. DOI: 10.1080/2162402X.2015.1112942.

[140]   M. A. Heinrich, A. M. R. H. Mostafa, J. P. Morton, L. J. A. C. Hawinkels, and J. Prakash, "Translating complexity and heterogeneity of pancreatic tumor: 3D in vitro to in vivo models", *Advanced Drug Delivery Reviews*, vol. 174, pp. 265–293, Jul. 2021, ISSN: 1872-8294. DOI: 10.1016/j.addr.2021.04.018.

[141]   S. Liot, J. Balas, A. Aubert, *et al.*, "Stroma Involvement in Pancreatic Ductal Adenocarcinoma: An Overview Focusing on Extracellular Matrix Proteins", *Frontiers in Immunology*, vol. 12, 2021, ISSN: 1664-3224.

[142]   M. Geyer and K. Queiroz, "Microfluidic Platforms for High-Throughput Pancreatic Ductal Adenocarcinoma Organoid Culture and Drug Screening", *Frontiers in Cell and Developmental Biology*, vol. 9, 2021, ISSN: 2296-634X.

[143]   Y. Fu, S. Liu, S. Zeng, and H. Shen, "The critical roles of activated stellate cells-mediated paracrine signaling, metabolism and onco-immunology in pancreatic ductal adenocarcinoma", *Molecular Cancer*, vol. 17, no. 1, p. 62, Feb. 19, 2018, ISSN: 1476-4598. DOI: 10.1186/s12943-018-0815-z.

[144]   M. Weniger, K. C. Honselmann, and A. S. Liss, "The Extracellular Matrix and Pancreatic Cancer: A Complex Relationship", *Cancers*, vol. 10, no. 9, p. 316, Sep. 6, 2018, ISSN: 2072-6694. DOI: 10.3390/cancers10090316.

[145]   M. Hidalgo, S. Cascinu, J. Kleeff, *et al.*, "Addressing the challenges of pancreatic cancer: future directions for improving outcomes", *Pancreatology: official journal of the International Association of Pancreatology (IAP) ... [et al.]*, vol. 15, no. 1, pp. 8–18, 2015, ISSN: 1424-3911. DOI: 10.1016/j.pan.2014.10.001.

[146]   T. Liang, S. Dolai, L. Xie, *et al.*, "Ex vivo human pancreatic slice preparations offer a valuable model for studying pancreatic exocrine biology", *The Journal of Biological Chemistry*, vol. 292, no. 14, pp. 5957–5969, Apr. 7, 2017, ISSN: 1083-351X. DOI: 10.1074/jbc.M117.777433.

[147]   S. Wang, Y. Li, C. Xing, *et al.*, "Tumor microenvironment in chemoresistance, metastasis and immunotherapy of pancreatic cancer", *American Journal of Cancer Research*, vol. 10, no. 7, pp. 1937–1953, Jul. 1, 2020, ISSN: 2156-6976.

[148]   M. V. Apte, J. S. Wilson, A. Lugea, and S. J. Pandol, "A starring role for stellate cells in the pancreatic cancer microenvironment", *Gastroenterology*, vol. 144, no. 6, pp. 1210–1219, Jun. 2013, ISSN: 1528-0012. DOI: 10.1053/j.gastro.2012.11.037.

[149]   M. V. Monteiro, L. P. Ferreira, M. Rocha, V. M. Gaspar, and J. F. Mano, "Advances in bioengineering pancreatic tumor-stroma physiomimetic Biomodels", *Biomaterials*, vol. 287, p. 121 653, Aug. 1, 2022, ISSN: 0142-9612. DOI: 10.1016/j.biomaterials.2022.121653.

[150]   H.-X. Zhan, B. Zhou, Y.-G. Cheng, *et al.*, "Crosstalk between stromal cells and cancer cells in pancreatic cancer: New insights into stromal biology", *Cancer Letters*, vol. 392, pp. 83–93, Apr. 28, 2017, ISSN: 1872-7980. DOI: 10.1016/j.canlet.2017.01.041.

[151] R. R. Bynigeri, A. Jakkampudi, R. Jangala, *et al.*, "Pancreatic stellate cell: Pandora's box for pancreatic disease biology", *World Journal of Gastroenterology*, vol. 23, no. 3, pp. 382–405, Jan. 21, 2017, ISSN: 2219-2840. DOI: 10.3748/wjg.v23.i3.382.

[152] M. F. B. Nielsen, M. B. Mortensen, and S. Detlefsen, "Key players in pancreatic cancer-stroma interaction: Cancer-associated fibroblasts, endothelial and inflammatory cells", *World Journal of Gastroenterology*, vol. 22, no. 9, pp. 2678–2700, Mar. 7, 2016, ISSN: 2219-2840. DOI: 10.3748/wjg.v22.i9.2678.

[153] S. T. Chari, "Detecting early pancreatic cancer: problems and prospects", *Seminars in Oncology*, vol. 34, no. 4, pp. 284–294, Aug. 2007, ISSN: 0093-7754. DOI: 10.1053/j.seminoncol.2007.05.005.

[154] R. H. Hruban, N. V. Adsay, J. Albores-Saavedra, *et al.*, "Pathology of genetically engineered mouse models of pancreatic exocrine cancer: consensus report and recommendations", *Cancer Research*, vol. 66, no. 1, pp. 95–106, Jan. 1, 2006, ISSN: 0008-5472. DOI: 10.1158/0008-5472.CAN-05-2168.

[155] S.-J. Cui, T.-Y. Tang, X.-W. Zou, Q.-M. Su, L. Feng, and X.-Y. Gong, "Role of imaging biomarkers for prognostic prediction in patients with pancreatic ductal adenocarcinoma", *Clinical Radiology*, vol. 75, no. 6, 478.e1–478.e11, Jun. 2020, ISSN: 1365-229X. DOI: 10.1016/j.crad.2019.12.023.

[156] D. Delle Cave, R. Rizzo, B. Sainz, G. Gigli, L. L. Del Mercato, and E. Lonardo, "The Revolutionary Roads to Study Cell-Cell Interactions in 3D In Vitro Pancreatic Cancer Models", *Cancers*, vol. 13, no. 4, p. 930, Feb. 23, 2021, ISSN: 2072-6694. DOI: 10.3390/cancers13040930.

[157] M. R. Haque, T. H. Rempert, T. A. Al-Hilal, C. Wang, A. Bhushan, and F. Bishehsari, "Organ-Chip Models: Opportunities for Precision Medicine in Pancreatic Cancer", *Cancers*, vol. 13, no. 17, p. 4487, Sep. 6, 2021, ISSN: 2072-6694. DOI: 10.3390/cancers13174487.

[158] H. Mollica, Y. J. Teo, A. S. M. Tan, *et al.*, "A 3D pancreatic tumor model to study T cell infiltration", *Biomaterials Science*, vol. 9, no. 22, pp. 7420–7431, Nov. 9, 2021, ISSN: 2047-4849. DOI: 10.1039/D1BM00210D.

[159] D.-H. T. Nguyen, E. Lee, S. Alimperti, *et al.*, "A biomimetic pancreatic cancer on-chip reveals endothelial ablation via ALK7 signaling", *Science Advances*, vol. 5, no. 8, eaav6789, Aug. 2019, ISSN: 2375-2548. DOI: 10.1126/sciadv.aav6789.

[160] D. Osuna de la Peña, S. M. D. Trabulo, E. Collin, *et al.*, "Bioengineered 3D models of human pancreatic cancer recapitulate in vivo tumour biology", *Nature Communications*, vol. 12, no. 1, p. 5623, 1 Sep. 24, 2021, ISSN: 2041-1723. DOI: 10.1038/s41467-021-25921-9.

[161] B. Schuster, M. Junkin, S. S. Kashaf, *et al.*, "Automated microfluidic platform for dynamic and combinatorial drug screening of tumor organoids", *Nature Communications*, vol. 11, no. 1, p. 5271, 1 Oct. 19, 2020, ISSN: 2041-1723. DOI: 10.1038/s41467-020-19058-4.

[162] V. Brancato, V. Comunanza, G. Imparato, *et al.*, "Bioengineered tumoral microtissues recapitulate desmoplastic reaction of pancreatic cancer", *Acta Biomaterialia*, vol. 49, pp. 152–166, Feb. 2017, ISSN: 1878-7568. DOI: 10.1016/j.actbio.2016.11.072.

[163] B. F. L. Lai, R. X. Z. Lu, Y. Hu, *et al.*, "Recapitulating Pancreatic Tumor Microenvironment through Synergistic Use of Patient Organoids and Organ-on-a-Chip Vasculature", *Advanced Functional Materials*, vol. 30, no. 48, p. 2 000 545, 2020, ISSN: 1616-3028. DOI: 10.1002/adfm.202000545.

[164] G. Lazzari, V. Nicolas, M. Matsusaki, M. Akashi, P. Couvreur, and S. Mura, "Multicellular spheroid based on a triple co-culture: A novel 3D model to mimic pancreatic tumor complexity", *Acta Biomaterialia*, vol. 78, pp. 296–307, Sep. 15, 2018, ISSN: 1878-7568. DOI: 10.1016/j.actbio.2018.08.008.

[165] M. V. Monteiro, M. Rocha, V. M. Gaspar, and J. F. Mano, "Programmable Living Units for Emulating Pancreatic Tumor-Stroma Interplay", *Advanced Healthcare Materials*, vol. 11, no. 13, e2102574, Jul. 2022, ISSN: 2192-2659. DOI: 10.1002/adhm.202102574.

[166] E. Tomás-Bort, M. Kieler, S. Sharma, J. B. Candido, and D. Loessner, "3D approaches to model the tumor microenvironment of pancreatic cancer", *Theranostics*, vol. 10, no. 11, pp. 5074–5089, Apr. 6, 2020, ISSN: 1838-7640. DOI: 10.7150/thno.42441.

[167] G. Wishart, P. Gupta, G. Schettino, A. Nisbet, and E. Velliou, "3d tissue models as tools for radiotherapy screening for pancreatic cancer", *The British Journal of Radiology*, vol. 94, no. 1120, p. 20 201 397, Apr. 1, 2021, ISSN: 1748-880X. DOI: 10.1259/bjr.20201397.

[168] B. Gündel, X. Liu, M. Löhr, and R. Heuchel, "Pancreatic Ductal Adenocarcinoma: Preclinical in vitro and ex vivo Models", *Frontiers in Cell and Developmental Biology*, vol. 9, 2021, ISSN: 2296-634X.

[169] B. Uzunparmak and I. H. Sahin, "Pancreatic cancer microenvironment: a current dilemma", *Clinical and Translational Medicine*, vol. 8, p. 2, Jan. 15, 2019, ISSN: 2001-1326. DOI: 10.1186/s40169-019-0221-1.

[170] Y. Yu, G. Yang, H. Huang, *et al.*, "Preclinical models of pancreatic ductal adenocarcinoma: challenges and opportunities in the era of precision medicine", *Journal of experimental & clinical cancer research: CR*, vol. 40, no. 1, p. 8, Jan. 5, 2021, ISSN: 1756-9966. DOI: 10.1186/s13046-020-01787-5.

[171] M. Hajiabbas, C. D'Agostino, J. Simińska-Stanny, S. D. Tran, A. Shavandi, and C. Delporte, "Bioengineering in salivary gland regeneration", *Journal of Biomedical Science*, vol. 29, no. 1, p. 35, Jun. 6, 2022, ISSN: 1423-0127. DOI: 10.1186/s12929-022-00819-w.

[172] J. Kota, J. Hancock, J. Kwon, and M. Korc, "Pancreatic cancer: Stroma and its current and emerging targeted therapies", *Cancer Letters*, vol. 391, pp. 38–49, Apr. 10, 2017, ISSN: 1872-7980. DOI: 10.1016/j.canlet.2016.12.035.

[173]   S. P. Pothula, R. C. Pirola, J. S. Wilson, and M. V. Apte, "Pancreatic stellate cells: Aiding
        and abetting pancreatic cancer progression", *Pancreatology: official journal of the
        International Association of Pancreatology (IAP) … [et al.]*, vol. 20, no. 3, pp. 409–418,
        Apr. 2020, ISSN: 1424-3911. DOI: 10.1016/j.pan.2020.01.003.

[174]   A. M. Charbonneau, J. M. Kinsella, and S. D. Tran, "3D Cultures of Salivary Gland Cells
        in Native or Gelled Egg Yolk Plasma, Combined with Egg White and 3D-Printing of
        Gelled Egg Yolk Plasma", *Materials (Basel, Switzerland)*, vol. 12, no. 21, p. 3480, Oct. 24,
        2019, ISSN: 1996-1944. DOI: 10.3390/ma12213480.

[175]   P. Gupta, P. A. Pérez-Mancera, H. Kocher, A. Nisbet, G. Schettino, and E. G. Velliou, "A
        Novel Scaffold-Based Hybrid Multicellular Model for Pancreatic Ductal Adenocarci-
        noma—Toward a Better Mimicry of the in vivo Tumor Microenvironment", *Frontiers
        in Bioengineering and Biotechnology*, vol. 8, p. 290, Apr. 24, 2020, ISSN: 2296-4185. DOI:
        10.3389/fbioe.2020.00290.

[176]   P. Jain, H. Kathuria, and N. Dubey, "Advances in 3D bioprinting of tissues/organs for
        regenerative medicine and in-vitro models", *Biomaterials*, vol. 287, p. 121 639, Jun. 20,
        2022, ISSN: 1878-5905. DOI: 10.1016/j.biomaterials.2022.121639.

[177]   S. M. Venis, H.-r. Moon, Y. Yang, S. M. Utturkar, S. F. Konieczny, and B. Han, "Engi-
        neering of a functional pancreatic acinus with reprogrammed cancer cells by induced
        PTF1a expression", *Lab on a chip*, vol. 21, no. 19, pp. 3675–3685, Sep. 28, 2021, ISSN:
        1473-0197. DOI: 10.1039/d1lc00350j.

[178]   A. Sola, J. Bertacchini, D. D'Avella, *et al.*, "Development of solvent-casting particulate
        leaching (SCPL) polymer scaffolds as improved three-dimensional supports to mimic
        the bone marrow niche", *Materials Science and Engineering: C*, vol. 96, pp. 153–165,
        Mar. 1, 2019, ISSN: 0928-4931. DOI: 10.1016/j.msec.2018.10.086.

[179]   C. Wex, M. Fröhlich, K. Brandstädter, C. Bruns, and A. Stoll, "Experimental analysis of
        the mechanical behavior of the viscoelastic porcine pancreas and preliminary case
        study on the human pancreas", *Journal of the Mechanical Behavior of Biomedical
        Materials*, vol. 41, pp. 199–207, Jan. 1, 2015, ISSN: 1751-6161. DOI: 10.1016/j.jmbbm.
        2014.10.013.

[180]   G. M. Lee, S.-j. Kim, E. M. Kim, *et al.*, "Free radical-scavenging composite gelatin
        methacryloyl hydrogels for cell encapsulation", *Acta Biomaterialia*, vol. 149, pp. 96–
        110, Sep. 1, 2022, ISSN: 1742-7061. DOI: 10.1016/j.actbio.2022.06.043.

[181]   M. Cortesi, M. Zanoni, F. Pirini, *et al.*, "Pancreatic Cancer and Cellular Senescence:
        Tumor Microenvironment under the Spotlight", *International Journal of Molecular Sci-
        ences*, vol. 23, no. 1, p. 254, Dec. 27, 2021, ISSN: 1422-0067. DOI: 10.3390/ijms23010254.

[182]   B. Farrow, D. Albo, and D. H. Berger, "The role of the tumor microenvironment in the
        progression of pancreatic cancer", *The Journal of Surgical Research*, vol. 149, no. 2,
        pp. 319–328, Oct. 2008, ISSN: 1095-8673. DOI: 10.1016/j.jss.2007.12.757.

[183] K. Gardian, S. Janczewska, W. L. Olszewski, and M. Durlik, "Analysis of Pancreatic Cancer Microenvironment: Role of Macrophage Infiltrates and Growth Factors Expression", *Journal of Cancer*, vol. 3, pp. 285–291, Jul. 1, 2012, ISSN: 1837-9664. DOI: 10.7150/jca.4537.

[184] M. Hadden, A. Mittal, J. Samra, H. Zreiqat, S. Sahni, and Y. Ramaswamy, "Mechanically stressed cancer microenvironment: Role in pancreatic cancer progression", *Biochimica et Biophysica Acta (BBA) - Reviews on Cancer*, vol. 1874, no. 2, p. 188 418, Dec. 1, 2020, ISSN: 0304-419X. DOI: 10.1016/j.bbcan.2020.188418.

[185] P. Procacci, C. Moscheni, P. Sartori, M. Sommariva, and N. Gagliano, "Tumor–Stroma Cross-Talk in Human Pancreatic Ductal Adenocarcinoma: A Focus on the Effect of the Extracellular Matrix on Tumor Cell Phenotype and Invasive Potential", *Cells*, vol. 7, no. 10, p. 158, Oct. 5, 2018, ISSN: 2073-4409. DOI: 10.3390/cells7100158.

[186] D. Thomas and P. Radhakrishnan, "Tumor-stromal crosstalk in pancreatic cancer and tissue fibrosis", *Molecular Cancer*, vol. 18, p. 14, Jan. 21, 2019, ISSN: 1476-4598. DOI: 10.1186/s12943-018-0927-5.

[187] W. J. Ho, E. M. Jaffee, and L. Zheng, "The tumour microenvironment in pancreatic cancer - clinical challenges and opportunities", *Nature Reviews. Clinical Oncology*, vol. 17, no. 9, pp. 527–540, Sep. 2020, ISSN: 1759-4782. DOI: 10.1038/s41571-020-0363-5.

[188] N. Sperb, M. Tsesmelis, and T. Wirth, "Crosstalk between Tumor and Stromal Cells in Pancreatic Ductal Adenocarcinoma", *International Journal of Molecular Sciences*, vol. 21, no. 15, p. 5486, Jul. 31, 2020, ISSN: 1422-0067. DOI: 10.3390/ijms21155486.

[189] J. Gehlen, W. Qiu, R. Müller, and X.-H. Qin, "Volumetric Tomographic 3D Bioprinting of Heterocellular Bone-like Tissues in Seconds", *bioRxiv*, 2021. DOI: 10.1101/2021.11.14.468504.

[190] C. K. Bektas and V. Hasirci, "Cell loaded 3D bioprinted GelMA hydrogels for corneal stroma engineering", *Biomaterials Science*, vol. 8, no. 1, pp. 438–449, Dec. 17, 2019, ISSN: 2047-4849. DOI: 10.1039/C9BM01236B.

[191] C. Colosi, S. R. Shin, V. Manoharan, *et al.*, "Microfluidic Bioprinting of Heterogeneous 3D Tissue Constructs Using Low-Viscosity Bioink", *Advanced Materials*, vol. 28, no. 4, pp. 677–684, 2016, ISSN: 1521-4095. DOI: 10.1002/adma.201503310.

[192] B. J. Klotz, D. Gawlitta, A. J. W. P. Rosenberg, J. Malda, and F. P. W. Melchels, "Gelatin-Methacryloyl Hydrogels: Towards Biofabrication-Based Tissue Repair", *Trends in Biotechnology*, vol. 34, no. 5, pp. 394–407, May 1, 2016, ISSN: 0167-7799. DOI: 10.1016/j.tibtech.2016.01.002.

[193] R. Leu Alexa, H. Iovu, J. Ghitman, *et al.*, "3D-Printed Gelatin Methacryloyl-Based Scaffolds with Potential Application in Tissue Engineering", *Polymers*, vol. 13, no. 5, p. 727, 5 Jan. 2021, ISSN: 2073-4360. DOI: 10.3390/polym13050727.

[194]   L. Moroni, T. Boland, J. A. Burdick, *et al.*, "Biofabrication: A Guide to Technology and Terminology", *Trends in Biotechnology*, vol. 36, no. 4, pp. 384–402, Apr. 2018, ISSN: 01677799. DOI: 10.1016/j.tibtech.2017.10.015.

[195]   H.-r. Moon, A. Ozcelikkale, Y. Yang, B. D. Elzey, S. F. Konieczny, and B. Han, "An engineered pancreatic cancer model with intra-tumoral heterogeneity of driver mutations", *Lab on a Chip*, vol. 20, no. 20, pp. 3720–3732, Oct. 13, 2020, ISSN: 1473-0189. DOI: 10.1039/D0LC00707B.

[196]   A. R. Freischel, M. Damaghi, J. J. Cunningham, *et al.*, "Frequency-dependent interactions determine outcome of competition between two breast cancer cell lines", *Scientific Reports*, vol. 11, no. 1, p. 4908, 1 Mar. 1, 2021, ISSN: 2045-2322. DOI: 10.1038/s41598-021-84406-3.

[197]   V. Sgarminato, C. Tonda-Turo, and G. Ciardelli, "Reviewing recently developed technologies to direct cell activity through the control of pore size: From the macro- to the nanoscale", *Journal of Biomedical Materials Research. Part B, Applied Biomaterials*, vol. 108, no. 4, pp. 1176–1185, May 2020, ISSN: 1552-4981. DOI: 10.1002/jbm.b.34467.

[198]   T. L. Downing, J. Soto, C. Morez, *et al.*, "Biophysical regulation of epigenetic state and cell reprogramming", *Nature Materials*, vol. 12, no. 12, pp. 1154–1162, 12 Dec. 2013, ISSN: 1476-4660. DOI: 10.1038/nmat3777.

[199]   S. Randriamanantsoa, A. Papargyriou, H. C. Maurer, *et al.*, "Spatiotemporal dynamics of self-organized branching in pancreas-derived organoids", *Nature Communications*, vol. 13, no. 1, p. 5219, 1 Sep. 5, 2022, ISSN: 2041-1723. DOI: 10.1038/s41467-022-32806-y.

[200]   Y. Fang and R. M. Eglen, "Three-Dimensional Cell Cultures in Drug Discovery and Development", *Slas Discovery*, vol. 22, no. 5, pp. 456–472, Jun. 2017, ISSN: 2472-5552. DOI: 10.1177/1087057117696795.

[201]   M. W. Laschke and M. D. Menger, "Life is 3D: Boosting Spheroid Function for Tissue Engineering", *Trends in Biotechnology*, vol. 35, no. 2, pp. 133–144, Feb. 2017, ISSN: 1879-3096. DOI: 10.1016/j.tibtech.2016.08.004.

[202]   R. Sears, B. Allen-Petersen, and E. Langer, "Three-dimensional bioprinted pancreatic tumor model", pat. WO2016022830A1, Feb. 11, 2016. [Online]. Available: https://patents.google.com/patent/WO2016022830A1/en (visited on 08/02/2023).

[203]   A. Paszke, S. Gross, F. Massa, *et al.* "PyTorch: An Imperative Style, High-Performance Deep Learning Library". (Dec. 3, 2019), [Online]. Available: http://arxiv.org/abs/1912.01703 (visited on 08/01/2023), preprint.

[204]   M. Fujiwara, K. Kanayama, Y. S. Hirokawa, and T. Shiraishi, "ASF-4-1 fibroblast-rich culture increases chemoresistance and mTOR expression of pancreatic cancer BxPC-3 cells at the invasive front in vitro, and promotes tumor growth and invasion in vivo", *Oncology Letters*, vol. 11, no. 4, pp. 2773–2779, Apr. 2016, ISSN: 1792-1074. DOI: 10.3892/ol.2016.4289.

[205] S.-Y. Jeong, J.-H. Lee, Y. Shin, S. Chung, and H.-J. Kuh, "Co-Culture of Tumor Spheroids and Fibroblasts in a Collagen Matrix-Incorporated Microfluidic Chip Mimics Reciprocal Activation in Solid Tumor Microenvironment", *PloS One*, vol. 11, no. 7, e0159013, 2016, ISSN: 1932-6203. DOI: 10.1371/journal.pone.0159013.

[206] J.-H. Lee, S.-K. Kim, I. A. Khawar, S.-Y. Jeong, S. Chung, and H.-J. Kuh, "Microfluidic co-culture of pancreatic tumor spheroids with stellate cells as a novel 3D model for investigation of stroma-mediated cell motility and drug resistance", *Journal of experimental & clinical cancer research: CR*, vol. 37, no. 1, p. 4, Jan. 12, 2018, ISSN: 1756-9966. DOI: 10.1186/s13046-017-0654-6.

[207] V. Sgarminato, S. Luigi Marasso, M. Cocuzza, *et al.*, "PDAC-on-chip for in vitro modeling of stromal and pancreatic cancer cell crosstalk", *Biomaterials Science*, vol. 11, no. 1, pp. 208–224, 2023. DOI: 10.1039/D2BM00881E.

[208] D. Van der Weken, M. Nachtegael, and E. E. Kerre, "Using similarity measures and homogeneity for the comparison of images", *Image and Vision Computing*, vol. 22, no. 9, pp. 695–702, Aug. 20, 2004, ISSN: 0262-8856. DOI: 10.1016/j.imavis.2004.03.002.

[209] S. Preibisch, S. Saalfeld, and P. Tomancak, "Globally optimal stitching of tiled 3D microscopic image acquisitions", *Bioinformatics*, vol. 25, no. 11, pp. 1463–1465, Jun. 1, 2009, ISSN: 1367-4803. DOI: 10.1093/bioinformatics/btp184.

[210] J. D. Hunter, "Matplotlib: A 2D graphics environment", *Computing in Science & Engineering*, vol. 9, no. 3, pp. 90–95, 2007. DOI: 10.1109/MCSE.2007.55.

[211] M. Waskom, "Seaborn: Statistical data visualization", *Journal of Open Source Software*, vol. 6, no. 60, p. 3021, Apr. 6, 2021, ISSN: 2475-9066. DOI: 10.21105/joss.03021.

[212] W. McKinney, "Data Structures for Statistical Computing in Python", presented at the Python in Science Conference, Austin, Texas, 2010, pp. 56–61. DOI: 10.25080/Majora-92bf1922-00a. [Online]. Available: https://conference.scipy.org/proceedings/scipy2010/mckinney.html (visited on 08/01/2023).

[213] D. de Faoite, D. J. Browne, F. R. Chang-Díaz, and K. T. Stanton, "A review of the processing, composition, and temperature-dependent mechanical and thermal properties of dielectric technical ceramics", *Journal of Materials Science*, vol. 47, no. 10, pp. 4211–4235, Dec. 2011. DOI: 10.1007/s10853-011-6140-1.

[214] S. Fu, M. Zhu, and Y. Zhu, "Organosilicon polymer-derived ceramics: An overview", *Journal of Advanced Ceramics*, vol. 8, no. 4, pp. 457–478, Dec. 2019. DOI: 10.1007/s40145-019-0335-3.

[215] P. Greil, "Advanced engineering ceramics", *Advanced Engineering Materials*, vol. 4, no. 5, pp. 247–254, 2002.

[216] R. He, W. Liu, Z. Wu, *et al.*, "Fabrication of complex-shaped zirconia ceramic parts via a DLP- stereolithography-based 3D printing method", *Ceramics International*, vol. 44, no. 3, pp. 3412–3416, Feb. 2018. DOI: 10.1016/j.ceramint.2017.11.135.

[217]   R. Janssen, S. Scheppokat, and N. Claussen, "Tailor-made ceramic-based compo-
        nents—Advantages by reactive processing and advanced shaping techniques", *Journal
        of the European Ceramic Society*, vol. 28, no. 7, pp. 1369–1379, 2008, ISSN: 0955-2219.
        DOI: 10.1016/j.jeurceramsoc.2007.12.022.

[218]   E. Zanchetta, M. Cattaldo, G. Franchin, *et al.*, "Stereolithography of SiOC Ceramic
        Microcomponents", *Advanced Materials*, vol. 28, no. 2, pp. 370–376, 2016, ISSN: 1521-
        4095. DOI: 10.1002/adma.201503470.

[219]   L.-A. Liew, Y. Liu, R. Luo, *et al.*, "Fabrication of SiCN MEMS by photopolymerization of
        pre-ceramic polymer", *Sensors and Actuators A: Physical*, Papers from the Proceedings
        of the 14th IEEE Internat. Conf. on MicroElectroMechanical Systems, vol. 95, no. 2,
        pp. 120–134, Jan. 1, 2002, ISSN: 0924-4247. DOI: 10.1016/S0924-4247(01)00723-3.

[220]   P. Colombo, G. Mera, R. Riedel, and G. D. Sorarù, "Polymer-Derived Ceramics: 40 Years
        of Research and Innovation in Advanced Ceramics", *Journal of the American Ceramic
        Society*, vol. 93, no. 7, pp. 1805–1837, 2010, ISSN: 1551-2916. DOI: 10.1111/j.1551-
        2916.2010.03876.x.

[221]   M. Schwentenwein, P. Schneider, and J. Homa, "Lithography-based ceramic manufac-
        turing: A novel technique for additive manufacturing of high-performance ceramics",
        in *Advances in Science and Technology*, vol. 88, Trans Tech Publ, 2014, pp. 60–64.

[222]   J. Schmidt and P. Colombo, "Digital light processing of ceramic components from
        polysiloxanes", *Journal of the European Ceramic Society*, vol. 38, no. 1, pp. 57–66, 2018.

[223]   T. A. Pham, D.-P. Kim, T.-W. Lim, S.-H. Park, D.-Y. Yang, and K.-S. Lee, "Three-dimensional
        SiCN ceramic microstructures via nano-stereolithography of inorganic polymer pho-
        toresists", *Advanced Functional Materials*, vol. 16, no. 9, pp. 1235–1241, 2006.

[224]   L. Brigo, J. E. M. Schmidt, A. Gandin, N. Michieli, P. Colombo, and G. Brusatin, "3D
        Nanofabrication of SiOC Ceramic Structures", *Advanced Science*, vol. 5, no. 12, p. 1 800 937,
        Oct. 23, 2018, ISSN: 2198-3844. DOI: 10.1002/advs.201800937.

[225]   G. Konstantinou, E. Kakkava, L. Hagelüken, *et al.*, "Additive micro-manufacturing of
        crack-free PDCs by two-photon polymerization of a single, low-shrinkage preceramic
        resin", *Additive Manufacturing*, vol. 35, p. 101 343, Oct. 1, 2020, ISSN: 2214-8604. DOI:
        10.1016/j.addma.2020.101343.

[226]   J. Lalevée and J.-P. Fouassier, *Dyes and Chromophores in Polymer Science.* John Wiley &
        Sons, 2015.

[227]   A. Eibel, D. E. Fast, and G. Gescheidt, "Choosing the ideal photoinitiator for free radi-
        cal photopolymerizations: Predictions based on simulations using established data",
        Polymer Chemistry, vol. 9, no. 41, pp. 5107–5115, 2018.

[228]   G. Mera, A. Navrotsky, S. Sen, H.-J. Kleebe, and R. Riedel, "Polymer -derived SiCN
        and SiOC ceramics – structure and energetics at the nanoscale", *Journal of Materials
        Chemistry A*, vol. 1, no. 12, pp. 3826–3836, 2013. DOI: 10.1039/C2TA00727D.

[229]   M. Graczyk-Zajac, L. Toma, C. Fasel, and R. Riedel, "Carbon-rich SiOC anodes for lithium-ion batteries: Part I. Influence of material UV-pre-treatment on high power properties", *Solid State Ionics*, Solid State Ionics 18 Proceedings of the 18th International Conference on Solid State Ionics Warsaw, Poland, July 3 -8, 2011, vol. 225, pp. 522–526, Oct. 4, 2012, ISSN: 0167-2738. DOI: 10.1016/j.ssi.2011.12.007.

[230]   J. Kaspar, M. Graczyk-Zajac, and R. Riedel, "Carbon-rich SiOC anodes for lithium-ion batteries: Part II. Role of thermal cross-linking", *Solid State Ionics*, Solid State Ionics 18 Proceedings of the 18th International Conference on Solid State Ionics Warsaw, Poland, July 3 -8, 2011, vol. 225, pp. 527–531, Oct. 4, 2012, ISSN: 0167-2738. DOI: 10.1016/j.ssi.2012.01.026.

[231]   P. V. W. Sasikumar, G. Blugan, N. Casati, *et al.*, "Polymer derived silicon oxycarbide ceramic monoliths: Microstructure development and associated materials properties", *Ceramics International*, vol. 44, no. 17, pp. 20 961–20 967, Dec. 1, 2018, ISSN: 0272-8842. DOI: 10.1016/j.ceramint.2018.08.102.

[232]   B. C. Smith, "Group Wavenumbers and an Introduction to the Spectroscopy of Benzene Rings", *Spectroscopy*, vol. 31, no. 3, pp. 34–37, Mar. 2016, ISSN: 08876703.

[233]   A. Łapiński, J. Spanget-Larsen, M. Langgård, J. Waluk, and J. G. Radziszewski, "Raman Spectrum of the Phenyl Radical", *The Journal of Physical Chemistry A*, vol. 105, no. 46, pp. 10 520–10 524, Nov. 1, 2001, ISSN: 1089-5639. DOI: 10.1021/jp0114900.

[234]   D. S. Knight and W. B. White, "Characterization of diamond films by Raman spectroscopy", *Journal of Materials Research*, vol. 4, no. 2, pp. 385–393, Mar. 1, 1989, ISSN: 2044-5326. DOI: 10.1557/JMR.1989.0385.

[235]   T. Jiang, Y. Wang, Y. Wang, N. Orlovskaya, and L. An, "Quantitative Raman Analysis of Free Carbon in Polymer-Derived Ceramics", *Journal of the American Ceramic Society*, vol. 92, no. 10, pp. 2455–2458, 2009, ISSN: 1551-2916. DOI: 10.1111/j.1551-2916.2009.03233.x.

[236]   A. B. Kousaalya, X. Zeng, M. Karakaya, T. Tritt, S. Pilla, and A. M. Rao, "Polymer-Derived Silicon Oxycarbide Ceramics as Promising Next-Generation Sustainable Thermoelectrics", *ACS Applied Materials & Interfaces*, vol. 10, no. 3, pp. 2236–2241, Jan. 24, 2018, ISSN: 1944-8244. DOI: 10.1021/acsami.7b17394.

[237]   G. D. Sorarù, G. D'Andrea, and A. Glisenti, "XPS characterization of gel-derived silicon oxycarbide glasses", *Materials Letters*, vol. 27, no. 1, pp. 1–5, May 1, 1996, ISSN: 0167-577X. DOI: 10.1016/0167-577X(95)00245-6.

[238]   R. J. P. Corriu, D. Leclercq, P. H. Mutin, and A. Vioux, "Preparation and structure of silicon oxycarbide glasses derived from polysiloxane precursors", *Journal of Sol-Gel Science and Technology*, vol. 8, no. 1, pp. 327–330, Feb. 1, 1997, ISSN: 1573-4846. DOI: 10.1007/BF02436860.

[239] J. Kaspar, M. Graczyk-Zajac, and R. Riedel, "Lithium insertion into carbon-rich SiOC ceramics: Influence of pyrolysis temperature on electrochemical properties", *Journal of Power Sources*, 16th International Meeting on Lithium Batteries (IMLB), vol. 244, pp. 450–455, Dec. 15, 2013, ISSN: 0378-7753. DOI: 10.1016/j.jpowsour.2012.11.086.

[240] C. Sugie, A. Navrotsky, S. Lauterbach, H.-J. Kleebe, and G. Mera, "Structure and Thermodynamics of Silicon Oxycarbide Polymer-Derived Ceramics with and without Mixed-Bonding", *Materials*, vol. 14, no. 15, p. 4075, 15 Jan. 2021, ISSN: 1996-1944. DOI: 10.3390/ma14154075.

[241] J. A. Gardella, S. A. Ferguson, and R. L. Chin, "* ← Shakeup Satellites for the Analysis of Structure and Bonding in Aromatic Polymers by X-Ray Photoelectron Spectroscopy", *Applied Spectroscopy*, vol. 40, no. 2, pp. 224–232, Feb. 1, 1986, ISSN: 0003-7028. DOI: 10.1366/0003702864509565.

[242] J. M. Hundley, Z. C. Eckel, E. Schueller, *et al.*, "Geometric characterization of additively manufactured polymer derived ceramics", *Additive Manufacturing*, vol. 18, pp. 95–102, Dec. 1, 2017, ISSN: 2214-8604. DOI: 10.1016/j.addma.2017.08.009.

[243] U. K. Roopavath, S. Malferrari, A. Van Haver, F. Verstreken, S. N. Rath, and D. M. Kalaskar, "Optimization of extrusion based ceramic 3D printing process for complex bony designs", *Materials & Design*, vol. 162, pp. 263–270, Jan. 15, 2019, ISSN: 0264-1275. DOI: 10.1016/j.matdes.2018.11.054.

[244] A. Erben, T. Kellerer, J. Lissner, *et al.* "Engineering Principles and Algorithmic Design Synthesis for Ultracompact Bio-Hybrid Perfusion Chip". (Mar. 18, 2022), [Online]. Available: https://www.biorxiv.org/content/10.1101/2022.03.16.484492v1 (visited on 10/11/2023), preprint.

[245] G. Strano, L. Hao, R. M. Everson, and K. E. Evans, "A new approach to the design and optimisation of support structures in additive manufacturing", *The International Journal of Advanced Manufacturing Technology*, vol. 66, no. 9, pp. 1247–1254, Jun. 1, 2013, ISSN: 1433-3015. DOI: 10.1007/s00170-012-4403-x.

[246] J. Jang, P. V. Warriam Sasikumar, F. Navaee, L. Hagelüken, G. Blugan, and J. Brugger, "Electrochemical performance of polymer-derived SiOC and SiTiOC ceramic electrodes for artificial cardiac pacemaker applications", *Ceramics International*, vol. 47, no. 6, pp. 7593–7601, Mar. 15, 2021, ISSN: 0272-8842. DOI: 10.1016/j.ceramint.2020.11.098.

[247] S. Packirisamy, K. J. Sreejith, D. Devapal, and B. Swaminathan, "Polymer-Derived Ceramics and Their Space Applications", in *Handbook of Advanced Ceramics and Composites*, Y. R. Mahajan and R. Johnson, Eds., Cham: Springer International Publishing, 2020, pp. 975–1080, ISBN: 978-3-030-16346-4 978-3-030-16347-1. DOI: 10.1007/978-3-030-16347-1_31.

[248] I. Cooperstein, E. Shukrun, O. Press, A. Kamyshny, and S. Magdassi, "Additive manufacturing of transparent silica glass from solutions", *ACS applied materials & interfaces*, vol. 10, no. 22, pp. 18879–18885, 2018.

[249] J. Klein, M. Stern, G. Franchin, *et al.*, "Additive manufacturing of optically transparent glass", *3D printing and additive manufacturing*, vol. 2, no. 3, pp. 92–105, 2015.

[250] F. Kotz, K. Arnold, W. Bauer, *et al.*, "Three-dimensional printing of transparent fused silica glass", *Nature*, vol. 544, no. 7650, pp. 337–339, 2017.

[251] C. Liu, B. Qian, X. Liu, L. Tong, and J. Qiu, "Additive manufacturing of silica glass using laser stereolithography with a top-down approach and fast debinding", *RSC advances*, vol. 8, no. 29, pp. 16 344–16 348, 2018.

[252] D. G. Moore, L. Barbera, K. Masania, and A. R. Studart, "Three-dimensional printing of multicomponent glasses using phase-separating resins", *Nature materials*, vol. 19, no. 2, pp. 212–217, 2020.

[253] D. T. Nguyen, C. Meyers, T. D. Yee, *et al.*, "3D-Printed Transparent Glass", *Advanced Materials*, vol. 29, no. 26, p. 1 701 181, Jul. 2017, ISSN: 09359648. DOI: 10.1002/adma.201701181.

[254] Z. Hong, P. Ye, D. A. Loy, and R. Liang, "High-precision printing of complex glass imaging optics with precondensed liquid silica resin", *Advanced Science*, vol. 9, no. 18, p. 2 105 595, 2022.

[255] X. Wen, B. Zhang, W. Wang, *et al.*, "3D-printed silica with nanoscale resolution", *Nature Materials*, vol. 20, no. 11, pp. 1506–1511, 2021, ISSN: 1476-4660.

[256] M. Wozniak, T. Graule, Y. de Hazan, D. Kata, and J. Lis, "Highly loaded UV curable nanosilica dispersions for rapid prototyping applications", *Journal of the European Ceramic Society*, vol. 29, no. 11, pp. 2259–2265, 2009.

[257] R. Arita, M. Iijima, Y. Fujishiro, *et al.*, "Rapid three-dimensional structuring of transparent SiO2 glass using interparticle photo-cross-linkable suspensions", *Communications Materials*, vol. 1, no. 1, p. 30, 2020.

[258] Y. Xu, Y. Li, N. Zheng, Q. Zhao, and T. Xie, "Transparent origami glass", *Nature Communications*, vol. 12, no. 1, p. 4261, 2021.

[259] P. Maniewski, F. Laurell, and M. Fokine, "Quill-free additive manufacturing of fused silica glass", *Optical Materials Express*, vol. 12, no. 4, pp. 1480–1490, 2022.

[260] J. F. Destino, N. A. Dudukovic, M. A. Johnson, *et al.*, "3D printed optical quality silica and silica–titania glasses from sol–gel feedstocks", *Advanced Materials Technologies*, vol. 3, no. 6, p. 1 700 323, 2018.

[261] T. Doualle, J.-C. André, and L. Gallais, "3D printing of silica glass through a multiphoton polymerization process", *Optics Letters*, vol. 46, no. 2, pp. 364–367, 2021.

[262] F. Kotz, A. S. Quick, P. Risch, *et al.*, "Two-photon polymerization of nanocomposites for the fabrication of transparent fused silica glass microstructures", *Advanced Materials*, vol. 33, no. 9, p. 2 006 341, 2021.

[263] C. Liu, B. Qian, R. Ni, X. Liu, and J. Qiu, "3D printing of multicolor luminescent glass", *RSC advances*, vol. 8, no. 55, pp. 31 564–31 567, 2018.

[264] B. Nan, P. Gołębiewski, R. Buczyński, F. J. Galindo-Rosales, and J. M. Ferreira, "Direct ink writing glass: a preliminary step for optical application", *Materials*, vol. 13, no. 7, p. 1636, 2020.

[265] P. Cai, L. Guo, L. Liu, Q. Zhang, J. Li, and Q. Lue, "Rapid manufacturing of silica glass parts with complex structures through stereolithography and pressureless spark plasma sintering", *Ceramics International*, vol. 48, no. 1, pp. 55–63, 2022.

[266] Z. Hong, P. Ye, D. A. Loy, and R. Liang, "Three-dimensional printing of glass micro-optics", *Optica*, vol. 8, no. 6, pp. 904–910, 2021.

[267] J. Luo, L. J. Gilbert, C. Qu, R. G. Landers, D. A. Bristow, and E. C. Kinzel, "Additive manufacturing of transparent soda-lime glass using a filament-fed process", *Journal of Manufacturing Science and Engineering*, vol. 139, no. 6, p. 061 006, 2017.

[268] M. Wozniak, Y. de Hazan, T. Graule, and D. Kata, "Rheology of UV curable colloidal silica dispersions for rapid prototyping applications", *Journal of the European Ceramic Society*, vol. 31, no. 13, pp. 2221–2229, 2011.

[269] C. T. Rueden, J. Schindelin, M. C. Hiner, *et al.*, "ImageJ2: ImageJ for the next generation of scientific image data", *BMC Bioinformatics*, vol. 18, no. 1, pp. 1–26, 2017.

[270] T. Niidome, K. Nakashima, H. Takahashi, and Y. Niidome, "Preparation of primary amine-modified gold nanoparticles and their transfection ability into cultivated cells", *Chemical Communications*, no. 17, pp. 1978–1979, 2004.

JORGE **MADRID WOLFF**
Photonics engineer

Avenue d'Epenex 4B, 1020 Renens, Suisse
+41 077 528 0264
j.madrid.w@gmail.com
Google scholar
10.09.1992

Education

2019 - present	**PhD. in Photonics**
	École polytechnique fédérale de Lausanne (EPFL), Switzerland
	Research on light-based additive manufacturing
2016 – 2019	**Master of Science, Biomedical Engineering**
	Universidad de los Andes, Colombia
	Research fellowship (Feb-Aug 2018) at ICFO – The Institute of Photonic Sciences, Spain
2011 - 2016	**Bachelor of Science, Physics**
	Universidad de los Andes, Colombia
	Exchange (2014) at the Niels Bohr Institute, Copenhagen, Denmark

Projects

2022	**Helical volumetric additive manufacturing**
	École polytechnique fédérale de Lausanne (EPFL), Switzerland
	Co-developed and built a functional prototype of a light-based 3D printer to build multi-cm scale objects within minutes. Wrote the code to integrate hardware (including optomechanics, DMD light modulator, cameras, and light sources).
2019 - present	**Volumetric printing in scattering media**
	École polytechnique fédérale de Lausanne (EPFL), Switzerland
	Developed new software methods to modulate light in 3D printers to enable the fabrication of hollow objects in diffusive media. The method, which is patented and GPU-accelerated, opens new avenues for 3D printing in resins filled with human cells. In close collaboration with the University of Utrecht and the Politecnico di Torino, I have used the method to fabricate models of the liver (Bernal *et al. Advanced Materials* 34.15 (2022)) and pancretic tissue (Sgarminato *et al. bioRxiv* (2023): 2023-01).

2018-2019	**Deep-learning based light field rendering**

Universidad de los Andes, Colombia

Designed a new neural-network architecture (PyTorch) to enhance resolution of depth estimation from light field images.

Spring 2018	**New microscope for fast live imaging**

Research fellowship. ICFO – The Institute of Photonic Sciences, Spain

Designed, built, and tested a fluorescence microscope to image 3D live neural cell cultures. Wrote code to synchronize the image acquisition from a sCMOS camera with the modulation of a tunable lens and the movement of galvo mirrors.

2016-2018	**Volumetric light sheet microscopy**

Universidad de los Andes, Colombia

Designed and assembled a fluorescence microscope combining light-sheet illumination and light field detection. The microscope allowed long (>24h), continuous imaging of live samples, such as transparent fish. The device had improved 3D resolution, and was used to follow the progression of cancerous tumors in the fish.

Skills

Technical competences	Microscopic imaging & optics, spatial light modulators, light-based additive manufacturing, optical metrology, Raman & UV-VIS spectroscopy; fabrication of plastics, ceramics and glass
Software	Scientific programs (MATLAB, ImageJ, iPython) Graphical design (vector graphics illustration), Mechanical design (FreeCAD), Office suite.
Bio	Cell culture, 3D bioprinting, immunofluorescence, live imaging
IT competences	Programming knowledge (MATLAB, Python) with practical experience in image processing and analysis and software-hardware interfaces. Notions of machine learning (TensorFlow, CUDA) and git.
Languages	**Spanish**: native **English**: profficient **French**: profficient **Italian**: intermediate

Publications

Patent | Moser, C., Boniface, A., & Madrid Wolff, J. (2022). *High resolution and three-dimensional printing in complex photosensitive materials* (WO2022243273).

Selected peer-reviewed articles | Madrid-Wolff, J., Boniface, A., Loterie, D., Delrot, P., & Moser, C. (2022). Controlling light in scattering materials for volumetric additive manufacturing. *Advanced Science,* 9(22), 2105144.

Madrid-Wolff, J., Castro, D., Arbeláez, P., & Forero-Shelton, M. (2018, February). Light-sheet enhanced resolution of light field microscopy for rapid imaging of large volumes. In *Three-dimensional and multidimensional microscopy: image acquisition and processing XXV* (Vol. 10499, pp. 148-156). SPIE.

Kollep, M., Konstantinou, G., Madrid-Wolff, J., Boniface, A., Hagelüken, L., Sasikumar, P. V. W., ... & Moser, C. (2022). Tomographic volumetric additive manufacturing of silicon oxycarbide ceramics. *Advanced Engineering Materials*, *24*(7), 2101345.

Boniface, A., Maître, F., Madrid-Wolff, J., Moser, C. Volumetric helical additive manufacturing. *Light: Advanced Manufacturing* 4, 12(2023). doi: 10.37188/lam.2023.012

Personal interests

Running (long distance & relay)
Theater (Member of *Le Vestiaire - Lausanne*)